Development of luminescent lanthanide-based supramolecular and interlocked architectures

A thesis presented in partial fulfilment of the requirements for the degree of

Master of Science

in

Chemistry

at Massey University (Albany), New Zealand.

Gabriela Sansom

2022

Abstract

The chemistry of mechanically interlocked molecules (MIMs), copper(I)-catalyzed azide-alkyne cycloaddition (click) reactions and lanthanide ions each individually are promising targets for the development of advanced luminescent materials, such as responsive molecular sensors and molecular switches.

Herein, the synthesis of a family of dipicolinic acid (DPA) ligands, one containing a propargyl group (**L_1**) and three containing bulky groups (*i.e.* a 1,8-naphthalimide (**L_2**), a *tert*-butylbenzyl (**L_3**) and a 9-anthracene (**L_4**) group) appended to their 4-pyridyl position through CuAAC click chemistry are presented. These groups were chosen based on their ability to sensitize Ln^{3+} emission as well as their potential to act as stopper groups for small macrocycles for the development of quasi-[4]-rotaxanes. **L_1 – L_3** formed highly luminescent complexes with Eu^{3+} and Tb^{3+}. A CuAAC reaction was successfully carried out on a tris-alkyne appended DPA lanthanide complex, **$[La(L_1)_3]^{3-}$**, however synthetic difficulties were faced whilst carrying out the AT-CuAAC derivative for the synthesis of quasi-[4]-rotaxanes. Due to this, slightly different DPA chelating systems were investigated such that they inherited both chelating and stoppering abilities. Thus, a series of methyl-protected DPA rotaxane ligands **R_2 – R_4** were synthesized and **R_3** was proven through photophysical titrations to form Ln^{3+} self-assemblies. UV/Vis titrations supported the formation of 2:1 **R_3**:Ln^{3+} species whereas fluorescence titrations supported the formation of 3:1 **R_3**:Ln^{3+} species (*i.e.* quasi-[4]-rotaxanes), thus further studies are ongoing to confirm this binding ratio. Lastly, preliminary findings regarding the synthesis of amide-protected DPA rotaxane ligands are also presented. The research herein integrates three highly valuable fields of chemistry and provides foundational results for the development of a range of advanced luminescent materials, such as Ln^{3+}-containing interlocked molecules.

Acknowledgements

I would firstly like to express my great appreciation to Dr. Jonathan A. Kitchen for supervising this project. I deeply appreciate the time and effort that you have dedicated towards supporting me over the last few years at Massey University. I would also like to give thanks to Alex T. O’Neil who, throughout my time at Massey, has used his experience to help guide me throughout my post-graduate journey and has provided valuable advice which I will forever be thankful for.

I am also very grateful and thankful for all the staff in the chemistry department at Massey University Albany for their support throughout this study. Thank you to Jade Pope and Erin Moffet (technicians) for generously donating your time to assist my experimental work. Additionally, thank you to Associate Professor John Harrison for your advice as well as for allowing me to carry out photophysical calculations using your spectrophotometer.

I would also like to thank and acknowledge Professor Stephen M. Goldup and the Goldup research group for sharing your experience and wisdom surrounding the chemistry of interlocked molecules as well as for supplying the small macrocycle which was used throughout the study. I also want to express my great appreciation for Trevor Loo from Massey University Palmerston North for making it possible to carry out mass spectrometry as well as Dr. Jack Chen from the Auckland University of Technology for generously allowing me to use their departments spectrophotometer for photophysical characterisations.

Last of all I want to express a big thank you to my family, especially my Mum (Lynn), Dad (Mike) and twin sister (Bianca). Without your support throughout this journey this would not have been possible and I am forever grateful for you all.

Table of Contents

1. Introduction

In society today, technological advancements are being made at ever-increasing rates.[1,2,26] One group of materials proven to be key to these advancements are those incorporating the lanthanide elements, referred to as lanthanide-based luminescent materials.[1-10,13,14,26] Traditionally, our display screens relied off the use of phosphors doped with lanthanides, which served the key role of producing visible light from cathode rays.[1-7,10,26] Additionally, the lanthanides (particularly neodymium) have had a vital role in the development of lasers.[1-5,10,13,14,26] These examples represent just a few of the applications where the lanthanides have established vital roles.[1-6,10,26]

Currently, a large amount of research is being focussed towards extending these applications of these lanthanide-based luminescent materials through the development of novel advanced materials, such as OLEDs (Organic Light Emitting Diodes) and luminescent lanthanide bio-probes (LLBs).[1-6,8-11,13,15-18,28,30] One example is research into the development of rapid, low-invasive methods of COVID-19 detection using lanthanide-doped materials, highlighting the importance of such materials in society today.[19,20]

The scope of this study focusses on the development of switchable luminescent lanthanide-based interlocked/supramolecular architectures, a field currently of high value.[3,6-8,13,17,23,29] These architectures have recently gained significant attention as highly valuable targets for the development of molecular machines, switches and sensors due to their responsive nature.[7,13,17] This property, combined with the photophysical features of lanthanide ions paves the way for the development of a range of responsive luminescent interlocked/architectures whereby changes in conformation (in response to an input) can be tracked/sensed through changes in lanthanide ion emission.[1-4,7,14,15,17,22-24,27-29]

1.1 Lanthanides, the rare earth elements

The lanthanides, commonly described as the ‘rare earth’ elements, exist on the periodic table with atomic numbers ranging from 57 (for lanthanum) to 71 (for lutetium), thus making up 15 elements (Table 1).[1,4-7,10,13,14,21,26] These elements typically exist in aqueous solutions as lanthanide ions with oxidation states of +3 (Table 1).[3-13,17,18,21,22,26,27] These lanthanide ions (Ln^{3+}’s) have electron configurations of $[Xe]4f^x$ (where x represents 4f orbital electron filling from 0 for lanthanum to 14 for lutetium) (Table 1).[2-8,10-14,22,26] The 4f orbitals experience shielding by exterior $5s^2$ and $5p^6$ orbitals, meaning that the electrons within these 4f orbitals only interact very weakly with their external environment, a feature which is key to the unique electronic properties of Ln^{3+}’s.[2-8,10-14,17,21-23,25,26,28,30]

Table 1. Summary of the lanthanides showing the electron configuration in their +3 oxidation state along with their primary emitting wavelengths. Image adapted from: 2, 3, 7, 9, 11, 18, 23, 30

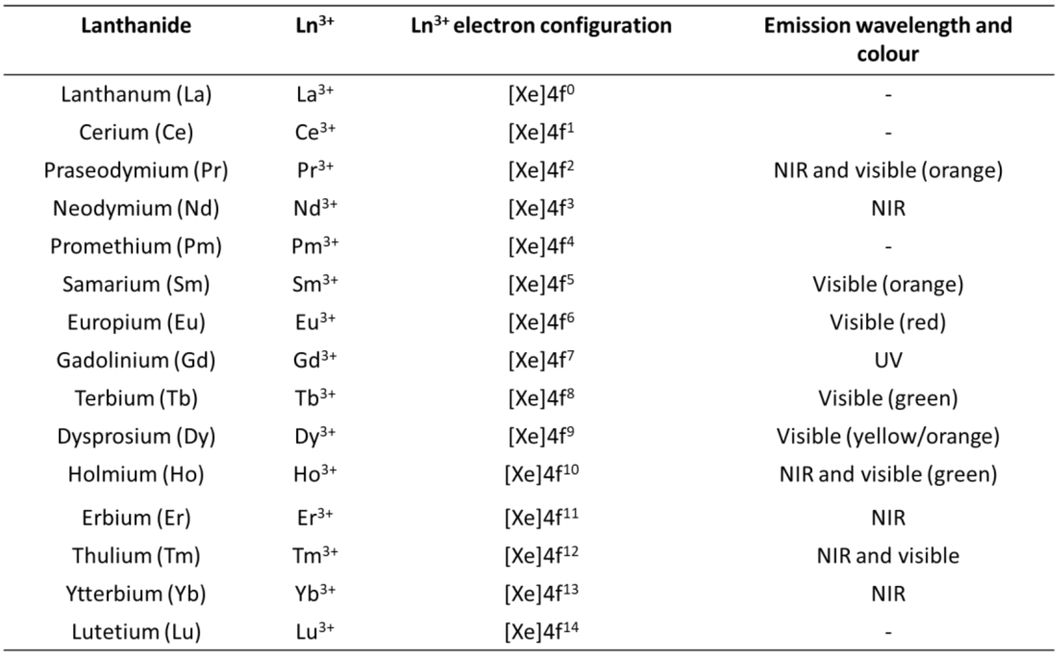

Lanthanide	Ln^{3+}	Ln^{3+} electron configuration	Emission wavelength and colour
Lanthanum (La)	La^{3+}	$[Xe]4f^0$	-
Cerium (Ce)	Ce^{3+}	$[Xe]4f^1$	-
Praseodymium (Pr)	Pr^{3+}	$[Xe]4f^2$	NIR and visible (orange)
Neodymium (Nd)	Nd^{3+}	$[Xe]4f^3$	NIR
Promethium (Pm)	Pm^{3+}	$[Xe]4f^4$	-
Samarium (Sm)	Sm^{3+}	$[Xe]4f^5$	Visible (orange)
Europium (Eu)	Eu^{3+}	$[Xe]4f^6$	Visible (red)
Gadolinium (Gd)	Gd^{3+}	$[Xe]4f^7$	UV
Terbium (Tb)	Tb^{3+}	$[Xe]4f^8$	Visible (green)
Dysprosium (Dy)	Dy^{3+}	$[Xe]4f^9$	Visible (yellow/orange)
Holmium (Ho)	Ho^{3+}	$[Xe]4f^{10}$	NIR and visible (green)
Erbium (Er)	Er^{3+}	$[Xe]4f^{11}$	NIR
Thulium (Tm)	Tm^{3+}	$[Xe]4f^{12}$	NIR and visible
Ytterbium (Yb)	Yb^{3+}	$[Xe]4f^{13}$	NIR
Lutetium (Lu)	Lu^{3+}	$[Xe]4f^{14}$	-

The lanthanide ions are largely known for their interesting magnetic and luminescent properties, the latter of which results from the transition of electrons within the 4f orbitals (4f-4f transitions) (which can be electric dipole (ED) and/or magnetic dipole (MD) in nature).[1-18,21-30] Luminescence can be used as a general term which encompasses two different processes, fluorescence (no change in electron spin) and phosphorescence (change in electron spin).[2,3,8,11,18,26] Lanthanide ion (Ln^{3+}) luminescence can display both, or either of these processes.[2,3,8,9,11-13,18,21,26,28] The emission wavelengths stemming from these transitions span a large fraction of the electromagnetic spectrum from the near infrared-range (e.g. neodymium) through the visible range (e.g. europium), to the UV range (e.g. gadolinium), a property which enables these rare earth elements to be used for many applications (Table 1).[1-14,17,18,21-23,28,30]

The luminescence resulting from direct Ln^{3+} excitation is typically very weak (with molar absorption coefficients (ε) up to a maximum of only 10 L mol^{-1} cm^{-1}).[1-15,17,18,21-24,26-28,30] Consequently, to achieve direct excitation, sources with high energies (such as lasers) are required making it an inefficient excitation method for Ln^{3+} luminescence and practical use.[3,5,9,11,12,14,18,21-25,27,28,30] This is because the 4f-4f ED transitions are forbidden by parity/Laporte-selection rules which can only be relaxed through processes such as orbital and vibronic mixing (contributing to the weak luminescence, based off the work of Görller-Walrand and Binnemans (as cited in ref [26]) the 4f-4f MD transitions which do fulfil the selection rules are weak).[1-18,21-28,30] Thus, to produce highly emissive species, this selection rule relaxation may be achieved through introducing a ligand into the Ln^{3+} coordination sphere whereby an alternative excitation method, indirect excitation (the antenna effect) can be used.[2-18,21-28,30]

1.1.1 The antenna effect

The antenna effect, also known as sensitization or indirect excitation, can be achieved through using an organic ligand system (chromophore/antenna) to encapsulate the Ln^{3+}, absorb wavelengths of light with large ε values (typically aromatic and/or heterocyclic compounds), and transfer this energy to the Ln^{3+} excited state for luminescence (Fig. 1).[1-18,21-28,30] This method of excitation benefits over the direct excitation as the antenna typically has much larger ε values, improving the efficiency of the process.[2-9,11-14,16,18,21,22,24,25,27,28,30]

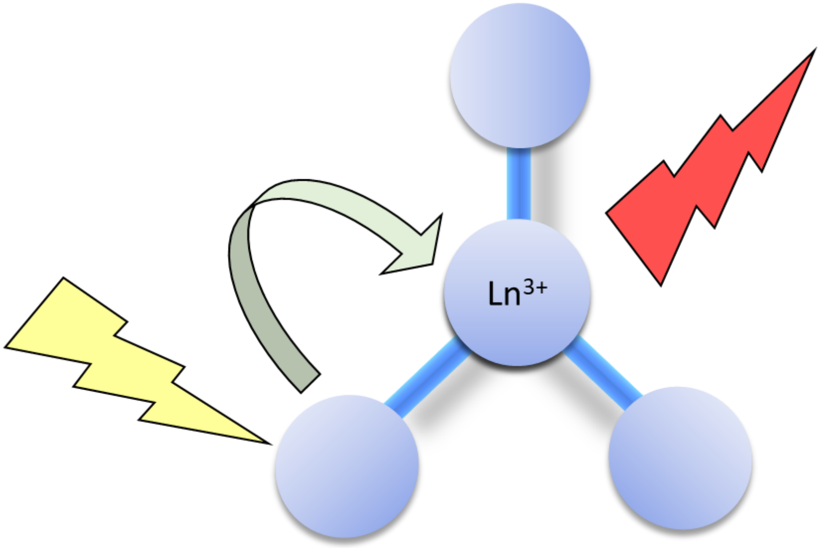

Figure 1. Simplified schematic of the antenna effect showing excitation, energy transfer, and Ln^{3+} *emission. Image adapted from: 3-5, 7, 9, 14, 16-18, 21-23, 27, 30*

On a small scale, this process can be split into four steps which compete with alternative quenching pathways (Fig. 2).[1-8,10-18,21-25,27,28,30] The first step is the initial excitation of the organic ligand to its first excited singlet (S_1) state from its ground singlet (S_0) state ($S_0 \rightarrow S_1$) (Fig. 2).[2-7,11-18,21-28] From here, intersystem crossing (ISC) (a spin-forbidden and non-radiative process) results in the population of the ligand triplet (T_1) state ($S_1 \rightarrow T_1$), which is typically a long-lived state (Fig. 2).[1-8,11-18,21-28,30,33] This ISC process competes with ligand fluorescence and the non-radiative $S_1 \rightarrow S_0$ decay process (Fig. 2).[2-7,11-18,23-28] Another competing pathway that has been reported is the $S_1 \rightarrow Ln^{3+}$ excited state ($Ln^{3+}*$) transition however this is restricted by the short-lived nature of S_1 (Fig. 2).[1-3,5,7-9,11-16,18,21-28,33] Additionally, based off work of dos Santos (as cited in ref [14]), the ISC process is favoured (despite being spin-forbidden) by the heavy atom effect (caused by the presence of Ln^{3+}) as this results in an increase in the spin-orbit coupling.[1-6,8,10-12,14,18,24-26,33] For maximal ISC efficiency, the difference in energy between the S_1 and T_1 ligand states should be approximately 5000 cm^{-1}.[2-5,7,11-15,17,18,21-24,26-28]

From the excited T_1 state, the ligand may undergo phosphorescence, non-radiative decay, or energy transfer (ET) to a nearby Ln^{3+} excited state ($T_1 \rightarrow Ln^{3+}*$) (Fig. 2).[1-18,21-25,27,28,30] For ET to be efficient, the difference in energy between the main Ln^{3+} emissive state and the ligand T_1 state should lie between 2500 – 4000 cm^{-1}.[2-4,6-8,11-18,21-23,27,28,30] If this $T_1 \rightarrow Ln^{3+}*$ energy gap is too high, ligand phosphorescence or non-radiative decay is favoured whereas if it is too low, back-energy transfer (BET) may occur ($Ln^{3+}* \rightarrow T_1$) (Fig. 2).[2-8,11-18,21-25,27,28,30]

After energy transfer, the Ln^{3+} excited state may relax from its emitting state to its ground state, undergoing the f-f transition and emitting light (Fig. 2).[1-7,12,18,26,27,30] The energy transfer process is generally thought to be either through Dexter, Förster, or both processes combined.[1-3,5-14,17,21,26,27] Dexter's process involves the simultaneous transfer of an electron from the T_1 state of the ligand to the Ln^{3+} excited state alongside a transfer of an electron from the ground Ln^{3+} state to the S_0 state of the ligand (hence referred to as a double electron exchange).[1-3,7,8,11-14,17,26,27] Based on the work of Moore and co-workers (as cited in ref [14]), this process results from the overlapping of orbitals which, according to the separate works of Eliseeva, Bünzli, Hagan, Zuchner and Piguet (as cited in ref [13]), is low for Ln^{3+} and its ligand.[2-8,10-14,17,21-23,25,26,28,30] In comparison, the Förster process results from the coupling of dipoles between the lanthanide 4f orbitals and the T_1 ligand state (referred to as the dipole-dipole process).[1-3,7-9,11-14,17] Both processes have a distance dependency such that the energy transfer process is more efficient when the donor component (*i.e.* the antenna) is closer to the acceptor (Ln^{3+}), with an e^{-d} distance dependency for the Dexter process and a d^{-6} distance dependency for the Förster process (where d represents the distance between the Ln^{3+} and the antenna).[1-3,5,7-9,11-14,17,21,25-27]

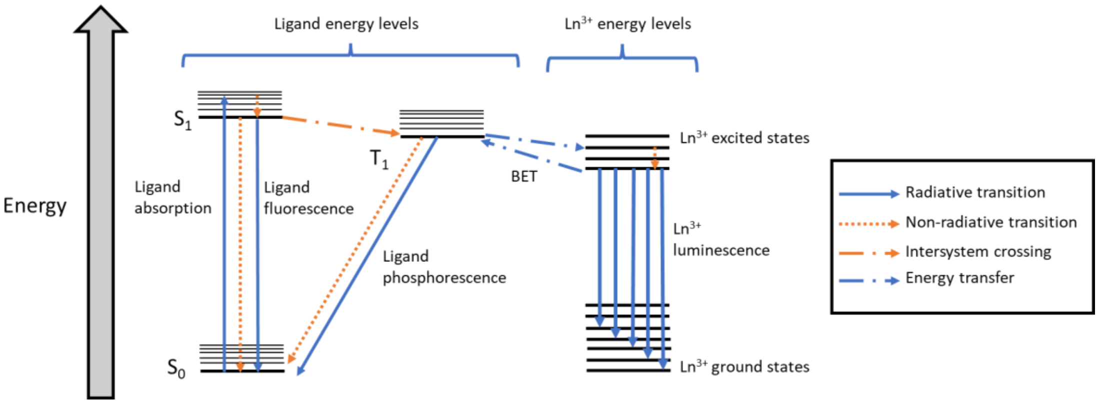

Figure 2. Jablonski diagram showing the ligand and Ln^{3+} energy levels involved in Ln^{3+} luminescence via the antenna effect. Image adapted from: 3-5, 7, 12-14, 18, 23

1.1.2 The key Ln^{3+} photophysical properties

The photophysical properties of the luminescence displayed by Ln^{3+} complexes have made them highly valuable targets for the development of advanced technologies/materials.[1-5,8-10,12-18,21-24]

The emission spectra of lanthanide ions are dominated by a multitude of peaks (Fig. 3).[2,4-11,12-18,21-26] This is because within Ln^{3+} 4f orbitals, the repulsive Coulombic interactions between electrons result in a large energy separation between ground and excited states (Fig. 3).[5,10-12,17,26] Furthermore, spin-orbit coupling, splits each of these states into different *J*-levels (Fig. 3).[1-5,8,10-12,14,17,18,26,33] It is the transition of electrons from the excited emissive Ln^{3+} state to these different *J*-levels within the ground Ln^{3+} state that is responsible for the multiple peaks in the Ln^{3+} emission spectra (Fig. 3).[2-5,8,10-12,14,17,18,22,26,28]

Sharp characteristic peaks

The first photophysical property of value is that the peaks are defined, sharp, and characteristic with widths of up to 10 nm in their luminescence spectra, irrespective of the external environment (Fig. 3).[1-18,21-28,30] This property results from the low interaction of the Ln^{3+} 4f orbitals with the covalent ligand orbitals, making this bond largely electrostatic in nature (*i.e.* only approximately 5 to 7 % covalency).[2-8,10-14,17,21-23,25,26,28,30] Consequently, perturbations in the bond resulting from f-f transitions are small giving sharp peaks at defined, characteristic wavelengths (Fig. 3).[1-18,21-28,30]

In saying this, even further, when the lanthanide ions are coordinated with organic ligands, these *J*-levels each can split even further into sublevels due to small crystal field effects, which can result in a hyperfine structure peak splitting (Fig. 3).[2-5,7,9-12,15,17,23,26] Based off the works of Görller-Walrand and Binnemans (as cited in ref [5]), it is these splitting's which can be used to derive information regarding changes in ligand structure and symmetry of the complex (Fig. 3).[2-5,9-12,14-18,21,22,24-26,28] Thus, although the peaks in the emission spectra of Ln^{3+} are well defined, the intensities and splitting/fine structures of these peaks can be used to derive information regarding the coordination environment and changes in ligand structure for certain Ln^{3+} (Fig. 3).[1-6,8-18,21-28,30]

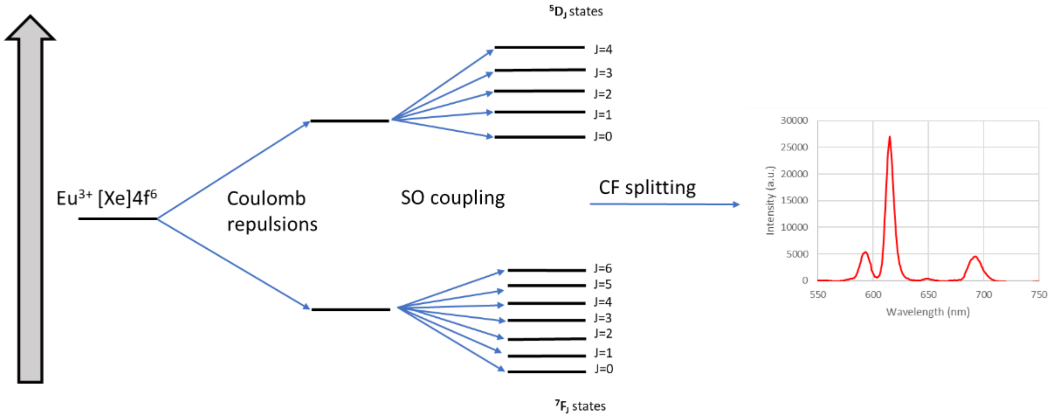

Figure 3. Schematic showing the different types of splitting which can be experienced by Eu^{3+} (with a ligand) and an example of a typical Eu^{3+} emission spectrum. Image adapted from: 5, 12, 17, 26

Large pseudo-Stokes shifts

As well as this, in Ln^{3+} luminescence resulting from indirect excitation has large pseudo-Stokes shifts (due to the population of the ligand triplet state) as opposed to the small Stokes shifts observed for direct excitation.[2-4,6-9,11-16,18,21-25,28] This property is beneficial for the development of luminescent materials as it enables an enhancement of the signal detection sensitivity as absorption and emission wavelengths are well separated.[2,3,5,8,9,11,13-16,18,22,23,25,28,30]

Long-lived luminescence

Lastly, resulting from the long-lived Ln^{3+} excited states (τ), luminescence displayed by lanthanide ions exists for long time periods, typically in the millisecond time range (as opposed to the excited states of organic molecules which are typically in the nanosecond time range) (Fig. 4).[1-3,5-11,13-15,17,18,21-28,30] This is a valuable property for the development of new materials and devices whereby the Ln^{3+} luminescence must be detected as it enables time-gated detection methods to be used (Fig. 4).[1-3,5,7-11,13-15,17,18,21-28,30] In this way, after excitation of a sample, any luminescence stemming from organic compounds decays off, leaving the Ln^{3+} luminescence for detection (with an enhanced signal-to-noise ratio) (Fig. 4).[1-3,5,7-11,13-15,17,18,21-28,30]

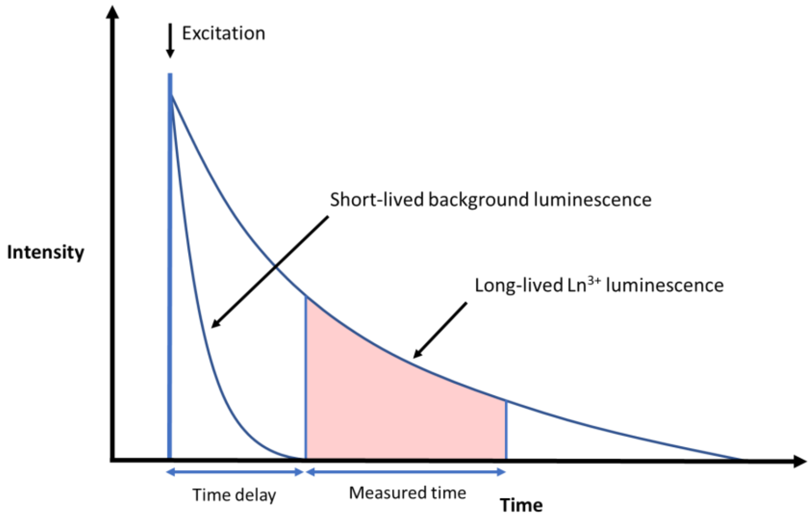

Figure 4. Long-lived Ln^{3+} luminescence enables time-gated detection methods to be used. Image adapted from: 3, 7, 13, 23, 30

1.1.3 Luminescence quenching

Due to their long-lived excited states, the lanthanide ions have an increased possibility of quenching processes occurring which results in Ln^{3+} excited state deactivation.[1-4,6-18,21-28,30] Luminescence quenching can occur through different methods, such as quenching from BET and photoinduced electron transfer (PeT, a quenching process associated with Ln^{3+} reduction), however, quenching due to vibrational energy transfer plays a large role in lanthanides.[1-9,11-18,21-28,30] This quenching occurs when energy is transferred non-radiatively from the Ln^{3+} excited state to high energy bonds (e.g. O-H, C-H, and N-H bonds) present in the coordination sphere of the Ln^{3+} (Fig. 4).[1-5,7-9,11-16,18,21-28,30]

To avoid this quenching effect, different strategies can be adopted to exclude molecules containing these high energy bonds (such as water) from the lanthanide coordination sphere.[1-5,7,8,11-16,18,21-24,26-28,30] One strategy is to shield the Ln^{3+} from these high energy bonds by saturating the coordination sphere of the Ln^{3+}.[2-5,7,8,11,13-15,21,22,24,26-28,30] This shielding can be further enforced through using bulky, rigid ligands as well as through using multidentate ligands (due to the macrocyclic/chelate effect).[2-5,7,8,11,13-15,21-24,26-28,30]

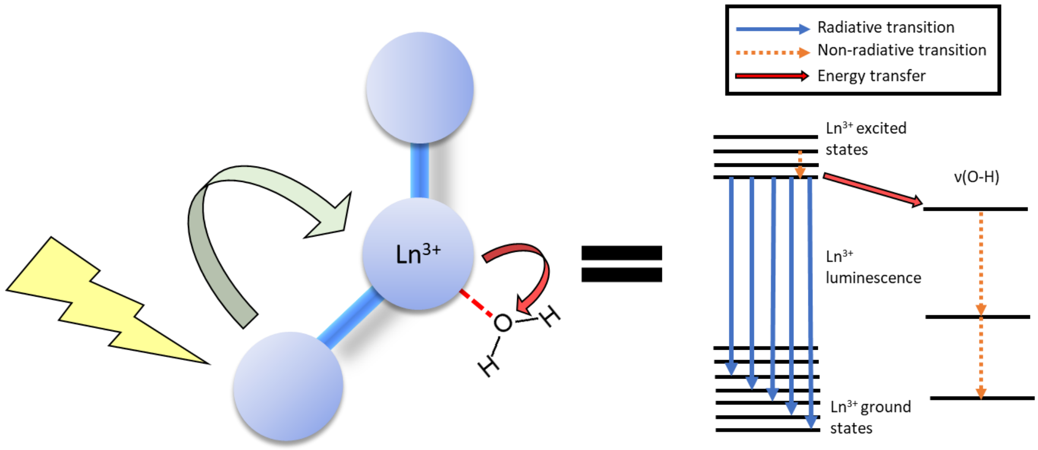

Figure 5. Simplified schematic showng the quenching of the Ln^{3+} *excited state by high energy O-H bonds. Image adapted from: 3, 4, 11, 12, 14-17, 23, 24, 27*

1.2 The dipicolinic acid (DPA) motif

In addition to the extensive energetic requirements of the ligand to enable lanthanide ion sensitization, there are also multiple structural requirements.[1-9,11-18,21-24,28,30,33] Ln^{3+}'s are hard Lewis acids, meaning that they prefer binding to nitrogen- and oxygen- containing ligands (*i.e.* hard Lewis bases), especially if they are negatively charged.[3-5,13-17,21,26-30,35,49,192,193] Additionally, the lanthanides readily combine with ligands to form complexes with a wide range of coordination numbers typically lying between 6 to 12 (although 8 and 9 coordinate complexes are most frequently observed).[3-5,7,11-13,17,21,22,24,26,28-31,33-38,40-50,193,197]

In line with these requirements, the dipicolinic acid (DPA) chelating motif has been extensively reported in literature to act as an excellent Ln^{3+} chelator and sensitizer.[2,4,5,9,11,13,14,17,18,22,25,26,31-50,192,193,195,196] The motif, contains a central pyridine ring (fulfilling the aromatic/heterocyclic antenna requirement) with carboxylic acid groups at the 2- and 6-positions of the pyridyl ring which, on deprotonation of these dicarboxylic acid groups (to form the dicarboxylate version of DPA) forms a tridentate O^N^O chelating pocket.[5,13-15,17,18,21,22,24-26,29-47,49,50,192,193,196,197] Throughout this thesis, when referring to DPA:Ln^{3+} complexes the DPA motif are in their dicarboxylate forms unless stated otherwise (*i.e.* methyl-protected or amide-protected DPA).

Lanthanide complexes can adopt several geometries which, based off the work of Richardson (as cited in ref [17]), largely depend on the Ln^{3+} radii in combination with steric impacts imposed by the ligand (as opposed to transition metals whereby geometry is dependent on the configuration with the greatest orbital overlap).[4,12-14,16,17,21,22,30,31,34,41,49] Based off the work of Grenthe (as cited in ref [13]) as well as the combined works of Werts, Gones and co-workers (as cited in ref [48]), DPA ligands readily form stable complexes with 3:1 ligand:Ln^{3+} ratios, thus forming complexes with nine coordination sites occupied, typically with a tri-capped trigonal prismatic geometry.[2,4,5,12,13,17,18,22,26,29,31,33-48,50,196,197,213,219]

In addition to the DPA chelating motif being a good antenna, it contains multiple sites that can be easily functionalised (*i.e.* the 3-, 4-, and 5-positions of the pyridyl ring), a vital property when considering the design of novel lanthanide complexes.[2,5,13,18,22,29,31-50,193,195,196] There have been many studies which have investigated different DPA ligand systems through attaching different substituents at the 4-pyridyl position.[31-50,65-76,196] For this study, we will be starting from chelidamic acid (CDA) which contains the DPA chelating motif but differs in that it is hydroxylated at the 4-pyridyl position (Fig. 6).[22,31-33,41-43,45-48,196]

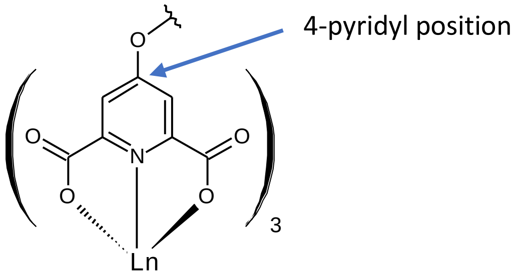

Figure 6. General structure of the 4-pyridyl substituted DPA chelating motif showing the coordination mode to Ln^{3+}

1.3 'Click' chemistry

The DPA chelating motif contains multiple sites for functionalization and as a result has large potential for the development of a range of different ligands, however it is important that adaptable methods exist to synthesise such ligands, such as click chemistry.[52,56,59,60,64] Click chemistry was developed by Sharpless and co-workers in 2001 to describe a family of reactions with several properties in common that could be used to improve the accessibility of new vital compounds.[1,51-60,63,64] The researchers defined click reactions as high-yielding, modular, stereospecific and easy-to-purify reactions that can be carried out from simple starting materials, irrespective of reaction conditions such as solvent or oxygen exposure.[51-60,62-64] Since its development, click chemistry has occupied a vital role in many fields including coordination chemistry (for ligand synthesis), materials chemistry, supramolecular chemistry and in the development of interlocked structures.[1,53,55-59,61,64]

1.3.1 Copper(I)-catalyzed azide-alkyne cycloaddition (CuAAC)

One key class of click reactions is the copper(I)-catalyzed azide alkyne cycloaddition reaction, the CuAAC reaction, specifically, the copper(I)-catalyzed alkyne-azide 1,3-cycloaddition derivative which was first developed in 2002 by two separate research groups.[51-64] This CuAAC click reaction is known for its ability to regioselectivly form 1,4-disubstituted 1,2,3-triazoles (as opposed to a mix of the 1,4- and 1,5-disubstituted products in the uncatalyzed version) from a copper(I) catalysed reaction between an alkyne and an azide.[51-64] One desirable feature of this reaction is that generally, it only requires three key components, an alkyne, an azide and a copper (I) source and can proceed despite the presence of a range of different functional groups in the molecule (Fig. 7).[51-64]

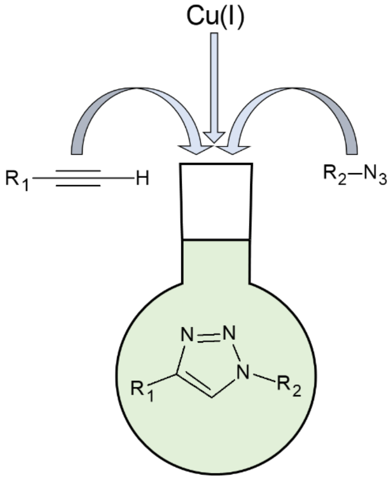

Figure 7. The copper(I)-catalyzed azide-alkyne cycloaddition reaction showing the 1,4-disubstituted 1,2,3-triazole product

In order to achieve the copper(I) source (*i.e.* copper in its +1 oxidation state), many researchers use copper(II) sulfate pentahydrate (copper in its +2 oxidation state) along with a reducing agent such as sodium ascorbate, whereas others use salts and complexes of copper(I) such as copper iodide and $[Cu(CH_3CN)_4]PF_6$ (respectively).[52-63] In saying this, based off the separate works of Simmons, Merrill, Ciavatta and co-workers (as cited in ref [62]), Cu(I) has a low thermodynamic stability meaning that it has a large tendency to form Cu(II) through oxidative processes as well as its tendency to form Cu(II) and Cu(0) through disproportionation.[52,53,58-63] Certain additives may be added to supplement and enhance the click reactions.[52-55,58,59,62-64] An example of one of these additives is *tris*-(benzyltriazolylmethyl)amine (TBTA), which acts as a Cu(I) ligand to stabilize it and prevent disproportionation.[52-55,58-60,62-64]

The main disadvantage of CuAAC is that the organic azides used can be explosive if they have low C/N ratios (low molar masses), which has posed problems regarding their isolation for use in these click reactions.[51-54,56,59] In saying this, the organic azides used for the current study were safe to isolate as they had low C/N ratios.[52,59]

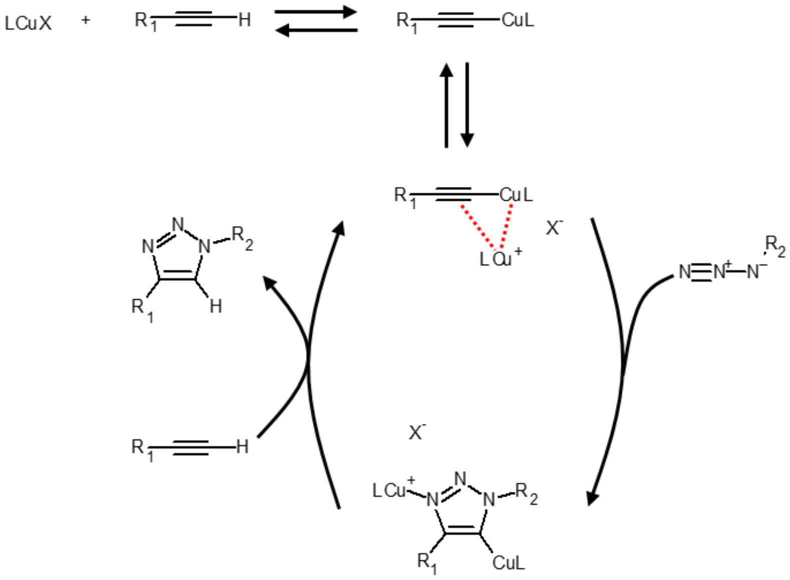

Figure 8. Proposed CuAAC mechanism. Image adapted from: 57

There has been uncertainty regarding the nature of the catalytically active intermediate in this reaction and whether it involves one or two copper atoms.[52-55,57,59,60,63] In saying this, relatively recently, two di-nuclear CuAAC intermediates were isolated for the first time, a bis(copper)-alkyne (with a σ-bonded and a π-coordinated copper) and a bis(copper)-triazole, suggesting that these intermediates play a vital role in the formation of the C-N bond (Fig. 8).[57,60,63,64] Although both mono- and bis- copper pathways are believed to be active, the bis-copper pathway is believed to be the pathway which is favoured by kinetics (Fig. 8).[52-55,57-60,63] In this way, the general mechanism of the reaction has been proposed to involve the initial formation of a catalytically active bis(copper)-alkyne intermediate followed by the formation of the C-N bond via the reaction of the nucleophilic alkyne carbon with the electrophilic azide nitrogen to form a bis(copper)-

triazole intermediate, ending with demetallation and protonation of the triazolide carbon.[52-55,57,59,60,63,64]

1.3.2 Clicking to the 4-pyridyl motif of DPA

A family of 4-pyridyl functionalised DPA ligands have been synthesised through CuAAC click chemistry (typically through carrying out the click reaction on a 4-azido DPA intermediate) (Fig 8).[65-76] The resulting Ln^{3+} complexes have been used for a range of applications, from their use for the development of luminescent nanoparticles to their use for the determination of protein structure.[65-74] One study in 2020 used this ligand synthesis method with 4-azido DPA and 2-ethynylpyridine to develop a 3:1 DPA ligand:Eu^{3+} complex which was able to act as a switch-on probe for the detection of hydrogen sulfide.[65,74] This family of studies were important as they proved that ligand modifications (via CuAAC chemistry) at the 4-pyridyl position of DPA can result in changes in lanthanide ion photophysics.[65-74] In this way, they display how Ln^{3+} emission can be tuned, a vital property for the development of responsive materials.[65-74]

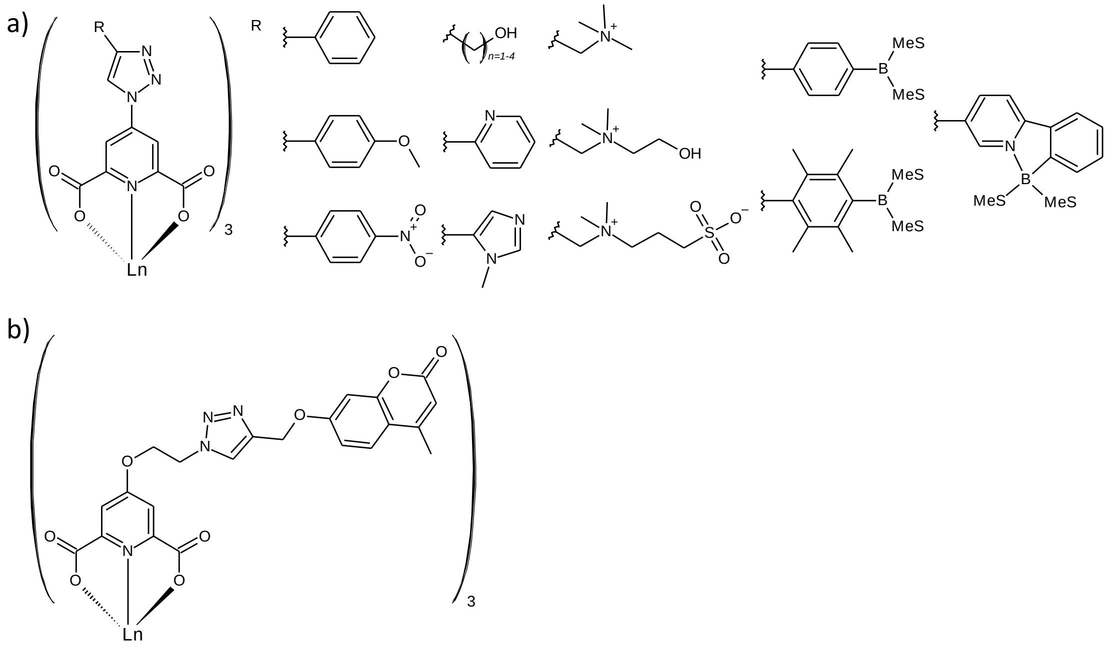

Figure 9. Examples of various DPA ligands reported in the literature via directly clicking to the 4-pyridyl motif (a) as well as via an ether linker (b). Image adapted from: 65-74

1.3.3 Performing click chemistry on lanthanide complexes

As discussed in section ***1.3.2***, there are many studies that use CuAAC chemistry for ligand synthesis and subsequent lanthanide complexation however, there are also extensive examples of studies which have carried out click reactions on lanthanide complexes, thus a achieving post-complexation modification.[77-113] However, these studies are limited such that the majority of these click reactions appear to be carried out on kinetically stable lanthanide complexes containing ligands of the cyclen macrocycle family, such as 1,4,7,10-tetraazadodecane-1,4,7,10-tetraacetic acid (DOTA) (Fig. 10).[77-113,162] This limitation is likely due to the reduced stability of non-cyclen complexes comparative to the cyclen complexes (as the macrocyclic effect is absent).[87,90-93,95,97-113] This is important as many of these complexes are synthesized for contrast agent development where, based off separate studies by Caravan, Polasek and their respective co-workers (as cited in ref [92]) the Ln^{3+} cannot be released due to toxicity (which may occur in the presence of copper via competitive binding).[4,79-87,90-93,95,97-113]

Click reactions have been carried out on these cyclen complexes containing azide functional groups appended to one (or more) of the cyclen nitrogen atoms (Fig. 10).[77-84,107,110,116] Alternatively, researchers also use alkyne groups appended to one (or more) of the cyclen nitrogens for the click reaction (Fig. 10).[81,85-109,113] Various studies have also coupled lanthanide complexes containing click-compatible functional groups together through click chemistry for the development of multi-metallic systems.[77,79-83,85,87-89,91,93,95-97,99,100,105-113]

In many of these cases, when the distance between the cyclen nitrogen and the click active component is short, one of the triazole nitrogen atoms which form during the click reaction appears to coordinate with the lanthanide centre.[84-93,98,104,107,108,110,113] This appears to be avoided by adding a functional group (such as an amide linker, alcohol or ketone) containing a donor atom (such as an oxygen atom of the carbonyl bond) that can coordinate with the lanthanide as opposed to the triazole nitrogen or by increasing the alkyl appendage (Fig. 10).[77-83,86,94-107,109,110]

This family of complexes have a vast range of applications, however by far the main use appears to be associated with contrast agent development.[77,79-83,86,87,89,91-93,95-103,105-110,112,113,136] Below are some examples of lanthanide complexes which click reactions have been carried out on (Fig. 10).

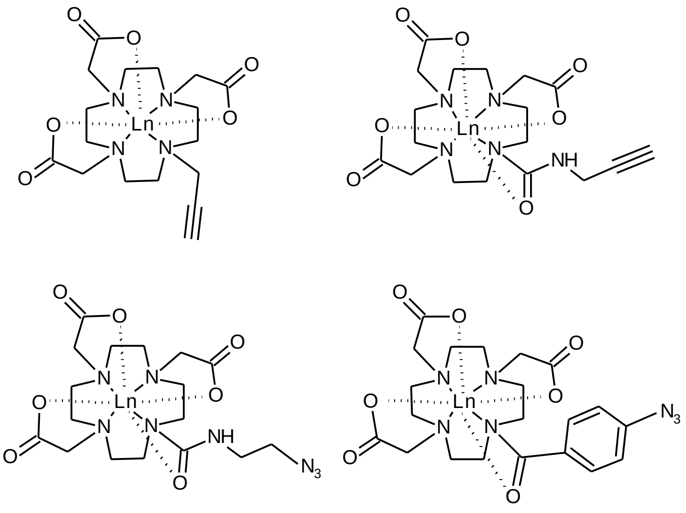

Figure 10. Examples of cyclen-containing lanthanide complexes which have been used in CuAAC reactions

Leigh and co-workers represent one of the few research groups that have performed click chemistry on lanthanide complexes with non-cyclen chelating motifs.[114,115,136] The researchers made lutetium complexes with a ligand containing three pyridine-dicarboxamide chelating motifs which, based off separate studies by Carina, Adams, Gil-Ramírez and Leigh (as cited in ref [115]) were known to coordinate to the Ln^{3+} in an orientation resembling an overhand knot.[13,29,114,115,117-120] These ligands were also functionalized at one end with an either an alkyne or an azide functional group such that one complex (containing an alkyne group) could be joined to another complex (containing an azide group) through CuAAC to form knotted lutetium complexes.[114,115,136] Thus, this study provided an example whereby CuAAC was carried out on a non-DOTA containing Ln^{3+} complex without copper-induced decomplexation.[114,115,136]

In a study Candelon and co-workers (2013) performed click chemistry on tris-4-azido DPA (*i.e.* non-cyclen) Ln^{3+} complexes and the resulting triazole-containing complexes displayed large changes in the photophysical properties when compared to their tris-4-azido DPA complex derivatives.[73] In saying this, a specific type of click chemistry called strain-promoted azide-alkyne cycloaddition (SPAAC) was used which does not require the use of copper.[73,103,104,117,121-125] In SPAAC, strained alkynes, such as bicyclononyne (BCN) (used in this study), are used due to their increased reactivity.[73,103,104,121-125] The researchers also used CuAAC to couple an alkyne appended peptide to the 4-azido-DPA Eu^{3+} and Tb^{3+} complex which, after gel electrophoresis, gave bands that were luminescent at 254 nm.[73] In saying this, the results were only analysed through gel electrophoresis and were giving luminescent bands at approximately 24,500 Da suggesting that the click reaction had only been carried out on a single azide group (as opposed to all three).[73]

Despite these studies, overall, the idea of carrying out click reactions on lanthanide complexes (specifically, non-cyclen lanthanide complexes) remains underdeveloped, restricting the possibility of developing large functional supramolecular and mechanically interlocked molecules and materials.[1,4,59,79-87,89-93,96,97-113] Studies in this field are important as the ability to achieve a range of different architectures from simple and adaptable pre-cursors is of high interest.[89,90,102,105,112-116]

1.4 Mechanically interlocked molecules

A family of molecules called mechanically interlocked molecules (MIMs) or mechanomolecules have established vital roles in science since their early establishment.[126-132,134,135,137,148] Most (but not all) MIMs contain a mechanical bond which is a type of physical bond that can only be broken on the destruction of one (or more) interatomic covalent bond.[126-128,130,131,133-135,137,138,148] This bond exists between molecular components/entities, and results in the entanglement of these components in space.[126-128,130-132,134,135,138,148] Currently, there are four main types of mechanically interlocked molecule (MIM) structures consistently reported including rotaxanes, pseudorotaxanes, catenanes and knots (some of which, *i.e.* pseudorotaxanes, have overlap with other chemical fields such as supramolecular chemistry) (Fig. 11).[126-139,141,147,148]

1.4.1 Rotaxanes and pseudorotaxanes

The scope of this project focuses on a specific type of MIM called a rotaxane (and its supramolecular analogue, pseudorotaxanes).[126-128,130-141,147,148] The simplest rotaxane consists of three main parts, an axle, a macrocycle, and stopper groups (Fig. 11).[126-128,130-135,138,148] These components are organised such that the macrocycle loops around the linear axle component which is terminated by bulky stopper groups on each end (Fig. 11).[126-128,130-140,142,143,148] In this way, the axle and stopper groups form a dumbbell-like unit, preventing the de-threading (or slippage) of the macrocycle, which is free to move along its axle (Fig. 11).[126-128,130-136,138-140,148] Overall, because covalent bonds (either on the axle or macrocycle) would be required to break the system, the rotaxane structure formed can be referred to as a MIM such that a mechanical bond exists between the macrocycle and dumbbell components.[126-135,137,138,143,148] These rotaxanes are described as [2]rotaxanes as they consist of two separate components, however multiple different types of rotaxanes can be achieved including [3]-, [4]- rotaxanes with three and four separate components (respectively).[126-129,133,137,148]

A similar subset of rotaxanes, pseudorotaxanes differ from rotaxanes such that they contain an axle and a macrocyclic wheel component, however there are no bulky stopper groups.[126,128,130-132,135,138-141,148] Because of this, pseudorotaxanes cannot strictly be considered as interlocked molecules, but more accurately fit the description of a supramolecular unit.[126-128,130-132,134,135,138,140,141,148]

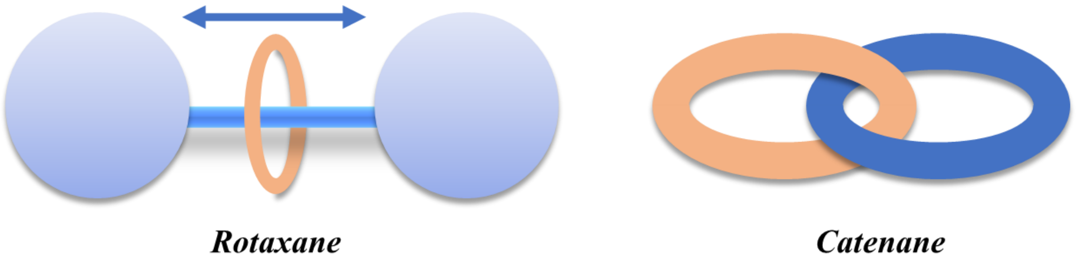

Figure 11. Schematic showing the interlocked nature of the rotaxane and catenane

Rotaxanes (and pseudorotaxanes) have been established in literature for a relatively long time and have emerged as highly value targets for the development of advanced materials such as systems for drug delivery (*i.e.* shuttles), artificial molecular machines (AMMs), and responsive molecular switches.[126-141,143,148] This interest stems from the intrinsic ability of rotaxanes to undergo different types of movement, particularly the shuttling and rotation of the macrocycle along and around its axle (respectively).[126-136,138,139,143,148] For instance, if the macrocyclic component can shuttle in response to an external signal, responsive interlocked systems may be achieved.[126-132,134,135,138,139,141,143,148] By incorporating photo-physically active lanthanides ions into these systems, information regarding changes in rotaxane/pseudorotaxane conformation may be detected (or other properties of lanthanides may be coupled to this).[126,127,132,135,136,141]

1.4.2 Synthesis of rotaxanes/pseudorotaxanes

Different methods/strategies have evolved over time for the development of MIMs from early statistical synthetic methods to covalent-directed methods to template-directed synthetic methods.[126-139,142-148,282] The templated synthetic methods make use of non-covalent interactions (e.g. hydrogen bonding and ionic interactions) for MIM synthesis.[126-139,142-144,147,148] This study will focus on metal-templated synthetic methods, particularly the passive and active metal-templated methods.[126-129,131-137,139,142,143,147,148]

1.4.2.1 Metal-templated methods taken over time

Overall, the metal-templated approaches make use of the predictable geometry of certain metal ions (such as tetrahedral Cu(I) ions) and non-covalent interactions to position covalent components/ligands together in a suitable configuration for the formation of the specific MIM.[126-129,131-136,139,142-144,147,148,282] One type of metal-templated approach is referred to as the passive metal-templated approach as the catalytic abilities of the metal are ignored throughout the process.[126-129,131-136,139,142-144,147]

The first report of MIM formation through passive metal-templated synthesis was in 1983 by Dietrich-Buchecker and co-workers (as cited in ref [131]) (from the Sauvage research group), whereby a catenane was obtained in 42 % yield through a reaction templated by a tetrahedral copper(I) ion.[126-131,133-135,137,142,144,147,148] This passive metal-templated method was a large improvement from the statistical method for catenane synthesis established earlier in 1960 by Wasserman (as cited in ref [131]) which was based on the random probability of a linear diester threading through a cyclic alkane (with small yields of approximately 1 %).[126-133,135,139,142,145-148,282] The passive metal-templated method also improved on the 22-step covalent directed method developed in 1964 by Schill and Lüttringhaus.[126-131,133,135,142,146,148] It was later realised that a "closing" reaction depending on the type of MIM being synthesized could be carried out *i.e.* for catenane synthesis (and rotaxane synthesis), a cyclisation "clipping" reaction and for rotaxane synthesis, a "stoppering" reaction with bulky groups.[126-128,131,134-139,142,143,147,148]

1.4.2.2 The active template CuAAC approach

More recently, active template methods of MIM synthesis have been developed.[126-129,131,133-135,137,142,143] Active template methods couple the ability of certain metals (such as copper, nickel, palladium and zinc) to both template and catalyse the formation of the specific MIM (thus the metal has two functions).[126-129,131-135,137,139,142,143] By templating the reaction, the metal positions the reactive components in the correct orientation for the formation of the specific MIM and by catalysing covalent bond formation, the closing and formation of the specific MIM is achieved (through mechanical bond formation).[126-129,131-135,137,139,142,143] Many different metal-reaction partners have been established, such as palladium(II) and its ability to form [2]rotaxanes through its templating and catalytic ability (*i.e.* C-C bond formation via a Heck-cross coupling reaction), however the active template click (AT-CuAAC) method has established a large role in MIM synthesis and will be the focus of the study.[126-129,131-135,137,142,143,150,151]

There are four key components to this reaction, an azide, and alkyne, a macrocycle and a Cu(I) source.[127-129,131-133,135,137,142,143] The endotopic binding of a tetrahedral Cu(I) ion within the macrocycle cavity enables the azide and alkyne half-axles to orientate (via Cu coordination) on opposing sides of the macrocycle so that the new C-N bond that forms, and hence the axle, is threaded through the macrocycle as required for rotaxane formation.[127-129,131-135,137,139,142,143,147]

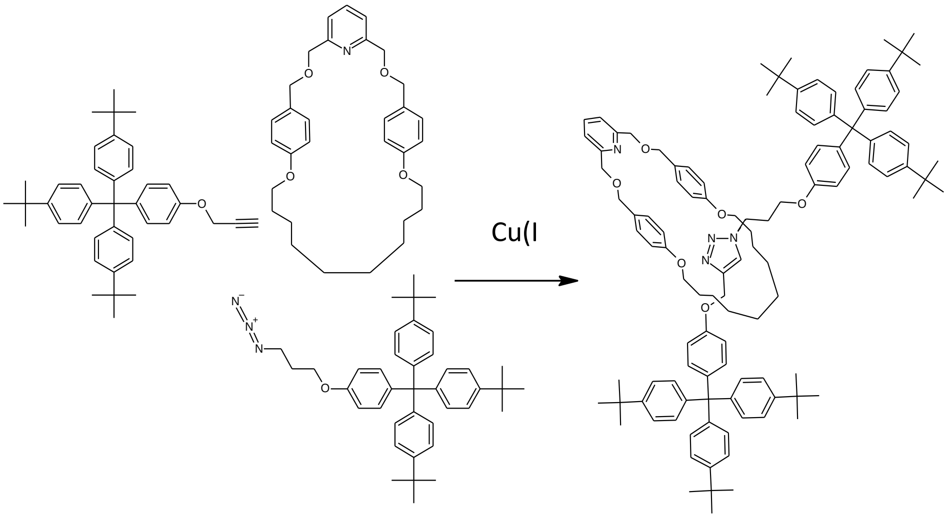

Figure 12. The first reported example of an AT-CuAAC reaction by Aucagne and co-workers in 2006. Image adapted from: 142, 143

The first active click template reaction (AT-CuAAC) was successfully carried out in 2006 by Leigh and co-workers whereby single equivalents of a bulky azide, a bulky alkyne, Cu(I) and macrocycle were stirred in dichloromethane at room temperature overnight to produce the resulting [2]rotaxane in 57 % yield (Fig. 12).[127,129,131,132,135,137,142,143] The reaction could be optimized (through both increasing the azide and alkyne equivalents and using stoichiometric amounts of the Cu(I)) to produce the [2]rotaxane in yields of 94 % (Fig. 12).[127,129,131,132,135,142,143] Extending on this, the reaction conditions were optimized further and sub-stoichiometric amounts of the Cu(I) were used to the obtain [2]rotaxane in 82 % (as the Cu(I) could be recycled throughout the reaction) (Fig. 12).[127,129,131-133,135,142,143]

In addition to these improved yields and sub-stiochiometric requirements, the AT-CuAAC method poses many advantages over the passive template methods.[127,129,131-133,135,137,142,143] Firstly, to obtain rotaxanes through passive template methods, recognition sites are required on both the macrocycle and the axle, which cannot be removed on formation of the rotaxane.[127,129,131,142,143,148] In comparison, this is not the case for the AT-CuAAC method of rotaxane synthesis as it involves the formation of a new axle with a triazole functional group (thus the azide and alkyne recognition sites are removed on formation of the rotaxane).[127,129,131,132,137,142,143] Due to this, some papers have previously referred to the AT-CuAAC method as being 'traceless' such that you cannot easily predict how the rotaxane was assembled, however other researchers disagree with this term as the rotaxane product still contains the macrocycle with its Cu(I) binding recognition site.[127,129,131-133,142,143] In saying this, overall, because rotaxanes made via AT-CuAAC methods only require a single recognition site (as opposed to two in those made via passive templated methods), there are a more diverse range of products obtainable.[127,129,131,132,135,142,143,148]

Another advantage of the AT-CuAAC reaction is that it is driven by kinetics as opposed to the thermodynamically driven passive template method.[129,131-133,135,137] The result of this is that the product that forms can have a reduced thermodynamic stability when compared to starting components.[131-135,137,143,152] This has been shown in a study by Lahlali and co-workers (2011) where small macrocycles were used to synthesize sterically strained rotaxanes in high yields.[127,131,132,134,135,137,152]

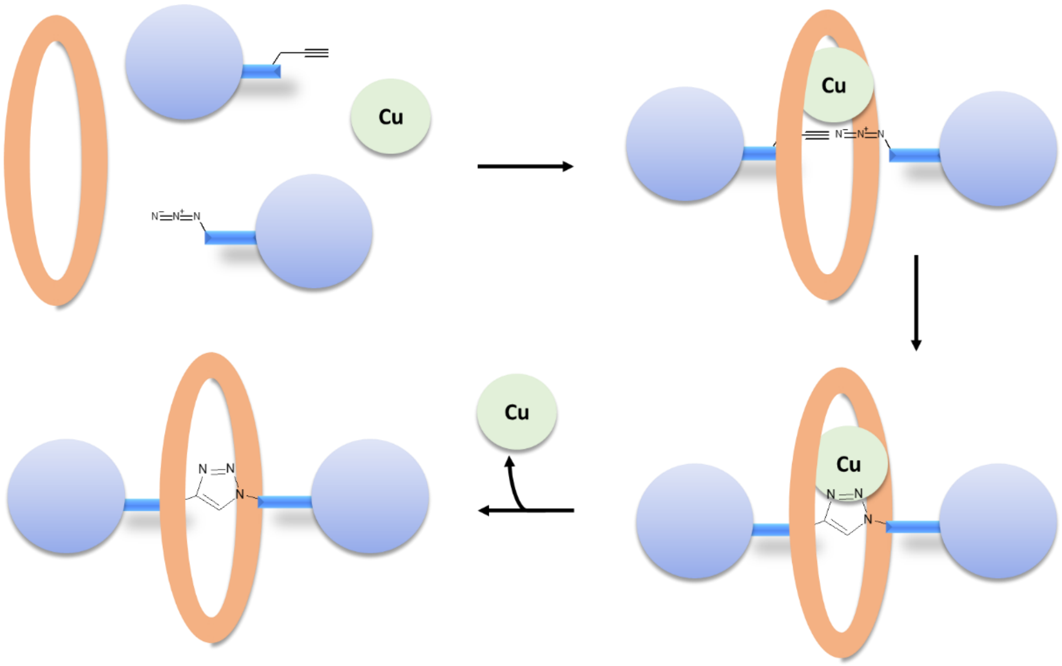

Figure 13. The active template CuAAC reaction. Image adapted from: 129, 131-133, 142, 143

The research group led by David Leigh has provided a few examples whereby AT-CuAAC reactions have been carried out on lanthanide-complexes.[114,115,136] In their 2018 study, a tris-pyridine-dicarboxamide knotted ligand containing a terminal alkyne group was complexed with Lu^{3+}, forming a knotted structure.[114,115,136] Next, the alkyne-appended Lu^{3+} complex knot was incorporated in an AT-CuAAC reaction with a bulky tert-butyl-containing azide and a macrocycle which formed a rotaxane structure whereby the lanthanide coordination sphere was acting as one stopper and the bulky azide group was acting as another stopper with the macrocycle threaded around the axle formed resulting from the click reaction.[114,115,136] However, in general this field still appears to be relatively under-studied.

Overall, the synthesis of interlocked molecules has come a long way since its initial development in the 1960s and, accordingly, their presence in literature is increasing rapidly.[126-135,139,142-148]

1.5 Luminescent lanthanide-containing rotaxane systems (literature review)

Many studies report the incorporation of transition metals into MIMs, particularly for the development of mechanical motors, however one field which remains relatively under-studied is the direct incorporation of Ln^{3+}'s into MIMs (despite their extensive incorporation into supramolecular edifices such as helicates and cages).[5,13,17,90,136,162,163-168,171] This research gap limits the opportunity for the development of new luminescent interlocked materials and nanotechnologies.[5,13,17,130,136,163,164,166] This literature review gives an overview of the research that has been done on luminescent lanthanide based MIM systems.[17,136,164,166]

1.5.1 Lanthanide-based rotaxane synthesized through anion templation

Finding from Paul Beer's and Stephen Faulkner's research groups have been key for the development of lanthanide-based rotaxane systems.[17,90,136,165-167]

In their 2006 study, Faulkner and co-workers developed heteronuclear [2]pseudorotaxanes using anion templation.[17,136,165] Anion templation uses the properties of ion-pairs to encourage molecular threading.[165] In their study, the Ln^{3+} was incorporated into the system such that it was complexed to a bi-pyridyl chelating motif containing a positively charged benzimidazole group (Fig. 14).[17,136,165] This benzimidazole group was further appended with an alkyl chain such that altogether, the Ln^{3+} complex was able to act as the axle and stopper components of the pseudorotaxane (Fig. 14).[17,136,165] This axle existed as its chloride salt, thus forming the ion-pair used for templation.[17,136,165] The macrocycle was designed such that it also contained a bi-pyridyl motif which was able to coordinate with a transition metal (TM), rhenium(I).[17,136,165] At the 4-pyridyl position of each pyridine motif were amide groups which contained linkers that eventually connected at each end to form the overall macrocyclic structure (Fig. 14).[17,136,165]

The axle and macrocycle were designed to contain their respective functional groups as, based off previous studies by Curiel and co-workers (as cited in ref [165]), the chloride anion had been used to encourage threading due to its interactions with the amide hydrogens on the macrocycle and the imidazolic hydrogen of the axle, thus holding the pseudorotaxane together.[17,136,165,176]

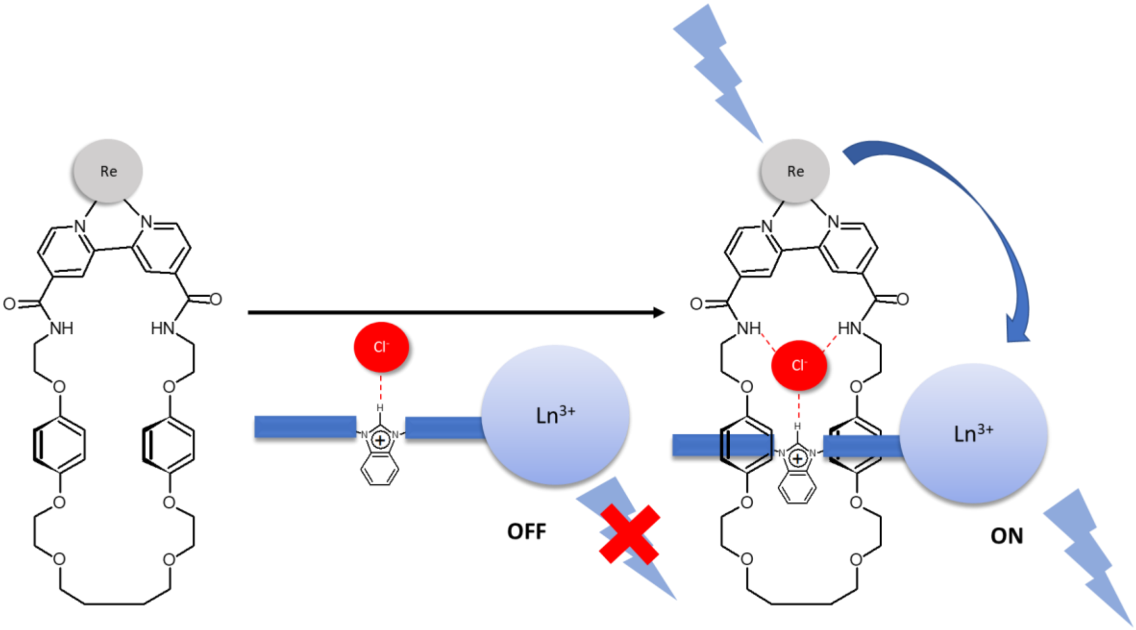

Figure 14. Anion templated lanthanide based pseudorotaxane formation by Sambrook et al., 2006. Image adapted from: 17, 136, 165

Although the visibly luminescent Ln^{3+}'s were not used, NIR-emitting Nd^{3+} or Yb^{3+} were used.[136,165] It was found that on excitation of the TM complex, the characteristic emission of Nd^{3+} or Yb^{3+} could be detected which only occurred when the pseudorotaxane was assembled).[17,136,165] This effect was accounted for by an increase in the efficiency of the energy transfer process as a result in the decrease in distance between the donor (TM complex) and the acceptor (Ln^{3+} complex) on formation of the pseudorotaxane.[17,136,165]

Later in their 2013 study, Beer, Faulkner and co-workers extended on their 2006 work by developing true interlocked Ln^{3+}-based rotaxanes which were responsive such that they were able to detect anions in solution through changes in Ln^{3+} luminescence .[17,90,136,165]

The Ln^{3+}-appended rotaxanes were synthesized using anion templation, in two key steps.[17,90,136,165] In the first step, an initial azide-appended rotaxane was produced through a “clipping reaction” between a 5-azidobenzene-1,3-dicarbonyl dichloride and a bis-amine terminated macrocycle precursor, enabling the closing of the macrocycle through bis-amide bond formation.[17,90,136] This reaction was carried out in the presence of a pyridinium containing axle (terminated by bulky stopper groups) as its chloride salt, which, due to the presence of the chloride ion, resulted in the formation of a rotaxane system (supported by X-ray analysis) (Fig. 15).[17,90,136] The resulting macrocycle of the chloride-templated rotaxane system contained an azide group (Fig. 15).[17,90,136] Thus, in the second step, a CuAAC click reaction was carried out with an alkyne appended DO3A Ln^{3+} complex (lutetium and europium) forming the lanthanide-based rotaxane systems, **Lu1** and **Eu1**, which were isolated as their hexafluorophosphate salts (Fig. 15).[17,90,136]

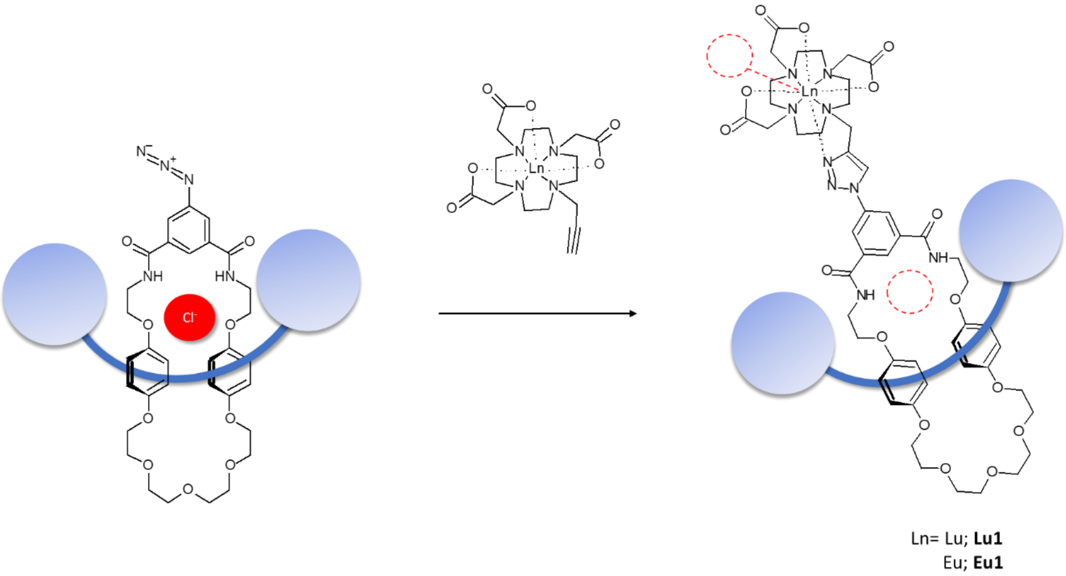

Figure 15. Anion templated lanthanide-based rotaxane formation by Allain et al., 2013. Image adapted from: 17, 90, 136

Eu1 alone was luminescent on excitation of the bis-amide substituted benzyl motif at 265 nm.[90] To analyse the changes in these photophysical properties on anion addition, titrations of **Eu1** were carried out in DCM against tetrabutylammonium (**TBA**) salts of the specific anion to be studied (TBA chloride (**TBA.Cl**), TBA dihydrogen phosphate (**TBA.H$_2$PO$_4$**) and TBA acetate

(**TBA.OAc**)).[90,136] Firstly, as **TBA.Cl** was titrated, the lifetime and intensity of **Eu1** luminescence on excitation at 265 nm displayed a sharp decline up to 1 equivalent of anion added.[17,90,136] This decline was observed alongside changes in the structure and intensity of the peaks corresponding to the hypersensitive $^5D_0 \rightarrow {}^7F_2$ and $^5D_0 \rightarrow {}^7F_4$ transitions relative to other bands.[4,17,90,136] As introduced in section 1.1.1, there is a strong interaction between ED transitions and the ligand field meaning that some of these transitions can be sensitive to changes in the coordination environment of the Ln^{3+}, termed hypersensitive transitions.[15-17,26,90,192] Thus, changes in structure and intensity of these hypersensitive peaks and can be used to draw conclusions regarding the Ln^{3+} coordination environment.[5,8,11,15,17,26,33,192] This differs from the MD transitions which are insensitive to coordinate environment changes, thus remain relatively constant.[26,192]

Following this decline, on the addition of more **TBA.Cl** up to 40 equivalents, the lifetime and intensity of **Eu1** luminescence slowly increased without the large changes in the peak structures and without the large change in intensity of the $^5D_0 \rightarrow {}^7F_2$ band (relative to the MD $^5D_0 \rightarrow {}^7F_1$ band).[26,17,90,192,136] These results suggested the presence of two distinct chloride binding sites within **Eu1** with different effects on Eu^{3+} luminescence (Fig. 15).[17,90,136]

The large changes in the intensity of the peak corresponding to the hypersensitive $^5D_0 \rightarrow {}^7F_2$ transition relative to that of the $^5D_0 \rightarrow {}^7F_1$ transition band on initial **TBA.Cl** addition along with the large lifetime decline supported the idea that chloride was binding directly to the ninth coordination site of Eu^{3+} centre, leading to quenching (Fig. 15).[17,90,136] The subsequent luminescence recovery of **Eu1** was predicted to result from changes in the coordination sphere of the Eu^{3+} elicited by the binding of the second chloride anion which was found to be situated within the cavity of the rotaxane system between the macrocycle and the axle (Fig. 15).[17,90,136]

Moreover, **Eu1** was also shown to be selective for the detection of chloride anions.[17,90,136] When titrations were carried out with **TBA.OAc** and **TBA.H$_2$PO$_4$**, there was initially a large decrease in luminescence intensity along with the $^5D_0 \rightarrow {}^7F_2$ peak changes (indicating binding to the vacant Eu^{3+} site), however, on further additions, the luminescence intensity plateaued off suggesting that these anions only bind to the Eu^{3+} centre (*i.e.* not within the rotaxane pocket).[90] Thus, Ln^{3+}-

appended rotaxane systems with photophysical properties dependant on the concentration of chloride ions were developed.[17,90,136]

1.5.2 Lanthanide-based rotaxanes synthesized through cationic templation

A few months later, Beer and co-workers set out to develop a similar system, however instead of appending the rotaxane distally to the Ln^{3+} complex, the Ln^{3+} was incorporated directly within the rotaxane and used as a cationic templating agent.[13,17,90,136,166] At the time, studies had shown the success of using this cationic templating method for the development of various MIMs using metal cations, however the use of Ln^{3+}'s remained a gap in the literature.[166]

In their synthetic procedure, the Ln^{3+} (Eu^{3+} or Lu^{3+}) was complexed within a DOTA ligand which itself was designed such that it formed a macrocyclic structure (**EuM** and **LuM**) (orange component in Fig. 16).[13,136,166] The axle was synthesized such that it contained a pyridine-*N*-oxide motif which was functionalised at its 3- and 5- positions with azido-groups (Fig. 16).[13,17,136,166] Thus, when the axle was exposed to **EuM** and **LuM**, the negatively charged oxygen atom of the pyridine-*N*-oxide motif (N^+-O^-) coordinated to the axial Ln^{3+} coordination site (as the DOTA ligand only occupied 8 coordination sites) by threading through the macrocycle, forming an azide-appended pseudorotaxane (Fig. 16).[13,17,136,166] Upon carrying out a CuAAC reaction on this azide-appended pseudorotaxane with alkyne-containing bulky terphenyl groups, the axle was stoppered, forming the lanthanide [2]rotaxanes (**Eu2** and **Lu2**) (Fig. 16).[13,17,136,166]

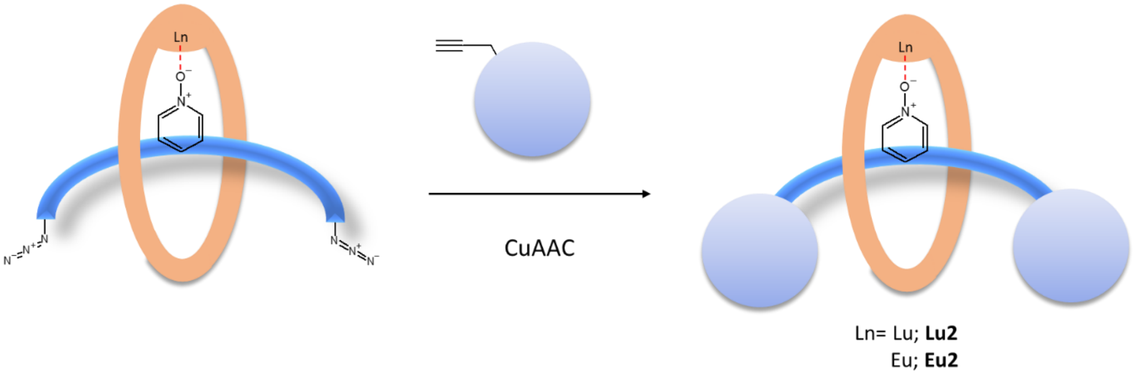

Figure 16. Lanthanide-based rotaxane formation through using a cationic templating agent by Zapata et al., 2013. Image adapted from: 136, 166

The emission lifetime of **Eu2** was studied in both a CH_2Cl_2:CH_3OH (1:1) and a CD_2Cl_2:CD_3OD (1:1) solvent mixture to confirm the axial donation of the pyridine-*N*-oxide oxygen to Eu^{3+}.[136,166] Using the assumption that only the methanol would coordinate to the Eu^{3+}, the lifetime in the CH_2Cl_2:CH_3OH (1:1) solvent mixture was 0.94 ms which increased to 1.18 ms when using the deuterated derivative.[136,166] Consequently, the hydration number (*q*) (which allows a prediction of the amount of water molecules occupying the Ln^{3+} coordination sites) was calculated to be 0, suggesting that no methanol molecules were coordinated to Eu^{3+} and supporting the idea of axial donation of the pyridine-*N*-oxide oxygen to Eu^{3+}.[3,8,14,136,166]

In saying this, the binding pocket within the rotaxane between the macrocycle and axle which had previously been used for sensing the binding of chloride through changes in Ln^{3+} luminescence, was absent due to the presence of the pyridine-*N*-oxide motif.[90,166] Thus to further develop these responsive lanthanide-based rotaxanes, there was a need to develop a removable template method.[13,166]

1.5.3 Lanthanide-based rotaxanes synthesized through removable anion templates

The next year, a slightly similar system was developed by the Beer and Faulkner group, inspired both by the architecture developed by Zapata and co-workers in 2013 and the anion templation method used by Allain and co-workers in 2011.[13,90,136,166,167] However, as opposed to using chloride as the templating anion, the bidentate nitrite anion was used which at the time had not been reported before as a templating anion.[13,90,136,167] The resulting luminescent lanthanide-based rotaxane structure was able to sense fluoride.[13,136,167]

The synthetic procedure began with the same macrocycle as used in the study carried out by Zapata and co-workers (2013), **LuM** and **EuM**.[13,136,166,167] Moreover, a similar axle to that used by Allain and co-workers (2013) was synthesized such that it also contained a pyridinium motif, however one side of the axle was already stoppered prior to threading and the counter ion was a nitrite anion as opposed to chloride.[13,90,136,167] The non-stoppered side of the axle was terminated by an azide group so that after threading, the axle could be stoppered through CuAAC chemistry.[13,136,167] Thus, combining the mono-stoppered axle with the macrocyclic complex, a pseudorotaxane was formed.[13,136,167] The nitrite anion carried out this templation by coordinating to both the Ln^{3+} centre and the pyridinium group on the axle through hydrogen-bonding interactions with the amide hydrogens (Fig. 17).[13,136,167] On further reacting the pseudorotaxane with an alkyne-appended stopper and a copper(I) catalyst, lanthanide-based rotaxanes containing the templating nitrite anion (**Lu3.NO$_2$** and **Eu3.NO$_2$**) could be isolated.[13,136,167]

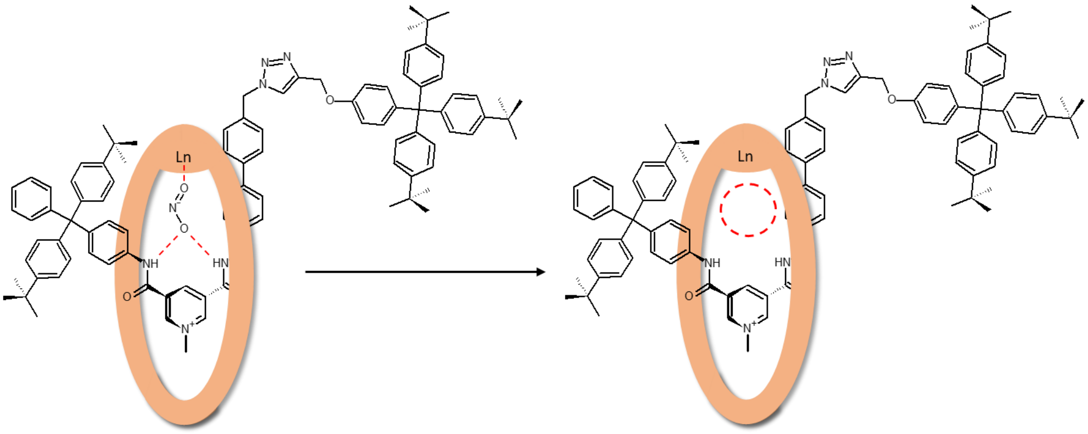

Ln= Lu; **Lu3.NO$_2$**
Eu; **Eu3.NO$_2$**

Ln= Eu; **Eu3.OTf**

Figure 17. Nitrite templated lanthanide-based rotaxanes by Langton et al., 2014. Image adapted from: 13, 167

Next, the nitrite anion was removed from **Eu3.NO$_2$** through exchanging with triflate (a weak coordinator) to form **Eu3.OTf**, containing a binding cavity (Fig. 17).[13,136,167] From here, titrations were carried out to investigate the changes in photophysical properties of **Eu3.OTf** on exposure to different anions (TBA salts) including fluoride (**TBA.F**), acetate (**TBA.OAc**), nitrite (**TBA.NO$_2$**), and chloride (**TBA.Cl**).[13,136,167]

When **TBA.F** was added to **Eu3.OTf**, the intensity of Eu^{3+} emission (on excitation at 360 nm) decreased largely which was observed alongside an increase in the Eu^{3+} luminescence lifetime.[13,136,167] On closer analysis of the emission spectra, there was also a large decrease in the emission intensity of the $^5D_0 \rightarrow {}^7F_2$ transition, suggesting a change in the Eu^{3+} coordination environment.[17,167] These results together suggested that when fluoride was added to **Eu3.OTf**, it was occupying a Eu^{3+} coordination site within the binding cavity.[167]

In comparison, when **TBA.NO$_2$** (nitrite) was added to **Eu3.OTf**, the emission intensity decline that was observed for fluoride was only observed to a small degree and the lifetime was unaffected.[13,136,167] Supplementing this, no changes were observed in the peak corresponding to the hypersensitive $^5D_0 \rightarrow {}^7F_2$ transition.[4,5,11,13,17,167] Accordingly, the nitrite anion was predicted to only interact with **Eu3.OTf** through interactions with its organic motifs (as opposed to occupying a coordination site).[13,136,167] This interaction would support the small degree of quenching observed through both the impedance of the energy transfer process and inhibition of water removal from the Eu^{3+} coordination sphere.[167]

For the acetate anion, a weak quenching effect was observed on its addition to **Eu3.OTf** along with an increase in the luminescence lifetime.[167] In saying this, these changes were not as large as those obtained for the fluoride, thus could be distinguished from the fluoride anion.[13,136,167] On the addition of **TBA.Cl** (chloride), there were no changes in the emission intensity of **Eu3.OTf**.[136,167]

This paper was important as it showed how the nitrite anion could be used such that it was able to act as a transient bridge between the axle and the Ln^{3+} motif of the macrocycle.[13,136,166,167] Upon completing its templating role, the nitrite could be removed to leave a single anion binding pocket with a preference for fluoride as opposed to chloride, nitrite, or acetate (*i.e.* an anion distinct from that used for templation).[13,90,136,167] The presence of fluoride binding in this pocket could be detected based on changes in Ln^{3+} luminescence.[13,136,167]

Overall, findings from the Beer and Faulkner research groups were important as they showed how Ln^{3+}'s can be incorporated into interlocked molecules and their properties can be used for anion sensing.[13,17,90,136,165-167]

1.5.4 Responsive luminescent lanthanide-based pseudorotaxanes

Another research group that has been key in the development of luminescent lanthanide-based pseudorotaxanes is Liu's research group.[17,136] In their initial 2008 study, Han and co-workers developed a reversible on/off luminescent Ln^{3+}-based pseudorotaxane.[17,48,136]

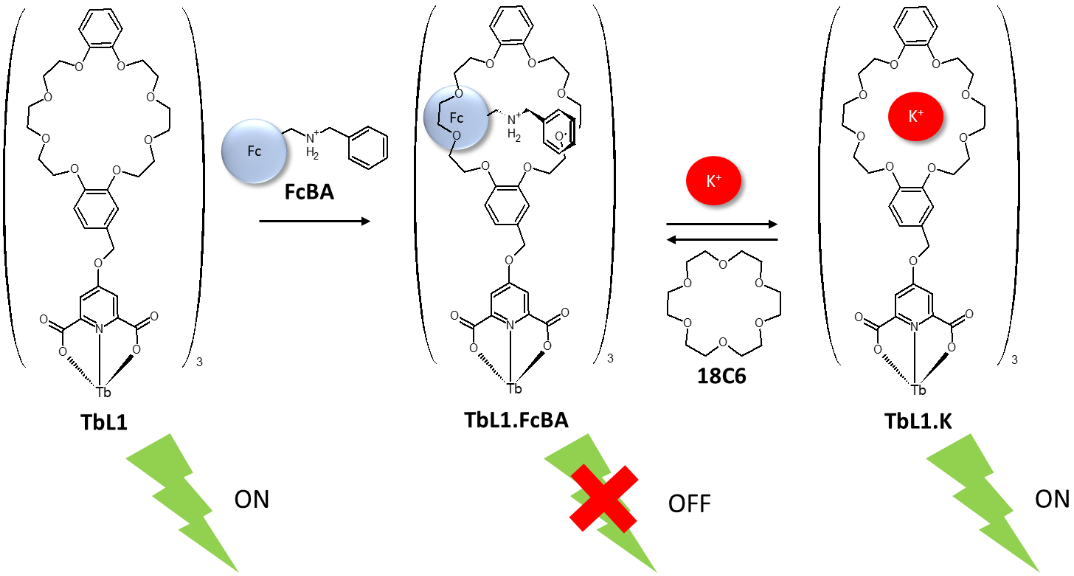

Figure 18. Schematic showing the responsive luminescent lanthanide-based pseudorotaxane developed by Han and co-workers (2008). Image adapted from: 48, 136

The ligand for Tb^{3+} complexation was designed to have two motifs, a strong chelating group/lanthanide sensitizer and a macrocyclic component (Fig. 18).[17,48,136] The chelating group/lanthanide sensitizer chosen was the DPA chelator (as used in the current study).[17,48,136] The 4-pyridyl position of the DPA chelator was functionalized with its second motif, the macrocyclic component, by attaching a dibenzo-24-crown-8 motif (Fig. 18).[17,48,136] After deprotection of the ethyl groups on the 2,6-positions of DPA, the desired ligand (**L1**) was isolated.[48] On complexation with Tb^{3+}, the formation of luminescent 3:1 **L1:Tb**$^{3+}$ complexes (**TbL1**) (on excitation at 282 nm) was achieved.[17,28,48]

The researchers then introduced an axle, consisting of a ferrocene group appended to a benzylammonium motif (**FcBA**), to the complex.[17,48,136,173-175] The researchers found that on the addition of **FcBA** to **TbL1**, there was a large quenching effect observed in the emission of the resulting tris[2]pseudorotaxane system (**TbL1.FcBA**) at 544 nm (corresponding to the hypersensitive $^5D_4 \rightarrow {}^7F_5$ transition) by 94 % (Fig. 18).[17,28,48,136] It was concluded that this decline associated with pseudorotaxane formation was resulting from an intramolecular photoinduced electron transfer (PET) process quenching process.[16,17,24,27,48] In general, PET refers to the quenching that occurs resulting from electron transfer.[16,27] In this case, intramolecular PET was occurring from the ferrocene component of **FcBA** axle to the dipicolinate motif.[14,16,17,27,48] On the addition of KPF_6 to **TbL1.FcBA**, the Tb^{3+} emission was regained, suggesting that the **FcBA** axle (responsible for the quenching) had been removed from the macrocycle and substituted with K^+ to form **TbL1.K**.[48,136]

Next, ability of reversing this process was investigated.[48] When 18-crown-6 (**18C6**) was added to **TbL1.K**, the emission was quenched again, suggesting that the K^+ had been pulled out of the crown macrocycle, allowing it to be rethreaded with **FcBA** thus enabling quenching.[48,136] These quenching and luminescence regaining cycles could be reproduced by adding **18C6** and K^+ (respectively) multiple times.[48,136]

The same research group extended on this study in 2011 by developing a Tb^{3+} complex with a ligand (**L2**) bearing a terpyridine (terpy) chelating group along with a dibenzo-24-crown-8 motif (as the macrocyclic component) appended to the 4-pyridyl position of the terpy chelating group (Fig. 19).[17,136,168] Instead of using a ferrocene-containing axle, a fullerene-containing axle was used (**FuBA**) and the researchers developed a responsive [2]pseudorotaxane system (**TbL2.FuBA**) (Fig. 19).[17,132,136,168]

Through titrations, **L2** was found to form complexes with a 1:1 Tb^{3+}:**L2** ratio (**TbL2**) which, on excitation at 319 nm, gave an emission spectrum with peaks characteristic of Tb^{3+} emission from the $^4D_4$ to the ^7F_J states.[28,136,168] However, on the addition of 1.3 equivalents of **FuBA** to **TbL2** to form the **TbL2.FuBA** pseudorotaxane, the intensity of the hypersensitive $^5D_4 \rightarrow {}^7F_5$ transition at 544 nm was reduced by 90 % (Fig. 19).[17,28,136,168] This large reduction was predicted, based off the combined studies of Zhou, Armspach, Schubert, Fu and Teari (as cited in ref [168]), to be due to intramolecular PET occurring from **TbL2** to the electron-accepting fullerene motif located on the threaded axle.[17,136,168]

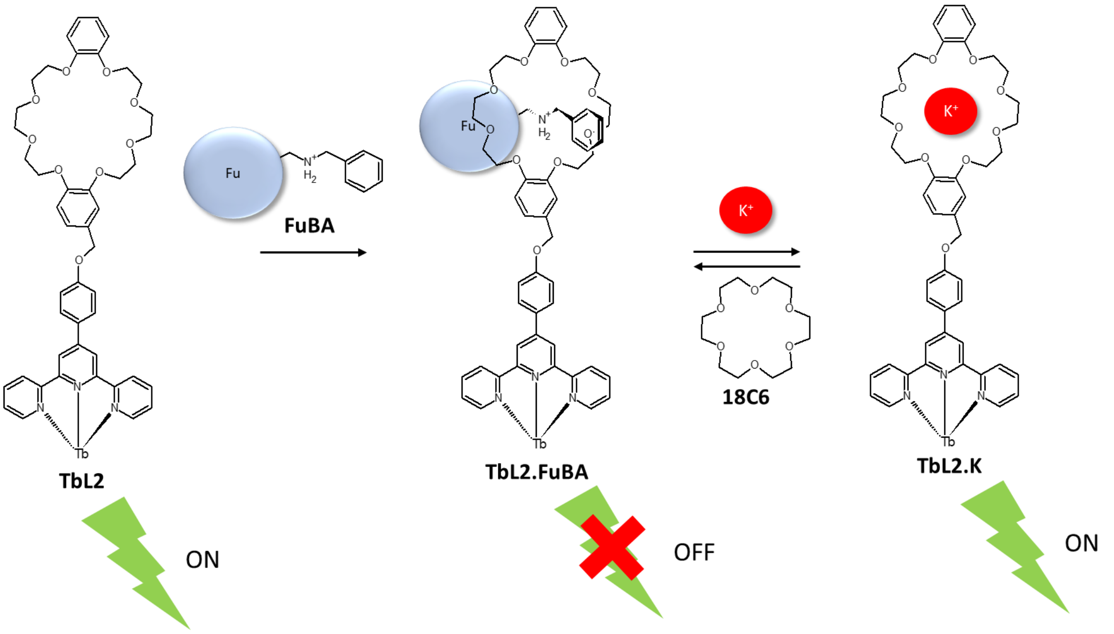

Figure 19. Schematic showing the responsive luminescent lanthanide-based pseudorotaxane developed by Ding and co-workers (2011). Image adapted from: 136, 168

As observed with **TbL1.FcBA**, when KPF_6 was added to **TbL2.FuBA**, the Tb^{3+} emission was re-established, implying that **FuBA** (responsible for the quenching PET process) had been de-threaded and replaced with K^+ (forming **TbL2.K**) (Fig. 19).[17,136,168] The quenching effect could be regained through the addition of **18C6** (as observed for the **TbL1** system) and this process could be repeated multiple times (Fig. 19).[17,136,168]

Later in 2013, the same research group developed a lanthanide based [2]-pseudorotaxane with Ln^{3+} photophysical properties switchable by two factors, the addition of an axle, and optical input.[17,136,164] The system was analogous to that reported in 2011, containing a terpy chelating group along with an appended dibenzo-24-crown-8 motif for the ligand (**L3**).[17,136,164,168] However, instead of a ferrocene or fullerene group substituted on the axle, a diarylethene (**DAE**) derivative was used to exploit the photochromic properties intrinsic to this class of molecules.[17,136,164]

An initial study was performed on the DAE-containing axle prior to complexation to probe its optical responsiveness.[164] On exposure of the colourless open form axle (**OF**) in a 1:1 ACN:$CHCl_3$ solution to UV light at 365 nm, the solution turned dark green in colour, accompanied by an increase in the intensity of an absorption band at 598 nm, indicative of the production of the closed form axle (**CF**).[164] On exposure of the dark green solution of **CF** to 614 nm visible light, the solution appeared to return to its original colourless state, suggesting the reformation of **OF**.[164] Thus, the axle could exist in two forms depending on light exposure.[17,136,164]

Following these studies, researchers then investigated the photophysical properties of the 1:1 Eu^{3+}:**L3** complex (**EuL3**) both with and without its axle.[136,164] Without its axle, **EuL3** exhibited peaks at 580, 594, 619, 656 and 700 nm (on excitation at 390 nm) characteristic of Eu^{3+} emission from the $^5D_0$ state to the ^7F_J states (Fig. 20).[136,164] On the addition of **OF** to **EuL3** the formation of **EuL3.OF,** a [2]-pseudorotaxane, was achieved and the intensity of Eu^{3+} emission from this [2]-pseudorotaxane was reduced by only 10 % when compared to **EuL3** (which could be attributed to minor PET processes) (Fig. 20).[17,48,136,164,168] However, on the exposure of **EuL3.OF** to UV light (365 nm) to form **EuL3.CF**, there was a large decline, by 80 %, observed in the intensity of the hypersensitive $^5D_0 \rightarrow {}^7F_2$ transition (at 619 nm) (Fig. 20).[17,136,164] This finding suggested that quenching was occurring from an intermolecular resonance energy transfer (RET) process between the Eu^{3+} centre (acting as a donor, with maximum emission at 619 nm) and the **CF axle** (acting as an acceptor, with max absorbance at 598 nm) resulting from their spectral overlaps.[17,136,164] This quenching effect was not observed in **EuL3.OF** as **OF** did not absorb in the Eu^{3+} emission range.[136,164] These photophysical changes were found to be reversible, with subsequent exposure of **EuL3.CF** to 614 nm visible light regaining the Eu^{3+} emission as observed for **EuL3.OF** (Fig. 20).[17,136,164]

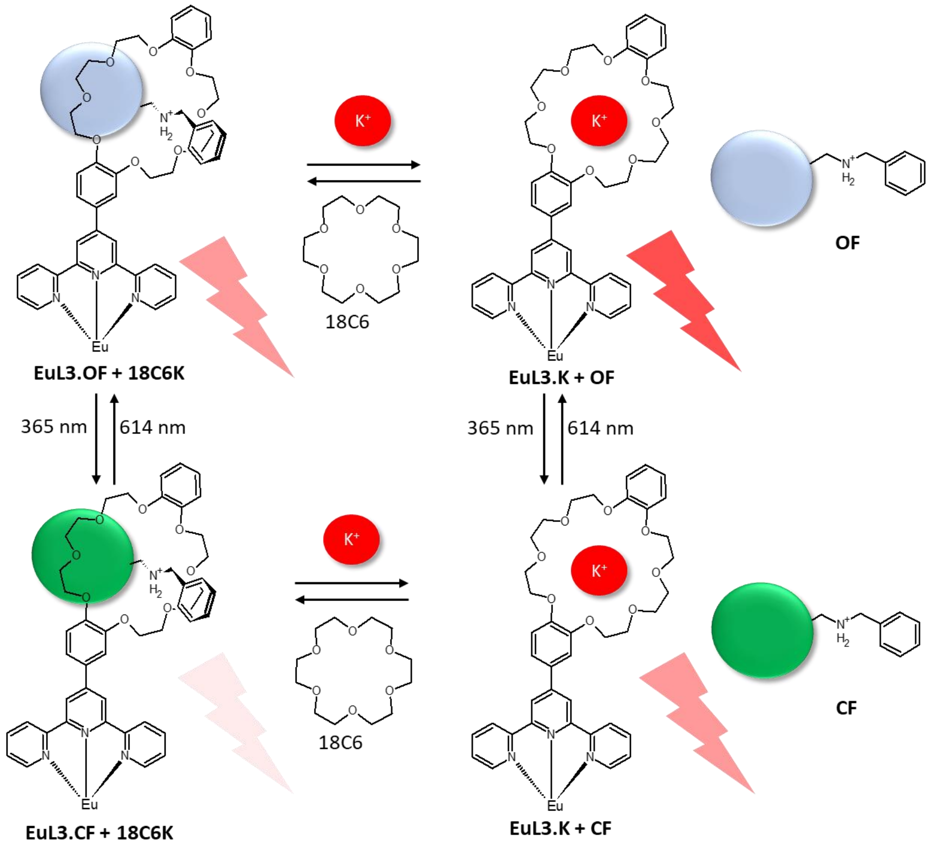

Figure 20. Schematic showing the responsiveness of the luminescent lanthanide-based system developed by Cheng and co-workers in 2013 depending on pseudorotaxane formation and axle type. Image adapted from: 164

Following this, the responsiveness of the complex to different axles was analysed due to earlier findings on similar systems in 2008 and 2011.[48,136,164,168] All threading and de-threading was supported by NMR analysis.[164] In terms of the photophysical changes, on the addition of KPF_6 to **EuL3.OF**, there was only a small increase in the emission intensity of the resulting **EuL3.K + OF** complex compared to that obtained for **EuL3.OF** (Fig. 20).[136,164] On the exposure of **EuL3.K + OF** to 365 nm light, the emission intensity was decreased only by a small amount (Fig. 20).[136,164] However, when **EuL3.K + OF** was exposed to **18C6** followed by 365 nm irradiation, the large quenching associated with the **OF** threading followed by **CF** formation was observed (Fig. 20).[136,164] In comparison, when **EuL3.CF** was exposed to KPF_6, the emission intensity was regained, suggesting that the RET process that was once inhibiting the emission had been removed due to the substitution of **CF** for K^+ (forming **EuL3.K + CF**) (Fig. 20).[136,164] On the subsequent exposure of **18C6** to **EuL3.K** + **CF**, the emission intensity was again quenched due to the rethreading of **CF** for K^+ (to form **EuL3.CF + 18C6K**), enabling the RET process to occur (Fig. 20).[136,164] Taken together, these results were important as they showed how changes in the conformation of the axle can only elicit changes in Eu^{3+} emission through RET when they are threaded.[136,164]

These studies were important as they showed how the luminescence of Ln^{3+}'s can be reversibly tuned in response to different hosts binding within a distal macrocycle attached to the 4-pyridyl position of terpy and DPA chelators (resulting in the assembly and disassembly of a pseudorotaxane structure depending on the host).[17,48,136,168]

More recently, Liu and co-workers developed a lanthanide-based poly-pseudorotaxane system displaying Ln^{3+} luminescence depending on the presence (or lack of) certain antibiotics.[141] The ligand, **L4**, contained the DPA chelating motif functionalised at its 4-pyridyl position with a naphthalene group containing a positively charged imidazolium motif as the linker.[141] The macrocyclic component was derived from the cucurbit[*n*]uril (CB[*n*]) family.[141] CB[8] was used as it had been previously reported by two separate research groups led by Scherman and Liu (as cited in ref [141]) to form 2:1 napthalene-imidazolium:CB[8] complexes, with the naphthalene motif lying within the CB[8] cavity.[141,170] This same 2:1 complexation was observed on the combination of **L4** with **CB[8]**, forming a pseudo[3]rotaxane **CB[8]L4** (Fig. 21).[141]

On addition of Tb^{3+} to **CB[8]L4**, each DPA chelating motif bound to a Tb^{3+} forming a poly-pseudorotaxane system with a 2:3 **Tb^{3+}:L4** ratio (**TbCB[8]L4**).[137] **L4** was also complexed with Tb^{3+} to form **TbL4** with a 1:3 **Tb^{3+}:L4** ratio.[141] The emission spectra of both **TbL4** and **TbCB[8]L4** on excitation at 254 nm showed peaks at 490, 545, 583 and 621 nm corresponding to the Tb^{3+} $^5D_4 \rightarrow {}^7F_J$ transitions where J = 6, 5, 4 and 3 respectively.[141] In saying this, after 8/15 equivalents of Tb^{3+} had been added to **TbCB[8]L4**, the intensity of emission at 545 nm was larger than that obtained for **TbL4** by a factor of 2, suggesting that the presence of CB[8] was enhancing the luminescence of **TbCB[8]L4**.[141] Moreover, **TbCB[8]L4** also displayed both a larger quantum yield (Φ = 7.81 %) and a longer emission lifetime (τ = 1.33 ms) compared to that obtained for

TbL4 of 0.89 % and 45.76 µs for the quantum yield and emission lifetime respectively.[141] This was found to be due to increased Tb^{3+} quenching due to more water molecules present in the coordination sphere of **TbL4** compared to **TbCB[8]L4**.[141]

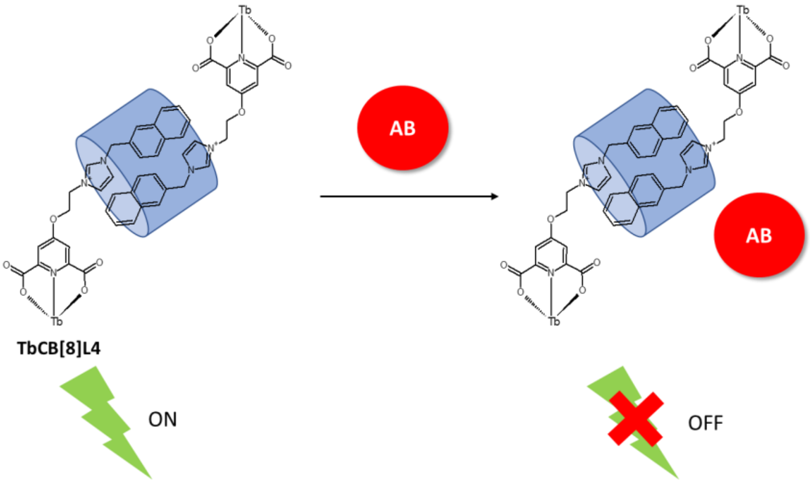

Figure 21. Schematic showing the Tb^{3+}-containing pseuedo[3]rotaxane developed by Zhou and co-workers (2019) and its responsiveness to the presence of an antibiotic (AB). Image adapted from: 141

Lastly the ability of **TbCB[8]L4** to detect certain antibiotics in aqueous solution was investigated. **TbCB[8]L4** was able to detect sulfamethazine and nitrofurazone as their presence induced the quenching of the Tb^{3+} $^5D_4 \rightarrow {}^7F_5$ peak at 545 nm by over 70 % compared to without these antibiotics present.[141] The same quenching effect was observed when **TbCB[8]L4** was doped into PVA, showing how it could act in both aqueous and solid phases.[141]

Overall, these studies were important as they represent the limited number of studies which combine the properties of interlocked molecules/supramolecular molecules with Ln^{3+}'s for the development of advanced technologies such as anion and antibiotic sensors and reversible molecular switches.[136] In saying this, in a large majority of these studies, the Ln^{3+} is integrated into the interlocked/supramolecular structure through its incorporation with the macrocycle.[48,90,164,166-168] Additionally, the synthesis of these structures appears to be dominated by templated-approaches.[48,90,164,166-168] We aim to take a slightly different approach which integrates three key fields of chemistry including the chemistry of MIMs, click chemistry and lanthanide luminescence, to develop responsive luminescent interlocked systems.

1.6 Aims of the thesis

The thesis can be split into two key parts, the first part involves a proof-of-concept study whereby Ln^{3+} complexes containing ligands with bulky R groups are synthesized through CuAAC chemistry (and a post-complex modification) and fully characterised. This will be achieved to ensure the bulky groups chosen are able to sensitize Ln^{3+} luminescence and (in the case of the post-complex modification method) to ensure that click reactions can be carried out on lanthanide complexes without decomplexation. The next part will focus on the testing of this concept and the ability of using it to synthesise luminescent interlocked quasi-[4]-rotaxanes through active template CuAAC methods. Overall, the aims of the thesis were:

- To synthesize and characterise ligands $\mathbf{L_1} - \mathbf{L_4}$ and their complexes with La^{3+}, Eu^{3+} and Tb^{3+}
- To analyse the photophysical properties of the corresponding $\mathbf{[Ln(L_{1\text{-}4})_3]^{3-}}$ complexes
- To investigate the ability of carrying out a CuAAC reaction on an alkyne-appended DPA complex to synthesize and extending this to AT-CuAAC reactions
- To use active-template click chemistry (AT-CuAAC) to synthesize rotaxane ligands
- To investigate the ability of these ligands to self-assemble with Ln^{3+}'s for the development of responsive luminescent lanthanide-based [4]-rotaxanes (with a general structure shown below).

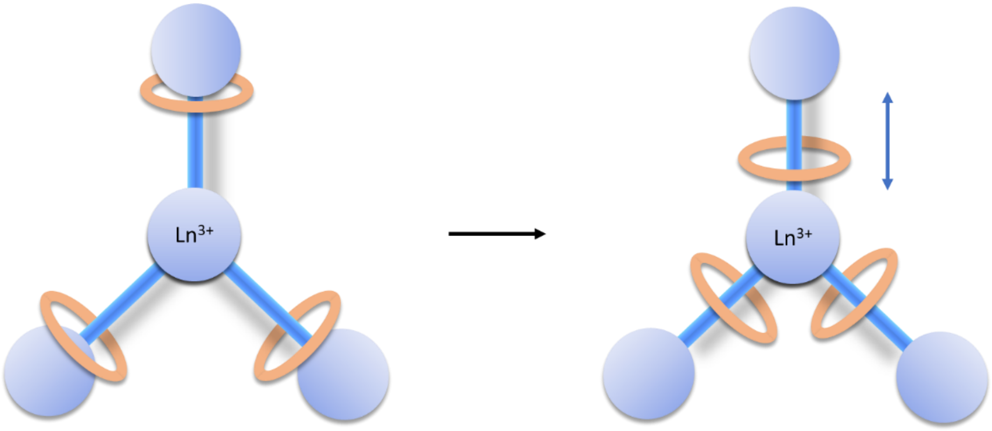

Figure 22. General structure of the target quasi-[4]-rotaxanes

2. Results and discussion

2.1 Ligand and complex design

Ligands were designed such that they contained groups bulky enough to act as stopper groups for the macrocycle (**M_1**) to be used in rotaxane synthesis, in addition to having an aromatic and/or heterocyclic component (for efficient Ln^{3+} sensitization) and an Ln^{3+} binding site.[152,196] Three potential stopper groups were investigated, a 1,8-naphthalimide, a di-*tert*-butyl benzyl and a 9-anthracene group.[152]

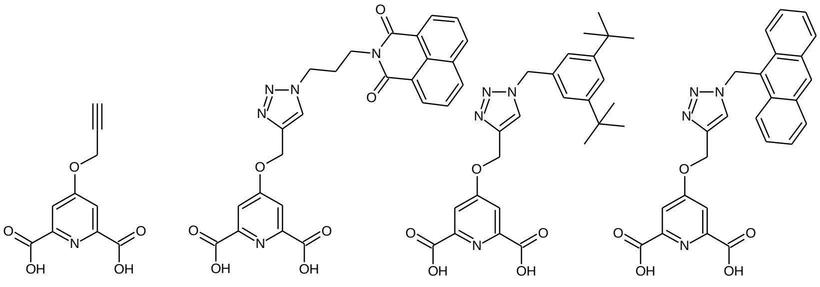

L_1 **L_2** **L_3** **L_4**

Figure 23. Target ligands, with L_2 – L_4 containing both a Ln^{3+} chelating motif and a stopper group

There appears to be an established family of 4-pyridyl substituted DPA lanthanide complexes made through clicking different alkynes to an azide group attached directly to the 4-pyridyl DPA intermediate during ligand synthesis.[65-73,198] This direct clicking poses a problem for the development of interlocked molecules as it does not give much space between the DPA chelating group and the clicked component which can pose synthetic problems when carrying out the AT-CuAAC reaction.[155] Thus, for the current study a balance between producing a relatively long axle but not long enough such that bulky groups can still impact Ln^{3+} emission was realized. This will be achieved through using a propargyl group appended to the 4-OH position of chelidamic acid, thus supplying a CH_2 linker between the oxygen atom at the 4-pyridyl position and the triazole. In the literature, only one study appears to exist which reports the clicking of an alkyne-functionalized coumarin derivative to the 4-pyridyl DPA position through an ether linker.[74]

Throughout the study, europium, terbium and lanthanum were chosen for complexation. Eu^{3+} and Tb^{3+} possess their main emissive excited states are at approximately 17,500 cm^{-1} and 20,000 cm^{-}

[1] for $^5D_0$ for Eu^{3+} and $^5D_4$ for Tb^{3+} respectively, thus are visibly emissive.[1-5,8,9,11,13,14,16,18,21,26,30,45,178,184,198-200,221,228,229] Accordingly, as mentioned by Wenkert and co-workers (as cited in ref [177]), lanthanum contains no unpaired electrons, making it diamagnetic in nature and enabling its use in ^{1}H NMR spectroscopy.[4,41,177,193,197,202,209]

There appears to be a research gap regarding the use of the DPA-lanthanide complex family for the development of MIMs through click chemistry (*i.e.* studies which combine click chemistry, lanthanide chemistry and the properties of MIMs). Thus, the systems under investigation have been designed to combine these features by using AT-CuAAC to synthesise quasi-[4]-rotaxanes incorporating a central luminescent Ln^{3+} edifice.[137] In this way, changes in the Ln^{3+} coordination sphere (such as the shuttling of the macrocycle along the axle) in response to different environments may lead to changes in Ln^{3+} luminescence.

These systems can be considered as quasi-[4]-rotaxanes as they contain three separate macrocycles which are separated from a single Ln^{3+} complex (containing both the stopper groups and the axle) by a mechanical bond.[137]

2.2 Synthetic procedures

Two synthetic procedures are referred to throughout this project, one where the ligand is made prior to Ln^{3+} complexation (preformed ligand method, section 2.4) and another whereby a complex containing adaptable functional groups is first synthesized, and the ligand is modified through a reaction carried out on the adaptable complex (the post-complexation modification method, section 2.5).[106,116] For both methods, the key intermediate is an alkyne-functionalized DPA motif (**2**), the protected form of which was used as a reagent for CuAAC chemistry (in the preformed ligand method) and the deprotected form of which complexes with Ln^{3+} for post-complexation modifications. Following this, the ability of using AT-CuAAC to synthesize quasi-[4]-rotaxanes is investigated.

2.3 Alkyne ligand (L_1) and complex $[Ln(L_1)_3]^{3-}$

2.3.1 Synthesis and characterization

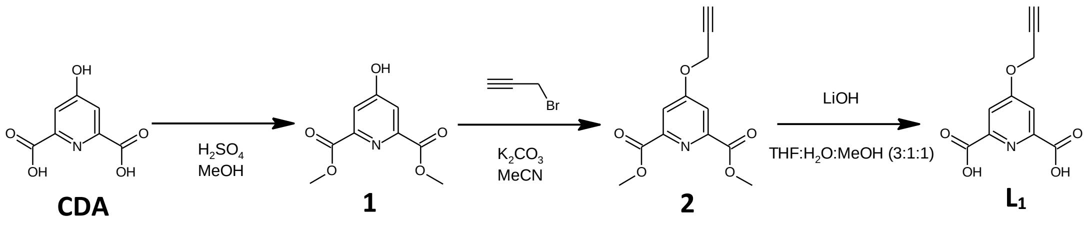

Figure 24. General reaction scheme for the synthesis of L_1

The synthesis of **L_1** involved three steps starting from chelidamic acid (4-hydroxypyridine-2,6-dicarboxylic acid) (CDA) (Fig. 24). In the first step, the carboxylic acid groups substituted at the 2,6-positions of the pyridyl ring of CDA were protected using a sulfuric acid catalysed Fischer esterification reaction with methanol.[179-181] The methyl-protected product (**1**) could be obtained in yields of 60 – 70 %. Next, a Williamson ether synthesis reaction was carried out with propargyl bromide (in the presence of potassium carbonate) to attach the propargyl group to the 4-pyridyl position of **1** to form **2** in yields of approximately 50 – 60 % (Fig. 24).[75,182,183,196] From here, **2** was either reacted with specific organic azides to form methyl-protected ligand precursors (*i.e.* preformed ligand method, section 2.4) or it was deprotected to form **L_1** which could be complexed and used for post-complexation modifications. Deprotection was carried out by stirring **2** in a THF:MeOH:H_2O (3:1:1) solvent mixture under nitrogen in the presence of lithium hydroxide (LiOH) at room temperature overnight. **L_1** was retrieved by adding 1 M HCl to the reaction mixture causing the pale-yellow solid, **L_1**, to precipitate out in yields of approximately 80 %.[69]

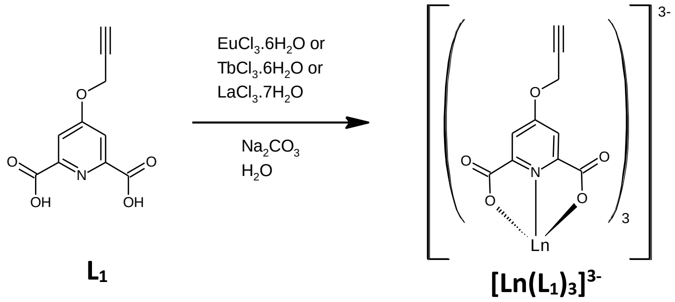

Figure 25. General reaction scheme for the synthesis of $[Ln(L_1)_3]^{3-}$ complexes where Ln = La^{3+}, Eu^{3+} and Tb^{3+}

To synthesise the **$[Ln(L_1)_3]^{3-}$** complexes (where Ln = La^{3+}, Eu^{3+} and Tb^{3+}), one equivalent of **L_1** was combined with two equivalents of Na_2CO_3 and dissolved in 2 – 3 mL of deionised H_2O at 60 – 80˚C for 10 – 30 minutes (Fig. 25).[37,65,67-70,72,74,184-186] Next, 0.33 equivalents of the respective lanthanide chloride salt ($LaCl_3·7H_2O$ for La^{3+}, $EuCl_3·6H_2O$ for Eu^{3+} and $TbCl_3·6H_2O$ for Tb^{3+}) dissolved in H_2O was pipetted into the mixture.[34,35,37,41-43,65,67-70,72,74,184] This resulted in the almost instant precipitation of a white solid that redissolved on further heating and stirring. The water was removed under reduced pressure leaving a white solid which, after resuspending and stirring in acetone overnight (to remove any unreacted **L_1**), gave a white solid which was filtered off and which appeared highly luminescent (red if Eu^{3+} and green if Tb^{3+}) under short wave UV light. Yields of 75 % up to quantitative amounts were obtained.

The ^1H NMR spectra of both **L_1** and the **$[Ln(L_1)_3]^{3-}$** complexes were obtained in DMSO-d_6 despite the competitive binding behaviour of DMSO (further confirming the strong binding ability of the DPA chelating motif) (Fig. 26).[2,4,5,12,13,17,18,22,26,29,31,33-48,50,196,197] The ^1H NMR spectrum obtained for the ligand, **L_1**, showed peaks strongly suggestive of its formation (Fig. 26). The singlet peak at 7.78 ppm could be assigned to the two hydrogen atoms at the 3- and 5- positions on the pyridyl-ring of **L_1** (pyridyl hydrogens, *Py-H*).[187,196,204,257] Additionally, the doublet at 5.10 ppm was assigned to the two hydrogen atoms belonging to the CH_2 linker of the alkyne (Fig. 26).[187,204,257] These protons coupled with the alkyne hydrogen, the peak of which appeared as a triplet at 3.75

ppm (Fig. 26).[187,257] Moreover, the ^{13}C NMR spectra showed a total of 7 peaks, of which 4 appeared in the ^{13}C DEPT spectra, in line with that expected for **L₁** supporting its formation.

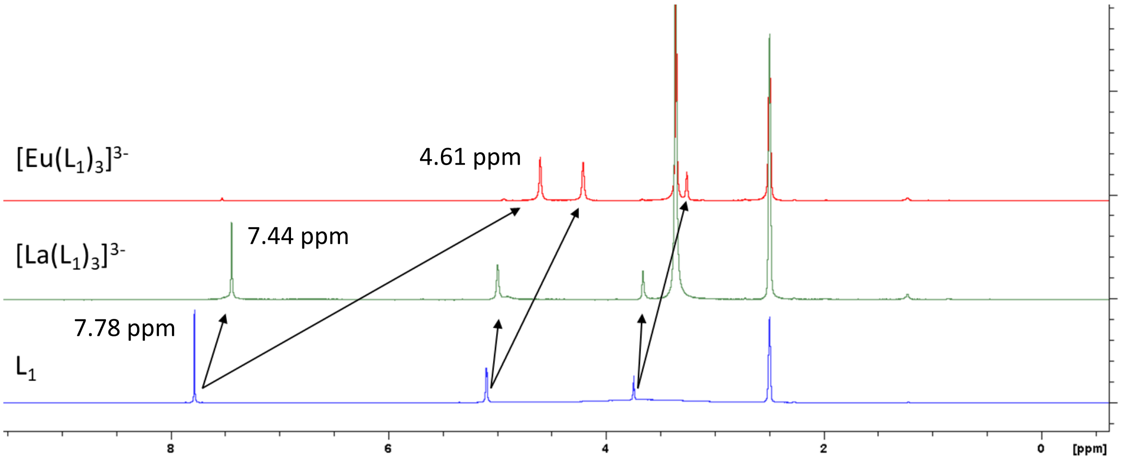

Figure 26. Comparison of ^{1}H NMR spectra of L_1 (blue, bottom), $[La(L_1)_3]^{3-}$ (green, middle) and $[Eu(L_1)_3]^{3-}$ (red, top) in DMSO-d_6 showing the up-field shifting effect on the peaks of L_1 on La^{3+} and Eu^{3+} complexation

The spectra of $\mathbf{[Ln(L_1)_3]^{3-}}$ strongly supported successful the formation of 3:1 $\mathbf{L_1}$:Ln^{3+} species as only three signals (a single set) could be observed, suggesting that the complexes inherited three-fold symmetry such that each ligand was equivalent (Fig. 26).[37,38,41,188,189,193,199,201,207] Unexpectedly, the ^{1}H NMR spectrum of $\mathbf{[La(L_1)_3]^{3-}}$ appeared to contain broad sub-peaks lying adjacent to the pyridyl, CH_2 and, in some cases, the alkyne signals. These broad sub-peaks did not line up with any free $\mathbf{L_1}$ peaks and so were predicted to be due to the presence of dynamic NMR time-scale processes (as explained further in section 2.4.1.1).[187,188,201,207,208] The ^{1}H NMR spectrum of $\mathbf{[Tb(L_1)_3]^{3-}}$ only showed one broad peak at 9.07 ppm thus was omitted from the comparison.[41,188,189,199,201,207]

In comparing the ^{1}H NMR spectra of $\mathbf{L_1}$ to that of $\mathbf{[La(L_1)_3]^{3-}}$, there was an up-field shift observed for all the peaks in the spectra (Fig. 26).[187] This same up-field shift was also observed in the ^{1}H NMR spectra of $\mathbf{[Eu(L_1)_3]^{3-}}$ but to a larger effect (Fig. 26).[187] Studies in the literature which report DPA systems complexed to Eu^{3+} show the same up-field shifts (to lower δ) as observed.[35,37,41,65,67-69,72,188,193,201,205] The larger shifts observed for the protons in the ^{1}H NMR spectrum of $\mathbf{[Eu(L_1)_3]^{3-}}$ compared to $\mathbf{[La(L_1)_3]^{3-}}$ was due to the paramagnetic nature of Eu^{3+}.[4,8,41,177,190,193,197,199,202,209]

For both **$[La(L_1)_3]^{3-}$** and **$[Eu(L_1)_3]^{3-}$** compared to **L_1**, the protons which experienced the largest up-field shift on complexation were the pyridyl protons (Fig. 26).[31,33,35,37,38,41,187,189,199,205] For **$[La(L_1)_3]^{3-}$**, the singlet *Py-H* peak was showing at 7.44 ppm compared to 7.78 ppm for **L_1**, a $\Delta\delta$ of 0.34 ppm).[31,33,35,37,38] For **$[Eu(L_1)_3]^{3-}$**, a larger shift was observed for *Py-H* from 7.78 ppm in **L_1** to 4.61 ppm in **$[Eu(L_1)_3]^{3-}$** (a $\Delta\delta$ of 3.17 ppm).[33,35,37,38,41,189,199,205] This shift observed for the pyridyl protons of **$[Eu(L_1)_3]^{3-}$** was discovered to be indicative of Eu^{3+} complexation with ligands containing the DPA chelating motif.[35,37,38,41,65,188,189,199,201,205] For instance, in a paper by Picot and co-workers, an ^1H NMR taken of a 4-pyridyl functionalized DPA complex in CD_3OD with 30 % $CDCl_3$ gave a peak which could be assigned to the pyridine hydrogen atoms at 5.0 ppm.[35] This peak had shifted up-field by 2.12 ppm when compared to the free ligand in $CDCl_3$, whereby the pyridyl protons were indicted by a singlet peak at 7.12 ppm.[35,188] Similar results have been observed in multiple studies, with up-field shifts as large as 3 – 5 ppm also being observed (depending on the specific system studied, the NMR solvent and whether or not the ligand is deprotonated or not).[35,38,41,188,201,205]

The large shifting observed for these pyridyl protons suggested that these protons were most impacted by complexation, which agreed with the location of the protons being closest to the Ln^{3+} centre compared to other protons.[41,187] Following this trend, for **$[La(L_1)_3]^{3-}$** and **$[Eu(L_1)_3]^{3-}$**, the CH_2 protons could be assigned to peaks appearing at 5.00 ppm and 4.21 ppm (respectively), compared to 5.10 ppm for **L_1**, producing shifts of 0.10 and 0.89 ppm (respectively) (Fig. 26).[41] Lastly, the alkyne hydrogen, located the furthest away from the Ln^{3+} centre, was assigned to the peaks at 3.66 and 3.26 ppm for **$[La(L_1)_3]^{3-}$** and **$[Eu(L_1)_3]^{3-}$** (respectfully), compared to 3.75 ppm for **L_1**, producing shifts of 0.09 and 0.49 ppm for **$[La(L_1)_3]^{3-}$** and **$[Eu(L_1)_3]^{3-}$** (respectfully), thus experiencing the smallest Ln^{3+} induced shifts.[41,187]

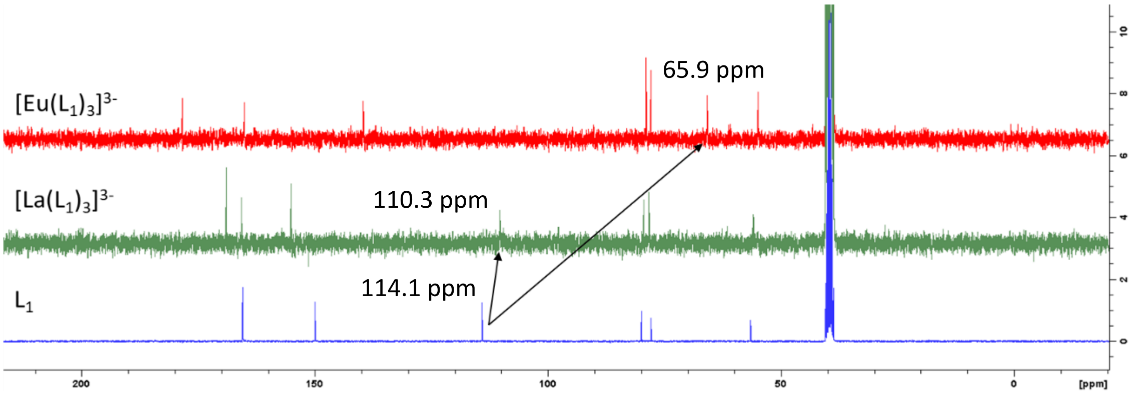

Figure 27. ^{13}C NMR spectra of L_1 (blue, bottom), $[La(L_1)_3]^{3-}$ (green, middle) and $[Eu(L_1)_3]^{3-}$ (red, top) in DMSO-d_6 showing the effect of complexation on the pyridyl carbon peak

A similar effect was observed in the ^{13}C NMR spectra of **$[Ln(L_1)_3]^{3-}$** compared to **L_1** (Fig. 27). In particular, the pyridyl carbons of **L_1**, assigned to the peak at 114.1 ppm, shifted up-field on complexation to Ln^{3+} to 110.3 and 65.9 ppm for **$[La(L_1)_3]^{3-}$** ($\Delta\delta$ of 3.8 ppm) and **$[Eu(L_1)_3]^{3-}$** ($\Delta\delta$ of 48.2 ppm) respectively (Fig. 27).[201] This same shifting was observed by Oauli and co-workers where the ^{13}C NMR spectra of $[La(DPA)_3]^{3-}$ and $[Eu(DPA)_3]^{3-}$ gave peaks corresponding to the pyridyl carbons at 126.8 and 85.2 ppm (respectfully), compared to the ^{13}C NMR spectra of DPA on its own whereby the pyridyl carbons were showing at 129.7 ppm.[188,201] These literature values translate to $\Delta\delta$ values of 2.9 ppm for $[La(DPA)_3]^{3-}$ and 44.5 ppm for $[Eu(DPA)_3]^{3-}$, being very comparable to those obtained for **$[La(L_1)_3]^{3-}$** (3.8 ppm) and **$[Eu(L_1)_3]^{3-}$** (48.2 ppm) (with slight differences expected due to different NMR solvents and systems).[188,201] Additionally, to ensure that the substituent at the 4-pyridyl position had no effect on this shift, the ^{13}C NMR spectrum taken of a 3:1 ligand:Eu^{3+} complex (with the ligand being a 4-pyridyl functionalized DPA derivative) in $CDCl_3$ by Picot and co-workers gave a peak which could be assigned to the pyridyl carbons at 84.4 ppm, being relatively comparable to that obtained for **$[Eu(L_1)_3]^{3-}$** of 65.9 ppm.[35,201]

The IR spectra of **$[Ln(L_1)_3]^{3-}$** also showed evidence of successful complexation of **L_1** to Ln^{3+} (Fig. 28).[47] In comparing the IR spectra of **L_1** and **$[Ln(L_1)_3]^{3-}$**, the main difference observed was the disappearance of the peak at 1735 cm^{-1} in **L_1** compared to **$[Ln(L_1)_3]^{3-}$**.[49,193,204-207] This peak was assigned to the stretching of the carbonyl C=O bond of the carboxylic acid motifs in **L_1** (Fig. 28).[185,186,193,195,197,202-207] However, on complexation, this C=O stretch was removed and instead, strong peaks at 1585, 1587 and 1588 cm^{-1} were observed for **$[Eu(L_1)_3]^{3-}$**, **$[Tb(L_1)_3]^{3-}$** and **$[La(L_1)_3]^{3-}$** (respectively), in the range expected for COO^- asymmetric stretching (Fig. 28).[38,40,47,49,185-187,193,195,199-207,218] Additionally, peaks observed at 1405, 1410 and 1365 cm^{-1} in the IR spectra of **$[Eu(L_1)_3]^{3-}$**, **$[Tb(L_1)_3]^{3-}$** and **$[La(L_1)_3]^{3-}$** (respectively) (which were absent in the IR spectrum of **L_1**) could be assigned to COO^- symmetric stretching (Fig. 28).[38,40,47,49,187,203,205,206,218] These peaks provided evidence of Ln^{3+} complexation as coordination of one of the oxygen atoms in the carboxylate functional groups to Ln^{3+} causes a weakening of the C=O bond thus changes its stretching frequency.[40,47,49,187,197,199,201,203,205,206,218]

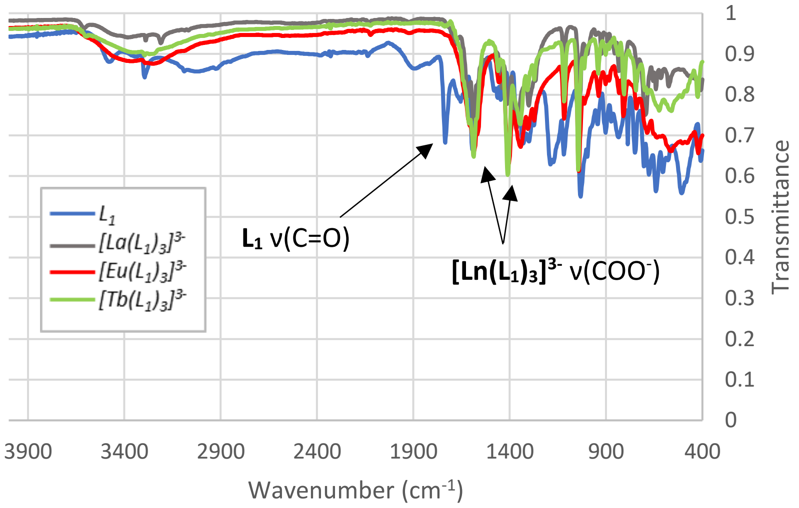

Figure 28. IR spectra of L_1 (blue), $[La(L_1)_3]^{3-}$ (grey), $[Eu(L_1)_3]^{3-}$ (red) and $[Tb(L_1)_3]^{3-}$ (green)

The broad peak spanning 2700 – 3300 cm^{-1} (centred at approximately 3034 cm^{-1}) in the IR spectrum of **L_1** was assigned to O-H stretching of the protonated carboxylic acid group which appeared to be removed in the IR spectra of **$[Ln(L_1)_3]^{3-}$**, supporting the deprotonated nature of the ligand (required for complexation) (Fig 28).[187,206] The presence of broad peaks spanning from approximately 2900 – 3700 cm^{-1} in the IR spectra of **[Ln(L$_1$)$_3$]$^{3-}$** suggested the presence of H_2O molecules in the complexes, expected as they were synthesized in H_2O (Fig. 28).[38,187,218]

2.3.2 Photophysical properties of [Ln(L$_1$)$_3$]$^{3-}$

The UV/Vis spectrum of **L$_1$** was collected (1 x 10^{-5} M in MeOH) and compared to that of **[La(L$_1$)$_3$]$^{3-}$**, **[Eu(L$_1$)$_3$]$^{3-}$**, and **[Tb(L$_1$)$_3$]$^{3-}$** (1 x 10^{-5} M in H_2O) (Fig. 29). Overall, the UV/Vis spectra of both **L$_1$** and its complexes contained their main peaks at relatively high energies, between 200 and 300 nm, which has been observed for similar systems (Fig. 29).[45,71,74,185,186,193-196,201,203,207]

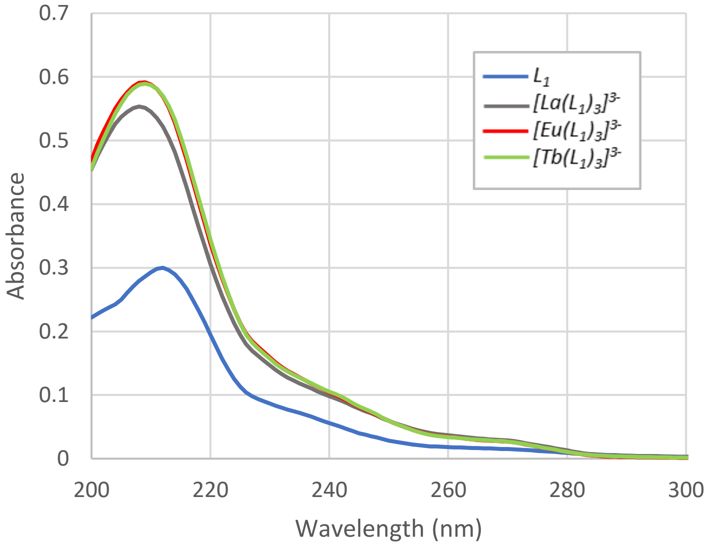

Figure 29. UV/Vis spectra of L$_1$ (1 x 10^{-5} M in MeOH) compared to [La(L$_1$)$_3$]$^{3-}$ (grey), [Eu(L$_1$)$_3$]$^{3-}$ (red) and [Tb(L-$_1$)$_3$]$^{3-}$ (green) (1 x 10^{-5} M in H_2O)

L$_1$ showed an absorption maximum ($\lambda_{abs}{}^{m}$) at 212 nm (with a smaller shoulder/plateau region at approximately 240 and 273 nm) and had a tail extending out to approximately 300 nm (Fig. 29).[31,41,45,47,71,74,187,193-196,201,207,208] On complexation, a small hypsochromic shift was observed in the $\lambda_{abs}{}^{m}$ (*i.e.* **[Eu(L$_1$)$_3$]$^{3-}$** and **[Tb(L$_1$)$_3$]$^{3-}$** both had an $\lambda_{abs}{}^{m}$ value of 209 nm and **[La(L$_1$)$_3$]$^{3-}$** had an $\lambda_{abs}{}^{m}$ of 208 nm compared to the $\lambda_{abs}{}^{m}$ value of **L$_1$** of 212 nm) which may have also been due to different solvent effects (Fig. 29).[45,47,71,187,207,208]

Literature examples of Ln^{3+} complexes containing ligands of the DPA chelating family, as well as those on Ln^{3+} complexes containing the closely related alkyl-protected DPA chelating motif and the pyridine-2,6-dicarboxamide (PDA) chelating motif (*i.e.* differing from the DPA chelating motif such that it contains ester and amide groups (respectfully) substituted at the 2- and 6-positions of the pyridyl ring as opposed to carboxyl groups), peaks in the region between 200 – 300 nm have been assigned to a combination of the pyridyl n → π* and the carbonyl π → π* transitions.[31,33,40,41,45,47,71,74,186,187,193-196,201,207,208,210] Thus, due to the similarities between the DPA and the PDA motif, the λ_{abs}^{m} at 212 nm observed in the absorbance spectra of $\mathbf{L_1}$ was assigned to these overlapping n → π* and π → π* transitions.[31,34,38,40,41,47,71,74,186,187,193-196,201,207,208,210]

On complexation to La^{3+}, Eu^{3+} or Tb^{3+}, the molar absorptivity value (ε) at the λ_{abs}^{m} was observed to increase in intensity when compared to $\mathbf{L_1}$ (Fig. 29).[32,40,41,185,192,201] Both this small shift and the increase in molar absorptivity has been observed on the complexation of ligands belonging to the DPA ligand family with Ln^{3+} and strongly supported the interaction of $\mathbf{L_1}$ with Ln^{3+}.[32,41,185,186,192,201,207,208]

Under a standard lab UV lamp, $\mathbf{[La(L_1)_3]^{3-}}$ (1 x 10^{-3} M in H_2O) was not luminescent under short wave UV light (expected based off its f electron count of 0) (Fig. 30).[195] In comparison, $\mathbf{[Eu(L_1)_3]^{3-}}$ (1 x 10^{-3} M in H_2O) was a bright red colour under short wave (254 nm) UV light and $\mathbf{[Tb(L_1)_3]^{3-}}$ (1 x 10^{-3} M in H_2O) was a bright green colour under short wave UV light, proving the ability of $\mathbf{L_1}$ to act as an efficient sensitizer for both Eu^{3+} and Tb^{3+} emission (Fig 30).[193,202]

Figure 30. $[La(L_1)_3]^{3-}$ (left), $[Eu(L_1)_3]^{3-}$ (middle) and $[Tb(L_1)_3]^{3-}$ (right) in H_2O (1 x 10^{-3} M) under short wave UV light

The photophysical properties of the complexes were studied further through fluorescence, phosphorescence, and lifetime measurements. The fluorescence excitation and emission spectra of **$[Eu(L_1)_3]^{3-}$** was obtained in H_2O (1 x 10^{-5} M) at room temperature (Fig. 31). The fluorescence excitation spectra of **$[Eu(L_1)_3]^{3-}$** on emission (λ_{em}) at 615 nm (*i.e.* the maximum Eu^{3+} emission) showed one main maximum peak at 221 nm (λ_{ex}^{m}) with a shoulder at 274 nm (Fig. 31).[34,193-195,204] This λ_{ex}^{m} was the range expected for simple DPA-containing Ln^{3+} complexes, which are well reported to require relatively short wavelengths of light for excitation *i.e.* a maximum wavelength of 300 nm.[32,34,37,39,40,42-47,50,65,67-69,71,72,74,75,184,196,204] For instance, the excitation spectrum of $[Eu(DPA)_3]^{3-}$ in aqueous solution was collected by Gaillard and co-workers (2013) and contained a λ_{ex}^{m} at 225 nm with shoulder peak at 269 nm.[69] The **$[Eu(L_1)_3]^{3-}$** excitation peak overlapped with (and was similar in shape compared to) its absorbance spectrum which indicated that sensitization of Eu^{3+} was most likely occurring via energy transfer from **L_1**.[71,185,186,195,198,202-204,229]

The fluorescence emission spectrum of **$[Eu(L_1)_3]^{3-}$** on excitation at the λ_{ex}^{m} of 221 nm showed peaks characteristic of Eu^{3+} emission from the lowest emitting $^5D_0$ level to the ^7F_J level at 593, 615, 650 and 692 nm for J = 1, 2, 3 and 4 respectively (*i.e.* the red region of the electromagnetic spectrum), supporting successful **L_1** induced Eu^{3+} sensitization (Fig. 31).[26,28,47,193,195,196,198,202,203] Moreover, excitation of **$[Eu(L_1)_3]^{3-}$** at 274 nm (corresponding to the small shoulder peak present in the excitation spectra) also resulted in characteristic Eu^{3+} emission (Fig. S25).[193,195,196,203]

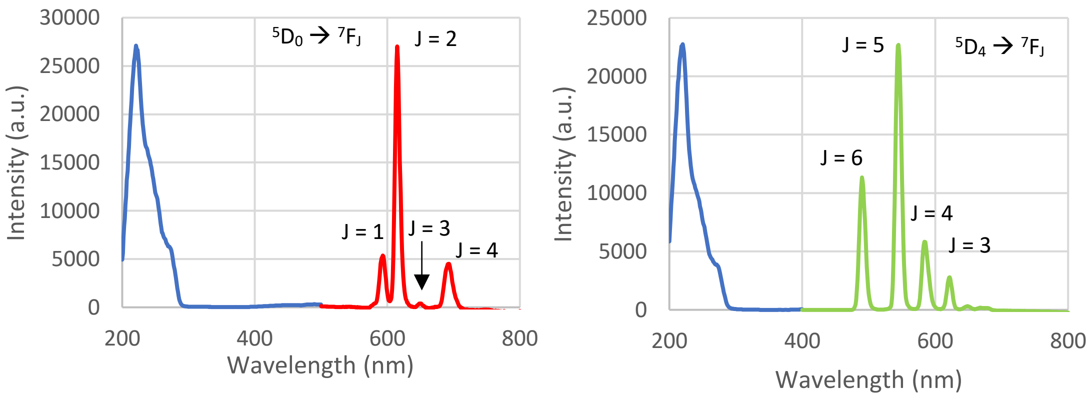

Figure 31. (Left) Fluorescence excitation (blue line) (λ_{em} = 615 nm) and emission spectra (red line) (λ_{ex} = 221 nm) of $[Eu(L_1)_3]^{3-}$ (1 x 10^{-5} M in H_2O). (Right) Fluorescence excitation (blue line) (λ_{em} = 545 nm) and emission spectra (green line) (λ_{ex} = 220 nm) of $[Tb(L_1)_3]^{3-}$ (1 x 10^{-5} M in H_2O). For the fluorescence excitation and emission measurements of $[Tb(L_1)_3]^{3-}$ (1 x 10^{-5} M in H_2O), excitation and emission slit widths were 3.0 and 5.0 nm (respectively)

The fluorescence excitation and emission spectra of **$[Tb(L_1)_3]^{3-}$** was also obtained in H_2O (1×10^{-5} M) at room temperature (Fig. 31). The fluorescence excitation spectra of **$[Tb(L_1)_3]^{3-}$** at 545 nm appeared similar in shape when compared to the **$[Eu(L_1)_3]^{3-}$**, containing a single main peak with a $\lambda_{ex}{}^{m}$ at 220 nm with a shoulder at approximately 274 nm (Fig. 31).[32,34,37,39,40,42-47,50,65,67-69,71,72,74,75,184,195,196,198,204] Additionally, as observed for **$[Eu(L_1)_3]^{3-}$**, the excitation spectra obtained for **$[Tb(L_1)_3]^{3-}$** was similar in shape and form when compared to its corresponding absorption spectrum supporting Tb^{3+} sensitization by **L_1**.[71,185,186,195,198,202-204,229] Excitation of **$[Tb(L_1)_3]^{3-}$** at the $\lambda_{ex}{}^{m}$ of 220 nm resulted in characteristic Tb^{3+} emission from lowest emitting $^5D_4$ level to the ^7F_J states at 490, 545, 584, 622, 649 nm for J = 6, 5, 4, 3 and 2 (respectively) (Fig. 31).[28,193,195,198,202,203] Moreover, excitation at 274 nm also resulted in characteristic Tb^{3+} emission (Fig. S34).[193,195,203]

As mentioned in section 1.1, the f-f transition from the excited Ln^{3+} state down to the ground Ln^{3+} state can be electric dipole (ED) or magnetic dipole (MD) in nature (or both).[1,2,4,5,7,8,10-12,16-18,22,192] ED transitions are parity forbidden and the MD transitions are allowed.[1,2,4,5,7,8,10-12,16-18,22,192] Because the ED f-f transitions are parity forbidden, they can be relaxed through the introduction of a ligand field, thus becoming induced ED transitions.[1,5,7,8,11,12,26,28,192] It is these induced ED transitions that are responsible for the luminescence displayed by the specific Ln^{3+}.[5,12,22,26,28] For Eu^{3+}, the $^5D_0 \rightarrow {}^7F_{0,2-6}$ transitions have (primarily) ED character, thus are influenced by their environment.[5,8,12,17,26,28,192] In particular, the $^5D_0 \rightarrow {}^7F_2$ ED transition is hypersensitive meaning that its structure (including intensity and shape) is largely influenced by its coordination environment.[5,8,12,22,26,28,47,192,197] In comparison, the $^5D_0 \rightarrow {}^7F_1$ has MD character (thus is parity allowed) and is relatively uninfluenced by its environment.[5,8,12,17,22,26,45,192] Thus, the emission spectra of Eu^{3+} complexes can be used to derive information regarding the symmetry and coordination environment of the complexes.[5,12,22,26,192]

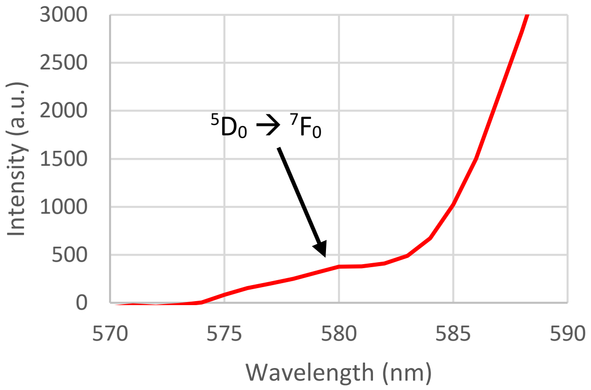

Figure 32. A zoom-in on the fluorescence spectrum of $[Eu(L_1)_3]^{3-}$ *(1 x* 10^{-5} *M in* H_2O*) showing a weak peak indicative of the* $^5D \rightarrow {}^7F_0$ *transition at approximately 580 nm*

Based off the works of Görller-Walrand and Binnemans (as cited in ref [192]), the $^5D_0 \rightarrow {}^7F_0$ peak is only observed for complexes possessing C_s, C_n and C_{nv} symmetry.[26,192,193] For highly symmetric complexes with 3:1 DPA ligand:Eu^{3+} ratios, D_3 symmetry is obtained.[1,15,26,37,38,41,43,46,67,158,162,184,188,189,191,192,208,213,219,252] For D_3 symmetric species, the $^5D_0 \rightarrow {}^7F_0$ and $^5D_0 \rightarrow {}^7F_3$ transitions are forbidden, thus would not be observed in the emission spectra of $[Eu(DPA)_3]^{3-}$.[26,31,38,41,162,185,186,192,193,210,213,252] In the fluorescence excitation spectra of **$[Eu(L_1)_3]^{3-}$**, small peaks at both 580 nm (in the range expected for the $^5D_0 \rightarrow {}^7F_0$ transition) and 650 nm (in the range expected for the $^5D_0 \rightarrow {}^7F_0$ transition) were observed, suggesting a deviation from this high symmetry and instead suggesting that the complex possesses C_3 symmetry (Fig. 32).[26,28,41,162,185,186,188,189,191,193,213] This was expected for the 1:3 Eu^{3+}:**L_1** complex as the alkyne group attached at the 4-pyridyl position was predicted to reduce the symmetry associated with the non 4-pyridyl functionalised DPA complex.[41,26,162,186,189,193] This was further backed up by X-ray diffraction measurements as discussed in section 2.3.4.

Lifetime measurements (monitoring 615 nm on excitation at 226 nm) were carried out on **$[Eu(L_1)_3]^{3-}$** (1 x 10^{-5} M in H_2O) and gave an average of 0.171 ms. Lifetime measurements were also carried out on **$[Tb(L_1)_3]^{3-}$** (1 x 10^{-5} M in H_2O) (monitoring 545 nm on excitation at 220 nm) and gave a much larger average of 0.983 ms when compared to Eu^{3+} (an effect which has been observed in complexes containing ligands of the PDA family).[185,186,204] These lifetimes showed slight differences when compared to similar complexes in the literature.[31-46,49,68,69,72-74,204] For example, in study by Li and co-workers (2018), the lifetimes of 1:3 Ln^{3+}:ligand complexes containing ligands differing from **L_1** such that an alkene group was present at the 4-pyridyl position (as opposed to an alkyne group in **L_1**), lifetimes of 0.27 ms and 0.53 ms were obtained for the Eu^{3+} and Tb^{3+} complexes (respectively) in H_2O.[204] These lifetime differences may be due to many different reasons such as a different quenching effect of water and/or energy level differences.[31-46,49,68,69,72-74] Measurements were carried out in triplicate and were best fit to a single exponential decay, indicating that emission was stemming from the 3:1 complex only (*i.e.* no contributions from other emitting species such as 2:1 **L_1**:Ln^{3+} species where Ln^{3+} = Eu^{3+} or Tb^{3+}).[31,71,185,186]

In their respective phosphorescence emission spectra, both **$[Eu(L_1)_3]^{3-}$** and **$[Tb(L_1)_3]^{3-}$** gave Eu^{3+}- and Tb^{3+}- centred emission (respectively) on excitation at 274 nm (Fig. S27 and Fig. S36).

2.3.3 UV/Vis titrations of $[Eu(L_1)_3]^{3-}$

To investigate the ability of **L_1** to coordinate with Eu^{3+} in aqueous solutions, UV/Vis titrations were carried out. For both titrations, stepwise additions of $EuCl_3 \cdot 6H_2O$ dissolved in H_2O were made to a solution of **L_1** (1 x 10^{-5} M) containing Na_2CO_3 as the base. UV/Vis titrations were carried out in triplicate.

The UV/Vis spectra of **L_1** and Na_2CO_3 alone had a λ_{abs}^{m} at 210 nm with a shoulder peak centred at approximately 265 nm (Fig. 33). As additions between 0 → 0.35 equivalents of $EuCl_3 \cdot 6H_2O$ (in H_2O) were made, the λ_{abs}^{m} at 210 nm underwent a very small shift to 211 nm, whilst the molar absorptivity (ε) values increased (hyperchromic effect).[187] Between 0.35 → 4.0 equivalents added, the λ_{abs}^{m} values switched between 210 and 211 nm and the ε values increase by smaller amounts (Fig. 33). Interestingly, a slightly different pattern was observed at broad shoulder peak at approximately 265 nm whereby as equivalents of Eu^{3+} are added from 0 → 4.0 equivalents, the ε values appeared to decline, thus showing hypochromicity (Fig. 33).[187]

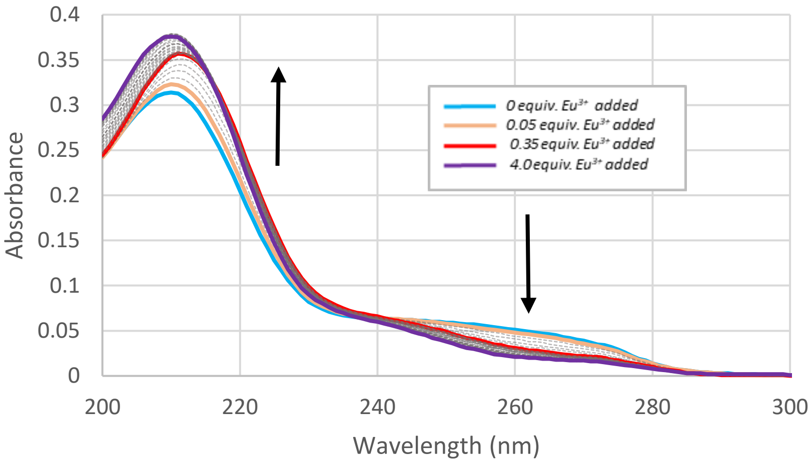

Figure 33. UV/Vis titration of L_1 and Na_2CO_3 on the stepwise addition of $EuCl_3{\cdot}6H_2O$ from 0 → 4.0 equivalents

In plotting the absorbance values obtained throughout the titration at 217 nm and 274 nm as a function of equivalents of Eu^{3+} added, these changes could be observed clearly (Fig. 34). For instance, between 0 → 0.40 equivalents, the absorbance values at 217 and 274 nm increased and decreased rapidly (respectively) (Fig. 34). At approximately 0.4 equivalents of Eu^{3+} added (shown by the arrow), these absorbance values appeared to plateau indicating the formation of the 1:3 Eu^{3+}:$\mathbf{L_1}$ species (expected to occur at approximately 0.33 equivalents of Eu^{3+} added) (Fig. 34).[185,186] Between 0.4 → 4.0 equivalents added, the absorbance values remain relatively constant which suggests that the complex retains 3:1 binding despite further additions of Eu^{3+} (Fig. 34).

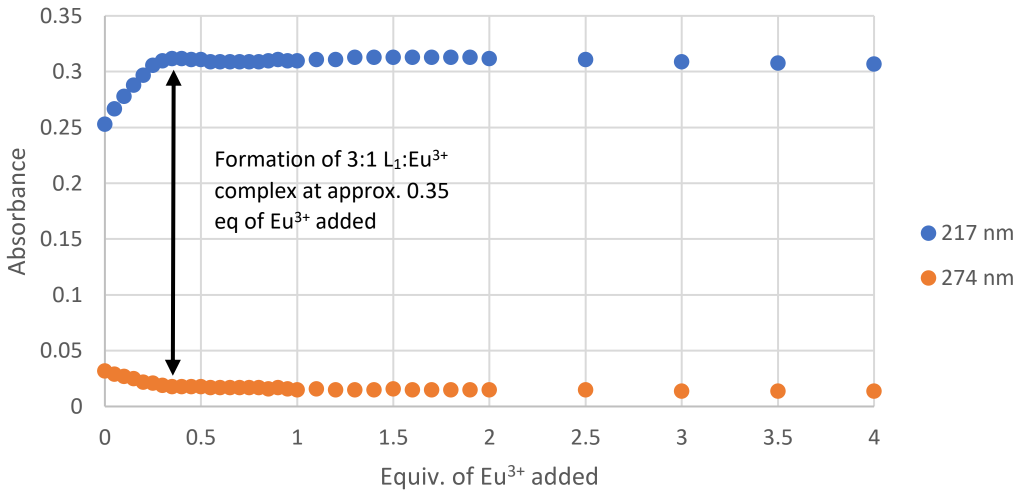

Figure 34. Plot showing the changes in absorbance values of L_1 and Na_2CO_3 at 217 nm (blue dots) and 274 nm (orange dots) as a function of equivalents of Eu^{3+} added

A crude fluorescence titration of **L_1** and Na_2CO_3 on the addition of Eu^{3+} aliquots was also performed to investigate the ability of **L_1** to coordinate with Eu^{3+} (Fig. S200). As expected, **L_1** and Na_2CO_3 on their own showed no emission between 550 – 750 nm, however, on the addition of Eu^{3+}, the sharp peaks characteristic of Eu^{3+} emission were observed, supporting **L_1** coordination and Eu^{3+} sensitization (Fig. S200).[28] However, in plotting the intensity of the hypersensitive $^5D_0 \rightarrow {}^7F_2$ peak relative to the equivalents of Eu^{3+} added, results were obtained which did not agree with those when compared to the UV/Vis titration. On the addition of 0 → 1.3 equivalents, the intensity of the $^5D_0 \rightarrow {}^7F_2$ peak increases largely, however at approximately 1.3 equivalents, the values begin to plateau (Fig. S200). These differences, when compared to the UV/Vis titrations, were most likely a quenching effect from solvent O-H vibrations in the second coordination sphere of Eu^{3+}. Despite this, the large increase in intensity on the addition of Eu^{3+} from 0 to 0.15 equivalents of Eu^{3+} and further up to 1 equivalent of Eu^{3+} added showed rapid complexation (Fig. S200).

2.3.4 Crystal structure of $\mathbf{Na_3[Eu(L_1)_3]\cdot16H_2O}$

Rod-shaped crystals of $\mathbf{[Eu(L_1)_3]^{3-}}$ suitable for X-ray diffraction were collected through the slow vapour diffusion of 2-propanol into water at room temperature (Fig. 35). $\mathbf{Na_3[Eu(L_1)_3]\cdot16H_2O}$ was found to crystalize in the triclinic P-1 space group and the low temperature (150 K) structure revealed that complexes inherited the expected 3:1 $\mathbf{L_1}$:Eu^{3+} binding.

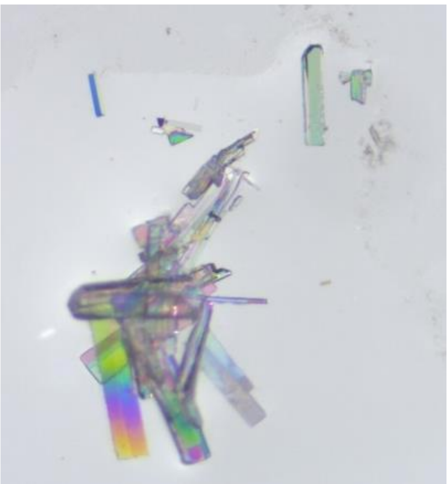

Figure 35. Rod-shaped crystals of $[Eu(L_1)_3]^{3-}$ grown from the vapour diffusion of 2-propanol into H_20

The asymmetric unit contained two crystallographically independent $\mathbf{Na_3[Eu(L_1)_3]}$ units, one belonging to Eu1 and another belonging to Eu2 (Fig. 36). These two complexes were linked together through a sodium bridge between carboxylate oxygen atoms (O55 of Eu2 and O31 and O24 of Eu1) (Fig. 36 and Fig. S203).[219] This was expected as sodium carbonate was used as a base in the synthesis. There appeared to be a large amount of water in the asymmetric unit, with 19 molecules bound to Na^+ and 13 interstitial H_2O molecules (36 H_2O molecules in total). This also was expected as the complexes were synthesized, and the crystals were grown from H_2O. Each $\mathbf{[Eu(L_1)_3]^{3-}}$ complex possessed an overall -3 charge (*i.e.* two negative charges per ligand plus 3 for Eu^{3+}), which were countered by 6 Na^+ ions in the asymmetric unit, achieving charge balance. The packing showed that $\mathbf{[Eu(L_1)_3]^{3-}}$ forms a polymeric network that is linked by sodium ions coordinated to the $\mathbf{L_1}$ carboxyl C=O bonds.[214]

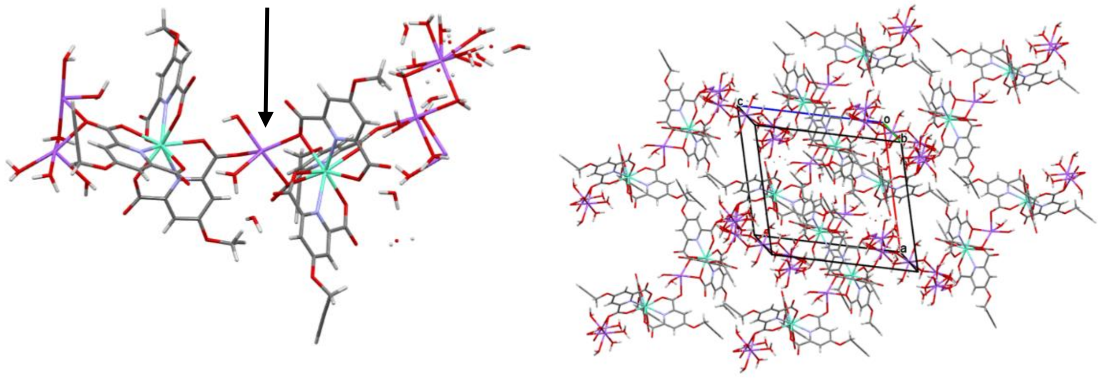

Figure 36. (Right) Asymmetric unit of $Na_3[Eu(L_1)_3]\cdot 16H_2O$ (Left) Packing diagram obtained for $Na_3[Eu(L_1)_3]\cdot 16H_2O$

The X-ray data supported the formation of **$[Eu(L_1)_3]^{3-}$** in the expected 3:1 **L_1**:Eu^{3+} ratio.[214,218] Each **L_1** chelating unit contained one nitrogen atom and two oxygen atoms, all of which coordinated with the Eu^{3+} ion forming a O^N^O chelating pocket (Fig. 7).[214,215,218] Additionally, there did not appear to be any water molecules occupying any Eu^{3+} coordination sites and **$[Eu(L_1)_3]^{3-}$** appeared to be a nine-coordinate complex (achieving coordinative saturation for Eu^{3+}).[214,215,218]

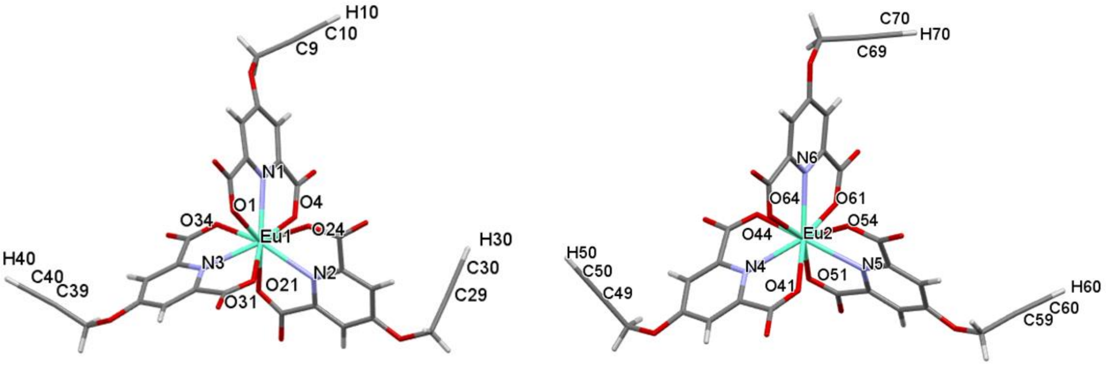

Figure 37. Capped stick representation of the two crystallographically distinct Eu1 (left) and Eu2 (right) complexes in the asymmetric unit with key atoms labelled

Overall, **$[Eu(L_1)_3]^{3-}$** appeared to adopt a distorted tricapped trigonal prism geometry, common for Ln^{3+} complexes containing DPA ligands with coordination numbers of 9 (Fig. 37).[8,38,213,218,267] The triangular prism is made up of the total 6 oxygen atoms, with two belonging to each DPA motif. Oxygen atoms O1, O24 and O31 make up one triangular face whereas O4, O21 and O34 make up the other (Fig. 38).[38,267] The oxygen atoms also form the rectangular sides and for each side, a nitrogen atoms sticks out, thus forming the caps of the tricapped trigonal prism (Fig. 38).[38,218,267]

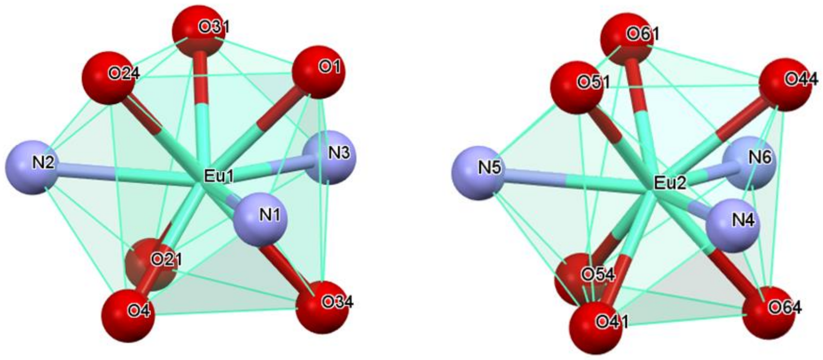

Figure 38. Ball and stick representation showing the coordination polyhedra for Eu1 (left) and Eu2 (right) and the tricapped trigonal prismatic geometry

In further analysing the coordination geometry about the Eu^{3+} centre as well as other important motifs of **L$_1$**, a table of selected bond lengths and angles was obtained and compared to the crystal structure of a 1:3 Eu^{3+}:ligand complex whereby the ligand was DPA containing an amino group (-NH$_2$) attached directly to the 4-pyridyl position. Because there were two complexes in the asymmetric unit, values for both are supplied.

Table 2. Selected bond length and angle ranges for $Na_3[Eu(L_1)_3]\cdot 16H_2O$

Bond	**Bond length range (Å)**	**Average bond length (Å)**
Eu1-O	2.434 – 2.478	2.453
Eu1-N	2.500 – 2.508	2.504
Eu2-O	2.416 – 2.461	2.444
Eu2-N	2.498 – 2.513	2.508
Bond angle	**Bond angle range (˚)**	**Average bond angle (˚)**
O-Eu1-O	127.0 – 127.2	127.1
O-Eu1-N	63.0 – 64.1	63.6
N-Eu1-N	116.8 – 122.0	120.0
O-Eu2-O	126.7 – 128.3	127.4
O-Eu2-N	63.3 – 64.5	63.7
N-Eu2-N	116.4 – 122.2	120.0

The Eu1-O bond lengths were found to range from 2.434 to 2.478 Å, averaging at 2.453 Å whereas the Eu2-O bond lengths had a slightly lower range from 2.416 to 2.461 Å with an average of 2.444 Å. In saying this, both ranges and averages were in line with those obtained in the literature (*e.g.* for the Eu-O bonds, ranging from 2.438 to 2.462 Å with an average of 2.455 Å).[43,218] The Eu1-N bond lengths were longer than those of the Eu1-O bond lengths, ranging from 2.500 to 2.508 Å with an average of 2.504 Å. The same pattern was observed for the Eu2-N bond lengths which ranged from 2.498 to 2.513 Å with an average of 2.508 Å. These values were in relatively good agreement with those obtained in the literature which were found to range from 2.481 to 2.531 Å, with an average of 2.512 Å.[43]

The O-Eu1-O angles for each $\mathbf{L_1}$ chelating motif ranged from 127.0 to 127.2° (with an average of 127.1°) which were similar compared to those values obtained for the O-Eu2-O angles which ranged from 126.7 to 128.3° (with an average of 127.4°). These values were in agreement with those obtained in the literature which ranged from 126.7 – 128.2 ° with an average of 127.2°.[43] The O-Eu1-N angles ranged from 63.0° to 64.1°, with an average angle of 63.6°. The O-Eu2-N angles were very similar, ranging from 63.3 to 64.5° with an average angle of 63.7°. These values were also comparable to those obtained in the literature which ranged from 63.0 to 64.7° with an average of 63.7°.[43] The N-Eu1-N bond angles ranged from 116.8 to 122.0° and the N-Eu2-N bond angles ranged from 116.4 to 122.2°, with both averaging at 120°, expected as each nitrogen atom forms the caps of the tricapped trigonal prism.

Overall, all bond lengths and angles obtained from the crystal structure of $\mathbf{[Eu(L_1)_3]^{3-}}$ appeared similar to the literature of a similar complex which contained a ligand differing from $\mathbf{L_1}$ such that it contained an -NH_2 group at the 4-pyridyl position as opposed to an alkyne group.[43] Slight differences observed between the literature complex (*i.e.* the slightly larger Eu-O and Eu-N bond averages) when compared to $\mathbf{[Eu(L_1)_3]^{3-}}$ may result from the effect of having different groups, attached to the 4-pyridyl position, or different counterions present.[43]

Overall, the bond lengths and angles were in line with the assignment of a distorted tricapped trigonal prismatic geometry.[193] There were only small deviations from ideal geometry observed, for instance, the angles between oxygen atoms making up triangular faces did not equal 60˚, which would be expected for an ideal tricapped trigonal prismatic structure.[193] As explained in section 2.3.2, the presence (or lack of) certain peaks in the fluorescence spectra of Eu^{3+} complexes can provide information regarding the symmetry of the complex.[193,214] Based off the photophysical data, as well as ^1H NMR data highly supporting the existence of trigonal symmetry for the **$[Eu(L_1)_3]^{3-}$** complex, a C_3 symmetry was predicted which was further supported by the crystal structure.[37,38,193,201]

2.4 Preformed-ligand method

2.4.1 Naphthalimide ligand (L_2) and complex $[Ln(L_2)_3]^{3-}$

2.4.1.1 Synthesis and characterization

The next ligand system explored incorporated a 1,8-naphthalimide functional group. The literature surrounding the use of 1,8-naphthalimides is abundant, primarily due to the photophysical properties intrinsic to this class of molecule, in addition to its singlet oxygen generating abilities.[103,209,221,222,227-235,277,278] In recognising these properties, as well as the potential of this group to act as a "stopper" for rotaxane formation (due to its bulky nature), we chose to investigate the complexes obtained through clicking a 1,8-naphthalimide azide (**$2N_3$**) to the 4-pyridyl position of DPA (Fig. 39).[152,209] Multiple studies have incorporated the naphthalimide motif into Ln^{3+} systems whereby the motif either interacts with the Ln^{3+} or is situated at far distances from.[227-236,246] In one study, the naphthalimide group was appended directly to the 4-pyridyl position of the DPA motif containing ester and amide chelating groups and the resulting ligand was complexed with Eu^{3+}.[209] In saying this, our systems differs from this such that we use CuAAC chemistry to append the 1,8-naphthalimide motif to the 4-pyridyl position of DPA and the stronger binding dicarboxylate derivative of the resulting ligand is used for complexation.[209]

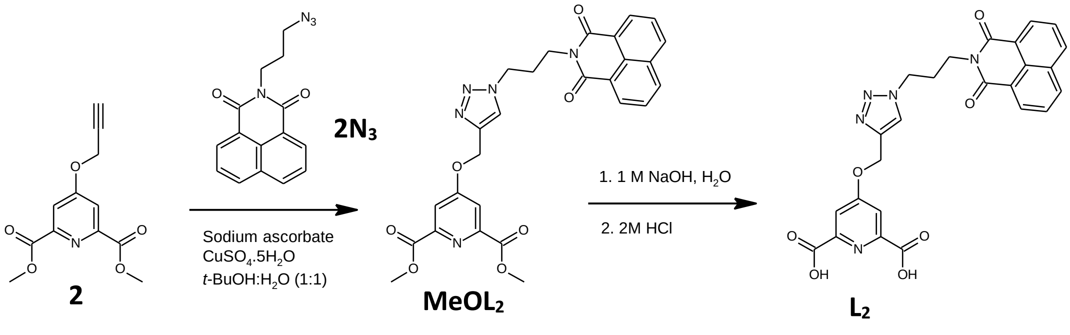

Figure 39. Reaction scheme for the synthesis of L_2

L_2 was synthesized through a mutli-step procedure whereby two separate motifs, 2-(3-azidopropyl)-1*H*-benzo[*de*]isoquinoline-1,3(2*H*)-dione (**$2N_3$**) and dimethyl 4-[(prop-2-yn-1-yl)oxy]pyridine-2,6-dicarboxylate (**2**) were synthesized separately and coupled together through the CuAAC click reaction to form the methyl-protected version of **L_2** (**$MeOL_2$**) (Fig. 39). The azide, **$2N_3$**, was synthesized in three steps from 1,8-naphthalic anhydride. In the first step, 3-amino-1-propanol was reacted with 1,8-naphthalic anhydride to append an *N*-substituted alcohol group.[223-225] Next, a bromination reaction was carried out on the *N*-substituted alcohol naphthalimide intermediate with phosphorus tribromide to transform the -OH to a -Br group for azide synthesis.[223-225] The azide (**$2N_3$**) was synthesized through reacting 2 equivalents of sodium azide with the *N*-substituted bromide version of the naphthalimide in DMF and was safe to isolate (although it was stored in a freezer).[51,223,226]

For the click reaction, relatively mild conditions were used with no effort to exclude air or H_2O (thus fulfilling the requirements for a CuAAC reaction).[51-60,62-64,223] Single equivalents of **2** and sodium ascorbate were combined with 0.05 equivalents of copper(II) sulfate pentahydrate ($CuSO_4{\cdot}5H_2O$) and a slight excess of **$2N_3$** (1.05 equivalents).[56,223] The solids were suspended in a 1:1 *tert*-Butanol:H_2O solvent mixture, forming a pale-yellow reaction mixture which was heated at 80 ˚C for 5 hours after which on the addition of H_2O caused a solid to precipitate out.[56,223] To remove unreacted copper remaining in the product, the crude solid was stirred in a 0.5 M EDTA/1 M NaOH solution which, after filtering, gave the pale-yellow solid product (**$MeOL_2$**). These conditions were also used for the synthesis of **L_3** and **L_4** and (as discussed in sections 2.4.2 and 2.4.3 respectively). Various literature studies performing CuAAC reactions on the 4-pyridyl DPA motif have reported long reaction times and low yields obtained using the $CuSO_4{\cdot}5H_2O$ and sodium ascorbate catalyst mixture due to competitive binding within the DPA chelating pocket, however this did not appear to be the case for the CuAAC reaction between **2** and **$2N_3$**.[66,72]

Figure 40. L_2 (1×10^{-5} M) in MeOH (from a stock 2:1 $CHCl_3$:MeOH solutions) under long wave UV light (365 nm)

In the last step, a deprotection was carried out which involved a saponification reaction.[25,31,34,35,37,40,41,43,45,46,65-70,72,74] **MeOL$_2$** was suspended in H_2O and 1 M sodium hydroxide (NaOH) forming a cloudy white reaction mixture which was stirred for approximately 4 hours at 50 ˚C, after which a transparent/slightly pale-yellow reaction mixture appeared. The formation of the increasingly transparent reaction mixture was indicative of a successful reaction as it suggested that the methyl groups had been cleaved off, leaving the carboxylic acid versions which deprotonate under basic conditions to form a partially water soluble negative charged product (**L$_2$**). This NaOH method appeared more successful for this system (*i.e.* better yields were obtained) when compared to the method used for the synthesis of **L$_1$** which involved lithium hydroxide. On the addition of 2 M hydrochloric acid (HCl) to the crude reaction mixture (containing negatively charged **L$_2$**), the carboxylic acids were protonated and a white solid precipitated out which could be filtered off and isolated as the product. When suspended in MeOH, **L$_1$** emitted a bright purple/blue colour on excitation at 254 nm (Fig. 40).

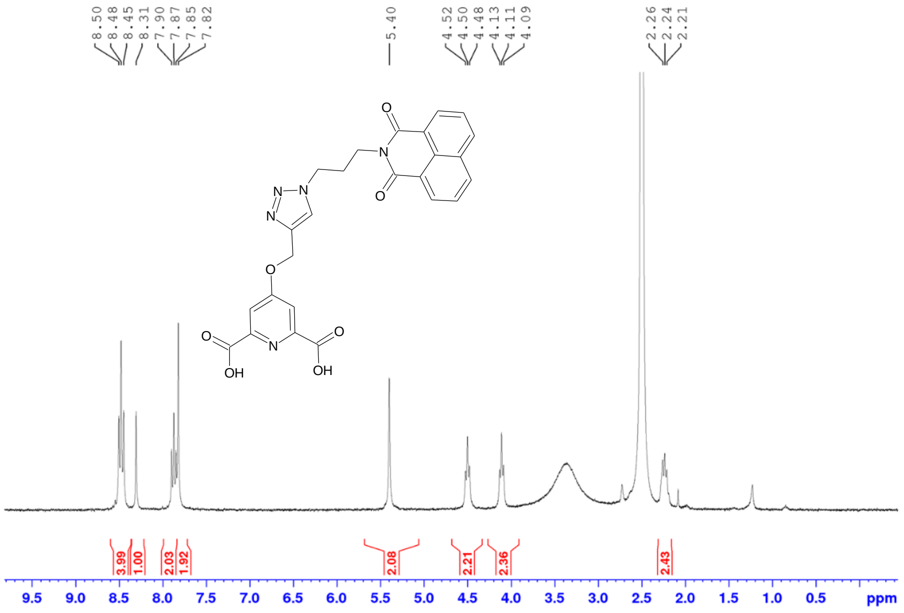

Figure 41. ^{1}H NMR spectrum of L$_2$ in DMSO-d$_6$

Key features in the ^{1}H NMR spectrum of **L$_2$** proving its formation were observed including the removal of the methyl peak (*i.e.* the singlet 3.90 ppm in **2** and 3.91 ppm in **MeOL$_2$**), and the presence of the singlet peak at 8.31 ppm (indicative of the triazole hydrogen) alongside the removal of alkyne peak at 3.76 ppm in **2** (Fig. 41).[185,186] Additionally, the downfield shift of the peak corresponding to the CH_2 protons situated between the DPA motif and the triazole group (CH_2^{DT}) and its transformation into a singlet (as opposed to a doublet in **2**) suggested the removal of the alkyne proton (which coupled to the CH_2 protons in **2**), expected for a successful CuAAC reaction (Fig. 41).[185,186] The triplet peaks 4.50 and 4.11 ppm as well as the quintet at 2.24 (only being resolved as a triplet due to the underlying solvent peak) all had integrals of 2 and were in the range expected for the CH_2 groups linking the triazole to the naphthalimide nitrogen (Fig. 41).[187] The triplets at 8.48 and 7.87 ppm could further be assigned to aromatic naphthalimide protons, leaving the last singlet peak at 7.82 ppm which was assigned to the aromatic pyridyl hydrogen atoms (Fig. 41).

In some cases, after the deprotection step, impurities were present which appeared as overlapping peaks in the aromatic region of the ^1H NMR spectrum (Fig. S63 and Fig. S64). These impurities could be removed through stirring **L_2** in acetone and filtering off the acetone soluble impurities (Fig. S63). A ^1H NMR spectrum of the impurities revealed the presence of peaks in the aromatic range but no alkyl peaks, suggesting that some of the alkyl chain had been cleaved off (via base) during deprotection, resulting in the formation of 1,8-naphthalic anhydride (Fig. S64). With this in mind, caution was taken whilst carrying out deprotection (as well as copper removal involved in the synthesis of precursor **$MeOL_2$**) such that the reaction mixture was not exposed to excessive heat or left for longer than required (*i.e.* after the reaction mixture turned transparent, it was only heated for a further two hours).[25,31,34,35,37,40,41,43,45,46,65-70,72,74]

To synthesise **$[Ln(L_2)_3]^{3-}$**, **L_2** (1 equivalent) and anhydrous sodium carbonate (2 equivalents) were suspended in deionised H_2O and stirred at 50 ˚C for 15 minutes, forming a transparent yellow reaction mixture (Fig. 42). Next, 0.33 equivalents of the appropriate lanthanide chloride salt in H_2O was added to the **L_2** and Na_2CO_3 reaction mixture, causing a white/pale yellow solid to precipitate. On further heating at 50 ˚C for 5 minutes, the solid appeared to redissolve and on cooling to room temperature, the solid reprecipitated. Leaving this crude reaction mixture overnight enabled the solid to settle on the bottom of the vial which, after decanting off the top water layer, could be isolated as the product.

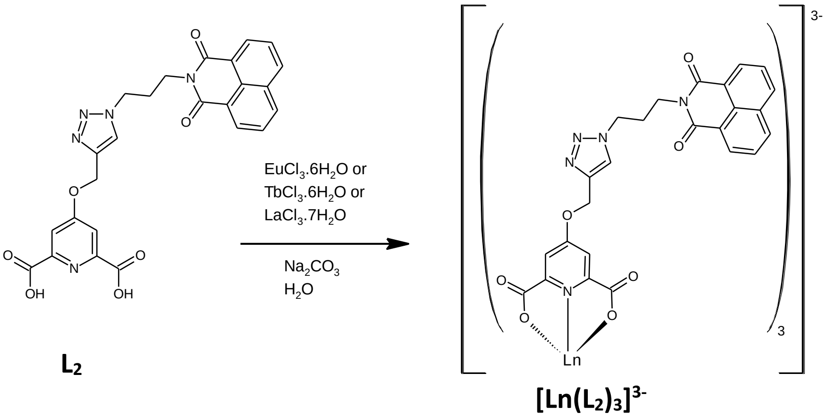

Figure 42. General reaction scheme for the synthesis of $[Ln(L_2)_3]^{3-}$ complexes where Ln = La^{3+}, Eu^{3+} and Tb^{3+}

As for the $\mathbf{[Ln(L_1)_3]^{3-}}$ complexes, the NMR spectra of $\mathbf{[Ln(L_2)_3]^{3-}}$ complexes were collected in DMSO-*d_6* (Fig. 43). As shown in the image below comparing the ^1H NMR spectra of $\mathbf{[La(L_2)_3]^{3-}}$**,** $\mathbf{[Eu(L_2)_3]^{3-}}$ to $\mathbf{L_2}$ ($\mathbf{[Tb(L_2)_3]^{3-}}$ was omitted as its ^1H NMR spectrum appeared broad), relatively large differences were observed in terms of peak shifts and splitting (Fig. 43). In saying this, in general, all NMR spectra gave one set of peaks, hence suggested successful complexation of $\mathbf{L_2}$ to the respective Ln^{3+} in the 3:1 L_2:Ln^{3+} ratio (*i.e.* each ligand was equivalent).[37,38,41,188,189,193,199,201,207]

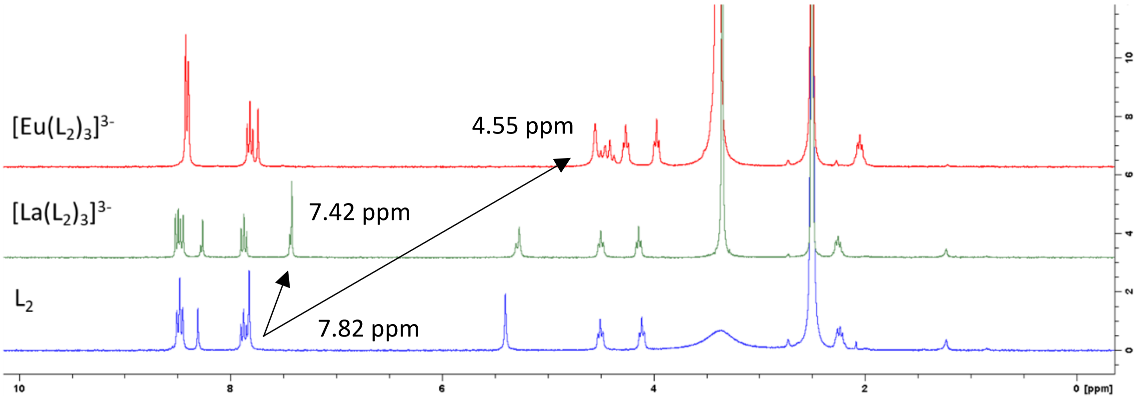

Figure 43. ^1H NMR spectra of $[Eu(L_2)_3]^{3-}$ (top, red), $[La(L_2)_3]^{2-}$ (middle, green) and L_2 (bottom, blue) in DMSO-d_6

In comparing the spectra obtained for **L_2** and **$[La(L_2)_3]^{3-}$**, peak splitting's were comparable, with the only discernible difference being the splitting of the triplet at 8.48 ppm in **L_2** into a doublet of doublets at 8.48 ppm (corresponding to 4 aromatic protons belonging to the naphthalimide motif) (Fig. 43). Additionally, peak shifts between **L_2** and **$[La(L_2)_3]^{3-}$** were relatively small, particularly for those peaks corresponding to alkyl linker protons (*i.e.* the triplets at 4.50 and 4.14 ppm and the quintet at 2.25 ppm) situated between the triazole and the naphthalimide component as well as those peaks assigned to aromatic naphthalimide protons likely due to the spatial distance from the La^{3+} centre.[41,187]

The peaks which appeared to be most impacted by La^{3+} complexation were those corresponding to the triazole, CH_2 and pyridyl protons (Fig. 43). The singlet peak at 8.31 ppm in the ^1H spectrum of **L_2**, assigned to the triazole hydrogen, was shifted up-field to 8.26 ppm in **$[La(L_2)_3]^{3-}$** (Fig. 43). Additionally, the singlet peaks at 5.40 and 7.82 ppm corresponding to the CH_2^{DT} and pyridyl protons of **L_2** (respectfully) were also shifted up-field to 5.27 and 7.42 ppm in **$[La(L_2)_3]^{3-}$** (respectfully) (Fig. 43). Thus, the $\Delta\delta$ values for the triazole, CH_2^{DT} and pyridyl peaks were 0.05, 0.13 and 0.40 ppm respectfully, following the trend that protons situated further from the La^{3+} centre experience smaller shifts when compared to those situated closer (Fig. 43).[41,187,190,193] On closer analysis of **$[La(L_2)_3]^{3-}$**, the singlet peaks corresponding to these La^{3+} sensitive protons appeared to have smaller sub-peaks which did not line up with free **L_2** contamination (Fig. 43). It was predicted that these peaks may result from exchange processes occurring on the same time scale as the NMR (as observed for **$[La(L_1)_3]^{3-}$**) (Fig. 43).[187,188,201,207,208]

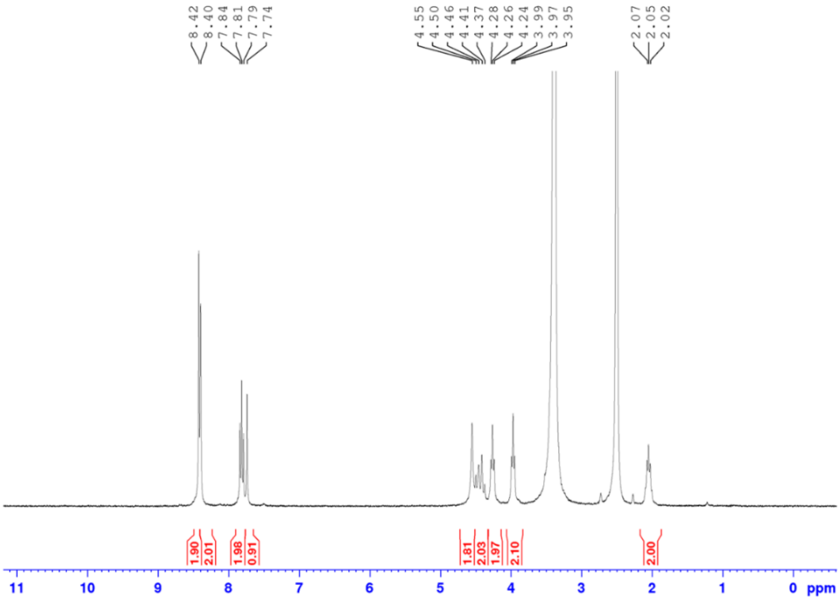

Figure 44. ^{1}H NMR spectrum of $[Eu(L_2)_3]^{3-}$ in DMSO-d$_6$

In comparing the ^{1}H NMR spectrum of $\mathbf{[Eu(L_2)_3]^{3-}}$ to that of $\mathbf{L_2}$, the similar up-field shifting pattern exhibited by the protons in $\mathbf{[La(L_2)_3]^{3-}}$ was observed, but to a larger extent (expected due to the paramagnetic nature of Eu^{3+}) (Fig. 44).[4,177,187,188,190,199,207,208,210,254] The quintet peak at 2.05 ppm (being resolved as a triplet) and the triplet peaks at 4.26 and 3.97 ppm were assigned to the CH_2 linkers between the triazole group and the naphthalimide nitrogen (being shifted from 4.50, 4.11 and 2.24 ppm (respectively) in $\mathbf{L_2}$) (Fig. 44). The aromatic naphthalimide protons were assigned to the triplet at 7.81 ppm and the two singlets at 8.42 and 8.40 ppm (thus experiencing a different splitting pattern when compared to $\mathbf{L_2}$) (Fig. 44). Although the two singlets at 8.42 and 8.40 ppm were in the ppm range expected for the triazole hydrogen, they were each integrating as two, thus were assigned to naphthalimide aromatic protons (further proved by the COSY spectrum) (Fig. S75).

Table 3. Summary of the main shifts observed in the ^{1}H NMR spectrum on the complexation of L_2 to La^{3+} and Eu^{3+}

	δ (ppm)			Δδ (ppm)	
Proton type	**L_2**	**$[La(L_2)_3]^{3-}$**	**$[Eu(L_2)_3]^{3-}$**	**$\delta L_2 - \delta[La(L_2)_3]^{3-}$**	**$\delta L_2 - \delta[Eu(L_2)_3]^{3-}$**
Triazole	8.31	8.26	7.74	0.05	0.57
CH_2^{DT}	5.40	5.27	4.41	0.13	0.99
Pyridyl	7.82	7.42	4.55	0.40	3.27

The last peaks to be assigned in the ^{1}H NMR spectrum of **$[Eu(L_2)_3]^{3-}$** were those corresponding to the triazole, pyridyl and CH_2^{DT} protons, which required the analysis of all spectral data. The singlet peak at 7.74 ppm integrating as 1 hydrogen was assigned to the triazole hydrogen, being shifted by 0.57 ppm ($\Delta\delta = 0.57$) when compared to **L_2** (Table 3). The same up-field shifting effect of Eu^{3+} complexation on triazole protons attached to the 4-DPA position has been observed in a literature study carried out by Mini and co-workers (2020) whereby a shift from 9.82 to 8.56 ppm ($\Delta\delta = 1.26$) in DMSO-d_6 was observed.[65]

The study by Mini and co-workers (2020) also showed that the up-field shifting effect observed for the triazole on Eu^{3+} complexation was also applicable to the pyridyl hydrogens, whereby a shift from 8.84 ppm to 5.68 ppm (in DMSO-d_6) on Eu^{3+} complexation (a $\Delta\delta$ of 3.16 ppm) was observed.[65] Thus, based on results from both the ^{1}H NMR spectrum of **$[Eu(L_1)_3]^{3-}$** as well as literature results, the peak corresponding to the pyridyl protons was expected as a singlet at approximately 4 – 6 ppm (*i.e.* showing the characteristic shift indicative of Eu^{3+} complexation).[35,37,41,65-67,207,208] Additionally, the CH_2^{DT} protons were expected to show up as a singlet at approximately 4.21 ppm based off results obtained for the analogous CH_2 protons in **$[Eu(L_1)_3]^{3-}$**. In saying this, the only peaks showing up in this range expected were a singlet at 4.55 pm which was superimposed on a multiplet at approximately 4.41 ppm. Both peaks were integrating as 2 hydrogens and were in the range expected for the pyridyl protons, as well as the CH_2^{DT} protons. Both peaks failed to line up with any peaks corresponding to free **L_2** as well as free **$2N_3$** and **2** (the starting materials used for the CuAAC reaction involved in the **L_2** synthetic pathway), supporting that the peaks were not arising due to contamination.

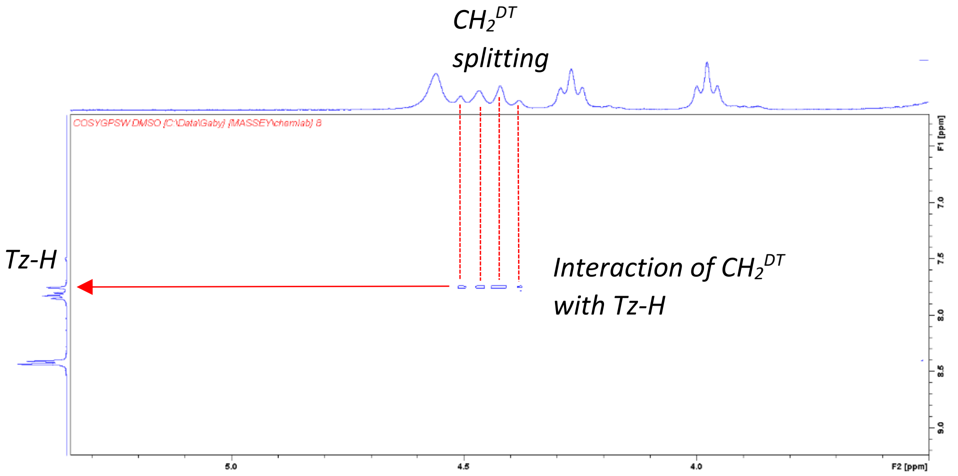

Figure 45. Close-up of COSY spectrum obtained for $[Eu(L_2)_3]^{3-}$ in DMSO-d_6 showing the interaction of the multiplet at 4.41 ppm with the triazole singlet at 7.74 ppm

Because these peaks could not be assigned based on the ^{1}H NMR spectrum alone, further analysis of the COSY spectrum was required. In the **$[Eu(L_2)_3]^{3-}$** COSY spectrum, the four peaks which made up the multiplet at 4.41 ppm appeared to each couple to the triazole hydrogen whereas the singlet at 4.55 ppm did not (Fig. 45). On the basis that the CH_2^{DT} group is situated closer to the triazole group when compared to the pyridyl motif (making them more likely to show this coupling with the triazole protons), the multiplet was loosely assigned to CH_2^{DT} hydrogens. This left the singlet peak at 4.55 ppm which was loosely assigned to the pyridyl hydrogen atoms. These assignments were later supported through analysis of the ^{13}C and HSQC NMR data. In saying this, although the **$[La(L_2)_3]^{3-}$** CH_2^{DT} hydrogens showed the same up-field shifting, it did not display the same splitting observed as for **$[Eu(L_2)_3]^{3-}$**. Accordingly, these differences suggested that the different lanthanide ions were eliciting different environments on the **L_2** protons.

The lanthanide ions display what is referred to as the lanthanide contraction, or the gradual decline in the ionic radii across the periodic table.[1,4,5,13,21,30,188,208,216,219,255] This results from the poor shielding (by the 4f orbitals) of the outer 5s and 5p orbitals from an increase in the nuclear charge meaning that as the nuclear charge increases, the relative effect of this felt by the 5s and 5p orbitals increases, causing a decrease in their ionic radii.[1,4,5,13,21,188,208,216,255] Thus, the ionic radii of La^{3+} (103.2 ppm) differs largely compared to that of Eu^{3+} (94.7 ppm).[1,4,5,201] In Ln^{3+} complexes containing ligands of the DPA family, this decrease in radii has been associated with a change in how the DPA ligand wraps around the specific Ln^{3+}.[188,207,208,254] Renaud and co-workers in 1997 reported the crystal structures of two 1:3 Ln^{3+}:ligand complexes (one La^{3+} and one Eu^{3+} complex) containing the PDA ligand (*i.e.* containing the same O^N^O motif as DPA).[188,207,208] In their study the researchers observed that the two complexes showed differences in the extent at which their pyridyl ring lay in the plane defined by the O^N^O pocket such that the La^{3+} complex showed an increased distortion from this plane.[188,207,208,254] Additionally, the pyridyl ring has also been observed to undergo fast oscillatory 'flip-flop' movements in and out of the plane defined by the O^N^O motif in DPA complexes with Eu^{3+}.[188,254] Based off these studies, in Ln^{3+} complexes containing the DPA ligand, there appears to be different dynamic processes occurring at different extents on the NMR timescale depending on the certain Ln^{3+} used for complexation, providing a possible explanation for the splitting of the CH_2^{DT} peak observed in the ^1H NMR spectra of **$[Eu(L_2)_3]^{3-}$** when compared to **$[La(L_2)_3]^{3-}$** in DMSO-d_6.[188,207,208,254]

Thus, as observed for **$[La(L_2)_3]^{3-}$**, the protons which appeared to be most shifted/affected by complexation in **$[Eu(L_2)_3]^{3-}$** were the those corresponding to the pyridyl, CH_2^{DT}, and triazole protons with $\Delta\delta$ values (relatively to **L_2**) of 3.27, 0.99 and 0.57 ppm (respectively) (Table 3). This was in line with what was expected as these protons are situated at increasing distances from the paramagnetic Eu^{3+} centre.[4,41,177,187-190,193,199,207,208,210,254]

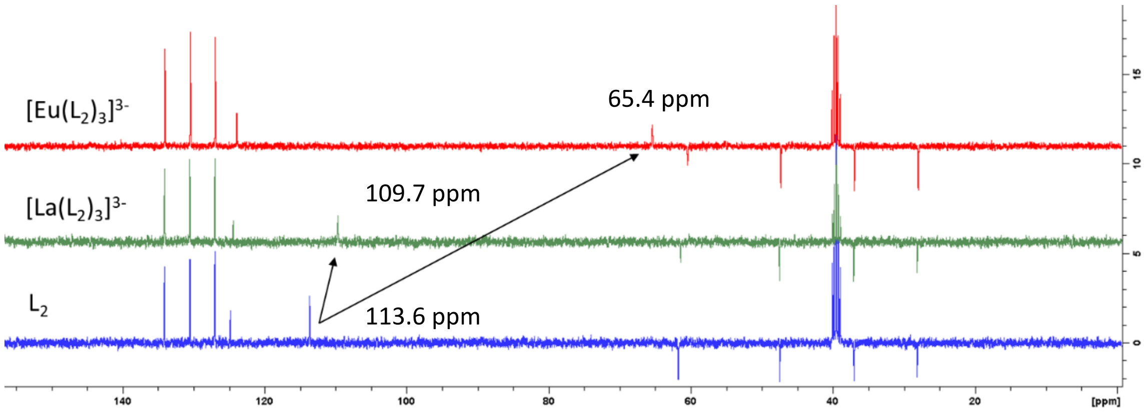

Figure 46. Comparison of the ^{13}C DEPT spectra of L_2 (blue, bottom) with $[La(L_2)_3]^{3-}$ (green, middle) and $[Eu(L_2)_3]^{3-}$ (red, top) in DMSO-d_6 showing the pyridyl carbon shift on complexation

The ^{13}C DEPT spectra of **L_2**, **$[La(L_2)_3]^{3-}$** and **$[Eu(L_2)_3]^{3-}$** appeared similar, with the largest and main shift being observed for the pyridyl carbons (Fig. 46). This effect was the largest for **$[Eu(L_2)_3]^{3-}$** as had been observed for **L_1** on complexation and on studies reporting similar systems.[3,188,201] For instance, the pyridyl carbon of **L_2** was observed at 113.6 ppm, compared to 109.7 ppm in **$[La(L_2)_3]^{3-}$** (a $\Delta\delta$ of 3.9 ppm) and 65.4 ppm in **$[Eu(L_2)_3]^{3-}$** (a $\Delta\delta$ of 48.2 ppm) which, as observed by various studies on the DPA/PDA ligand family, was good evidence of complexation.[35,188,201]

This ^{13}C DEPT data, combined with the HSQC data, supported the CH_2^{DT} and pyridyl proton assignments in the ^{1}H NMR spectrum of **$[Eu(L_2)_3]^{3-}$** (Fig. 47). Based on the HSQC data of **$[Eu(L_2)_3]^{3-}$**, the hydrogen atoms corresponding to the singlet peak at approximately 4.57 ppm (corresponding to the 4.55 ppm peak in the ^{1}H NMR spectrum) interact with the carbon atoms corresponding to the peak at approximately 66.0 ppm (corresponding to the 65.4 ppm peak in the ^{13}C DEPT spectrum) (with slight differences likely being due to calibration differences) (Fig. 47). Thus, because the peak at approximately 66.0 ppm was determined (based on the ^{13}C and ^{13}C DEPT spectra) to correspond to the 3- and 5- pyridyl carbons, the assignment of the singlet peak at approximately 4.57 ppm to the attached 3- and 5- pyridyl hydrogen atoms was well supported (Fig. 47).

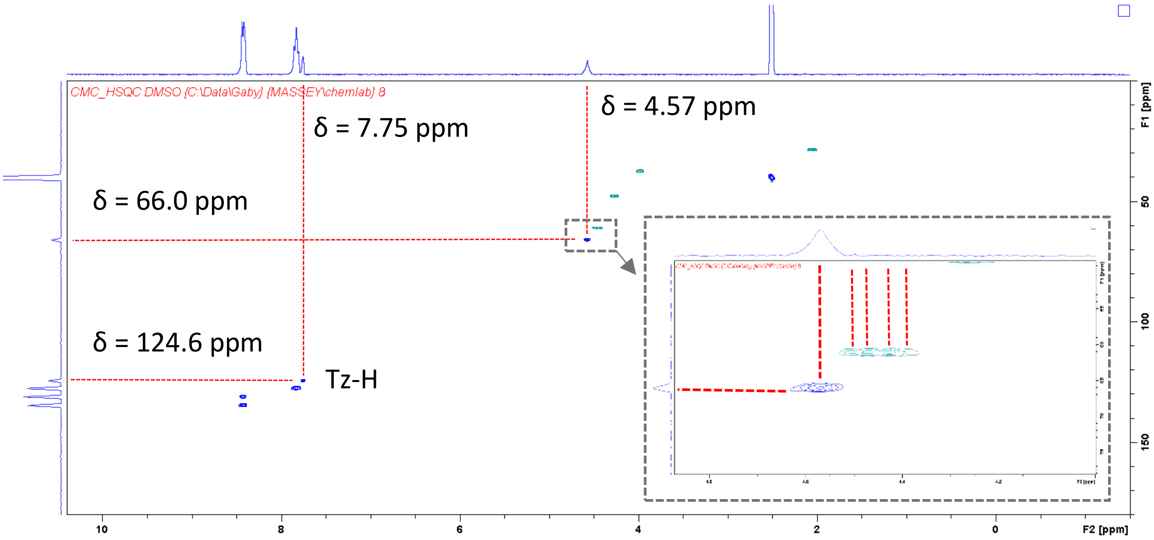

Figure 47. HSQC spectrum of $[Eu(L_2)_3]^{3-}$ in DMSO-d_6 showing the coupling of the Py-H peak at 4.57 ppm with the pyridyl-C peak at 66.0 ppm

Additionally, on closer analysis of the HSQC spectrum of **$[Eu(L_2)_3]^{3-}$**, there appeared to be a set of approximately four peaks in the range expected for the multiplet at 4.41 ppm that were coupling to a carbon peak below 66.0 ppm (at approximately 61.0 ppm) (Fig. 47). These peaks were showing a similar splitting as what was observed in the COSY spectrum and, based off the ^{13}C DEPT spectrum, lined up with a CH_2^{DT} peak at 60.4 ppm (Fig. 45 and Fig. 47). This further supported the assignment of the multiplet in the ^{1}H NMR spectrum of **$[Eu(L_2)_3]^{3-}$** to the CH_2^{DT} protons. The C-H triazole carbon could also be assigned, based off the HSQC spectrum, to the small peak at approximately 124.6 ppm, being similar to that reported for triazole groups attached to the 2,6-PDA positions of 123 ppm (Fig. 47).[185,186]

The IR spectra of **L_2** was collected and compared to that of **$[La(L_2)_3]^{3-}$**, **$[Eu(L_2)_3]^{3-}$** and **$[Tb(L_2)_3]^{3-}$** for further evidence of complexation (Fig. 48). The peak corresponding to C=O stretching of the carboxylic acid motif of **L_1** could be assigned to the group of peaks centred at approximately 1714 cm^{-1} (Fig. 48).[185,186,193,195,197,202-207] On complexation, these peaks appeared to be reduced and instead were dominated by peaks at 1587 cm^{-1} for **$[Eu(L_2)_3]^{3-}$** and **$[Tb(L_2)_3]^{3-}$** and 1586 cm^{-1} for **$[La(L_2)_3]^{3-}$**, indicative of COO^- asymmetric stretching (Fig. 48).[38,40,47,49,185-187,193,199,201,203-206,218] There appeared to be small sub-peaks at 1696 cm^{-1} for **$[Eu(L_2)_3]^{3-}$** and **$[La(L_2)_3]^{3-}$** and 1695 cm^{-1} for **$[Tb(L_2)_3]^{3-}$** which overlapped with the group of peaks assigned to the C=O stretch in **L_2**, suggestive of some **L_2** contamination in the complexes (Fig. 48).[185,186,193,195,197,202-207]

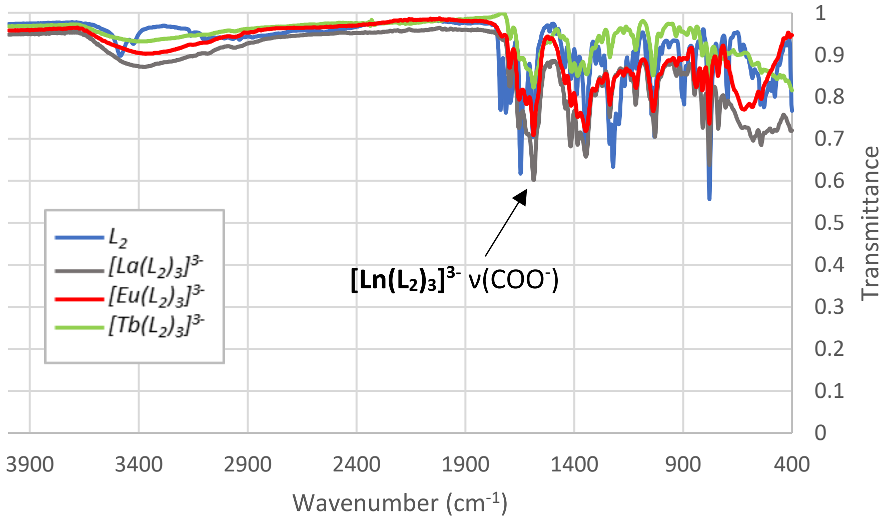

Figure 48. IR spectra obtained for L_2 (blue), $[La(L_2)_3]^{3-}$ (grey), $[Eu(L_2)_3]^{3-}$ (red) and $[Tb(L_2)_3]^{3-}$ (green)

The broad peaks centred at approximately 3375 cm^{-1} for **[Ln(L$_2$)$_3$]$^{3-}$** supported the presence of water in the complexes, expected due to their water-based synthesis (Fig. 48).[38,187,218]

[Eu(L$_2$)$_3$]$^{3-}$ mass spectrum analysis

The full mass spectrum obtained for **[Eu(L$_2$)$_3$]$^{3-}$** (*i.e.* **[$C_{75}H_{51}N_{15}O_{21}Eu$]$^{3-}$**) is supplied in the supplementary information (Fig. S79). The mass spectrum for **[Eu(L$_2$)$_3$]$^{3-}$** was obtained using negative mode and showed successful formation of the 3:1 **L$_2$**:Eu^{3+} complex based on the peak at 550.0883 *m/z* which agreed with the monoisotopic mass calculated for [$C_{75}H_{51}N_{15}O_{21}Eu$]$^{3-}$ (*i.e.* 1650.260 g mol^{-1} which, when considering the -3 charge of the complex gives a *m/z* ratio of 550.0867) (Fig. 49). As shown by the insert in Fig. 49, the peaks belonging to this series were separated by *m/z* values of approximately 0.33, confirming the 3- charge of the ion corresponding to the peak.

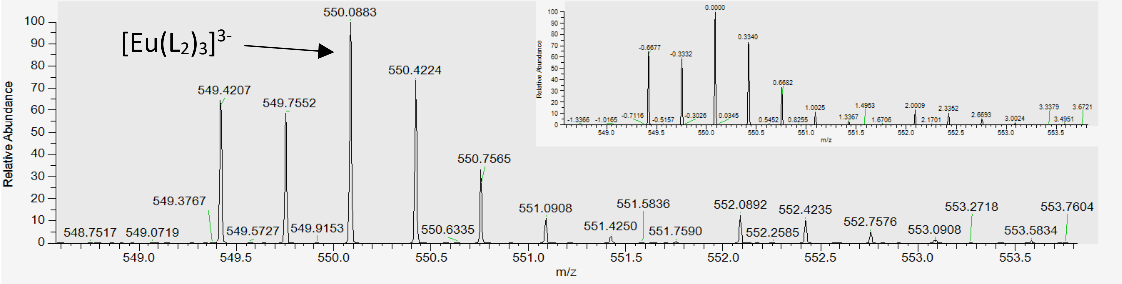

Figure 49. HRMS of [Eu(L$_2$)$_3$]$^{3-}$ showing the peak corresponding to the [Eu(L$_2$)$_3$]$^{3-}$ ion at m/z = 550.0883 (calc. for [$C_{75}H_{51}N_{15}O_{21}Eu$]$^{3-}$, 550.0867 g mol^{-1}). (Insert) m/z labelled relative to the [Eu(L$_2$)$_3$]$^{3-}$ peak, confirming the 3- charge

Another peak was observed at an *m/z* of 825.6360 in the mass spectrum of **[Eu(L$_2$)$_3$]$^{3-}$** which was assigned to the {**[Eu(L$_2$)$_3$]$^{3-}$** + H$^+$}$^{2-}$ ion (Fig. 50 and Table 4). This value was in good agreement with the calculated monoisotopic mass value of 825.6335 g mol^{-1} (for {**[$C_{75}H_{51}N_{15}O_{21}Eu$]$^{3-}$** + H$^+$}$^{2-}$) (Table 4). Additionally, the series belonging to this peak were separated by *m/z* values of approximately 0.50, confirming the 2- charge of the ion (Fig. 50).

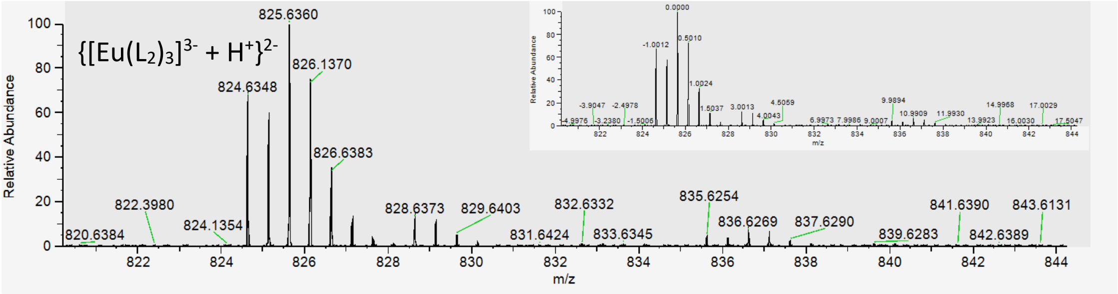

Figure 50. HRMS of [Eu(L$_2$)$_3$]$^{3-}$ showing the peak corresponding to the {[Eu(L$_2$)$_3$]$^{3-}$ + H$^+$}$^{2-}$ ion at m/z = 825.6360 (calc. for {[C$_{75}$H$_{51}$N$_{15}$O$_{21}$Eu]$^{3-}$ + H$^+$}$^{2-}$, 825.6335 g mol^{-1}). (Insert) m/z labelled relative to the {[Eu(L$_2$)$_3$]$^{3-}$ + H$^+$}$^{2-}$ peak, confirming the 2- charge

The mass spectrum also showed peaks indicative of the 2:1 **L$_2$**:Eu^{3+} complex (*i.e.* **[Eu(L$_2$)$_2$]**$^-$ or **[C$_{50}$H$_{34}$N$_{10}$O$_{14}$Eu]**$^-$) with the calculated monoisotopic mass of 1151.147 g mol^{-1} being in good agreement with the peak observed at the *m/z* 1151.150. The peaks in this series were separated by *m/z* values of 1 (although being overlapped with other peaks showing complex splitting), confirming the -1 charge of the 2:1 species (Fig. S83). There was also a relatively large peak observed at an *m/z* of 500.1219, being in close agreement to the monoisotopic mass of deprotonated **L$_2$** with one hydrogen counterion (*i.e.* [(C$_{25}$H$_{17}$N$_5$O$_7$)$^{2-}$ + H$^+$]$^-$) of 500.1206 g mol^{-1} (Fig. S82). It is difficult to tell whether the peaks corresponding to the 2:1 and free ligand are due to impurities in the solution or the result of ionization causing the complex to fall apart.

Table 4. Summary table showing the peaks observed in the HRMS indicative of [Eu(L$_2$)$_3$]$^{3-}$ formation

Ion observed	**Calculated mass (g mol^{-1})**	**Calculated *m/z***	**Observed *m/z***
[Eu(L$_2$)$_3$]$^{3-}$	1650.260	550.0867	550.0883
{[Eu(L$_2$)$_3$]$^{3-}$ + H$^+$}$^{2-}$	1651.267	825.6335	825.6360

[Tb(L$_2$)$_3$]$^{3-}$ mass spectrum analysis

The full mass spectrum obtained for **[Tb(L$_2$)$_3$]$^{3-}$** (*i.e.* **[C$_{75}$H$_{51}$N$_{15}$O$_{21}$Tb]$^{3-}$**) is supplied in the supplementary information (Fig. S97). As observed for **[Eu(L$_2$)$_3$]$^{3-}$**, key peaks were observed which were highly suggestive of the successful formation of the 3:1 **L$_2$**:Tb^{3+} complex. Firstly, the peak was observed at the *m/*z value of 552.0894 which agreed with the value calculated for the **$[C_{75}H_{51}N_{15}O_{21}Tb]^{3-}$** ion of 552.088 g mol^{-1} (*i.e.* the monoisotopic mass was calculated to be 1656.264 g mol^{-1} which, when considering the -3 charge of the complex gives a *m/z* of 552.088) (Fig. 51 and Table 5). Additionally, the peaks belonging to this series were separated by *m/z* values of approximately 0.33, confirming the 3- charge of the ion (Fig. 51).

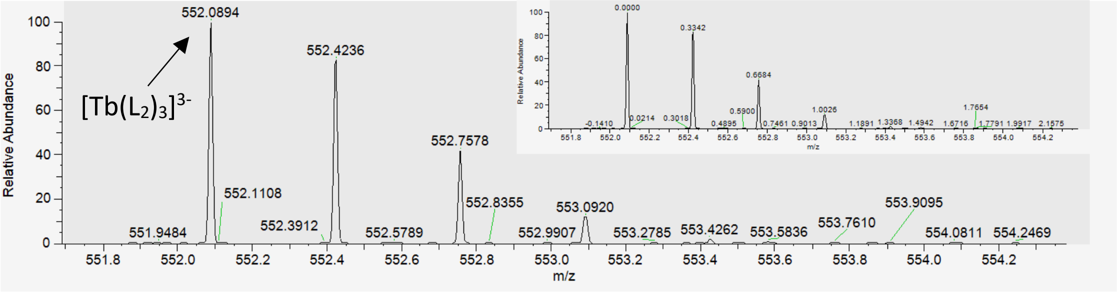

Figure 51. HRMS of $[Tb(L_2)_3]^{3-}$ showing the peak corresponding to the $[Tb(L_2)_3]^{3-}$ ion at m/z = 552.0894 (calc. for $[C_{75}H_{51}N_{15}O_{21}Tb]^{3-}$, 552.0880 g mol^{-1}). (Insert) m/z labelled relative to the $[Tb(L_2)_3]^{3-}$ peak, confirming the 3- charge

Another peak was observed in the mass spectrum of **$[Tb(L_2)_3]^{3-}$** at an *m/z* of 828.6374 (Fig. S99) which could be assigned to {**$[Tb(L_2)_3]^{3-}$** + H^+}$^{2-}$, in good agreement with the calculated monoisotopic mass of 828.6360 g mol^{-1} (Table 5). As observed for the corresponding peak obtained in the mass spectrum of **$[Eu(L_2)_3]^{3-}$**, the series belonging to this peak at 828.6374 were separated by *m/z* values of approximately 0.50, confirmed the 2- charge on the ion (Fig. S99).

Table 5. Summary table showing the peaks observed in the HRMS indicative of $[Tb(L_2)_3]^{3-}$ formation

Ion observed	Calculated mass (g mol^{-1})	Calculated *m/z*	Observed *m/z*
$[Tb(L_2)_3]^{3-}$	1656.264	552.0880	552.0894
$\{[Tb(L_2)_3]^{3-} + H^+\}^{2-}$	1657.272	828.6360	828.6374

There was also a peak in the mass spectrum of **$[Tb(L_2)_3]^{3-}$** observed at an *m/z* value of 1157.1534 which could be assigned to 2:1 L_2:Tb^{3+} complex (*i.e.* **$[Tb(L_2)_2]^-$** or **$[C_{50}H_{34}N_{10}O_{14}Tb]^-$**) with a calculated monoisotopic mass of 1157.1510 g mol^{-1} (Fig. S101). The peaks belonging to this series were separated by *m/z* values of approximately 1, confirming the -1 charge of this complex (Fig. S101). Additionally, as observed in the mass spectrum of **$[Eu(L_2)_3]^{3-}$**, a peak at an *m/z* value of

500.1219 was in agreement with the presence of deprotonated $\mathbf{L_2}$ with a single hydrogen counter ion (*i.e.* $\{(C_{25}H_{17}N_5O_7)^{2-} + H^+\}^-$) (with peaks belonging to this series being separated by *m/z* values of 1, confirming the total -1 charge of the ion) (Fig. S100). However, it was difficult to determine whether these peaks were resulting from impurities or the result of ionisation.

2.4.1.2 Photophysical properties of $\mathbf{L_2}$ and $\mathbf{[Ln(L_2)_3]^{3-}}$

In the solid state, the red emission of $\mathbf{[Eu(L_2)_3]^{3-}}$ under short wave UV light could be observed, proving the ability of $\mathbf{L_2}$ to successfully sensitize Eu^{3+} emission. In the case of $\mathbf{[Tb(L_2)_3]^{3-}}$, the green emission was more difficult to observe which was predicted to be either due to overlap with naphthalimide emission, poor sensitization of the Tb^{3+} excited state by $\mathbf{L_2}$, or a combination of both processes. Moreover, in the solid state, $\mathbf{[Eu(L_2)_3]^{3-}}$ appeared to exhibit dual-emission whereby under short wavelengths of UV light (254 nm), the characteristic red Eu^{3+} emission was observed whereas under long wavelengths of UV light (365 nm), the complexes appear blue in colour resulting from naphthalimide emission (Fig. 52).[240] This property is of high value for the development of dual-emissive systems.

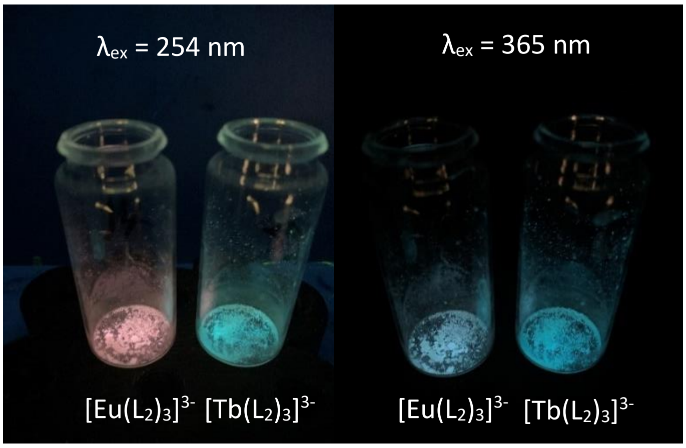

Figure 52. Solid-state emission of $[Eu(L_2)_3]^{3-}$ and $[Tb(L_2)_3]^{3-}$ under short (left) and long (right) wavelengths of UV light

$[Eu(L_2)_3]^{3-}$ and $[Tb(L_2)_3]^{3-}$ photophysical studies in H_2O

$[Eu(L_2)_3]^{3-}$ and **$[Tb(L_2)_3]^{3-}$** displayed limited solubility in solvents compatible for photophysical analysis.[244] The complexes did appear to be partially soluble in water at low concentrations or when heated. Thus, photophysical studies of **$[Ln(L_2)_3]^{3-}$** were carried out using 1 x 10^{-5} M solutions of the respective lanthanide complex in H_2O. Interestingly, the solution-based complexes, particularly the **$[Eu(L_2)_3]^{3-}$** complex, appeared much different under short wave UV light when compared to its solid-state derivative. As shown in the image below, under short wave UV light, **$[Eu(L_2)_3]^{3-}$** appeared white and **$[Tb(L_2)_3]^{3-}$** appeared teal in colour (Fig. 53).

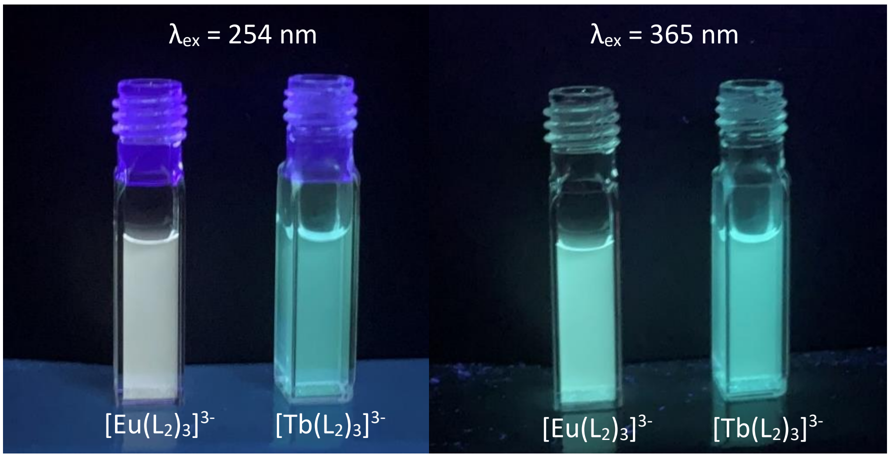

Figure 53. Emission of $[Eu(L_2)_3]^{3-}$ and $[Tb(L_2)_3]^{3-}$ in H_2O (1 x 10^{-5} M) under short (left) and long (right) wavelengths of UV light

UV/Vis spectra of $[Eu(L_2)_3]^{3-}$ and $[Tb(L_2)_3]^{3-}$ in H_2O

To investigate these photophysical properties further, UV/Vis, fluorescence, phosphorescence, and lifetime measurements were carried out. Subsequently, using fluorescence results, a 1931 CIE chromaticity diagram was generated and used to compare **$[Eu(L_2)_3]^{3-}$** emission at different excitation wavelengths.

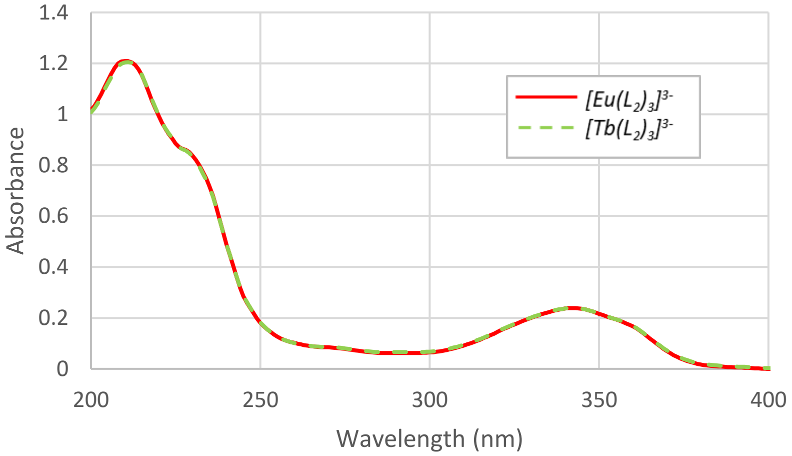

Figure 54. UV/Vis absorption spectra of $[Eu(L_2)_3]^{3-}$ (red line) and $[Tb(L_2)_3]^{3-}$ (green dashed line) in H_2O (1×10^{-5} M)

Firstly, the absorbance spectra of **$[Eu(L_2)_3]^{3-}$** (red line) and **$[Tb(L_2)_3]^{3-}$** (green dashed line) were collected in H_2O (1×10^{-5} M) and appeared to be almost identical (Fig. 54). The absorbance spectra of **L_2** could only be collected in MeOH (which was diluted down from a stock solution of **L_2** in 2:1 $CHCl_3$:MeOH), thus was omitted from the comparison. The absorption spectra appeared to be dominated by one peak with a λ_{abs}^{m} at 211 nm ($\varepsilon = 120,854.0$ L mol^{-1} cm^{-1}) (with a defined shoulder at 228 – 232 nm) and a slight bump at 277 nm which was in the range expected for the combined pyridyl n $\rightarrow \pi^*$ and carbonyl $\pi \rightarrow \pi^*$ transitions.[31,33,40,41,45,47,71,74,185,186,187,193-196,201,207-210] Another broad peak was observed at 342 and 343 nm for **$[Eu(L_2)_3]^{3-}$** and **$[Tb(L_2)_3]^{3-}$** respectively which fell within the range expected for the naphthalimide $\pi \rightarrow \pi^*$ transition.[209,226,228,230,231,235-238,244,246,248]

Fluorescence excitation and emission spectra of $[Eu(L_2)_3]^{3-}$ in H_2O

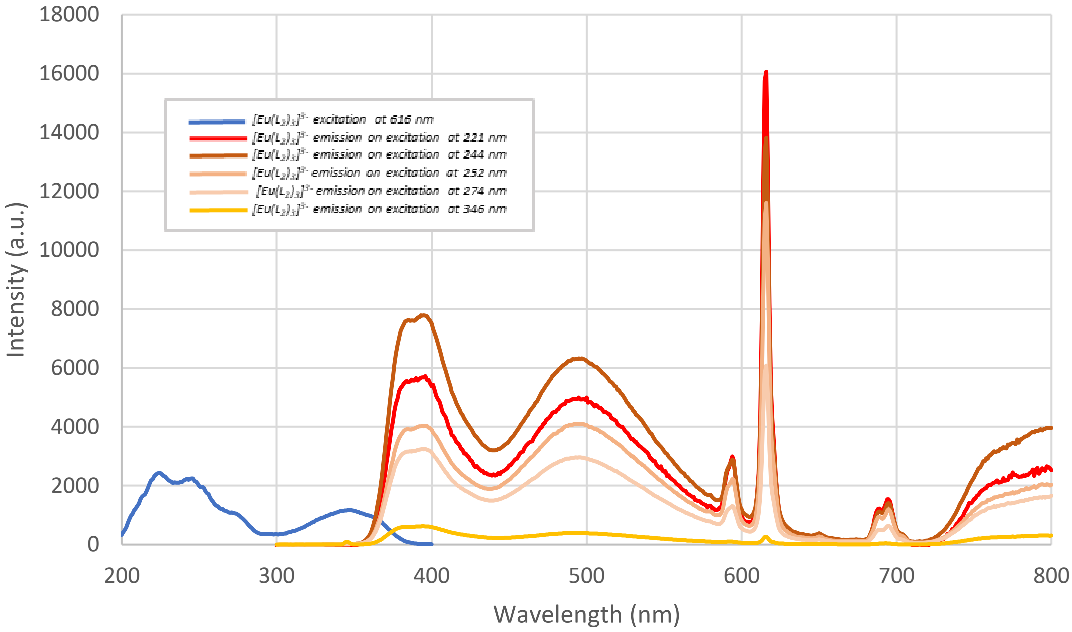

Figure 55. Fluorescence excitation (blue line) (λ_{em} = 616 nm) and emission spectra (λ_{ex} = 221, 244, 252, 274 and 346 nm) of $[Eu(L_2)_3]^{3-}$ (1×10^{-5} M in H_2O)

Next, the fluorescence excitation and emission spectra of $\mathbf{[Eu(L_2)_3]^{3-}}$ was collected in H_2O (1×10^{-5} M) (Fig. 55). The excitation spectra of $\mathbf{[Eu(L_2)_3]^{3-}}$ at 616 nm was comparable to its corresponding absorbance spectra (Fig. 55), suggesting that $\mathbf{L_2}$ to Eu^{3+} energy transfer had occurred.[71,185,186,195,198,202-204,229,235] There appeared to be one key peak spanning 200 – 290 nm, falling in the range expected for the excitation of 1:3 Ln^{3+}:DPA complexes (depending on the 4-pyridyl substituent *i.e.* between 250 – 400 nm).[31-34,37,39-47,50,65,67-69,71,72,74,75,185,186,187,193-196,201,204,207-210,256] This broad peak was split into three smaller shoulders with λ_{ex}^{m} values of 224, 245 and 271 nm (Fig. 55). Additionally, another broad peak spanning 310 – 380 nm (with a λ_{ex}^{m} of 347 nm) could be assigned to naphthalimide-based excitation, being comparable to values obtained in the literature of approximately 300 – 400 nm (Fig. 55).[209,229,231,233,235,236,246]

On excitation of $\mathbf{[Eu(L_2)_3]^{3-}}$ at 221 nm, a broad peak spanning from approximately 360 – 440 nm (centred at approximately 390 nm) was observed which was assigned to naphthalimide fluorescence resulting from singlet π to π^* relaxation, being within the expected range of 330 –

525 nm (*i.e.* the purple/blue region of the electromagnetic spectrum) with slight differences being due to different solvent and/or different systems) (Fig. 55).[209,226,228-231,233-235,237,238,240,244,246,247]

Additionally, excitation of **$[Eu(L_2)_3]^{3-}$** at 221 nm resulted in sharp emission bands characteristic of Eu^{3+} relaxation from the $^5D_0$ state to the ^7F_J states at 594, 616, 649 and 694/695 nm for J = 1, 2, 3 and 4 (respectively).[28] Excitation of **$[Eu(L_2)_3]^{3-}$** at the other λ_{ex}^m values of 244, 252 and 274 nm (corresponding to DPA-based excitation) also gave peaks corresponding to characteristic Eu^{3+} emission (Fig. 55).[32,34,37,39,40,42-47,50,65,67-69,71,72,74,75,184,196,204] Interestingly, excitation of **$[Eu(L_2)_3]^{3-}$** at 346 nm (corresponding to naphthalimide excitation) gave weak Eu^{3+} emission, as seen by the small peak at 616 nm, suggesting that although at relatively large distances from the Eu^{3+} centre, energy transfer between the naphthalimide motif and Eu^{3+} can occur (Fig. 55).[209,229,231,233,235,236,246]

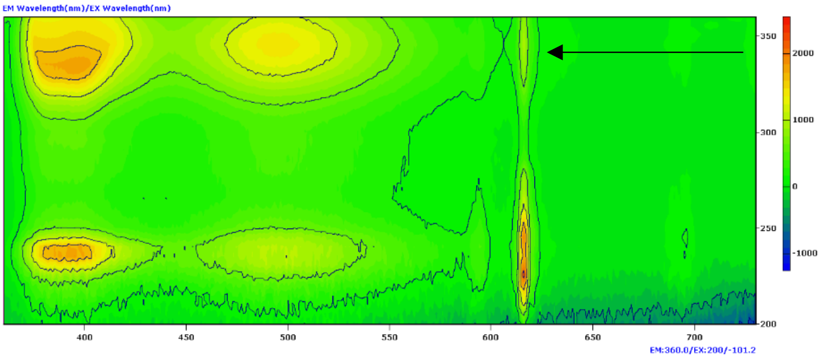

Figure 56. 2D fluorescence excitation and emission plot of $[Eu(L_2)_3]^{3-}$ (1 x 10^{-5} M) in H_2O

A 2D fluorescence excitation and emission plot was also collected and gave more information regarding **$[Eu(L_2)_3]^{3-}$** emission on excitation over the whole 200 – 350 nm range (Fig. 56). As expected, the maximum emission of the hypersensitive peak corresponding to $^5D_0 \rightarrow {}^7F_2$ transition at approximately 616 nm could be observed to occur at approximately 221 nm (Fig. 56).[28] However, there also appeared to be a small peak emitting in the range expected for the $^5D_0 \rightarrow {}^7F_2$ transition (at 616 nm) on excitation at approximately 340 nm, corresponding to the excitation of the naphthalimide motif (shown by the arrow in Fig. 56).[209,229,231,233,235,236,246] This was an important result as it suggested that despite its relatively large distance from the Eu^{3+}, the naphthalimide motif can still sensitize Eu^{3+} emission.

In addition to the peaks corresponding to naphthalimide and Eu^{3+} emission in the fluorescence emission spectrum of **[Eu(L$_2$)$_3$]$^{3-}$** in H$_2$O, there appeared to be another unexpected broad peak centred at approximately 490 nm (Fig.).[221,222,228,231,238,240,243,248] Molecules containing naphthalimide motifs have been well reported to aggregate together in certain states and/or solvents, resulting in excimer formation.[221,222,227,228,230,231,235,238,240,244,248] These naphthalimide aggregates/excimers emit at different wavelengths/lower energies (approximately 500 nm *i.e.* the blue/green region of the electromagnetic spectrum) when compared to isolated naphthalimide units which stems from the fact that intramolecular rotations (which typically quench this emission) are physically restricted in these aggregates.[221,222,228,230,231,235,238-241,243-245,248] This process, known as aggregation induced emission (AIE), provided a probable explanation for the broad peak observed at 490 nm in the emission spectrum of **[Eu(L$_2$)$_3$]$^{3-}$** in H$_2$O.[221,222,227,228,230,231,235,238,240,244,248]

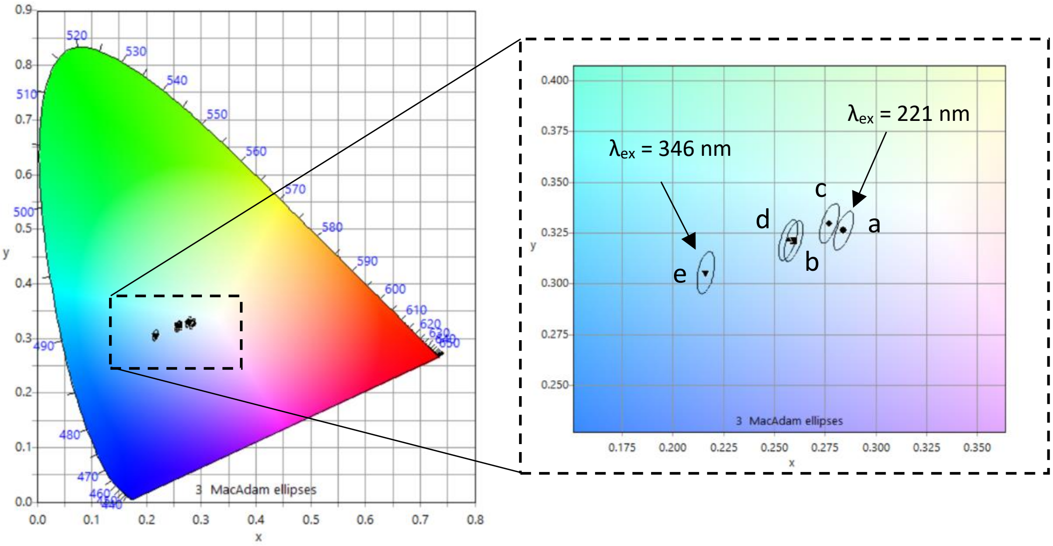

Figure 57. 1931 CIE plot showing CIE coordinates calculated for [Eu(L$_2$)$_3$]$^{3-}$ on excitation at 221 nm (a), 224 nm (b), 252 nm (c), 274 nm (d) and 346 nm (e)

The fluorescence data for **[Eu(L$_2$)$_3$]$^{3-}$** was further plotted in a 1931 CIE plot (Fig. 57). The CIE coordinates of **[Eu(L$_2$)$_3$]$^{3-}$** (1 x 10^{-5} M in H$_2$O) on excitation at 221 nm were x=0.2841 and y=0.3262 (Fig. 57). These CIE coordinates were close to those for perfect white emission (x=0.33 and y=0.33) suggesting that the red- and blue- emitting components (*i.e.* the Eu^{3+} and naphthalimide or excimer component, respectively) were in the ideal ratio for white light emission.[221,222,228,230,240] As the excitation wavelength increased from 221 to 346 nm (through 224, 252 and 274 nm), a shift in the colour of **$[Eu(L_2)_3]^{3-}$** emission was observed to a more blue-light dominated emission (Fig. 57).[233,235]

Combining AIE with Ln^{3+} luminescence has been reported as being an effective approach to achieve white-light emission from single complexes.[221,222,228,230,231,233,235] In particular, this has been observed for multiple naphthalimide-Eu^{3+} containing systems as they emit complementary colours.[221,222,228,230,233,235] In saying this, a possible cause of the white-light emission observed on the excitation of **$[Eu(L_2)_3]^{3-}$** at 221 nm in H_2O was predicted to result from the combination of the naphthalimide (and/or excimer) emission (blue/green) and Eu^{3+} emission (red) (Fig. 49).[28,221,228,230,240,248] Based on the nature of AIE, it was expected that the white-light emission would be observed in the solid state, however this was not observed and instead the red emission characteristic of Eu^{3+} was observed on excitation of solid **$[Eu(L_2)_3]^{3-}$** at 254 nm (Fig. 48).[221,222,230,243,244] This observation suggested that a decrease in AIE was occurring and instead suggested that an aggregation caused-quenching (ACQ) effect was present in the solid state.[221,222,228,239,240,243,245]

ACQ is commonly observed for planar aromatic molecules (such as pyrenes) in their solid state due to the intrinsically dense and large amount of intermolecular π-π stacking that occurs when these molecules are in this state.[221,222,227,228,236,239-245] According to several different studies (as cited in ref [243]), this means that when these molecules are excited, non-radiative decay processes are favoured.[221,222,227,228,239,240,242-245] Alternatively, molecules that show AIE tend to be propeller shaped as this means makes dense π-π stacking in the aggregates difficult to achieve.[222,240,241,243,245] Instead, these propeller shaped molecules tend to interlock with each other in their aggregates meaning that intramolecular rotations are physically restricted, and AIE becomes possible.[222,228,230,240,241,243-245] The coordination geometry of 3:1 DPA:Eu^{3+} complexes show similarities to a propeller (as observed based off the crystal structure obtained for **$Na_3[Eu(L_1)_3]\cdot 16H_2O$**), making it possible that the **$[Eu(L_2)_3]^{3-}$** complexes interlock in a similar way to the propeller-shaped molecules.[222,228,230,240,241,243-245]

Thus, it is possible that **$[Eu(L_2)_3]^{3-}$** exhibits both ACQ and AIE such that in solid state, the π-π stacking is large enough to restrict blue/green aggregate emission (meaning ACQ is active and so Eu^{3+} emission is observed) whereas in water, this large amount of π-π stacking is reduced, however the remaining aggregates still have restricted rotation, thus we observe AIE which, in addition to Eu^{3+} emission, produces white light.[221,222,228,230,233,234,239-245,248]

Alternatively, the cause of white light emission of **$[Eu(L_2)_3]^{3-}$** in H_2O on excitation at 221 nm may also be due to the presence of water causing the quenching of Eu^{3+} emission such that the perfect ratio between naphthalimide blue emission and Eu^{3+} red emission is obtained.[228,230,231,240] As mentioned by Plyusnin and co-workers (2013), the presence of two complementary emitters is not enough for white light emission.[230,231] White light emission requires the emission intensities of the complementary emitters to be in an ideal ratio.[230,231]

The lifetime (τ) of **$[Eu(L_2)_3]^{3-}$** (1 x 10^{-5} M in H_2O) (monitoring 616 nm) on excitation at 220 nm was 0.607 ms and best fit to a single exponential curve. The lifetime of **$[Eu(L_2)_3]^{3-}$** (1 x 10^{-5} M in D_2O) (monitoring 545 nm) was 0.769 ms and could also be fit to a single exponential curve.[204] In substituting these values into the Horrocks and Sudnick equation for the determination of the hydration number (q) of the complex, a value of 0.36 was obtained.[26,208,249-253] Although this value was very low (and could be rounded down to zero), it suggested that a small amount of water was interacting with the Eu^{3+} centre which may provide some quenching.[26,193,194,203-205,207,250-253] However, without further photophysical studies, it is difficult to identify the cause of this deviation.

Fluorescence excitation and emission spectra of [Tb(L_2)$_3$]$^{3-}$ in H_2O

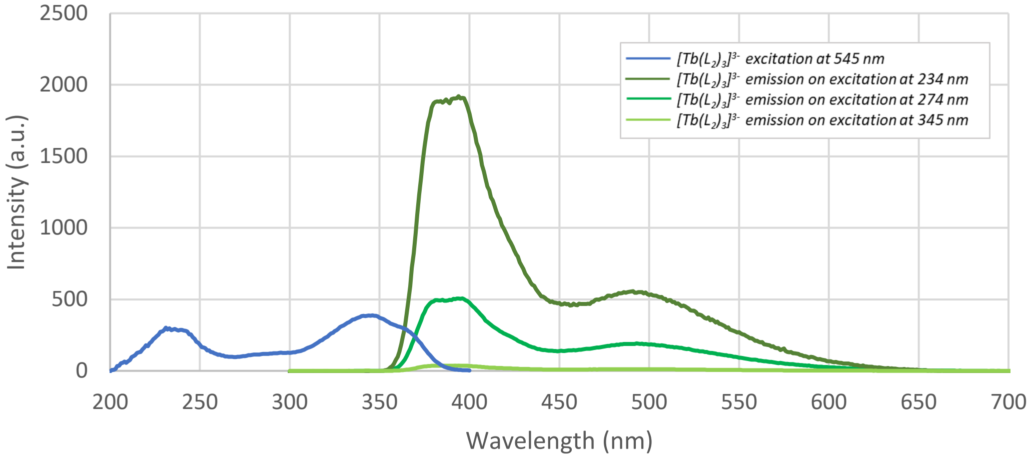

Figure 58. Fluorescence excitation (blue line) (λ_{em} = 545 nm) and emission spectra of [Tb(L_2)$_3$]$^{3-}$ (1 x 10^{-5}) at λ_{ex} = 234, 274 and 345 nm in H_2O. For the fluorescence excitation measurement, excitation and emission slit widths were both 3.0 nm. For the fluorescence emission measurements, excitation and emission slit widths were also both 3.0 nm except for the case of [Tb(L_2)$_3$]$^{3-}$ on excitation at 345 nm whereby the excitation and emission and excitation slit widths were 3.0 and 1.0 nm (respectively)

Next, the fluorescence excitation and emission spectra of **[Tb(L_2)$_3$]$^{3-}$** was recorded in H_2O (1 x 10^{-5} M). The excitation spectra of **[Tb(L_2)$_3$]$^{3-}$** at 545 nm contained two broad peaks, one spanning from 210 – 260 nm (centred at approximately 234 nm) and another one spanning from 310 – 380 nm (corresponding to naphthalimide excitation) (Fig. 58).[32,33,37,42-47,50,68,69,71,72,74,196,209,231,233,235,236] Another peak can be observed at approximately 280 nm. The excitation spectrum was similar in shape and form when compared to the absorbance spectrum of **[Tb(L_2)$_3$]$^{3-}$**, suggesting that **L_2** was able to sensitize Tb^{3+} emission.[71,185,186,195,198,202-204,229]

However, as opposed to the emission spectra of **[Eu(L_2)$_3$]$^{3-}$**, the emission spectra of **[Tb(L_2)$_3$]$^{3-}$** on excitation at 234 and 274 nm (corresponding to the λ_{ex}^{m}) was only dominated by two key peaks. The first peak, centred at approximately 390 nm could be assigned to naphthalimide-based fluorescence, as had been observed in previous studies (Fig. 58).[226,228-231,233-235,237,238,240,244,246,247] The second broad peak, centred at approximately 490 nm, was in the range expected for the naphthalimide-excimer, suggestive of AIE as observed for **[Eu(L_2)$_3$]$^{3-}$**.[221,222,227,228,230,231,238,240,244,248] The broad nature of this peak (as well as that of naphthalimide fluorescence) caused any peaks corresponding to Tb^{3+} emission to be masked (as Tb^{3+} emission occurs at wavelengths spanning from 485 – 655 nm).[28] There was also a possibility that the lack of Tb^{3+} emission may also be due to poor energy match between the **L$_2$** excited states and the $^{5}D_4$ emitting state, however it was difficult to draw conclusions due to the overlapping nature of the excimer fluorescence.[229,230]

The lifetime of **[Tb(L$_2$)$_3$]$^{3-}$** emission (monitoring the $^{5}D_4 \rightarrow {}^{7}F_5$ peak) on excitation at 247 nm was best fit to a double exponential curve and gave an average lifetime of 0.629 ms for the longer emitting species and 0.208 ms for the shorter emitting species.

Phosphorescence excitation and emission spectra of [Eu(L$_2$)$_3$]$^{3-}$ and [Tb(L$_2$)$_3$]$^{3-}$ in H$_2$O

To further probe the presence (or lack of) Ln^{3+}-centred luminescence from **L$_2$**, the time-delayed phosphorescence excitation and emission spectra of **[Eu(L$_2$)$_3$]$^{3-}$** and **[Tb(L$_2$)$_3$]$^{3-}$** were collected in H$_2$O. Photophysical measurements taken in this mode occur after a 0.2 ms time delay meaning that emission stemming from Ln^{3+} can be isolated due to its long lifetime.

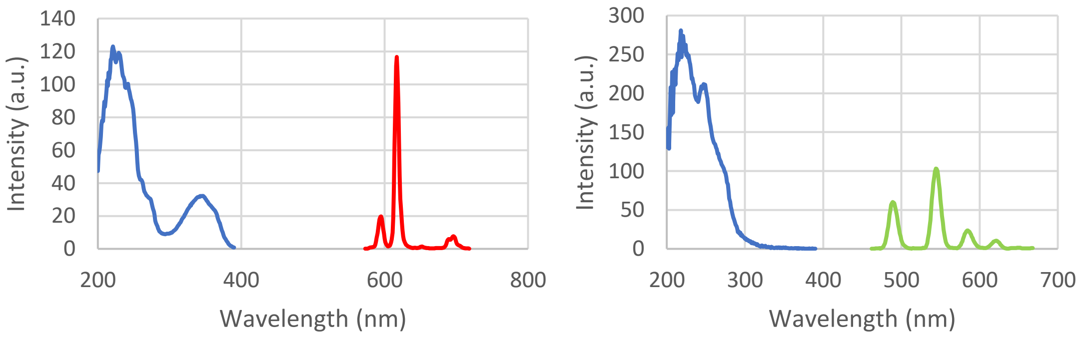

Figure 59. (Left) Phosphorescence excitation (blue line) (λ_{em} = 616 nm) and emission (red line) (λ_{ex} = 279 nm) spectra of [Eu(L$_2$)$_3$]$^{3-}$ (1 x 10^{-5} M) in H$_2$O showing Eu^{3+}-centred emission. For both the phosphorescence excitation and emission measurements of [Eu(L$_2$)$_3$]$^{3-}$ (1 x 10^{-5} M) in H$_2$O, excitation and emission slit widths were 5.0 nm. (Right) Phosphorescence excitation (blue line) (λ_{em} = 545 nm) and emission (green line) (λ_{ex} = 274 nm) spectra of [Tb(L$_2$)$_3$]$^{3-}$ (1 x 10^{-5} M) in H$_2$O showing Tb^{3+}-centred emission. For both the phosphorescence excitation and emission measurements of [Tb(L$_2$)$_3$]$^{3-}$ (1 x 10^{-5} M) in H$_2$O, excitation and emission slit widths were 10.0 nm

On the excitation of **[Eu(L$_2$)$_3$]$^{3-}$** in H$_2$O at 279 nm, sharp peaks characteristic of Eu^{3+}-centred emission could be observed at 594, 616, 651, and 695 nm for the $^{5}D_0 \rightarrow {}^{7}F_J$ transitions of J= 1, 2, 3 and 4 (respectively) (Fig. 59).[28] Although the phosphorescence emission spectrum was not collected at wavelengths corresponding to naphthalimide excitation, the broad peak at 346 nm in the phosphorescence excitation spectra suggested that the naphthalimide component of **L_2** can sensitize Eu^{3+} emission despite its far distance.[209,229,231,233,235,236,246]

On excitation of **$[Tb(L_2)_3]^{3-}$** in H_2O at 274 nm, Tb^{3+}-centred emission was observed which suggested that **L_2** does sensitize Tb^{3+} emission and that the lack of any visible peaks indicating Tb^{3+} emission in the fluorescence spectrum was due to masking by the naphthalimide excimer peak (Fig. 59).[221,222,227,228,230,231,235,238,240,244,248] However, a large difference was observed in the phosphorescence excitation spectra when compared to that of **$[Eu(L_2)_3]^{3-}$** such that the broad peak centred at 346 nm (assigned to naphthalimide excitation) was absent.[209,229,231,233,235,236,246] The absence of this peak suggested that the naphthalimide motif of **L_2** has no role in Tb^{3+} sensitization.

Overall, the phosphorescence spectra suggests that both the DPA motif as well as the naphthalimide group at the 4-pyridyl position can sensitize Eu^{3+} emission but not Tb^{3+} emission (which is only excited by DPA-based excitation) (Fig. 59).[246] The lowest lying emitting level of Eu^{3+} ($^5D_0$) lies at 17,500 cm^{-1} whereas for Tb^{3+} ($^5D_4$) it lies at approximately 20,000 cm^{-1}.[3,4,45,178,184,198-200,221,228-231,241,246] In comparison, the 1,8-naphthalimide motif is known to contain a T_1 state of 18,500 cm^{-1} in acetonitrile.[228-231,235,246-248] In saying this, the $^5D_4$ Tb^{3+} level is too high to be populated by the naphthalimide T_1 state.[3,4,45,178,184,198-200,221,228-231,235,246-248] As mentioned in section 1.1.1, for efficient energy transfer, the energy gap between the ligand triplet state and the main Ln^{3+} emitting state must be between 2500 – 4000 cm^{-1}.[2-4,6-8,11-18,21-23,27,28,30,228,235] The energy gap between the Eu^{3+} emitting state and the naphthalimide T_1 state was calculated to be approximately 1000 cm^{-1}.[229,230,235,246-248] Although this energy gap lies below this optimal range, it is still able to sensitize some Eu^{3+} emission although some BET is likely.[228-231,235,246]

$[Eu(L_2)_3]^{3-}$ and $[Tb(L_2)_3]^{3-}$ photophysical studies in MeOH

The fluorescence spectra of $\mathbf{[Eu(L_2)_3]^{3-}}$ and $\mathbf{[Tb(L_2)_3]^{3-}}$ showed AIE in water, thus photophysical data was also measured in methanol (MeOH) (1 x 10^{-5} M made from a 1 x 10^{-3} M stock solution of $\mathbf{[Eu(L_2)_3]^{3-}}$ or $\mathbf{[Tb(L_2)_3]^{3-}}$ in H_2O).[244] This change in solvent appeared to have a large change in the colour observed under UV light. Under short wave UV light, $\mathbf{[Eu(L_2)_3]^{3-}}$ appeared red in colour (expected for Eu^{3+} sensitization) and $\mathbf{[Tb(L_2)_3]^{3-}}$ appeared slightly blue in colour (suggesting poor Tb^{3+} sensitization). Under long wave UV light, $\mathbf{[Eu(L_2)_3]^{3-}}$ appeared teal blue in colour (expected for naphthalimide emission) and $\mathbf{[Tb(L_2)_3]^{3-}}$ appeared slightly lighter blue when compared to its short wave colour (Fig. 60). In this sense, the $\mathbf{[Eu(L_2)_3]^{3-}}$ derivative in appeared to show solution-based red/blue dual emission in MeOH but not in H_2O.

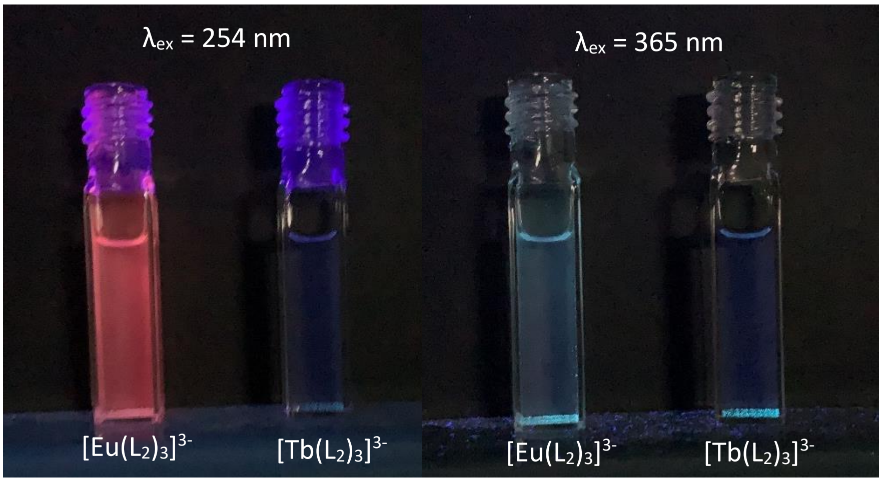

Figure 60. Emission of $[Eu(L_2)_3]^{3-}$ and $[Tb(L_2)_3]^{3-}$ in MeOH (1 x 10^{-5} M) under short (left) and long (right) wavelengths of UV light

To investigate these changes induced by the solvent change, fluorescence, phosphorescence, and lifetime measurements were carried out and the emission was plotted on a 1931 CIE chromatograph.

Fluorescence excitation and emission spectra of $[Eu(L_2)_3]^{3-}$ in MeOH

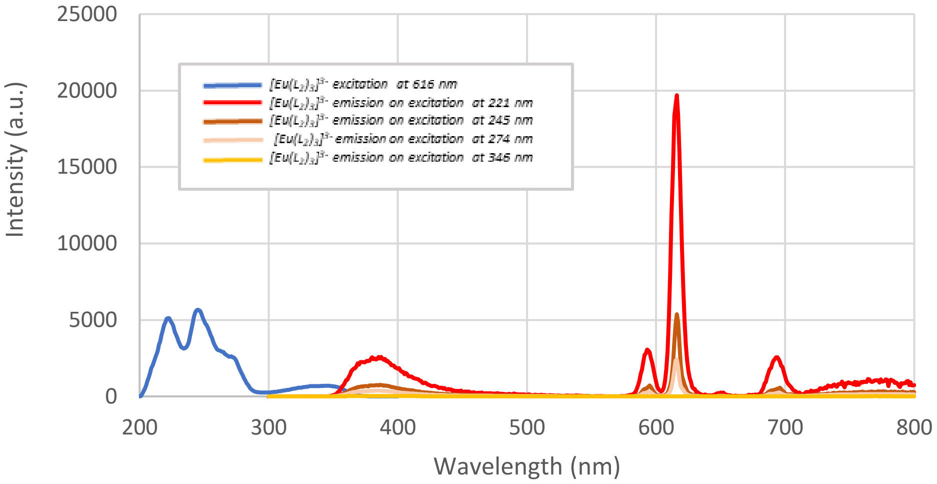

Figure 61. Fluorescence excitation (blue line) (λ_{em} = 616 nm) and emission spectra (λ_{ex} = 221, 245, 274 and 346 nm) of $[Eu(L_2)_3]^{3-}$ (1×10^{-5} M in MeOH). For the fluorescence excitation measurement, excitation and emission slit widths were both 3.0 nm. For the fluorescence emission measurements, excitation slit widths were 3.0 nm and emission slit widths ranged from 1.0 – 5.0 nm

In MeOH, the excitation spectra of $\mathbf{[Eu(L_2)_3]^{3-}}$ at 616 nm, revealed two main peaks with superimposed sub-peaks. The main peak spanned the 200 – 280 nm range (expected for the excitation of DPA-containing Ln^{3+} complexes) and contained two relatively sharp components (one centred at 222 nm and another centred at 245 nm) along with a shoulder at approximately 271 nm (Fig. 61).[32,34,37,39,40,42-47,50,65,67-69,71,72,74,75,204] A second broad peak was observed at approximately 346 nm, expected for naphthalimide excitation (Fig. 61).[209,229,231,233,235,236,246] Thus overall, the excitation spectra of $\mathbf{[Eu(L_2)_3]^{3-}}$ in MeOH was similar in shape when compared to in H_2O (whereby λ_{ex}^{m} values of 224, 245, 271 and 347 nm were obtained), however the key peaks were more defined and enhanced.

Next, the emission spectra of $\mathbf{[Eu(L_2)_3]^{3-}}$ in MeOH at different excitation wavelengths was investigated (Fig. 61). Excitation of $\mathbf{[Eu(L_2)_3]^{3-}}$ at 221 nm resulted in a broad peak spanning 360 – 440 nm, falling in the range expected for naphthalimide emission.[209,226,228-231,233-235,237,238,240,244,246,247] Additionally, excitation of $\mathbf{[Eu(L_2)_3]^{3-}}$ at 221 nm resulted in the presence of narrow bands characteristic of Eu^{3+} emission from its $^5D_0$ level to its ^7F_J levels of 593, 616, 652, and 693 nm for J = 1, 2, 3 and 4 (respectively) (Fig. 61).[28] The intensity of these peaks were in the order expected, with the $^5D_0 \rightarrow {}^7F_2$ transition being most intense (due to hypersensitivity), followed by the peak corresponding to the $^5D_0 \rightarrow {}^7F_1$ transition, followed by the peak corresponding to the $^5D_0 \rightarrow {}^7F_4$ transition and the weakest being that of the $^5D_0 \rightarrow {}^7F_3$ transition.[28] The lifetime of **$[Eu(L_2)_3]^{3-}$** on excitation at 220 nm could be fit to a single exponential curve and gave a value of 1.449 ms. Thus, the lifetime of **$[Eu(L_2)_3]^{3-}$** in MeOH was over two times longer when compared to in H_2O, expected due to less O-H quenching in MeOH.

Excitation of **$[Eu(L_2)_3]^{3-}$** at 245 and 274 nm in MeOH also resulted in the narrow bands characteristic of Eu^{3+} emission. Excitation of **$[Eu(L_2)_3]^{3-}$** at 346 nm gave no peaks indicative of emission from Eu^{3+}, suggesting that in MeOH, excitation of the naphthalimide motif does not sensitize Eu^{3+}.

However, the main difference between the fluorescence emission spectra of **$[Eu(L_2)_3]^{3-}$** in H_2O compared to MeOH is the removal of the band centred at 490 nm corresponding to naphthalimide excimer emission.[221,222,227,228,230,231,235,238,240,243,244,248] This suggested that in MeOH, **$[Eu(L_2)_3]^{3-}$** does not aggregate to the same extent as in H_2O and as a result has a large difference in the emission observed which can be visualised on the CIE diagram (Fig. 62).[221,222,228,231,238,240,243,248]

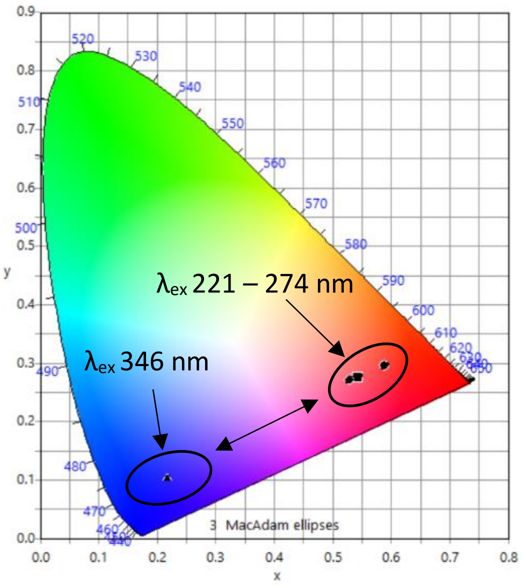

Figure 62. 1931 CIE plot showing the CIE coordinates calculated for $[Eu(L_2)_3]^{3-}$ (1 x 10^{-5} M) on excitation at short UV wavelengths (λ_{ex} = 221, 245 and 274 nm) compared to long UV wavelengths (λ_{ex} = 346 nm) showing the dual red-blue emission

Based on the CIE plot, emission of **$[Eu(L_2)_3]^{3-}$** in MeOH on excitation at 221, 245 and 274 nm is primarily red (thus is dominated by the Eu^{3+} emission) (Fig. 62).[28] On excitation of **$[Eu(L_2)_3]^{3-}$** at longer wavelengths (*i.e.* 346 nm), the blue emission typical of the naphthalimide motif dominates.[209,226,228-231,233-235,237,238,240] Thus, as a result of this excimer emission peak removal, **$[Eu(L_2)_3]^{3-}$** showed dual emission in MeOH.[228,231]

Overall, the results suggest that in H_2O, the intramolecular rotations of **$[Eu(L_2)_3]^{3-}$** are restricted (due to aggregate formation), which favours the excimer radiative decay process after excitation, resulting in a broad band at 490 nm in the fluorescence emission spectrum.[221,222,228,230,231,240,241,243-245,248] In contrast, in MeOH, these restrictions are relieved meaning that more non-radiative decay pathways are available after excitation leading to the removal of the excimer peak at 490 nm.[221,222,228,230,231,240,243-245,248]

Alternatively, it is also possible that the stronger red emission observed for **$[Eu(L_2)_3]^{3-}$** in MeOH results from less Eu^{3+} quenching when compared to when the complex is in H_2O.[230] Further photophysical studies are required to confirm these processes.

Fluorescence excitation and emission spectra of $[Tb(L_2)_3]^{3-}$ in MeOH

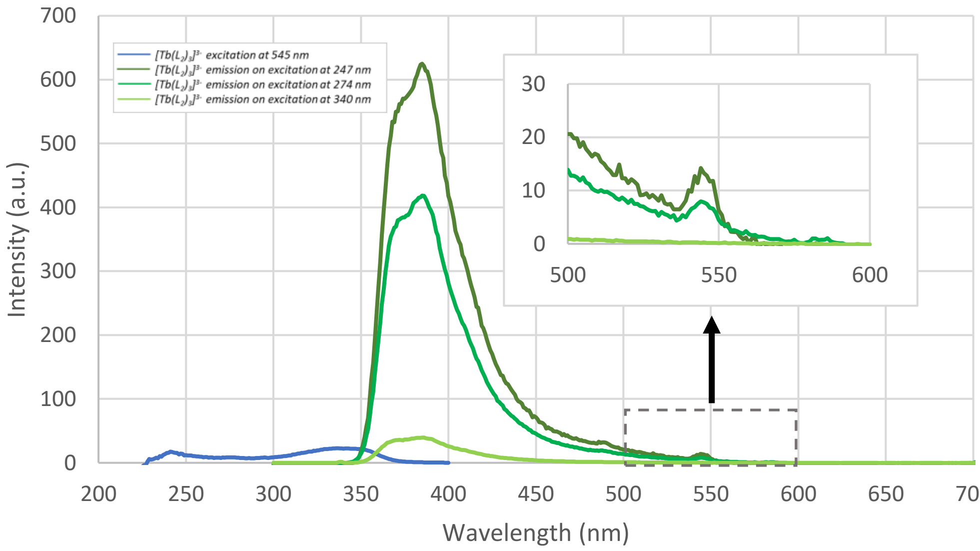

Figure 63. Fluorescence excitation (blue line) (λ_{em} = 545 nm) and emission spectra of $[Tb(L_2)_3]^{3-}$ (1×10^{-5}) at λ_{ex} = 247, 274 and 340 nm in MeOH. For the fluorescence excitation measurement, excitation and emission slit widths were both 3.0 nm. For the fluorescence emission measurements, excitation and emission slit widths were also both 3.0 nm except for the case of $[Tb(L_2)_3]^{3-}$ on excitation at 340 nm whereby the excitation and emission slit widths were 3.0 and 1.0 nm (respectively)

In MeOH, the excitation spectrum of **$[Tb(L_2)_3]^{3-}$** at 545 nm showed two main λ_{ex}^{m} peaks, one at 241 nm and another centred at approximately 344 nm, thus resembling its excitation spectrum in H_2O (Fig. 63).

Next, the emission spectra of **$[Tb(L_2)_3]^{3-}$** in MeOH at different wavelengths was investigated (Fig. 63). The emission spectra of **$[Tb(L_2)_3]^{3-}$** contained a broad peak spanning from approximately 350 – 450 nm on excitation at 247, 274 and 340 nm, corresponding to naphthalimide emission (Fig. 63).[209,226,228-231,233-235,237,238,240,244,246,247] Additionally, when compared to H_2O, the emission spectrum of **$[Tb(L_2)_3]^{3-}$** in MeOH (on excitation at 247 and 274 nm) lacked the broad peak that was observed at 490 due to AIE which revealed a small peak at 544 nm, in the wavelength range expected for the hypersensitive $^5D_4 \rightarrow {}^7F_5$ Tb^{3+} transition.[28,221,222,228,231,238,240,243,248] Despite the removal of the AIE peak, and because Tb^{3+} emits at shorter wavelengths (*i.e.* between 485 – 655 nm) when compared to Eu^{3+} (*i.e.* 578 – 705 nm) (thus will overlap more with the band corresponding to naphthalimide emission), no other peaks indicative of Tb^{3+} emission could be observed.[28] The emission spectrum of **$[Tb(L_2)_3]^{3-}$** in MeOH on excitation at 340 nm (corresponding to naphthalimide excitation) gave no indication of Tb^{3+} emission and only displayed a broad band at approximately 385 nm corresponding to naphthalimide emission.[209,226,228-231,233-238,240,244,246,247] The lifetime decay of the $^5D_4 \rightarrow {}^7F_5$ transition on excitation of **$[Tb(L_2)_3]^{3-}$** at 247 nm was best fit to a double exponential curve and gave values of 0.769 ms for the longer emitting species and 0.070 ms for the shorter emitting species.

The CIE plots for emission of **$[Tb(L_2)_3]^{3-}$** in MeOH on excitation at 247, 274 and 340 nm were dominated by blue naphthalimide fluorescence whereas when compared to **$[Tb(L_2)_3]^{3-}$** in H_2O on excitation at 234, 274 and 345 nm, AIE skews the emission more towards the white region ($x = 0.33$, $y = 0.33$).[221]

Phosphorescence excitation and emission spectra of [Eu(L_2)$_3$]$^{3-}$ and [Tb(L_2)$_3$]$^{3-}$ in MeOH

To further confirm **L_2** sensitization of Eu^{3+} and Tb^{3+} in MeOH, phosphorescence measurements were carried out and similar results were obtained when compared to those in H_2O.

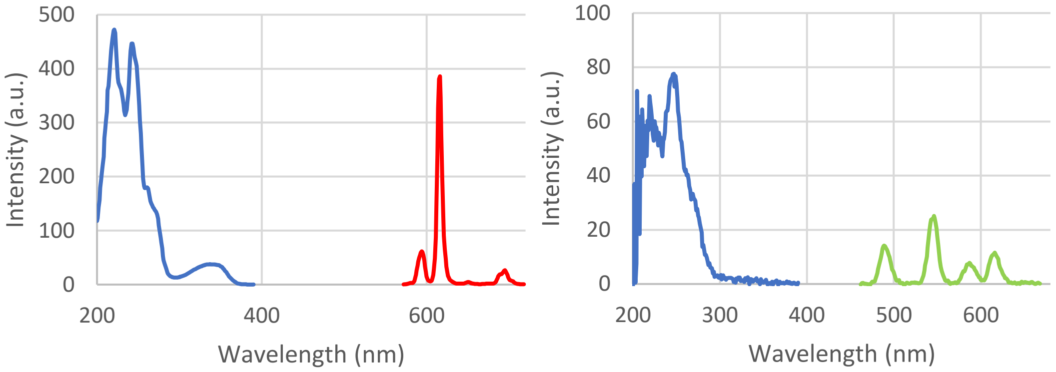

Figure 64. (Left) Phosphorescence excitation (blue line) (λ_{em} = 616 nm) and emission (red line) (λ_{ex} = 279 nm) spectra of [Eu(L_2)$_3$]$^{3-}$ (1 x 10^{-5} M) in MeOH showing Eu^{3+}-centred emission. For both the phosphorescence excitation and emission measurements of [Eu(L_2)$_3$]$^{3-}$ (1 x 10^{-5} M) in MeOH, excitation and emission slit widths were 5.0 nm. (Right) Phosphorescence excitation (blue line) (λ_{em} = 545 nm) and emission (green line) (λ_{ex} = 274 nm) spectra of [Tb(L_2)$_3$]$^{3-}$ (1 x 10^{-5} M) in MeOH showing Tb^{3+}-centred emission. For both the phosphorescence excitation and emission measurements of [Tb(L_2)$_3$]$^{3-}$ (1 x 10^{-5} M) in MeOH, excitation and emission slit widths were 10.0 nm

The phosphorescence excitation (λ_{em} = 616 nm) and emission (λ_{ex} = 279 nm) spectra of **[Eu(L_2)$_3$]$^{3-}$** in MeOH (1 x 10^{-5} M) was collected (Fig. 64). The excitation spectrum showed two main groups of peaks. The first group contained two sharp components at λ_{ex}^{m} values of 221 and 243 nm with a shoulder at approximately 273 nm. The second group was a broad peak at approximately 337 nm corresponding to naphthalimide based emission.[209,226,228-231,233-235,237,238,240,244,246,247] The emission spectrum of **[Eu(L_2)$_3$]$^{3-}$** in MeOH on excitation at 279 nm gave sharp peaks characteristic of Eu^{3+}-centred emission (Fig. 64).[28]

The phosphorescence excitation (λ_{em} = 545 nm) and emission (λ_{ex} = 274 nm) spectra of **[Tb(L_2)$_3$]$^{3-}$** in MeOH was also collected (Fig. 64). The excitation spectrum contained a maximum at 247 nm which was supplemented by a shoulder at approximately 269 nm (Fig. 64). As observed for the excitation spectrum of **[Tb(L_2)$_3$]$^{3-}$** in H_2O, the excitation spectrum of **[Tb(L_2)$_3$]$^{3-}$** in MeOH showed no peak corresponding to naphthalimide excitation, highlighting that the energy mismatch between the naphthalimide T_1 state and the Tb^{3+} $^5D_4$ level still applies in MeOH.[3,4,45,178,198-

[200,221,228-231,235,246-248] However, emission spectrum of **[Tb(L_2)$_3$]$^{3-}$** on excitation at 274 nm showed key characteristic peaks expected for Tb^{3+}-centred emission (although there was contamination observed due to Eu^{3+} remaining on the cuvettes) (Fig. 64).[28]

CIE plot comparing the emission of [Eu(L_2)$_3$]$^{3-}$ in H_2O and MeOH

A CIE plot comparing the colour of **[Eu(L_2)$_3$]$^{3-}$** emission on excitation at short and long wavelengths of UV light highlighted the differences between the two systems in different solvents (Fig. 65). In H_2O the differences in emission on excitation at 221 and 346 nm were observed to be small. In comparison, in MeOH, the differences in emission on excitation at 221 and 346 nm where much larger such that it displayed dual emission (*i.e.* on 221 nm excitation, the red emission typical of Eu^{3+} was observed whilst on 346 nm, the blue emission typical of the naphthalimide motif was observed) (Fig. 65).

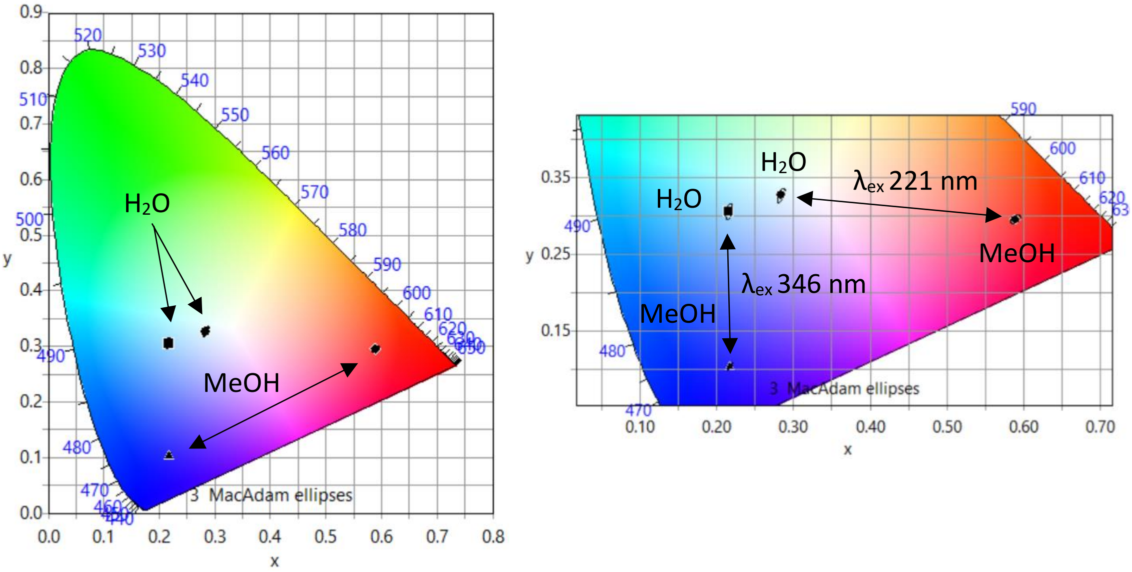

Figure 65. 1931 CIE plot comparing the differences in emission of [Eu(L_2)$_3$]$^{3-}$ in H_2O and MeOH on excitation at 221 nm and 346 nm

2.4.2 Tert-butyl ligand (L_3) and complex $[Ln(L_3)_3]^{3-}$

2.4.2.1 Synthesis and characterisation

The next ligand system explored incorporated the bulky 3,5-di-*tert*-butyl benzyl motif which has been extensively reported as a stopper group for **M_1** (and similar macrocycles).[137,152,157]

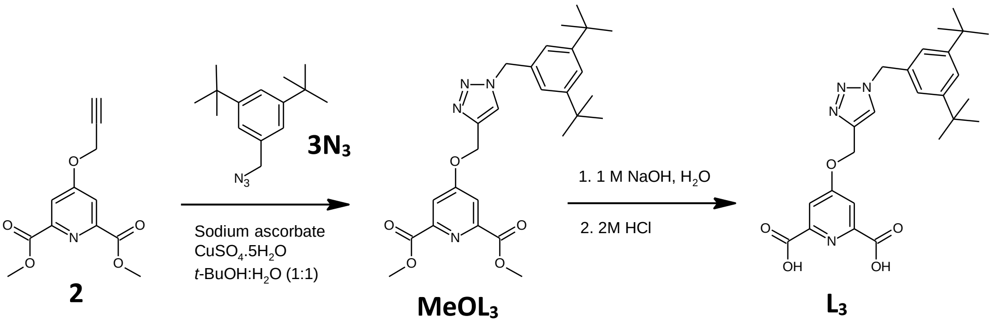

Figure 66. General reaction scheme for the synthesis of L_3

L_3 could be synthesized through a multi-step procedure that was almost identical as that used for **L_2** (Fig. 66). The first part involved the synthesis of 1-(azidomethyl)-3,5-di-*tert*-butylbenzene (**$3N_3$**) which involved stirring 3,5-di-*tert*-butylbenzyl bromide in 3 equivalents of NaN_3 in DMF at room temperature overnight.[259] Next, as for **L_2**, the CuAAC reaction was carried out using the standard conditions such that 1 equivalent of **2** and sodium ascorbate were combined with 0.05 equivalents of $CuSO_4 \cdot 5H_2O$ and a slight excess of **$3N_3$** (1.05 equivalents) and suspended in a 1:1 *tert*-Butanol:H_2O solvent mixture forming a yellow reaction mixture (Fig. 66). On stirring this reaction mixture at 60 ˚C overnight, a pale orange reaction mixture resulted which on the addition of H_2O encouraged the further precipitation of a solid crude **$MeOL_3$**. To remove remaining copper, the solid was suspended in 0.5 M EDTA/1 M NaOH solution and filtered slowly. After another water wash, **$MeOL_3$** could be isolated as a beige solid in yields of approximately 60 %.

Initially, these click attempts were carried out with 1-(bromomethyl)-3,5-di-*tert*-butylbenzene (the bromo-derivative of **$3N_3$**) due to concerns with isolating the potentially explosive azide.[51,56] However, these attempts gave a mixture of products which could not be purified through simple procedures (*i.e.* acetone and water washing). Additionally, the azide-form of the bulky group is required for the AT-CuAAC reaction (the planned method for rotaxane synthesis), thus the azide was isolated as a clear oil and stored in the freezer.

Next, a deprotection reaction was carried out on **MeOL$_3$** to remove the methyl-protecting groups and form **L$_3$** as its dicarboxylic acid. **MeOL$_3$** was suspended in H_2O and 1 M NaOH (4 equivalents) was added to the stirring solution (*i.e.* the saponification method as for **L$_2$** synthesis) (Fig. 66).[25,31,34,35,37,40,41,43,45,46,65-70,72,74] On stirring of the reaction mixture at 50 ˚C over 4 hours, a colour change from pale beige to transparent light-yellow was observed. This change was used as an indication that the methyl groups had been cleaved off as, under the basic conditions used, the resulting **L$_3$** would exist in its negatively charged deprotonated form, soluble in the aqueous reaction mixture. On the addition of hydrochloric acid (2 M), a white solid precipitated which could be filtered off an isolated as the product, **L$_3$**, in yields of approximately 70 %.

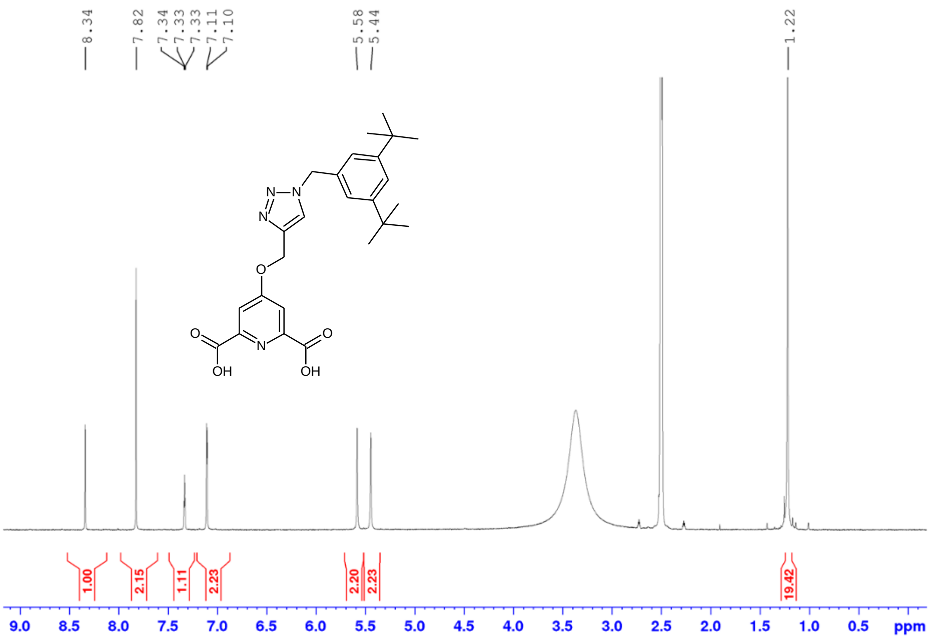

*Figure 67. ^{1}H NMR spectrum of **L$_3$** in DMSO-d$_6$*

The ^{1}H NMR spectrum of **L$_3$** appeared pure, and all peaks could be assigned (Fig. 67). As observed for **L$_2$**, key signs in the ^{1}H NMR spectra of **L$_3$** supported its formation, primarily the removal of the methyl singlet peak at 3.90 ppm in **MeOL$_3$** (Fig. 67). The singlet at 8.34 ppm was assigned to the triazole hydrogen, being of a similar shift when compared to that obtained for the

L_2 triazole hydrogen (8.31 ppm) (Fig. 67).[185,186] The singlet peak at 7.82 ppm was assigned to the pyridyl hydrogens, consistent with the analogous peaks obtained for **L_1** (7.78 ppm) and **L_2** (7.82 ppm) (Fig. 67). The aromatic *tert*-butyl benzyl protons were observed as a triplet and doublet peak at 7.33 and 7.10 ppm (respectively). Lastly, two singlets at 5.58 and 5.44 ppm could be assigned to the remaining two CH_2 groups, with CH_2^{DT} being at 5.44 ppm and the other linking the triazole to the *tert*-butyl motif (CH_2^{TB}) being at 5.58 ppm.

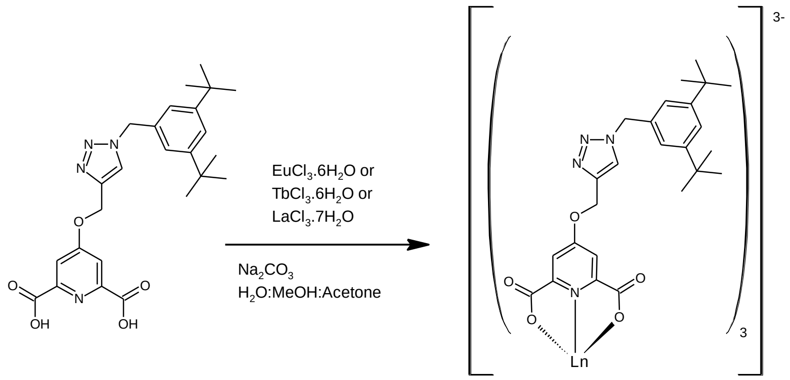

L_3 **$[Ln(L_3)_3]^{3-}$**

Figure 68. Synthesis of $[Ln(L_3)_3]^{3-}$ complexes

Following this, complexation was carried out through dissolving **L_3** (1 equivalent) and Na_2CO_3 (2 equivalents) in either a 4:2:1 or 3:2:1 H_2O:MeOH:acetone solvent mixture at 80 ˚C, followed by the addition of the respective lanthanide chloride salt (0.33 equivalents) (Fig. 68). This resulted in the precipitation of a white solid which could be isolated as the desired **$[Ln(L_3)_3]^{3-}$** complex in 60 – 85 % yield.

As for **$[Ln(L_1)_3]^{3-}$** and **$[Ln(L_2)_3]^{3-}$**, the NMR spectra of **$[Ln(L_3)_3]^{3-}$** was obtained in DMSO-*d*$_6$ despite the competitive binding nature of this NMR solvent.

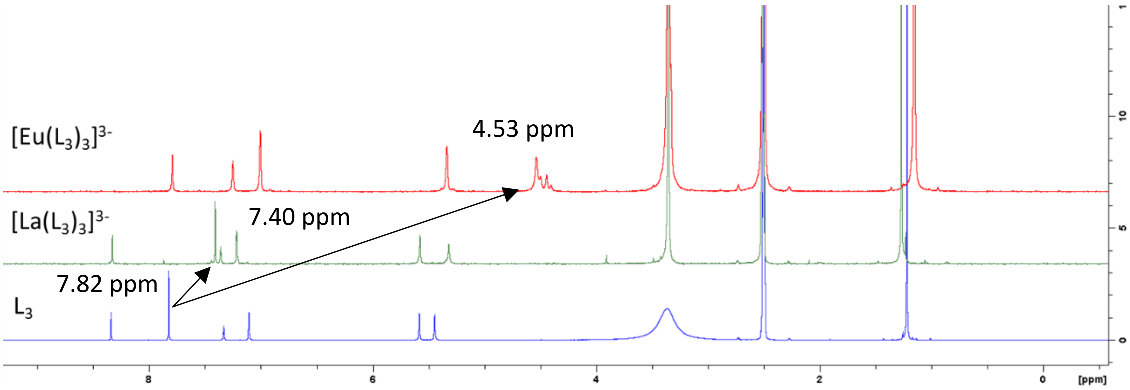

Figure 69. ^{1}H NMR spectra comparing $[Eu(L_3)_3]^{3-}$ (red, top), $[La(L_3)_3]^{3-}$ (green, middle) and L_3 (blue, bottom) in DMSO-d_6

Peaks belonging to hydrogen atoms on the distal *tert*-butyl benzyl group were only shifted by small amounts (Fig. 69). The doublet at 7.10 ppm in the ^{1}H NMR spectrum of **L_3** (assigned to 2,6-protons of the *tert*-butyl benzyl group) was shifted down-field to 7.20 ppm in **$[La(L_3)_3]^{3-}$** however in **$[Eu(L_3)_3]^{3-}$** it was shifted up-field to 7.01 ppm. The triplet at 7.33 ppm in the ^{1}H NMR spectrum of **L_3** (assigned to the 4-proton of the *tert*-butyl benzyl group) was shifted downfield to 7.35 ppm in **$[La(L_3)_3]^{3-}$** however in **$[Eu(L_3)_3]^{3-}$** it was shifted up-field to 7.25 ppm. The singlet at 1.22 ppm in **L_3** (assigned to the methyl groups of the *tert*-butyl motif) was shifted downfield to 1.26 ppm in **$[La(L_3)_3]^{3-}$** and up-field to 1.15 ppm in **$[Eu(L_3)_3]^{3-}$**. The singlet peak observed at 5.58 ppm in **L_3** (assigned to CH_2^{TB}) was shifted up-field to 5.57 ppm in **$[La(L_3)_3]^{3-}$** and to 5.33 ppm in **$[Eu(L_3)_3]^{3-}$**.

Table 6. Summary of the main shifts observed on the complexation of L_3 to La^{3+} and Eu^{3+}

	δ (ppm)			Δδ (ppm)	
Proton type	**L_3**	**$[La(L_3)_3]^{3-}$**	**$[Eu(L_3)_3]^{3-}$**	**$\delta L_3 - \delta[La(L_3)_3]^{3-}$**	**$\delta L_3 - \delta[Eu(L_3)_3]^{3-}$**
Triazole	8.34	8.32	7.79	0.02	0.55
CH_2^{DT}	5.33	5.31	4.44	0.02	0.89
Pyridyl	7.82	7.40	4.53	0.42	3.29

The last peaks to be assigned were those which in **[Ln(L$_1$)$_3$]$^{3-}$** and **[Ln(L$_2$)$_3$]$^{3-}$** also experienced the largest Ln^{3+} induced shifts. The peak corresponding to the triazole hydrogen was observed as a singlet at 8.34 ppm in **L$_3$**, being similar to that obtained for the triazole hydrogen in **L$_2$** (8.31 ppm). This peak was shifted up-field to 8.32 ppm in **[La(L$_3$)$_3$]$^{3-}$** ($\Delta\delta$ of 0.02 ppm) and further to 7.79 in **[Eu(L$_3$)$_3$]$^{3-}$** ($\Delta\delta$ of 0.55 ppm) (supported by the COSY spectra), being similar to those values obtained for the triazole proton in **[La(L$_2$)$_3$]$^{3-}$** and **[Eu(L$_2$)$_3$]$^{3-}$** of 8.26 and 7.74 ppm (respectfully).[189]

The CH$_2^{DT}$ protons, observed as a singlet at 5.33 ppm in **L$_3$**, were shifted up-field to 5.31 ppm in **[La(L$_3$)$_3$]$^{3-}$** ($\Delta\delta$ of 0.02 ppm). As observed for **[Eu(L$_2$)$_3$]$^{3-}$**, this same CH$_2^{DT}$ peak was appearing as a multiplet at approximately 4.44 ppm in the ^{1}H NMR spectrum of **[Eu(L$_3$)$_3$]$^{3-}$** ($\Delta\delta$ of 0.89 ppm), experiencing a similar shift when compared to its **[Ln(L$_2$)$_3$]$^{3-}$** derivative (with a $\Delta\delta$ of 0.99 ppm) (Table 6). In the COSY spectrum of **[Eu(L$_3$)$_3$]$^{3-}$**, this multiplet appeared to show similar coupling with the triazole hydrogen, expected for the CH$_2^{DT}$ hydrogens, with splitting being accounted for by motions on the NMR time scale associated with Eu^{3+} complexation (Fig. 145 and Fig. 146).[188]

The peak corresponding to the pyridyl hydrogen atoms was assigned to the singlet at 7.82 ppm in **L$_3$** and experienced a relatively large up-field shift to 7.40 ppm in **[La(L$_3$)$_3$]$^{3-}$** ($\Delta\delta$ value of 0.42 ppm) (Fig. 69). In **[Eu(L$_3$)$_3$]$^{3-}$**, this pyridyl peak (based off analogous results obtained for **[Eu(L$_2$)$_3$]$^{3-}$**) could be assigned to the singlet observed at 4.53 ppm (with a $\Delta\delta$ of 3.29 ppm) (Fig. 69). Thus, the pyridyl, CH$_2^{DT}$ and triazole protons showed the same pattern as observed for **[Eu(L$_2$)$_3$]$^{3-}$** such that the protons situated at further distances from the Eu^{3+} experience smaller shifts on complexation (Table 6).

The same large up-field shifting observed for the pyridyl carbon atoms in the ^{13}C DEPT spectrum of **[Eu(L$_2$)$_3$]$^{3-}$** was also observed for **[Eu(L$_3$)$_3$]$^{3-}$**, being shifted from 113.7 ppm in **L$_3$** to 65.1 ppm in **[Eu(L$_3$)$_3$]$^{3-}$** (a $\Delta\delta$ of 48.6 ppm compared to 48.2 ppm in **[Eu(L$_2$)$_3$]$^{3-}$**), supporting successful complexation.[35,188,201]

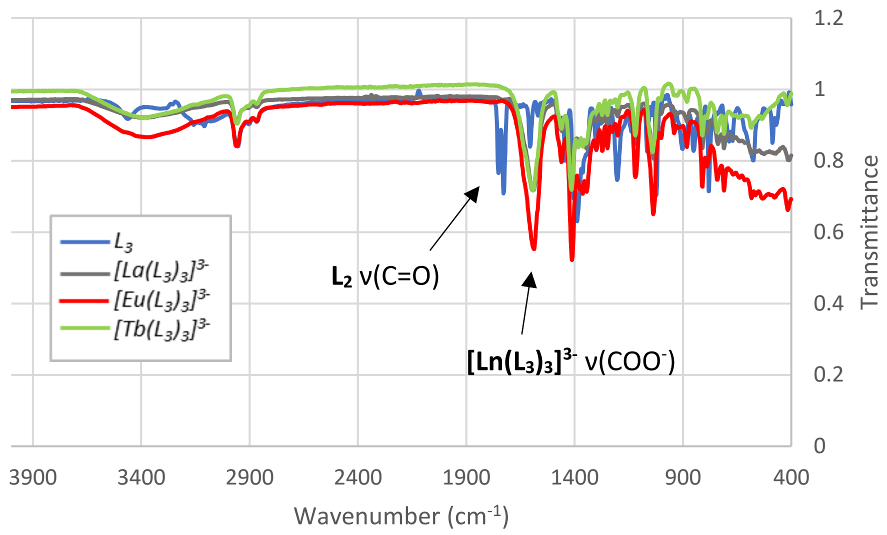

Figure 70. FTIR spectra of L_3 (blue), $[La(L_3)_3]^{3-}$ (grey), $[Eu(L_3)_3]^{3-}$ (red) and $[Tb(L_3)_3]^{3-}$ (green)

As observed for the **$[Ln(L_1)_3]^{3-}$** and **$[Ln(L_2)_3]^{3-}$** complex family, the primary difference between the IR spectra of **L_3** compared to **$[Ln(L_3)_3]^{3-}$** was the removal of the peak corresponding to dicarboxylic acid C=O stretching at 1751 and 1727 cm^{-1}.[40,49,185-187,193,195,197,202-207] This peak appeared to have been removed on Ln^{3+} complexation and replaced by an intense peak corresponding to the COO$^-$ asymmetric stretch at 1593 cm^{-1} for **$[La(L_3)_3]^{3-}$**, 1588 cm^{-1} for **$[Eu(L_3)_3]^{3-}$**, and 1592 cm^{-1} for **$[Tb(L_3)_3]^{3-}$**.[38,40,47,49,185-187,193,199,201,203-206] The broad peak centred at approximately 3109 cm^{-1} (assigned to carboxylic acid O-H stretching) in **L_3** was absent in the IR spectra of **$[Ln(L_3)_3]^{3-}$** (which instead showed broad peaks at approximately 3400 cm^{-1} corresponding to O-H stretching of H_2O), suggesting that **L_3** existed in its carboxylate form in the complexes.[38,187,206] Additionally, sharp peaks at approximately 2867, 2904 and 2953 cm^{-1} in the IR spectrum of **L_3** could be assigned to non-aromatic C-H stretching resulting from the presence of the *tert*-butyl substituent (which were retained on complexation).[187] Another large difference between the IR spectra obtained for **L_3** compared to **$[Ln(L_3)_3]^{3-}$** was observed between 400 – 700 cm^{-1} whereby the overall resolution of the spectra was poor for the complexes when compared to **L_3**.

2.4.2.2 Photophysical properties of [Ln(L$_3$)$_3$]$^{3-}$

The UV/Vis spectrum of **L$_3$** was collected and compared to those of **[La(L$_3$)$_3$]$^{3-}$**, **[Eu(L$_3$)$_3$]$^{3-}$** and **[Tb(L$_3$)$_3$]$^{3-}$** (1 x 10^{-5} M in methanol) (Fig. 71). **L$_3$** appeared to have one main λ_{abs}^{m} at 212 nm with an ε of 37,975.7 L mol^{-1} cm^{-1}, containing a shoulder in the 274 nm range (Fig. 71). In comparison, **[La(L$_3$)$_3$]$^{3-}$**, **[Eu(L$_3$)$_3$]$^{3-}$**, and **[Tb(L$_3$)$_3$]$^{3-}$** were all found to have λ_{abs}^{m} at 210 nm (thus experiencing a slightly hypsochromic shift on complexation).[187] These peaks were assigned to the pyridyl n → π* and carbonyl π → π* transitions, as observed in the literature.[31,33,40,41,45,47,71,74,185,186,187,193-196,201,207,208,210] Additionally, as observed for **[Ln(L$_1$)$_3$]$^{3-}$**, there was large increase observed in the ε values on complexation to the respective lanthanide ion. With much larger ε values, averaging as 118,062.3 L mol^{-1}, being three times higher compared to that obtained for **L$_3$**, indicative of the formation of a 3:1 ligand:Ln^{3+} complex (Fig. 71).[32,40,41,185,186,192,201,207,208]

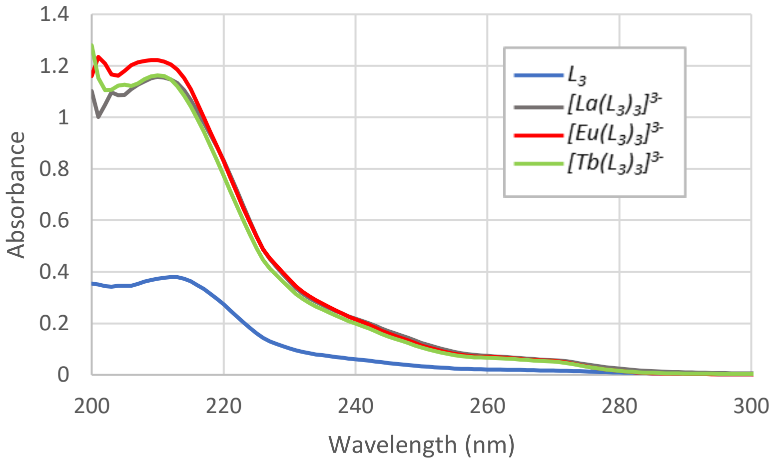

Figure 71. UV/Vis spectra of L$_3$ (blue), [La(L$_3$)$_3$]$^{3-}$ (grey), [Eu(L$_3$)$_3$]$^{3-}$ (red) and [Tb(L$_3$)$_3$]$^{3-}$ (green) (1 x 10^{-5} M) in MeOH

Under a standard lab short wave (254 nm) UV lamp, **$[Eu(L_3)_3]^{3-}$** in methanol (1 x 10^{-5} M) appeared bright red in colour whereas **$[Tb(L_3)_3]^{3-}$** was bright green suggesting that **L_3** was successfully sensitizing both Eu^{3+} and Tb^{3+} luminescence (Fig. 72). The photophysical properties of these luminescent complexes were studied further through fluorescence, phosphorescence, and lifetime measurements (1 x 10^{-5} M in methanol).

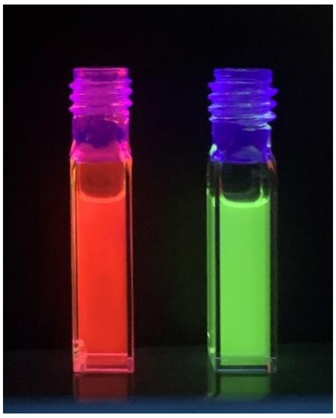

Figure 72. $[Eu(L_3)_3]^{3-}$ (left) and $[Tb(L_3)_3]^{3-}$ (right) in MeOH under short wave UV light (254 nm)

The fluorescence excitation spectrum of **$[Eu(L_3)_3]^{3-}$** (at 614 nm) was dominated by one main peak spanning between 200 – 300 nm with λ_{ex}^{m} of 226 nm along with a shoulder at 274 nm, expected for DPA-based excitation.[32,34,37,39,40,42-47,50,65,67-69,71,72,74,75,184,196,204,229,235] Thus, overall the excitation spectra of **$[Ln(L_1)_3]^{3-}$** compared to both **$[Ln(L_2)_3]^{3-}$** and **$[Ln(L_3)_3]^{3-}$** did not change much despite the inclusion of the triazole group and the naphthalimide and *tert*-butyl benzyl substituents (respectfully).[69] Excitation wavelengths have been reported to be lengthened through attaching groups to the 4-pyridyl position that extend the DPA conjugation, however, in **L_2** and **L_3**, this conjugation is hindered by the CH_2 linkers, providing a possible explanation as to why the excitation wavelengths do not differ much between the **$[Ln(L_1)_3]^{3-}$** and **$[Ln(L_{2-3})_3]^{3-}$** complexes.[69] In saying this, the excitation spectrum had similar shape and form when compared to the absorption spectrum, suggestive of **L_3** to Eu^{3+} energy transfer.[71,185,186,195,198,202-204,229]

The fluorescence emission spectrum of **[Eu(L$_3$)$_3$]$^{3-}$** (on excitation at 227 nm) showed peaks characteristic of Eu^{3+} emission from the $^5D_0 \rightarrow {}^7F_J$ transitions at 592, 614, 649 and 693 nm corresponding to transitions to the J=1, 2, 3 and 4 ^7F_J levels (respectively).[28] Excitation of **[Eu(L$_3$)$_3$]$^{3-}$** at 274 nm (corresponding to the shoulder observed in the excitation spectrum) also resulted in characteristic Eu^{3+} emission (Fig. S147). As observed for **[Eu(L$_1$)$_3$]$^{3-}$**, there appeared to be a small peak present at 580 nm corresponding to the $^5D_0 \rightarrow {}^7F_0$ transition in the excitation spectrum of **[Eu(L$_3$)$_3$]$^{3-}$**, supporting the presence of a C$_3$ axis.[26,28,41,162,185,186,188,189,191-193,213]

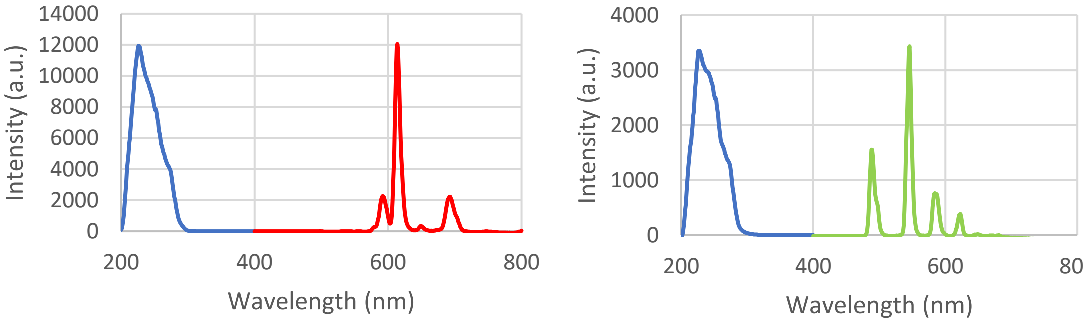

Figure 73. Fluorescence excitation (blue line) (λ_{em} = 614 nm) and emission spectra (red line) (λ_{ex} = 227 nm) of [Eu(L$_3$)$_3$]$^{3-}$ (1 x 10^{-5} M in MeOH). For the fluorescence excitation and emission measurements of [Eu(L$_3$)$_3$]$^{3-}$ (1 x 10^{-5} M in MeOH), excitation and emission slit widths were 3.0 and 5.0 nm (respectively). (Right) Fluorescence excitation (blue line) (λ_{em} = 545 nm) and emission spectra (green line) (λ_{ex} = 227 nm) of [Tb(L$_3$)$_3$]$^{3-}$ (1 x 10^{-5} M in MeOH). For both the fluorescence excitation and emission measurements of [Tb(L$_3$)$_3$]$^{3-}$ (1 x 10^{-5} M in MeOH), excitation and emission slit widths were 3.0 nm

The fluorescence excitation and emission plots of **[Tb(L$_3$)$_3$]$^{3-}$** were also collected. The fluorescence excitation plot (at 545 nm) resembled that of **[Eu(L$_3$)$_3$]$^{3-}$**, with one main peak with an $\lambda_{ex}{}^{m}$ of 227 nm containing a 274 nm shoulder. Moreover, the excitation plot of **[Tb(L$_3$)$_3$]$^{3-}$** also resembled its corresponding absorbance spectra supporting successful sensitization of Tb^{3+} from **L$_3$**.[71,185,186,195,198,202-204,229] The fluorescence emission spectrum of **[Tb(L$_3$)$_3$]$^{3-}$** on excitation at 227 nm showed peaks characteristic of Tb^{3+} emission stemming from the $^5D_4 \rightarrow {}^7F_J$ transitions at 489, 546, 584, 623 and 649 nm corresponding to the J=6, 5, 4, 3 and 2 ^7F_J levels (respectively).[28] Moreover, excitation of **[Tb(L$_3$)$_3$]$^{3-}$** at 274 nm also gave rise to characteristic Tb^{3+} emission (Fig. S156).

The lifetimes of **[Eu(L$_3$)$_3$]$^{3-}$** and **[Tb(L$_3$)$_3$]$^{3-}$** on excitation at 230 and 229 nm (respectively) in MeOH were best fit to double exponential decay curves. For **[Eu(L$_3$)$_3$]$^{3-}$**, the lifetime calculated for the longer emitting species was 1.906 ms, whereas for the shorter emitting species it was 0.631 ms. For **[Tb(L$_3$)$_3$]$^{3-}$**, the lifetime calculated for the longer emitting species was 1.683 ms, whereas for the shorter emitting species was 0.622 ms. Additionally, the phosphorescence emission spectrum of both **[Eu(L$_3$)$_3$]$^{3-}$** and **[Tb(L$_3$)$_3$]$^{3-}$** on excitation at 274 nm showed sharp emission bands characteristic of Eu^{3+} and Tb^{3+} (respectively) (Fig. S149 and Fig. S158).[28]

2.4.3 Anthracene ligand (L$_4$) and complex Ln(L$_4$)$_3$

2.4.3.1 Synthesis and characterisation

Next, the ability of clicking an anthracene motif to the 4-pyridyl position was explored. This group was chosen for two key reasons, the first being its bulky nature, thus inherent ability to potentially act as a stopper group for **M$_1$** and the second being its possible ability to interact with singlet oxygen.[260-262]

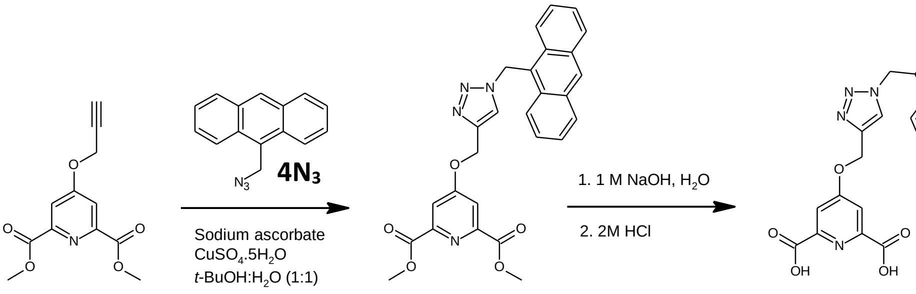

2 **MeOL$_4$** **L$_4$**

Figure 74. General reaction scheme for the synthesis of L$_4$

As for the synthesis of **L$_2$** and **L$_3$**, the key step involved in the synthesis of **L$_4$** was a CuAAC click reaction between **2** and 9-(azidomethyl)-anthracene (**4N$_3$**) to generate the methyl-protected form of **L$_4$**, **MeOL$_4$** (Fig. 74). In saying this, **4N$_3$** was synthesized in two steps from 9-anthracenemethanol.[263] In the first step, 9-anthracenemethanol was converted to its 9-(bromomethyl)- anthracene derivative using phosphorus tribromide.[263] Next, **4N$_3$** was synthesized by stirring 9-(bromomethyl)-anthracene with sodium azide in DMSO whereby it could be isolated as a yellow solid in 66 % yield.[264]

Initially, a slightly different solvent system was planned to be used based off literature studies reported click reactions with azido-anthracene derivatives.[265] In saying this, as an attempt to develop a single method for the synthesis of the **L_2** – **L_4**, the click reaction was first attempted using the standard conditions as used for **$MeOL_2$** and **$MeOL_3$** synthesis, with the 1:1 *tert*-Butanol:H_2O solvent mixture (Fig. 74). This method appeared to work (despite a relatively low yield possibly due to competitive binding with copper) with reasonable reaction times, thus was used throughout for the synthesis of **$MeOL_4$**.[66,72] As for **$MeOL_2$** and **$MeOL_3$**, all solids used in the click reactions were combined, suspended in the solvent mixture, and stirred at 60 ˚C overnight after which on the addition of water, the crude solid **$MeOL_4$** precipitated out which could be further purified.

To synthesise **L_4**, a deprotection reaction was carried out by stirring **$MeOL_4$** in water in the presence of 1 M NaOH (4 equivalents).[25,31,34,35,37,40,41,43,45,46,65-70,72,74] The pale orange reaction mixture was stirred at 50 ˚C overnight followed by 80 ˚C for a further 3 hours after which the reaction mixture appeared slightly more transparent, suggesting the formation of the aqueous soluble, negatively charged carboxylic acid. On the addition of 2 M HCl, a yellow/orange solid precipitate was formed which was isolated as the product, **L_4**.

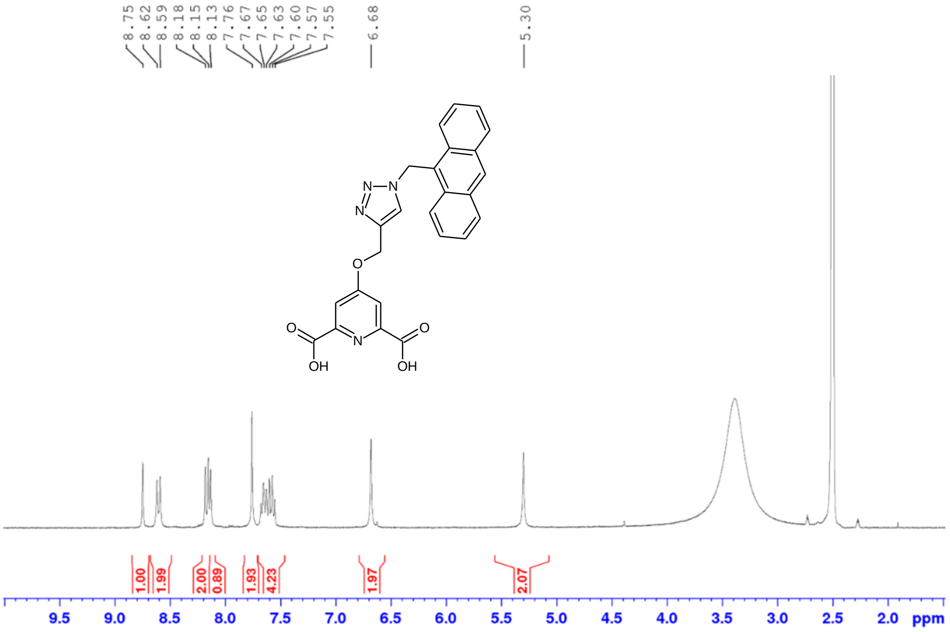

Figure 75. ^1H NMR spectrum of L_4 in DMSO-d_6

All peaks in the ^{1}H NMR spectrum of **L_4** could be assigned and the major indication of a successful **$MeOL_4$** deprotection, the removal of the singlet peak at 3.87 ppm in **$MeOL_4$** (corresponding to the methyl protecting groups), was observed (Fig. 75).[185] The aromatic anthracene hydrogens were assigned to the singlet at 8.75 ppm, the doublets at 8.59 and 8.15 ppm and the doublet of triplets at 7.61 ppm (Fig. 75). The singlet peak at 8.13 ppm was assigned to the triazole proton, being similar to that obtained for **L_2** (8.31 ppm) and **L_3** (8.34 ppm).[185] The singlet peak corresponding to the pyridyl hydrogens was observed at 7.76 ppm (compared to 7.82 ppm for **L_2** and **L_3**). Lastly, the peaks corresponding to the CH_2 linkers were observed as singlets at 6.68 and 5.30 ppm (Fig. 75). The more de-shielded singlet at 6.68 ppm was assigned to the CH_2 protons situated between the triazole and the anthracene motif (CH_2^{TA}) whereas the peak at 5.30 ppm was assigned to the CH_2^{DT} protons.

To synthesize **$[Ln(L_4)_3]^{3-}$** complexes, **L_4** (1 equivalent) and anhydrous sodium carbonate (2 equivalents) were stirred in deionised H_2O (2 mL) at 80 ˚C for approximately 15 minutes. Due to time restraints, only **$[La(L_4)_3]^{3-}$** was synthesized and characterised. On the addition of 0.33 equivalents of lanthanum(III) chloride, the formation of a yellow precipitate was observed. The reaction mixture was stirred at room temperature for an extra hour after which it was diluted with deionised H_2O and the complex was collected by filtration as a pale yellow/beige solid. A ^{1}H NMR spectrum of the solid could be obtained and supported the formation of **$[La(L_4)_3]^{3-}$**.

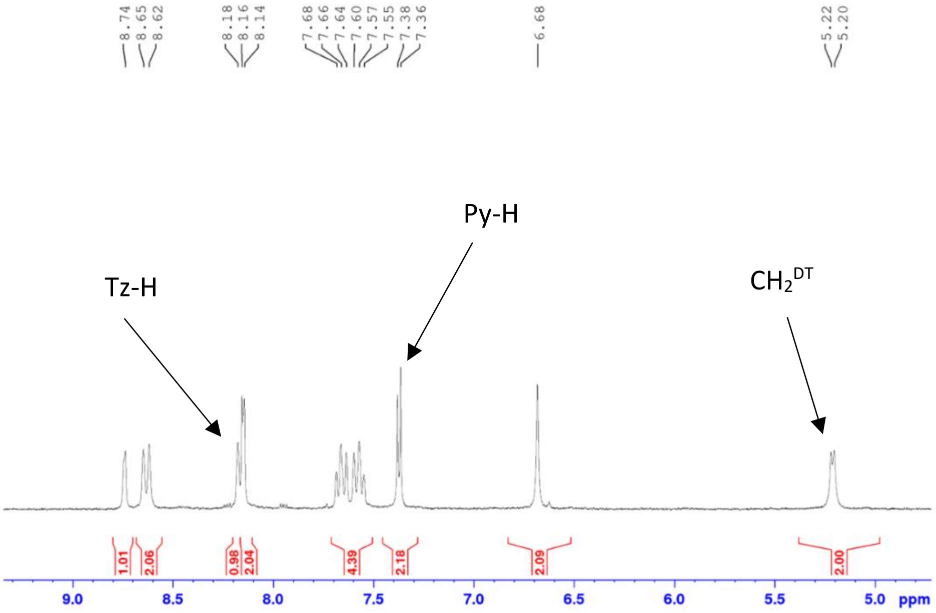

Figure 76. ^1H NMR spectrum of $[La(L_4)_3]^{3-}$ in DMSO

Key signs were observed in the ^1H NMR spectrum of $\mathbf{[La(L_4)_3]^{3-}}$ in DMSO-d_6 which supported $\mathbf{L_4}$ complexation with La^{3+} in a 3:1 $\mathbf{L_4}$:La^{3+} ratio (Fig. 76). Although only small shifts were observed for the aromatic anthracene hydrogens of $\mathbf{[La(L_4)_3]^{3-}}$ when compared to $\mathbf{L_4}$, the peaks assigned to the pyridyl and CH_2^{DT} protons were significantly affected by La^{3+} complexation (Fig. 76). This was expected based off previous results showing that these protons, situated closest to the La^{3+} centre, experience larger shifts in their NMR spectra on complexation.

The singlet peak at 8.18 ppm in the ^1H NMR spectrum of $\mathbf{[La(L_4)_3]^{3-}}$ was assigned to the triazole hydrogen which had been shifted down-field by 0.05 ppm when compared to $\mathbf{L_4}$ (Fig. 76). The doublet at 7.36 ppm was assigned to the pyridyl hydrogens as this peak was in the expected range based off the analogous $\mathbf{[La(L_2)_3]^{3-}}$ and $\mathbf{[La(L_3)_3]^{3-}}$ complexes with pyridyl hydrogen shifts of 7.42 and 7.40 ppm (respectively). In saying this, a key difference was observed when compared to $\mathbf{[La(L_2)_3]^{3-}}$ and $\mathbf{[La(L_3)_3]^{3-}}$ complexes such that the pyridyl peak was experiencing splitting into a doublet. There was also a doublet at 5.20 ppm, in the range expected for the CH_2^{DT} protons which had not been observed for $\mathbf{L_2}$ or $\mathbf{L_3}$ on La^{3+} complexation. Thus, although the shifts were in the range expected for La^{3+} complexation, the splitting was unexpected. This was predicted to be due to dynamics occurring on the NMR time scale causing these protons to experience different environments which has been observed for DPA ligands with different lanthanides.[188,207,208,254] Despite this splitting, complexation in the 3:1 $\mathbf{L_4}$:La^{3+} ratio was predicted to be successful as only one signal was showing for the triazole hydrogen and aromatic anthracene hydrogens, which would not be the case if the splitting of the CH_2^{DT} and pyridyl protons was due to the presence of other 1:1 or 2:1 species.

Due to time constraints, $\mathbf{L_4}$ complexation was only attempted with Eu^{3+}. In the ^1H NMR spectrum of the crude $\mathbf{[Eu(L_4)_3]^{3-}}$ complex, the similar pyridyl and CH_2 shifts and splittings as was observed for $\mathbf{[Eu(L_2)_3]^{3-}}$ and $\mathbf{[Eu(L_3)_3]^{3-}}$ was seen and the peaks were shifted compared to free $\mathbf{L_4}$, indicative of successful complexation (Fig. S189 and Fig. S190). However, there appeared to be impurities remaining in the reaction mixture which was not purified due to time constraints. Interestingly, the crude mixture under short wave UV light did not show the same bright red emission as $\mathbf{[Eu(L_{1-3})_3]^{3-}}$ complexes suggesting that the anthracene may quench Eu^{3+} emission or that ACQ processes may be active however further studies are required to confirm this.[221,222,239-241,243,245]

2.5 Post-complexation modification method

To perform AT-CuAAC reactions on the $\mathbf{[Ln(L_1)_3]^{3-}}$ complex family, it was important to carry out a proof-of-concept study to prove that reactions can be carried out on these complexes in the presence of copper, despite competitive binding. Moreover, developing a method for clicking to $\mathbf{[Ln(L_1)_3]^{3-}}$ complexes, would provide a modular way to functionalize the 4-pyridyl position of DPA complexes for the synthesis of new complexes with a range of different applications.

2.5.1 Clicking of the naphthalimide group to $[Ln(L_1)_3]^{3-}$

2.5.1.1 Lanthanum complex $[La(L_2{}^*)_3]^{3-}$

The CuAAC reaction was first carried out on **$[La(L_1)_3]^{3-}$** with **$2N_3$** so that any successfully clicked material could be identified via ^{1}H NMR spectroscopy (Fig. 77). Similar CuAAC reaction conditions to those used for the synthesis of **$MeOL_2$**, **$MeOL_3$** and **$MeOL_4$** were applied, however all equivalents (apart from that of **$[La(L_1)_3]^{3-}$**) were multiplied by three to achieve stoichiometric amounts of reactants. Thus, 1 equivalent of **$[La(L_1)_3]^{3-}$** was combined with 3 equivalents of sodium ascorbate, 3.15 equivalents of **$2N_3$** and 0.15 equivalents of $CuSO_4 \cdot 5H_2O$. The solids were combined, suspended in the 1:1 *tert*-Butanol:H_2O (17.5 mL) solvent mixture and the resulting pale yellow reaction mixture was stirred at approximately 80 ˚C for 12 hours. After 12 hours, the reaction mixture appeared transparent and yellow in colour which went cloudy as it cooled to room temperature. The addition on H_2O further encouraged precipitation. The reaction mixture was then washed with diethyl ether to remove any unreacted **$2N_3$**. After an NMR of the crude solid remaining in the aqueous layer on the removal of the H_2O revealed impurities, the aqueous solid was resuspended in deionised H_2O, heated, filtered whilst warm, and a solid precipitate was collected. After stirring this precipitate in diethyl ether, the product, **$[La(L_2{}^*)_3]^{3-}$** (with * indicating that the ligand was made via the post-complex modification), could be obtained by filtration (in very small yields).

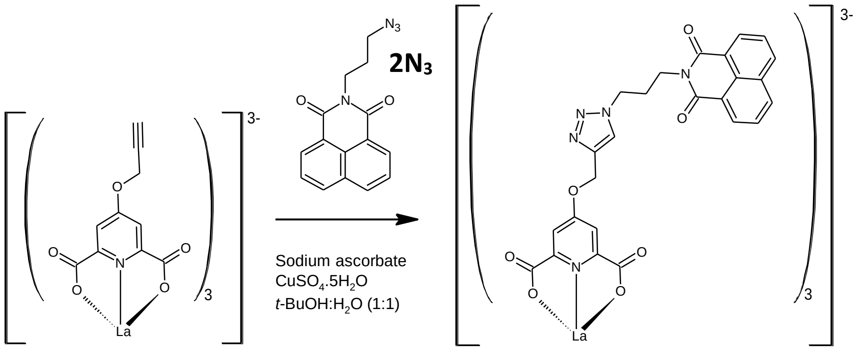

$[La(L_1)_3]^{3-}$ **$[La(L_2{}^*)_3]^{3-}$**

Figure 77. Proposed reaction scheme for the synthesis of $[La(L_2{}^*)_3]^{3-}$

In the ^{1}H NMR spectrum of **$[La(L_2*)_3]^{3-}$** was collected in DMSO-d_6. A comparison of the ^{1}H NMR spectrum obtained for **$[La(L_2)_3]^{3-}$** (made through the preformed ligand method) compared to that obtained via the post-complexation modification method (**$[La(L_2*)_3]^{3-}$**) is shown in Fig. 78. Since the final product should be the same, irrespective of the method used, for the post-complexation modification method to have worked, both spectra should be the same, which was observed (with slight differences discussed below).

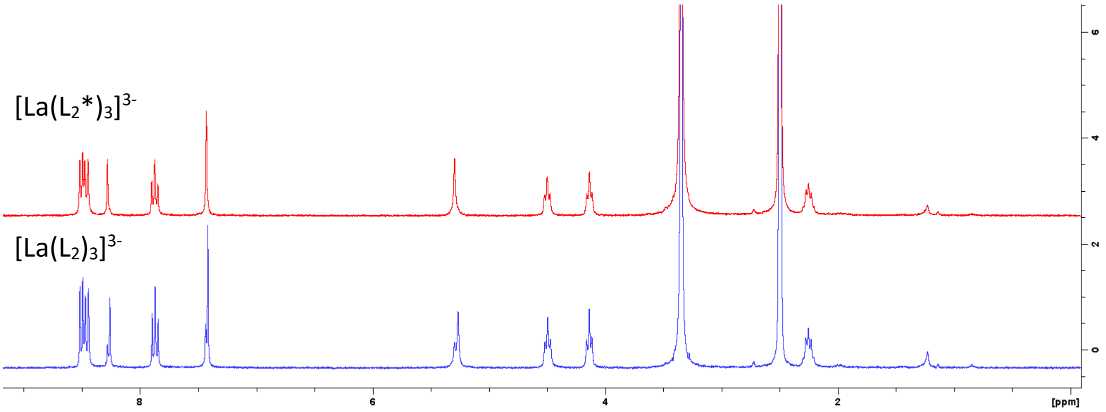

Figure 78. ^{1}H NMR spectrum of $[La(L_2*)_3]^{3-}$ (made via the post-complexation modification method) (red, top) compared to $[La(L_2)_3]^{3-}$ (made via the preformed ligand method) (blue, bottom)

The doublet of doublets at approximately 8.49 ppm, assigned to four aromatic naphthalimide protons in **$[La(L_2*)_3]^{3-}$**, were observed at almost identical shifts compared to those obtained for **$[La(L_2)_3]^{3-}$** (appearing at 8.48 ppm) (Fig. 78). The triplet peak at 7.87 ppm in the ^{1}H NMR spectrum of **$[La(L_2*)_3]^{3-}$** lined up perfectly with that obtained for **$[La(L_2)_3]^{3-}$** (7.87 ppm), assigned to the remaining two aromatic naphthalimide protons (Fig. 78). The alkyl peaks situated between the naphthalimide and triazole motifs also showed identical shifts (and splitting) between complexes, being at 4.50 ppm (triplet), 4.14 ppm (triplet), and 2.25 ppm (quintet) in both **$[La(L_2*)_3]^{3-}$** and **$[La(L_2)_3]^{3-}$** (Fig. 78).

When comparing the shifts (and splitting) of the peaks corresponding to the hydrogen atoms observed to be most impacted by complexation (*i.e.* triazole, CH_2^{DT} and pyridyl), only slight differences were observed (Fig. 78). Interestingly, the sub-peaks that were observed in the ^{1}H

NMR spectrum of the **[La(L$_2$)$_3$]$^{3-}$** complex for the triazole, CH$_2^{DT}$ and pyridyl hydrogens (which were attributed to exchange processes) were not observed. However, in all cases, the peaks corresponding to the triazole, CH$_2^{DT}$ and pyridyl hydrogens in the ^{1}H NMR spectrum of **[La(L$_2$*)$_3$]$^{3-}$** lined up better with the sub-peaks observed for the corresponding hydrogen atoms in the ^{1}H NMR spectrum of **[La(L$_2$)$_3$]$^{3-}$** (Fig. 78). For instance, the singlet peak corresponding to the triazole hydrogen was observed at 8.29 ppm in **[La(L$_2$*)$_3$]$^{3-}$** compared to 8.27 ppm (for the main peak) and 8.28 ppm (for the sub-peak) in **[La(L$_2$)$_3$]$^{3-}$**. Similar results were found for the CH$_2^{DT}$ and pyridyl peaks, being observed at 5.30 and 7.43 ppm (respectively) in **[La(L$_2$*)$_3$]$^{3-}$** compared to 5.27 ppm (with a sub-peak of 5.30 ppm) and 7.42 ppm (with a sub-peak at 7.44) for the CH$_2^{DT}$ and pyridyl peaks (respectively) in **[La(L$_2$)$_3$]$^{3-}$**.

The ^{13}C DEPT spectra of **[La(L$_2$*)$_3$]$^{3-}$** compared to **[La(L$_2$)$_3$]$^{3-}$** also suggested that a successful click reaction had occurred between **[La(L$_1$)$_3$]$^{3-}$** and **2N$_3$** as the shifts observed were either the same or differed by only 0.1 ppm (Fig. 79).

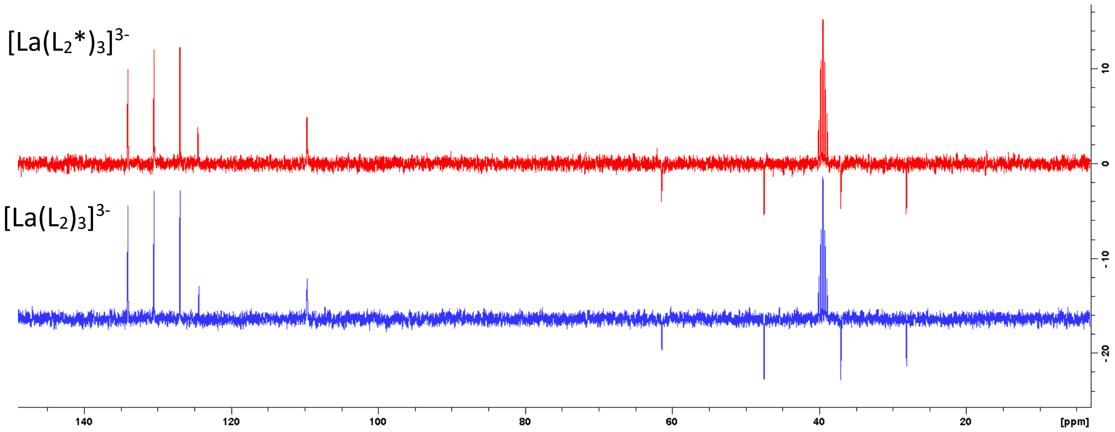

Figure 79. ^{13}C DEPT spectrum of [La(L$_2$)$_3$]$^{3-}$ (made via the post-complexation modification method) (red, top) compared to [La(L$_2$)$_3$]$^{3-}$ (made via the preformed ligand method) (blue, bottom)*

In comparing the IR spectra obtained for **[La(L$_2$*)$_3$]$^{3-}$** compared to **[La(L$_2$)$_3$]$^{3-}$** all stretches were almost identical (within experimental error) (Fig. 80). For instance, the peaks at 1587 and 1345 cm^{-1} corresponding to the COO$^-$ asymmetric and symmetric stretches (respectively) in **[La(L$_2$*)$_3$]$^{3-}$** were observed at 1586 and 1347 cm^{-1} (respectively) in the IR spectrum of **[La(L$_2$)$_3$]$^{3-}$** (Fig. 80).[40,47,49,185-187,193,199,201,203-206] The broad bands observed at 3378 cm^{-1} for **[La(L$_2$)$_3$]$^{3-}$** and

3380 cm^{-1} for **$[La(L_2*)_3]^{3-}$** indicated the presence of H_2O remaining in the complexes (Fig. 80).[187,218]

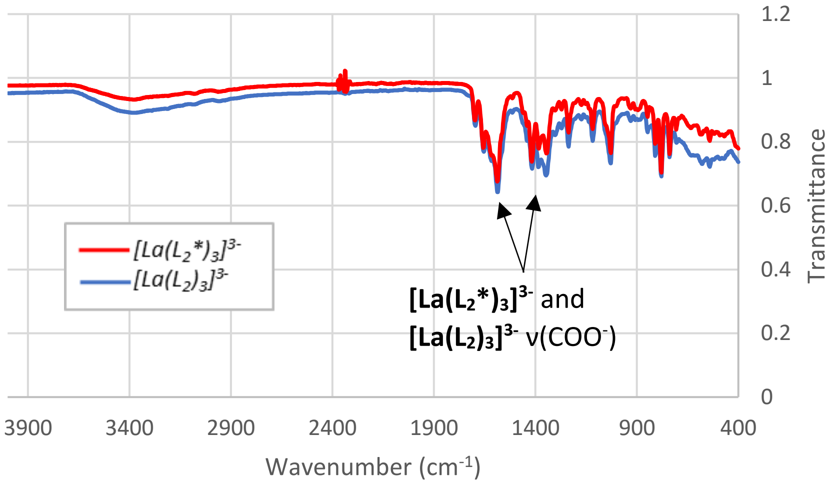

Figure 80. FTIR spectrum of $[La(L_2*)_3]^{3-}$ (red) compared to $[La(L_2)_3]^{3-}$

With preliminary studies suggesting that a click reaction had occurred between **$[La(L_1)_3]^{3-}$** and **$2N_3$** without decomplexation, we next chose to investigate the ability of carrying out the same reactions with emissive **$[Eu(L_1)_3]^{3-}$** and **$[Tb(L_1)_3]^{3-}$** complexes.

2.5.1.2 Europium complex $[Eu(L_2*)_3]^{3-}$

In carrying out the same reactions with **$[Eu(L_1)_3]^{3-}$** and **$[Tb(L_1)_3]^{3-}$**, the same conditions for the CuAAC reaction were used as those that were used for **$[La(L_1)_3]^{3-}$**. The reactants were combined, suspended in a 1:1 *tert*-Butanol:H_2O solvent mixture and stirred at 80 ˚C overnight. The crude product could be obtained by quenching the reaction mixture with H_2O followed by a wash of this H_2O layer with diethyl ether. On removal of the H_2O under reduced pressure, a brown/orange solid was obtained. An ^{1}H NMR of this solid showed that the CuAAC reaction appeared to work to a very small degree (*i.e.* a singlet peak at 7.73 ppm, similar to that obtained for **$[Eu(L_2)_3]^{3-}$** of 7.74 ppm for the triazole hydrogen, could be observed along with other peaks that were lining up with its preformed ligand method analogue**,** **$[Eu(L_2)_3]^{3-}$**), however the spectrum was contaminated by large amounts of **$2N_3$** and other water-soluble impurities such as copper (causing ^{1}H NMR broadening) (Fig. S114 and Fig. S115). Additionally, under a standard short wave UV lamp, the crude solid appeared to have patches of red-emitting solid which also appeared blue under a standard long-wave UV lamp, showing the dual-emission expected for **$[Eu(L_2)_3]^{3-}$**.

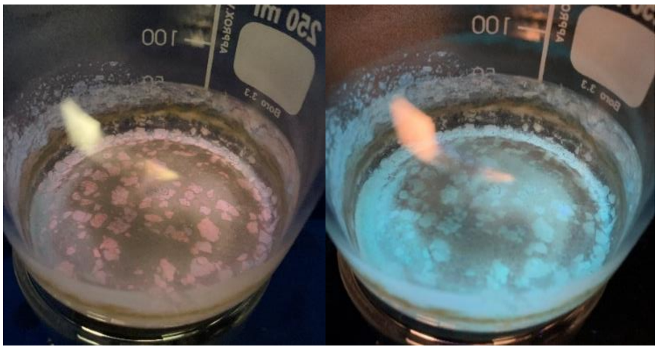

Figure 81. Crude $[Eu(L_2*)_3]^{3-}$ under short wave UV light (left) compared to long-wave UV light (right) showing the dual emission expected for the successful clicking of $2N_3$ to $[Eu(L_1)_3]^{3-}$

However, was a need to separate water-soluble product from unwanted side products. Due to the limited solubility of the complex in solvents other than water (restricting purification methods) and because of the large differences in mass between **$[Eu(L_2*)_3]^{3-}$** and the likely water-soluble impurities (*i.e.* Cu(II) and unreacted **$[Eu(L_1)_3]^{3-}$**), purification was attempted through dialysis, as had been carried out by the Faulkner research group.[87,89-92,101,110,268-271] Dialysis works by selectively allowing molecules of a molar mass smaller than the molecular weight cut-off (MWCO) defined by the membrane lining the dialysis tubing to pass through the membrane through diffusion (Fig. 82 and Fig. S116). The mass of **$Na_3[Eu(L_2*)_3]$** was calculated to be 1719.2 g mol^{-1} and the mass of **$[Eu(L_2*)_3]^{3-}$** (*i.e.* without its associated counter ions) was calculated to be 1650.3 g mol^{-1}. Thus, membranes with a 1000 g mol^{-1} MWCO were used as any water-soluble impurities smaller than this cut-off would be able to diffuse through the membrane, leaving purified **$[Eu(L_2*)_3]^{3-}$** physically restricted to the dialysis tubing (Fig. 82).

To do this, crude **$[Eu(L_2*)_3]^{3-}$** was suspended in H_2O (20 mL) and added into the dialysis tubing (Fig. S116). Next, this tube was placed in a floating rack and suspended in a beaker full of H_2O (Fig. S116). This mixture was left to stir for 2 days at room temperature, with the bulk water being swapped daily (due to the nature of diffusion). After 2 days, the **$[Eu(L_2*)_3]^{3-}$** solution inside the dialysis appeared visibly less yellow, suggesting the removal of Cu(II) (Fig. S116).

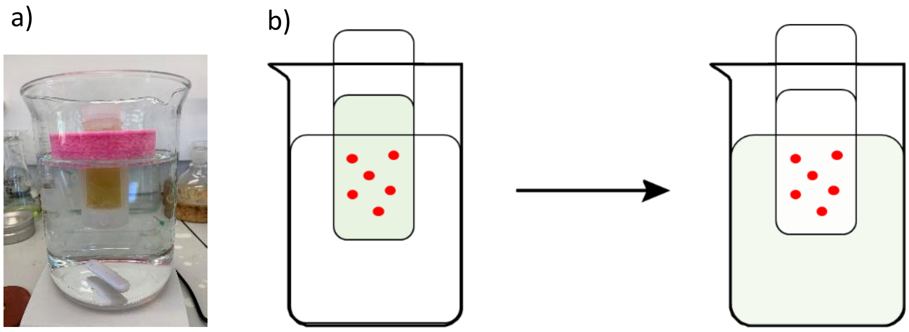

Figure 82. (Left/a) Experimental setup showing crude $[Eu(L_2^*)_3]^{3-}$ *dissolved in deionised* H_2O *(20 mL) within the dialysis tube which was suspended in deionised* H_2O *via a floating rack. (Right/b) Simplified schematic showing the proposed dialysis mechanism for the removal of water-soluble impurities leaving purified* $[Eu(L_2^*)_3]^{3-}$ *(red spots)*

In saying this, an NMR of the solid after removing H_2O gave a broadened spectrum and peaks could not be distinguished suggesting that the dialysis was unsuccessful. This may be due to many reasons, such as the large amount of water causing $\mathbf{[Eu(L_2^*)_3]^{3-}}$ dissociation.

One option for future studies may be to attempt the dialysis with the presence of a Cu(II) chelating agent, such as EDTA, in the bulk solution to encourage the Cu^{2+} out of the reaction mixture within the dialysis tubing.[273] Other methods for aqueous purification such as carrying out an aqueous column or investigating the possibility of using copper-free click reactions to synthesize the complexes may be possible alternative methods of generation more pure $\mathbf{[Eu(L_2^*)_3]^{3-}}$ in aqueous conditions.

2.6 Active template methods

In synthesizing complexes **$[Ln(L_2)_3]^{3-}$**, **$[Ln(L_3)_3]^{3-}$** and **$[Ln(L_4)_3]^{3-}$**, the axle and stopper groups required for the formation of the rotaxane was accomplished meaning that the next step was to incorporate the macrocycle into the click reaction, making it an AT-CuAAC reaction, to develop the quasi-[4]-rotaxane system.[126-129,131,132,134,135,137,142,143,152,154-160]

There are many different macrocycles able to be used in active template reactions including monodentate, bidentate and tridentate macrocycles, all with different outcomes on the reaction making it an important component to consider.[127-132,134,135,137-139,142,143,152,159,160] The macrocycle which was used in this study was Goldup's small 2,2-bipyridine macrocycle, **M_1** (Fig. 83).[131,135,137,152,154-156,158-160] This macrocycle is bidentate in nature (containing two nitrogen atoms belonging to the bipyridine motif), thus binds to copper such that sufficient coordination sites (required for the coordination of the azide and alkyne) are vacant for the AT-CuAAC reaction to occur (Fig. 83).[129,131,135,137,152,154-156,158-160] This is important as some tridentate macrocycles have been found to be incompatible for various AT-CuAAC reactions as they leave insufficient coordination sites on the copper for the AT-CuAAC reaction to occur.[129,131,143]

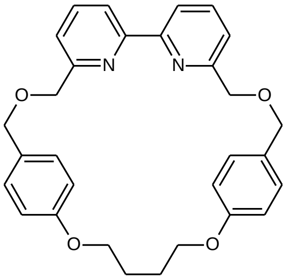

Figure 83. Goldup's small 2,2'-bipyridine macrocycle used for the AT-CuAAC reactions. Image adapted from 152, 160

Studies have also found that macrocycle choice has a large impact on yield and product distribution.[131,133,152,156,159,160] In 2015, Neal and Goldup showed that when using small macrocycles (*i.e.* **M_1**), [2]rotaxanes are the main product formed whereas if the macrocycle size is increased (for instance, through adding CH_2 linkers), different ratios of [2]:[3] rotaxanes are formed.[131,156] In addition to **M_1** being able to form the desired [2]rotaxanes with selectivity over [3]rotaxanes, it has also been reported to form [2]rotaxanes with naphthalimide and *tert*-butyl benzyl stopper groups in close to quantitative yields, further supporting its use.[128,131,133,135,152,154-156,158-160] This is important as that macrocycle and stopper group are highly linked such that if large macrocycles are used, larger stopper groups are required to achieve rotaxane formation whereas if small macrocycles are used, smaller groups are required. In saying this, **M_1** appeared to be suitable for the *tert*-butyl benzyl and naphthalimide stopper groups (it was also predicted to be suitable for the anthracene stopper group due to the bulky nature of anthracene) (Fig. 83).[128,131,133,152,159,160,261,262]

In saying this, to synthesize the target quasi-[4]-rotaxanes from DPA-ligands pre-threaded with the macrocycle, a deprotection step was required for complexation (as for **L_1** – **L_4**). However, there was a concern that this deprotection would lead to macrocycle de-threading as, based off results from the Goldup research group, a bipyridine macrocycle similar to **M_1** was reported to de-thread off its axle when a 2,6-dicarboxyl substituted benzyl motif was used as the stopper group (*i.e.* similar to the DPA motif such that a benzyl group is in place of the pyridine group) (Fig. 84).

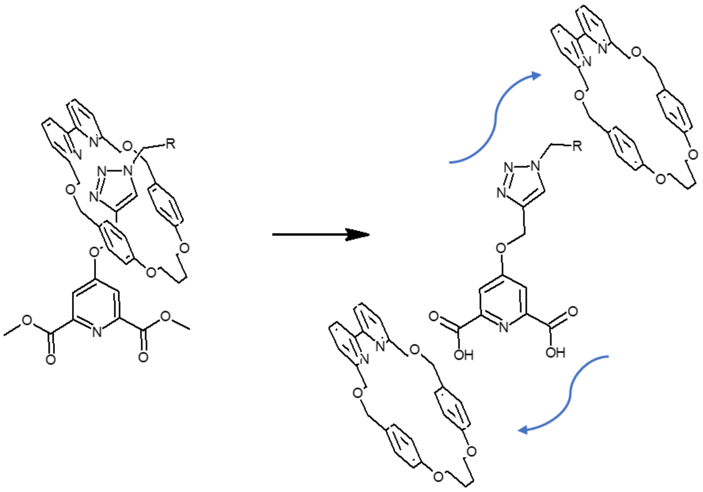

Figure 84. Possible routes for de-threading on deprotection of the DPA chelating group required for Ln^{3+} complexation

In recognising this, a different method for the synthesis of the quasi-[4]-rotaxanes was proposed. With preliminary studies supporting that **$[La(L_1)_3]^{3-}$** remains in its complexed form in the presence of copper, the possibility of performing AT-CuAAC reaction on this complex was proposed. The AT-CuAAC reaction was to be carried out with **$2N_3$**, **$3N_3$** and **$4N_3$** however due to time limitations, initial studies were only carried out on **$2N_3$**. The ability of the naphthalimide group to act as a complete stopper group for **M_1** was met with caution.[152] Whilst some studies had reported the ability of naphthalimides with *N*-substituted ethyl groups to act as a full stoppers for **M_1**, other studies with slightly different axles had reported the de-threading of **M_1** with the same naphthalimide stopper.[152,169] This suggested that whether **M_1** de-threads or not in the presence of a naphthalimide stopper group depends on multiple components including axle flexibility.[152,169] In saying this, there was a high desire to develop this system due to the attractive photophysical properties which may be achieved from the development of such a rotaxane.[152]

2.6.1 AT-CuAAC on $[La(L_1)_3]^{3-}$ complexes (initial attempts)

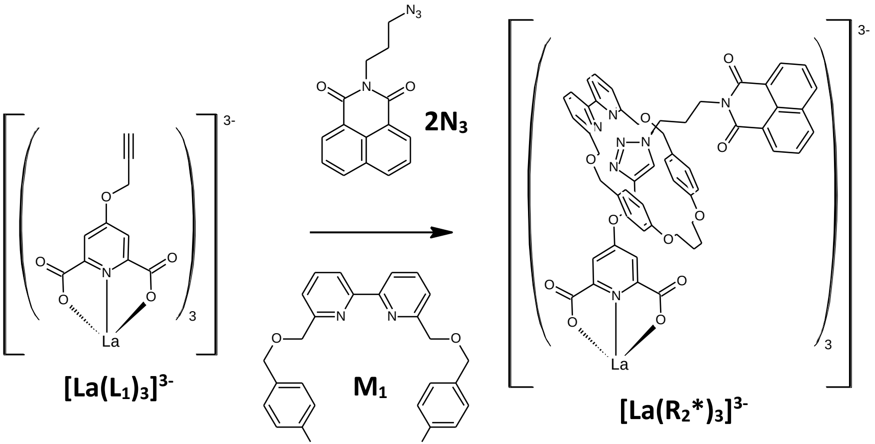

Figure 85. Proposed reaction scheme for the synthesis of $[La(R_2^*)_3]^{3-}$ *through a AT-CuAAC reaction on* $[La(L_1)_3]^{3-}$

With proof-of-concept studies proving that copper does not rip apart $\mathbf{[La(L_1)_3]}^{3-}$, the next goal was to incorporate a macrocycle into the click reactions (thus turning it to an AT-CuAAC) to synthesise quasi-[4]-rotaxane $\mathbf{[La(R_2^*)_3]^{3-}}$. The development of this method was of high interest as it would provide a rapid, adaptable way to synthesise a large family of luminescent lanthanide-based quasi-[4]-rotaxanes (Fig. 85). The first attempt was carried out in a DCM:MeOH solvent mixture (as opposed to the standard 1:1 *tert*-Butanol:H_2O solvent mixture used in all of the click reactions up until this point) and the conditions used were inspired by those published by Goldup's research group in 2011 (Fig. 85) (conditions 1).[152] This solvent mixture was used due to concerns regarding the solubility of $\mathbf{M_1}$ in the *tert*-Butanol:H_2O (1:1) solvent mixture. Accordingly, the copper(I) source was also changed from aqueous soluble $CuSO_4 \cdot 5H_2O$ (and sodium ascorbate) to tetrakis(acetonitrile)copper(I) hexafluorophosphate $[(CH_3CN)_4Cu]PF_6$.

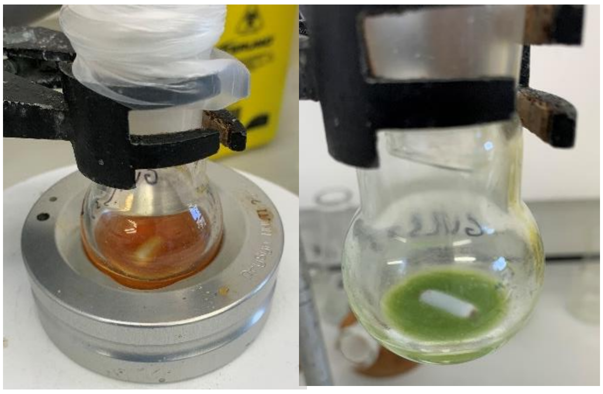

Figure 86. (Left) Reaction mixture before heating using conditions 1, showing the presence of Cu(I). (Right). Reaction mixture after stirring for three days using conditions 1, showing the presence of Cu(II)

The AT-CuAAC reactions were carried out using stoichiometric amounts of reagents. One equivalent of $\mathbf{[La(L_1)_3]^{3-}}$ was combined with approximately three equivalents of $\mathbf{M_1}$, $\mathbf{2N_3}$ and $[(CH_3CN)_4Cu]PF_6$. The solids were suspended in the appropriate volume of a 1:1 dried DCM:MeOH solvent mixture to make up a concentration of 0.01 M with respect to $\mathbf{M_1}$. On the addition of the solvent, the reaction mixture turned bright orange straight away (expected due to the Cu(I) present) and was stirred under nitrogen at 50 ˚C for 1 day after which the heat was turned off and the reaction was stirred for a further two days at room temperature (Fig. 86). After two days, the reaction mixture appeared green in colour (suggesting that the Cu(I) had been oxidised to its Cu(II) form) (Fig. 86). The workup procedure involved extracting the product with DCM and washing with a 0.5 M EDTA/NaOH solution to remove the remaining copper. An orange waxy solid was retrieved which was not blue under short wave UV light.

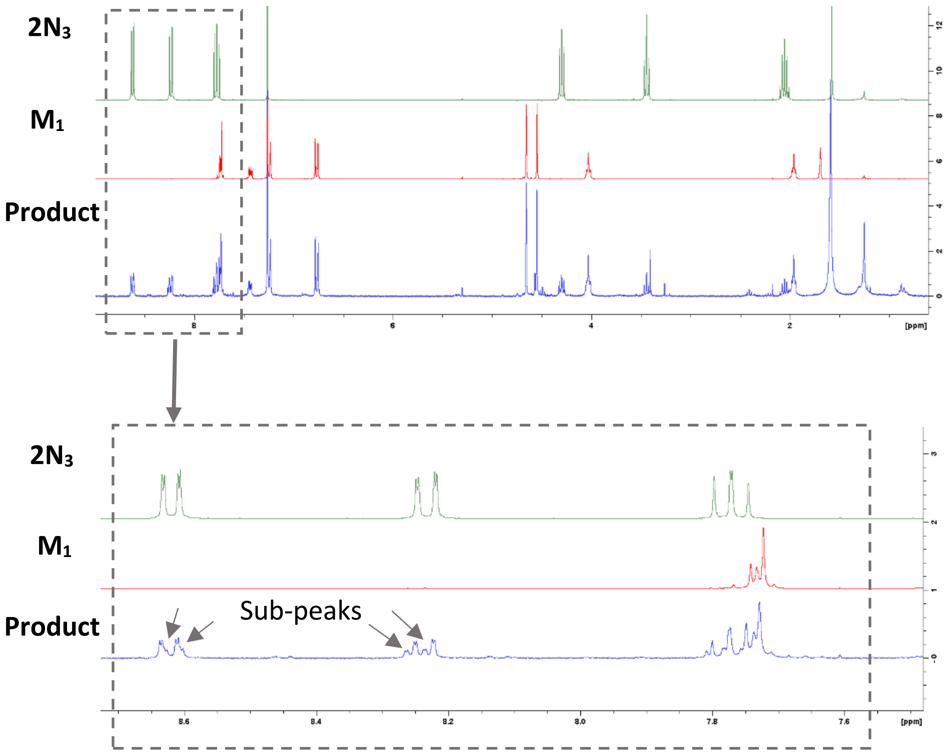

Figure 87. (Top) Full ^{1}H NMR spectra comparing the orange waxy solid product (blue) made using conditions 1, M_1 (red) and $2N_3$ (green) in $CDCl_3$. (Bottom) Zoom in on the aromatic section of the ^{1}H NMR spectra showing the sub-peaks observed for the aromatic naphthalimide protons of the orange waxy solid product

The ^{1}H NMR spectrum of the orange waxy solid was obtained in $CDCl_3$ and was compared to that of **$2N_3$** and **M_1** in $CDCl_3$ (the ^{1}H NMR spectrum **$[La(L_1)_3]^{3-}$** could not be obtained in $CDCl_3$ due to solubility issues) (Fig. 87). There are key features in the ^{1}H NMR spectrum of rotaxanes that indicated successful threading via a AT-CuAAC reaction.[152,155,157] One of these features includes the presence of a down-field shifted singlet peak corresponding to the triazole hydrogen, however this was absent in the ^{1}H NMR spectrum obtained for the orange waxy solid (Fig. S207).[152,155,157] In saying this, studies carried out by the Goldup research group have shown that when a rotaxane is sterically crowded (*i.e.* through using short half threads as well as a small macrocycle), the mechanical bond elicits stability upon a triazolide intermediate of this reaction, with Cu(I) bound to the C-atom of the triazole ring.[127,133,157] This finding suggested that the lack of a peak corresponding to the triazole hydrogen does not necessarily mean the lack of rotaxane formation.[127,157]

Another key feature indicative of successful rotaxane formation is large **M_1** peak shifts and splitting, however this was not observed in the ^{1}H NMR spectrum obtained for the product which instead was dominated by peaks indicative of unreacted **M_1** (and **$2N_3$**). This supported the idea that the lack of a peak in the range expected for the triazole hydrogen was not due to the presence of a triazolide intermediate, but rather due to an unsuccessful AT-CuAAC reaction (Fig. 87). Interestingly, there appeared to be smaller "sub-peaks" emerging beneath the peaks corresponding to aromatic naphthalimide protons of the **$2N_3$** impurities, suggesting that there was another naphthalimide-containing species present. However due to the small nature of these peaks, it was difficult to determine the nature of this product (*i.e.* it may result from a small amount of non-threaded axle) (Fig. 87). In saying this, the reactions conditions used (conditions one) were very mild (*i.e.* it was only heated at 50 ˚C for 1 day) and strict O_2 exclusion conditions were not enforced, proving a possible reason for the lack of rotaxane formation. Thus, in attempt 2 (conditions 2), the reaction conditions were altered slightly.

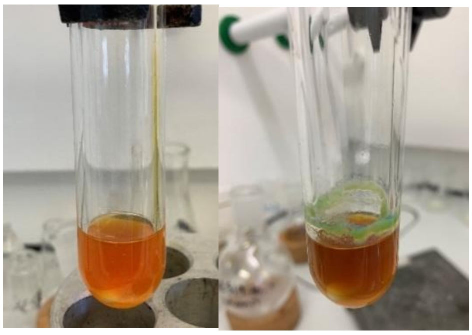

Figure 88. (Left) Reaction mixture before heating using conditions 2, showing the presence of Cu(I). (Right) Reaction mixture after stirring for three days using conditions 2, showing the sustained presence of Cu(I) with some possible Cu(II) precipitate

For the second attempt to synthesize **$[La(R_2^*)_3]^{3-}$** through an AT-CuAAC reaction between **$[La(L_1)_3]^{3-}$**, **$2N_3$** and **M_1**, the reaction conditions were altered such that the reaction was carried out in a pressure vial (as opposed to a round bottomed flask) so that heat and stricter O_2 exclusion conditions could be used. On the suspension of the solids into the DCM:MeOH solvent mixture, a bright orange reaction mixture was observed, as for attempt 1 (Fig. 88). The reaction mixture was flushed with nitrogen and stirred at 60 ˚C for 3 days. After 3 days, the reaction mixture was darker orange in colour and appeared to have a green/blue precipitate surrounding the side of the vial (suggestive of Cu(II) present) (Fig. 88). A slightly different workup procedure was also used such that the copper removal was carried out using a 0.5 M EDTA/NH_4OH solution as had been used in the method by Neal and Goldup (2015) **(**as opposed to a 0.5 M EDTA/NaOH solution).[152,155-157] A waxy pale orange/colourless solid was extracted which appeared blue under UV light. The ^1H NMR spectrum obtained for this waxy solid appeared very similar to that obtained for the product obtained using conditions 1, containing sub-peaks but no $\mathbf{M_1}$ shifts. There was a very small down-field peak observed at 10.17 ppm, the large shift of which had been observed for the triazole hydrogen of a range of rotaxanes developed by Lahlali and co-workers (2011) however it was difficult to determine whether this peak was stemming from the triazole hydrogen present in $\mathbf{[La(R_2^*)_3]^{3-}}$ or impurities (Fig. S210).

Taking the results from these two attempts together, the reaction conditions were altered further, forming conditions 3. Due to the water-soluble nature of $\mathbf{[La(L_1)_3]^{3-}}$, a different solvent mixture, THF:H_2O (1:1) was used, which contained an aqueous component.[155] Due to this solvent change, the Cu(I) source was also changed back to the copper(II) sulfate pentahydrate and sodium ascorbate combination.[155] These conditions had been reported by Acevedo-Jake and co-workers (2020) to be successful in a AT-CuAAC reaction between two oligonucleotides and a small macrocycle related to $\mathbf{M_1}$.[155]

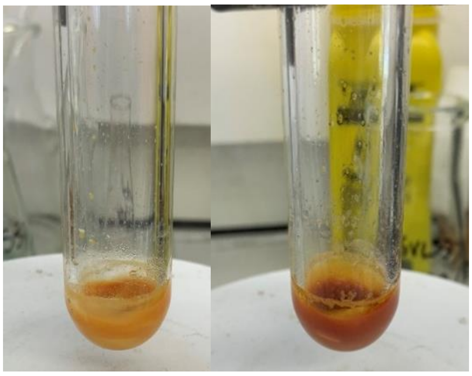

Figure 89. (Left) Reaction mixture using conditions 3 on day one. (Right) Reaction mixture using conditions 3 on day two, with the lack in colour change suggesting that Cu(I) remained in its +1 oxidation state

One equivalent of $\mathbf{[La(L_1)_3]^{3-}}$ and three equivalents of $\mathbf{M_1}$ and $\mathbf{2N_3}$ were combined in a pressure vial and suspended in THF. In a separate vial, three equivalents of copper(II) sulfate pentahydrate and fifteen equivalents of sodium ascorbate were suspended in deionised H_2O and subsequently added to the pressure vial, formed a bright orange reaction mixture. Next, *N*,*N*-Diisopropylethylamine (DIPEA) (3.3 equivalents) (a base known to speed up AT-CuAAC reactions) was added to the reaction mixture which was subsequently flushed with N_2 and left to stir at room temperature under N_2 for 2 days. After 2 days, the reaction mixture appeared darker orange in colour, suggesting that the copper remained in its +1 oxidation state (Fig. 89).[155-157] The workup procedure included a DCM extraction and a washing step with a 0.5 M EDTA/NH_4OH solution, resulting in the formation of a pale yellow/white waxy solid. The resulting ^1H NMR spectrum (Fig. S213) showed no evidence of a successful AT-CuAAC reaction, with no $\mathbf{M_1}$ peak shifts as well as no triazole peak or sub-peaks evident.

Taking all the attempts for $\mathbf{[La(R_2{*})_3]^{3-}}$ synthesis into account, the AT-CuAAC reaction conditions between $\mathbf{[La(L_1)_3]^{3-}}$, $\mathbf{2N_3}$ and $\mathbf{M_1}$ requires further optimization. Thus, with restrictions in the amount of $\mathbf{M_1}$ available, the focus was turned to the development of a slightly different system, as explained in section 2.6.2.

2.6.2 Rotaxane ligands and their potential self-assembling properties

With attempts of performing AT-CuAAC on **$[La(L_1)_3]^{3-}$** posing synthetic difficulties, the focus was turned to the possibility of developing rotaxanes ligands able to form pseudo-[4]-rotaxanes through self-assembly with lanthanide ions.[209] For this to be successful, one end of the ligand must contain a group that is able to act as both a stopper as well as a Ln^{3+} chelator.[156] In recognising this, two weaker chelators related to the DPA family were investigated; one containing ester groups substituted at the 2- and 6- positions of the pyridine ring (referred to as the methyl-protected DPA motif) and another containing amide groups substituted at the 2- and 6- positions of the pyridine ring (referred to as the amide-protected DPA motif) (Fig. 90).[156,196]

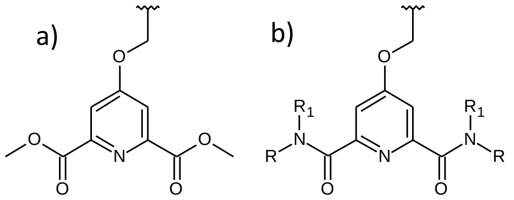

Figure 90. General structures of the chelating motifs designed for both Ln^{3+} complexation and M_1 stoppering including (a) the methyl-protected DPA motif (b) the amide-protected DPA motif

Although being constantly reported as being a weaker chelator when compared to its dicarboxylate derivative, multiple studies have reported the formation of 3:1 ligand:Ln^{3+} complexes using the alkyl-protected DPA motif.[71,72,196,201-203,207-209] Studies have also shown that amide-protected DPA motifs form 3:1 ligand:Ln^{3+} coordination complexes.[196] In saying this, differences have been observed between the properties of these 3:1 complexes containing methyl-protected and amide-protected DPA motifs.[194,196,201-203,207,208]

For 3:1 ligand:Ln^{3+} complexes, ligands containing the amide-protected DPA motif have been reported as having much larger stability constants when compared to analogous complexes with ligands containing the alkyl-protected DPA motif.[194,201-203,207,208] Consequently, the amide-protected DPA chelators appear to be better at binding to lanthanide ions when compared to alkyl-protected DPA chelators.[194,201-203,207,208] In saying this, the methyl-protected DPA motif has been shown to be a better Eu^{3+} sensitizer such that it forms 3:1 ligand:Eu^{3+} complexes that emit with a quantum yield 400 times higher compared to that obtained for the amide-protected DPA analogue in acetonitrile.[196,207,208] Despite these differences, we chose to investigate the ability of these groups to act as both a Ln^{3+} chelator, as well as a **M$_1$** stopper group, to form the desired quasi-[4]-rotaxanes.

2.6.2.1 Methyl-protected rotaxane ligands- simultaneous chelator and stopper

Findings from the Goldup research group have shown that a benzyl motif containing methyl protected carboxylic acid groups (*i.e.* methyl esters) at their 2- and 6- positions is able to act as a stopper group for a macrocycle similar to **M$_1$**.[156] Thus, we explored the possibility of using the methyl-protected DPA motif as both a chelator and a stopper group.

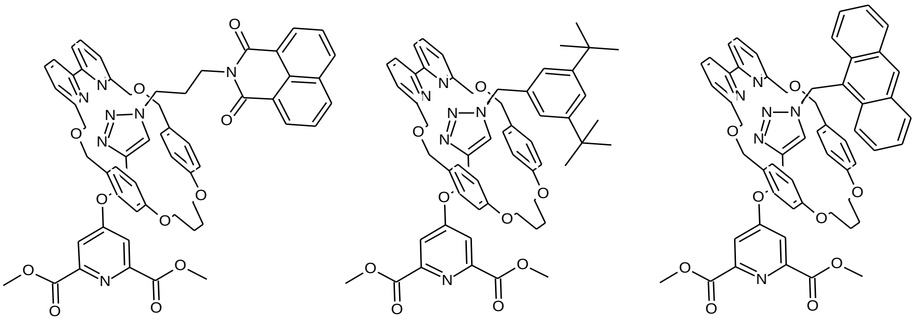

R$_2$ **R$_3$** **R$_4$**

Figure 91. Structures of the target methyl-protected rotaxane ligands R$_2$, R$_3$ and R$_4$

A family of three different rotaxanes, **R$_2$**, **R$_3$** and **R$_4$** were aimed to be synthesized, each differing by their stopper group (being a 1,8-naphthalimide for **R$_2$**, a *tert*-butyl benzyl group for **R$_3$**, and a 9-anthracene group for **R$_4$**) (Fig. 91). These were planned to be synthesized through an AT-CuAAC method between **2**, **M$_1$** and either **2N$_3$**, **3N$_3$**, or **4N$_3$** depending on the target rotaxane.

R$_2$ synthesis and characterisation

For the synthesis of **R$_2$**, the conditions used were based off those published by Neal and Goldup in 2015.[156] In summary, approximately 1.2 equivalents of **2** and **2N$_3$** were combined with 1 equivalent of **M$_1$** and 0.1 equivalents of $[(CH_3CN)_4Cu]PF_6$ (Fig. 92).[156] These solids were suspended in anhydrous THF to make a 0.05 M solution (with respect to **M$_1$**).[156] Next, 1.10 equivalents of DIPEA was added and the yellow reaction mixture was left to stir under N_2 at 30˚C for approximately 3 days.[153,155-160] After 3 days, the reaction mixture was extracted with DCM and to remove any remaining copper it was washed with a 0.5 M EDTA/NH_4OH solution. On removal of the DCM, the product appeared as a white/pale yellow waxy solid which was analysed by NMR spectroscopy.

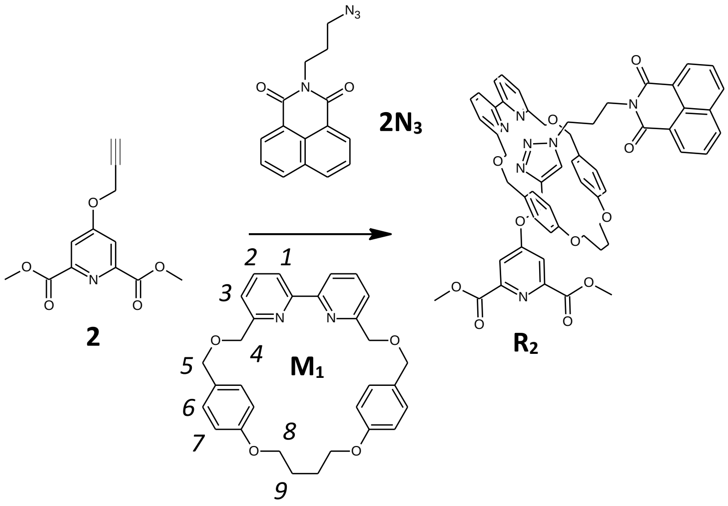

Figure 92. General reaction scheme for the synthesis of R$_2$ using AT-CuAAC

A ^{1}H NMR spectrum of the solid was collected and gave evidence suggesting successful threading (Fig. 93). As introduced in section 2.6.1, there are key signs in the ^{1}H NMR spectrum of rotaxanes to look for to support **M$_1$** threading. One sign is the downfield shifting of the triazole peak in the rotaxane (when compared to free axle) as well as the shifting and splitting of the **M$_1$** protons.[152,155-157] The downfield shifting of the triazole peak observed for **M$_1$**-containing rotaxanes synthesized through AT-CuAAC chemistry has been attributed to the introduction of a C-H···N interaction on threading, such that the triazole C-H group interacts with nitrogen atoms of the bipyridine motif of **M$_1$**.[152,155] The macrocycle splitting has been attributed to the loss of bilateral symmetry associated with **M$_1$** on threading.[137,152,155,157,159,187,274] Accordingly, depending on what face the **M$_1$** protons are situated on, they experience different environments and hence appear as different signals in the ^{1}H NMR spectrum (*i.e.* they become diastereotopic hydrogens).[137,152,155,157,159,187,274]

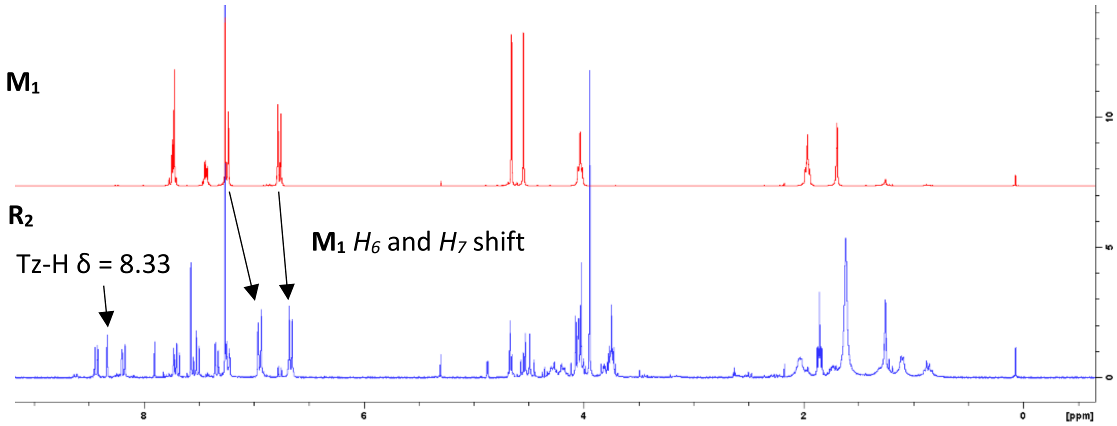

Figure 93. ^{1}H NMR spectrum of R_2 (blue, bottom) compared to M_1 (red, top) in $CDCl_3$

In the ^{1}H NMR spectrum obtained for **R$_2$** in CDCl$_3$, the singlet peak at 8.33 ppm was assigned to the **R$_2$** triazole hydrogen, indicative of a successful CuAAC reaction (Fig. 93). This triazole peak appeared to be shifted downfield from 7.96 ppm in **MeOL$_2$** (free axle) (a $\Delta\delta$ of -0.37 ppm), indicative of macrocycle threading and rotaxane formation (Fig. S220).[152,155]

The presence of separate peaks corresponding to **M$_1$** splitting was difficult to distinguish for **R$_2$** due to the crowded nature of the ^{1}H NMR spectrum (Fig. 93). In saying this, the key **M$_1$** shifts expected for rotaxane formation were observed, supporting the nature of the CuAAC reaction as an AT-CuAAC reaction (Fig. 93). For instance, the doublet peaks at 7.23 and 6.75 ppm in **M$_1$**, assigned to the aromatic benzyl protons in the 2,6- and 3,5- positions of the two macrocyclic benzyl groups (*i.e.* H_6 and H_7 in Fig. 92) appeared to have shifted significantly up-field to 6.93 and 6.65 ppm for H_6 and H_7 (respectfully) in the ^{1}H NMR spectrum of **R$_2$** (Fig. 93). This same shifting was observed by Lahlali and co-workers (2011) whereby the analogous protons shifted from 7.24 ppm (for H_6) and 6.76 ppm (for H_7) in **M$_1$** to 6.81 and 6.59 ppm on rotaxane formation for H_6 and H_7 (respectively).[152]

Although the major product based off the ^{1}H NMR spectra was **R_2**, there did appear to be a small amount of **$2N_3$**, **M_1** and **2** present suggesting that future studies require the optimization of reaction conditions or purification (Fig. 93). There was a possibility that the presence of free **M_1** was arising from de-threading processes occurring. In saying this, there were no peaks that lined up with those in ^{1}H NMR spectrum of **$MeOL_2$** (*i.e.* free axle) in $CDCl_3$, suggesting that the small number of peaks corresponding to free **M_1** resulted from unreacted **M_1**, however further studies are required to confirm this (Fig. 93 and Fig. S220).

After analysis via NMR spectroscopy, the formation of **R_2** was supported by HRMS (Fig. 94). There appeared to be a peak in the mass spectrum at an *m/z* ratio of 1012.3859 which was assigned to the **$[R_2 + H^+]^+$** ion (with a calculated monoisotopic mass calculated for $[C_{57}H_{54}N_7O_{11}]^+$ of 1012.3880 g mol^{-1}) (Fig. 94 and Table 7). Additionally, as shown by the insert in Fig. 94, the peaks belonging to this series were separated by *m/z* values of approximately 1, confirming the +1 charge of the **$[R_2 + H^+]^+$** ion.

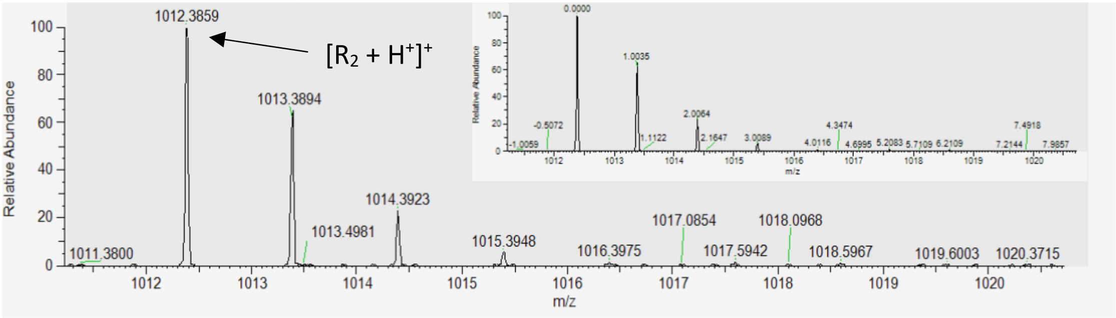

Figure 94. HRMS m/z = 1012.3859 $[R_2 + H^+]^+$ (calc for $[C_{57}H_{54}N_7O_{11}]^+$, 1012.3880 g mol^{-1}). (Insert) m/z labelled relative to the $[R_2 + H^+]^+$ peak, confirming the +1 charge

There was also peak in the mass spectrum of **R_2** at an *m/z* ratio of 250.0706, which was in agreement with the calculated monoisotopic mass of the **$[2 + H^+]^+$** ion (calculated for $[C_{12}H_{12}NO_5]^+$, 250.0715 g mol^{-1}) (Table 7). Additionally, a peak was observed at an *m/z* ratio of 483.2274 which was assigned to the **$[M_1 + H^+]^+$** ion due to its good agreement with the calculated monoisotopic mass for $[C_{30}H_{31}N_2O_4]^+$ of 483.2284 g mol^{-1} (Table 7). Lastly, a peak at an *m/z* ratio of 530.1665 was in good agreement with the calculated monoisotopic mass of the **$[MeOL_2 + H^+]^+$**

ion (calculated for $[C_{27}H_{24}N_5O_7]^+$, 530.1676 g mol^{-1}) (Table 7). The presence of these ions, particularly the **$[M_1 + H^+]^+$** and **$[MeOL_2 + H^+]^+$** ions, suggested that some de-threading may be occurring. These peaks may also result from fragmentation processes during mass spectroscopy, making it difficult to confirm the occurrence of any de-threading processes.

Table 7. Summary of key peaks observed in the HRMS of R_2 compared to their calculated m/z

Ion observed	Calculated m/z	Observed m/z
$[R_2 + H^+]^+$	1012.3880	1012.3859
$[2 + H^+]^+$	250.0715	250.0706
$[M_1 + H^+]^+$	483.2284	483.2274
$[MeOL_2 + H^+]^+$	530.1676	530.1665

R_3 synthesis and characterisation

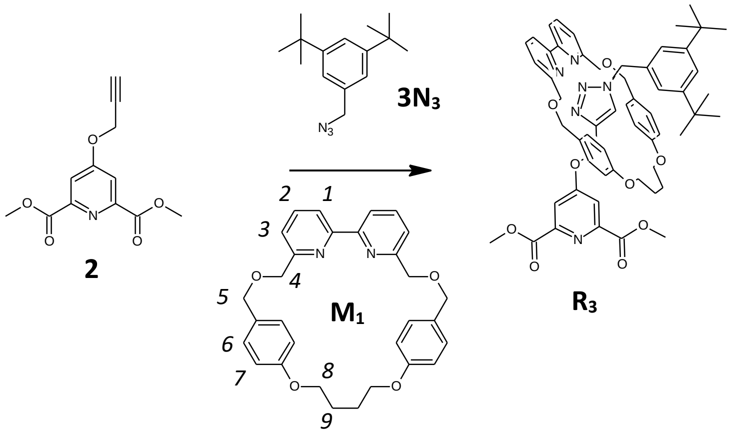

Figure 95. General reaction scheme for the synthesis of R_3 using AT-CuAAC

To synthesise **R_3**, the same conditions were used as those for **R_2** such that one equivalent of **M_1** was combined with 0.1 equivalent of $[(CH_3CN)_4Cu]PF_6$, and 1.2 equivalents of **2** and **$3N_3$** (Fig. 95). The solids were suspended in the appropriate amount of anhydrous THF such that a 0.05 M reaction mixture (with respect to **M_1**) existed. Next, a slight excess of DIPEA was added to the bright orange reaction mixture which was left to stir in a pressure vial under nitrogen at 30 ˚C for approximately 2 days. **R$_3$** was then extracted with DCM and washed with a 0.5 M EDTA/NH_4OH solution to form a pale yellow waxy solid in 20 % yield. The ^{1}H NMR spectra of **R$_3$** could be collected in $CDCl_3$ and showed evidence of successful macrocycle threading (Fig. 96).

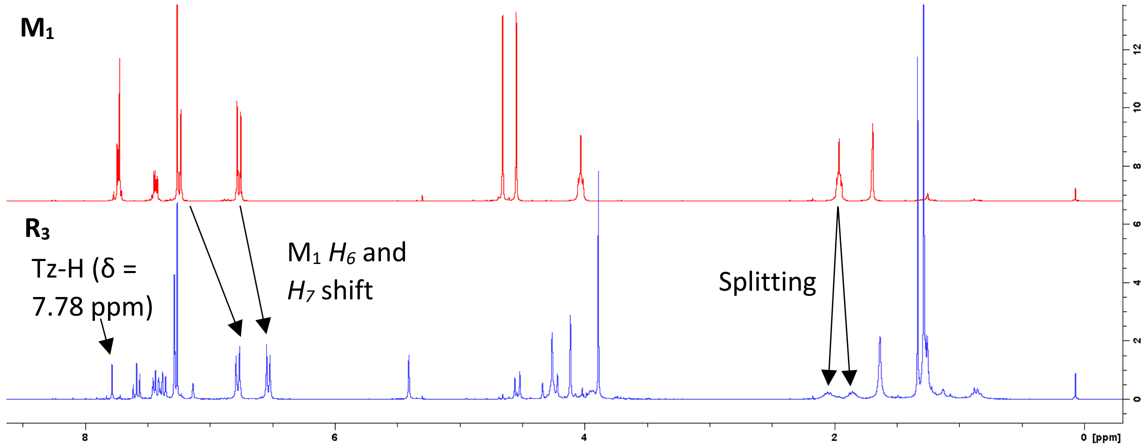

Figure 96. ^{1}H NMR spectrum of R_3 (blue, bottom) compared to M_1 (red, top) in $CDCl_3$

Firstly, the singlet peak at 7.78 ppm was assigned to the triazole hydrogen of **R$_3$**, being shifted downfield by 0.21 ppm when compared to the analogous triazole peak in **MeOL$_3$** (appearing at 7.57 ppm), providing evidence of a successful AT-CuAAC reaction (Fig. 96 and Fig. S228). When analysing the whole ^{1}H NMR spectrum of **R$_3$**, the peaks corresponding to free macrocycle **M$_1$** appeared to be absent (supporting threading) (Fig. 96). Instead, most of the peaks corresponding to **M$_1$** in the ^{1}H NMR spectrum of **R$_3$** appeared to be shifted and/or split into diastereotopic signals due to the decrease in **M$_1$** symmetry on threading (Fig. 96).[137,152,155,157,159,187,274] Firstly, the doublets at 7.23 and 6.75 ppm in **M$_1$**, corresponding to H_6 and H_7 (respectively), appeared to be shifted up-field to 6.76 and 6.52 ppm for H_6 and H_7 (respectively) in **R$_3$** (Fig. 96). As explained for **R$_2$** and as has been observed for multiple studies, this shift is frequently observed in the ^{1}H NMR spectrum of rotaxanes containing **M$_1$**, supporting threading.

Additionally, **M$_1$** splitting, which was not able to be resolved in **R$_2$**, was observed in the ^{1}H NMR spectrum of **R$_3$**. For instance, the quintet in the ^{1}H NMR spectrum of **M$_1$** at 1.96 ppm (integrating as 4 protons) could be assigned, based off previous studies by Lahlali and co-workers (2011), to the H_9 protons. On threading, these protons appeared to split into two multiplets at 2.07 – 1.96

ppm and 1.88 – 1.84 ppm, each integrating as 2 protons (Fig. 96).[152] These features supported **R_3** formation as they suggested that the **M_1** protons were experiencing different environments depending on their orientation elicited by the formation of the mechanical bond.[137,152,155,157,159,187,274]

The HRMS of **R_3** was collected and supported its formation (Fig. 97). The mass spectrum showed a peak at an *m/z* value of 977.4793 which was in good agreement with the calculated monoisotopic mass of the **$[R_3 + H^+]^+$** ion of 977.4813 g mol^{-1} (for $[C_{57}H_{65}N_6O_9]^+$) (Fig. 97). As shown by the insert in Fig. 97, the peaks belonging to this series were separated by *m/z* values of approximately 1, confirming the +1 charge of the **$[R_3 + H^+]^+$** ion. This peak was appearing as the primary peak in the mass spectrum of **R_3**, suggesting that it is the main product that forms (Fig. S233).

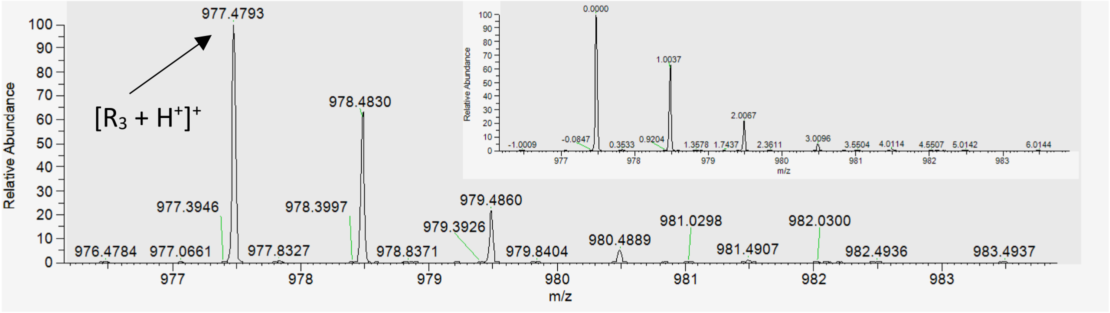

Figure 97. HRMS m/z = 977.4793 $[R_3 + H^+]^+$ (calc. for $[C_{57}H_{65}N_6O_9]^+$, 977.4813 g mol^{-1}). (Insert) m/z labelled relative to the $[R_3 + H^+]^+$ peak, confirming the +1 charge

In saying this, there were small peaks observed corresponding to starting materials. There was a peak at an *m/z* value of 250.0707, being in the range expected for the **$[2 + H^+]^+$** ion (with a calculated monoisotopic mass of 250.0715 g mol^{-1}), however this peak was very small (Fig. S236).

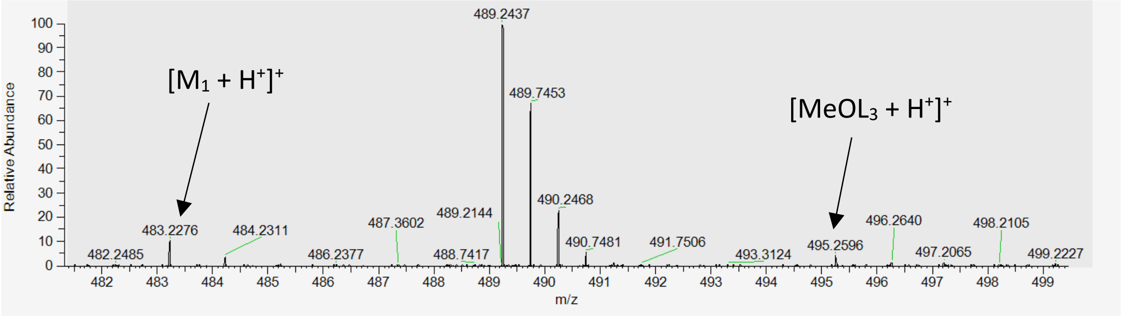

Figure 98. HRMS m/z = 483.2276 $[M_1 + H^+]^+$ (calc. for $[C_{30}H_{31}N_2O_4]^+$, 483.2284 g mol^{-1}) and m/z = 495.2596 $[MeOL_3 + H^+]^+$ (calc for $[C_{27}H_{35}N_4O_5]^+$, 495.2607 g mol^{-1})

There also appeared to be a small peak with an *m/z* value of 483.2276, which matched the monoisotopic mass calculated for the **[M$_1$ + H$^+$]$^+$** ion of 483.2284 g mol^{-1} (calculated for [$C_{30}H_{31}N_2O_4$]$^+$), suggesting the presence of free **M$_1$** (Fig. 98 & Table 8). This peak was also observed alongside a very small peak at an *m/z* value of 495.2596 which was in good aggreement with that based off the calculated monoisotopic mass of **[MeOL$_3$ + H$^+$]$^+$** of 495.2607 g mol^{-1} (calculated for [$C_{27}H_{35}N_4O_5$]$^+$) (Fig. 98 and Table 8). As observed for **R$_2$**, the presence of these **M$_1$** and **MeOL$_3$** peaks may arise due to multiple reasons such as fragmentation, de-threading or unreacted starting materials.

Table 8. Summary of key peaks observed in the HRMS of R$_3$ compared to their calculated m/z

Ion observed	Calculated m/z	Observed m/z
[R$_3$ + H$^+$]$^+$	977.4813	977.4793
[2 + H$^+$]$^+$	250.0715	250.0707
[M$_1$ + H$^+$]$^+$	483.2284	483.2276
[MeOL$_3$ + H$^+$]$^+$	495.2607	495.2596

R_4 synthesis and characterisation

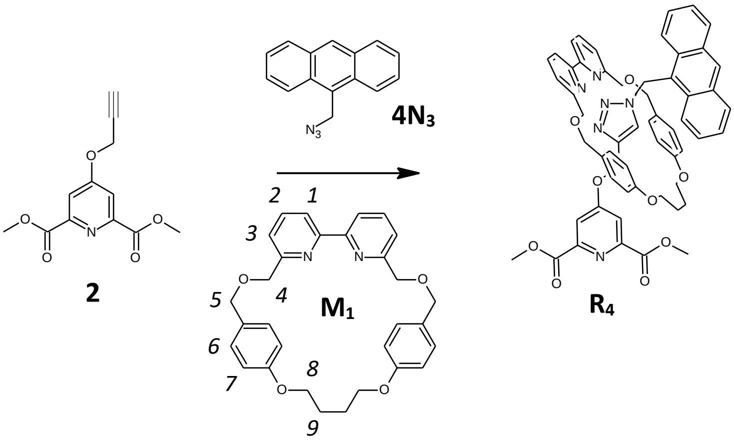

Figure 99. General reaction scheme for the synthesis of R_4 using AT-CuAAC

To synthesise **R_4**, a similar procedure as that used for **R_2** and **R_3** whereby one equivalent of **M_1** was combined with 1.2 equivalents of **2** and **$4N_3$** and 0.1 equivalents of $[(CH_3CN)_4Cu]PF_6$ in a pressure vial (Fig. 99). The solids were then suspended in anhydrous THF (to make a 0.05 M reaction mixture with respect to **M_1**) under N_2. Next, 1.1 equivalents of DIPEA were added and the orange reaction mixture was left to stir under N_2 at 30 ˚C for 2 days after which a slight precipitate could be observed. As for **R_2** and **R_3**, the reaction mixture was extracted with DCM and washed with a 0.5 M EDTA/NH_4OH solution to remove any copper remaining. The product was isolated as an oily yellow solid in 23 % yield which appeared green/blue in colour under long wave UV light (Fig. S237). A ^{1}H NMR spectrum of the product could be collected and showed evidence of successful **M_1** threading along with **2** and **$4N_3$** clicking (Fig. 100).

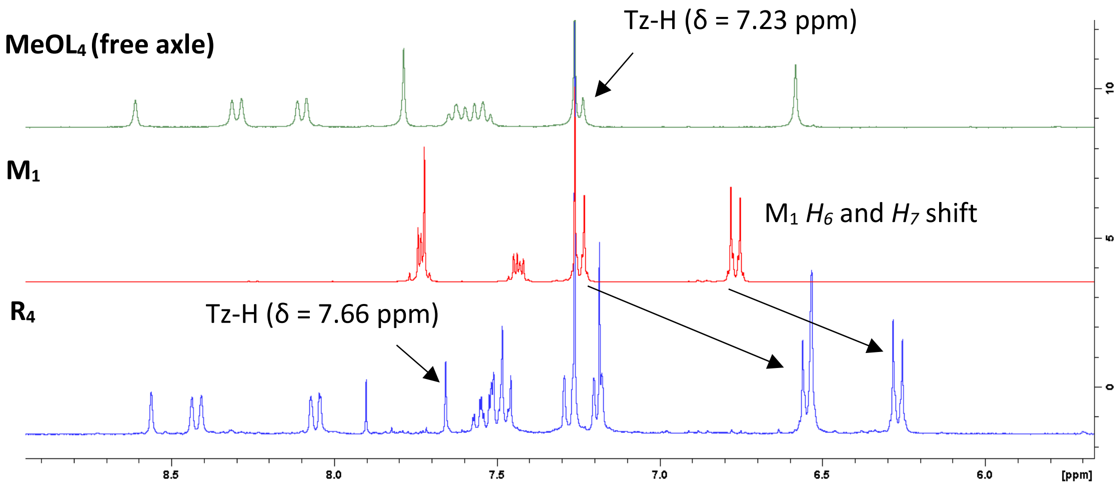

Figure 100. ^{1}H NMR spectrum of R_4 (blue, bottom) compared to M_1 (red, middle) and MeOL$_4$ (free axle) (green, top) in CDCl$_3$

Due to the crowded nature of the ^{1}H NMR spectrum obtained for the product, only aromatic region is shown in Fig. 100, containing the key signs for **R₄** formation (the full spectrum is supplied in the supplementary information). Firstly, the triazole peak was assigned to the singlet at 7.66 ppm, being shifted downfield from 7.23 ppm in **MeOL₄** (a Δδ of 0.43 ppm), supporting a successful AT-CuAAC reaction (Fig. 100). Initially, the singlet peak appearing at 8.56 ppm in the ^{1}H NMR spectrum of **R₄** was predicted to correspond to the triazole hydrogen however on closer analysis, this peak was found to be present in the ^{1}H NMR spectrum of **MeOL₄** (and other anthracene derivatives) and was assigned to one of the aromatic anthracene protons (Fig. 100). Additionally, this 8.56 ppm peak appeared to only interact with other anthracene aromatic protons in the COSY spectrum of **R₄** whereas the singlet peak at 7.66 ppm was interacting with the singlet peaks assigned to the CH_2^{DT} and CH_2^{TA} protons at 4.09 and 6.53 ppm (respectively), expected for the triazole proton due to its close proximity to these protons (Fig. 100).

In addition to triazole proton shifting, key shifts in **M₁** peaks were observed which supported threading (Fig. 100). For instance, the two doublets at 6.53 and 6.25 ppm in the ^{1}H NMR spectrum of **R₃**, assigned to the H_6 and H_7 protons (respectively) had been shifted up-field from 7.23 ppm (for H_6) and 6.75 ppm (for H_7) in the ^{1}H NMR spectrum of **M₁** (Fig. 100).[152]

A detailed analysis of the alkyl region in ^{1}H NMR spectrum of **R₄** was restricted by the crowded nature of this region. However, a clear quintet peak could be observed at 1.85 ppm, in the range expected for the H_9 protons of **M_1** which appeared to have shifted up-field from 1.96 ppm in **M_1**, supporting threading (Fig. S240). In saying this, the splitting that was observed for the analogous protons in **R_3** was not observed which suggested that the **M_1** had either retained its symmetry upon threading, or it had not threaded successfully. However, the **M_1** peak shifting in combination with the shifting of most peaks corresponding to the axle component of **R_4** (**$MeOL_4$**) strongly disfavoured this latter possibility, supported the successful threading of **M_1** (Fig. 100).

The HRMS of **R_4** was also collected and supported its formation (Fig. 101). There appeared to be a peak observed at an *m/z* ratio of 965.3860 which was in the range expected for the **$[R_4 + H^+]^+$** ion based off the monoisotopic mass calculated for $[C_{57}H_{53}N_6O_9]^+$ of 965.3874 g mol^{-1} (Fig. 101 and Table 9) The peaks belonging to this series were separated by *m/z* values of approximately 1, confirming the +1 charge of the **$[R_4 + H^+]^+$** ion (Fig. 101).

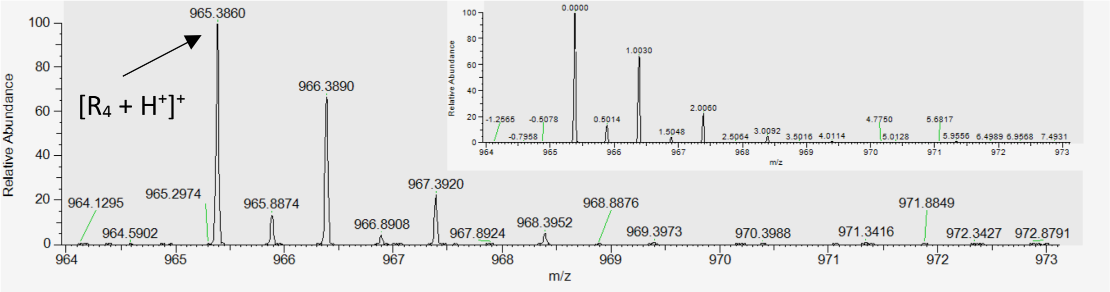

Figure 101. HRMS m/z = 965.3860 $[R_4 + H^+]^+$ (calc. for $[C_{57}H_{53}N_6O_9]^+$, 965.3874 g mol^{-1}). (Insert) m/z labelled relative to the $[R_4 + H^+]^+$ peak, confirming the +1 charge

In saying this, a peak appearing at an *m/z* value of 250.0708 appeared to dominate the mass spectrum of **R_4**, in the range expected for the **$[2 + H^+]^+$** ion (250.0715 g mol^{-1}) (Fig. S246). This finding, combined with the presence of peaks corresponding to free **2** in the ^{1}H NMR spectrum of **R_4** suggested that the reaction had not gone to completion, thus future studies are required for the optimization and/or purification of **R_4** synthesis (Table 9).

Next, as had been observed for **R_2** and **R_3**, any peaks corresponding to free **M_1** and **$MeOL_4$** with protons were investigated. The calculated monoisotopic masses of the **$[M_1 + H^+]^+$** and **$[MeOL_4 + H^+]^+$** ions were very similar, being 483.2284 and 483.1668 g mol^{-1} (respectively), thus would have some overlapping peaks in the mass spectrum (Fig. S249). There did appear to be a small peak at an *m/z* ratio of 483.2268 which was situated next to a larger peak at 483.1973 (Fig. S249). The peak at 483.2268 appeared to belong to a series of peaks separated by *m/z* values of approximately +1 thus was assigned to the **$[M_1 + H^+]^+$** ion (Table 9). The neighbouring peak at the *m/z* ratio of 483.1973 was close to the monoisotopic mass of **$[MeOL_4 + H^+]^+$** however it was far enough away such that this assignment could not be made with confidence (Fig. S249). Additionally, the peaks belonging to these series appeared to be separated by *m/z* values of approximately 0.50, suggesting that the ion corresponding to this peak carried a +2 charge which did not agree with the charge of the **$[MeOL_4 + H^+]^+$** ion.

Table 9. Summary of key peaks observed in the HRMS of R_4 compared to their calculated m/z

Ion observed	Calculated m/z	Observed m/z
$[R_4 + H^+]^+$	965.3874	965.3860
$[2 + H^+]^+$	250.0715	250.0708
$[M_1 + H^+]^+$	483.2284	483.2268

Overall, the rotaxanes **R_2**, **R_3**, and **R_4** were synthesized using relatively mild conditions (*i.e.* no heating above 30 ˚C) and adequate yields were obtained. In saying this, based off ^{1}H NMR and mass spectral data, in some cases there did appear to be indications of starting material remaining in the product suggesting that further studies are required to optimize these reaction conditions, or, alternatively, an extra purification step is required to separate these impurities from the rotaxanes. In saying this, because these impurities were very small (particularly for **R_3**) studies investigating the ability of these rotaxanes to self-assemble with Ln^{3+} into the target quasi-[4]-rotaxane structures were carried out.

Self-assembly studies: R_3 titrations with Eu^{3+}

Alkyl-protected DPA ligands have been reported to coordinate with Ln^{3+} in 3:1 ligand:Ln^{3+} ratios (Fig. 102).[71,72,196,201-203,207-209] Thus, to investigate the ability of our methyl-protected DPA ligand, **R_3**, to form self-assemblies with lanthanide ions, UV/Vis and fluorescence titrations were carried out.[194] All titrations were carried out at room temperature in acetonitrile using europium(III) triflate and titrations were carried out in duplicate.

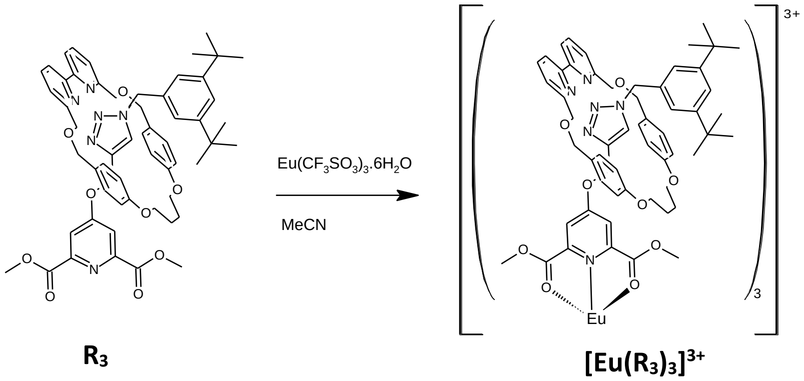

Figure 102. Proposed self-assembly of R_3 in the presence of Eu^{3+}, resulting in the formation of quasi-[4]-rotaxane $[Eu(R_3)_3]^{3+}$

R_3 UV/Vis titrations with $Eu(CF_3SO_3)_3{\cdot}6H_2O$

Firstly, changes in the UV/Vis spectrum of **R_3** on the addition of Eu^{3+} were investigated (Fig. 103). To a solution containing **R_3** (1 x 10^{-5} M) in acetonitrile, stepwise additions of $Eu(CF_3SO_3)_3{\cdot}6H_2O$ dissolved in acetonitrile from 0 → 3.37 equivalents were made at room temperature.

The UV/Vis absorbance spectrum of **R_3** (1 x 10^{-5} M) in acetonitrile (with 0 equivalents of Eu^{3+} added) was dominated by a region of high absorbance between 200 – 250 nm, with a shoulder peak at approximately 221 nm (Fig. 103). This region of high absorption was expected for DPA-based absorption and, as observed in earlier studies, could be assigned to overlapping pyridyl n → π* and carbonyl π → π* transitions.[31,33,40,41,45,47,71,74,185,186,187,193-196,201,207,208,210,211] In saying this, there also appeared to be a much more obvious peak with a $\lambda_{abs}{}^{m}$ value of 282 nm which had not been observed in the NMR spectra of the methyl-protected clicked DPA systems, thus was predicted to result from **M_1** absorption (Fig. 103). This 282 nm peak was assigned to the **M_1** bipyridine motif π → π* transition, being similar to that obtained in the literature of 291 nm.[255,281]

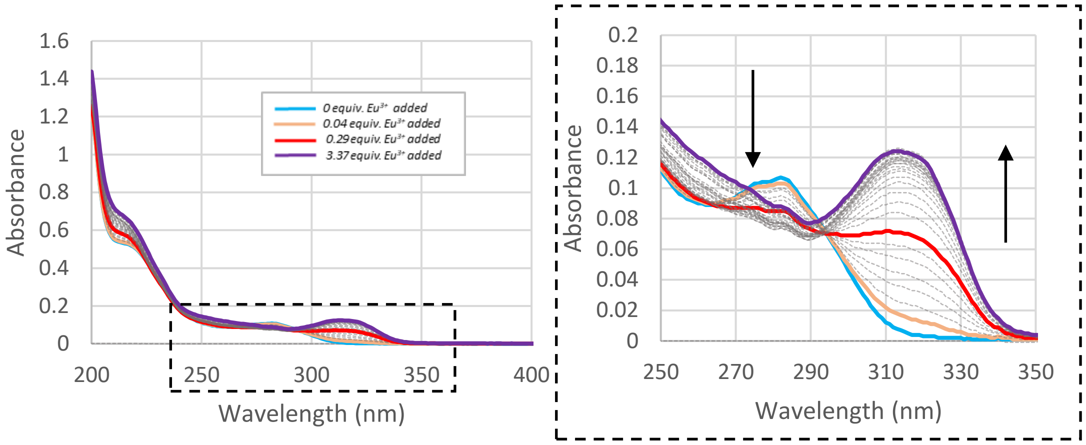

Figure 103. UV/Vis titration of R_3 (1×10^{-5} M in ACN) on the stepwise addition of $Eu(CF_3SO_3)_3{\cdot}6H_2O$ from 0 → 3.37 equivalents. (Insert) Close up showing the changes in the transition at 282 nm on the stepwise addition of $Eu(CF_3SO_3)_3{\cdot}6H_2O$ from 0 → 3.37 equivalents

On the addition of $Eu(CF_3SO_3)_3{\cdot}6H_2O$ to **R_3**, key changes were observed which suggested that the Eu^{3+} was interacting with **R_3**. Firstly, the shoulder peak observed at approximately 221 nm appeared to experience a hyperchromic effect (Fig. 103).[187] This effect has been observed in UV/Vis studies on ligands of the DPA/PDA family on Ln^{3+} complexation, thus was predicted to result from Eu^{3+} complexation.[32,41,185,186,192-194,201,207,208]

Additionally, a large change was observed for the $\lambda_{abs}{}^{m}$ at 282 nm, corresponding to the π – π* **M_1** bipyridine transition (Fig. 103).[255,281] As Eu^{3+} additions were carried out from 0 → 3.37 equivalents, this 282 nm peak appeared to be removed and instead, a new lower energy peak at was established at approximately 312 – 314 nm, with the $\lambda_{abs}{}^{m}$ at 3.37 equivalents of $Eu(CF_3SO_3)_3{\cdot}6H_2O$ (Fig. 103).[281] An isosbestic point was observed at approximately 292 nm (Fig. 103).[196] Similar changes have been observed in the literature, for instance, Charbonierre and co-workers analysed the ability of a ligand containing a bis-bipyridyl motif to bind to Ln^{3+} and found that prior to complexation, the bipyridine π → π* transition was at 291 nm however on the addition of certain Ln^{3+} ions, this peak shifted to 313 nm (Fig. 103).[281] However, in this case, the shift was observed associated with the direct coordination of Ln^{3+} within the bis-pyridyl pocket (as opposed to a distinct coordination site on the ligand which was expected to be the case for

R_3).[281] Thus, this was important as it suggested that the **M_1** shift is possibly due to Eu^{3+} binding within the rotaxane pocket (between **M_1** and the **$MeOL_3$** axle). In saying this, the crowded nature of the **R_3** pocket did not agree with this idea, thus further studies are required to confirm whether this **M_1** shift on the addition of Eu^{3+} is due to methyl-protected DPA motif Eu^{3+} coordination, rotaxane pocket Eu^{3+} coordination, or a combination of both coordination events.

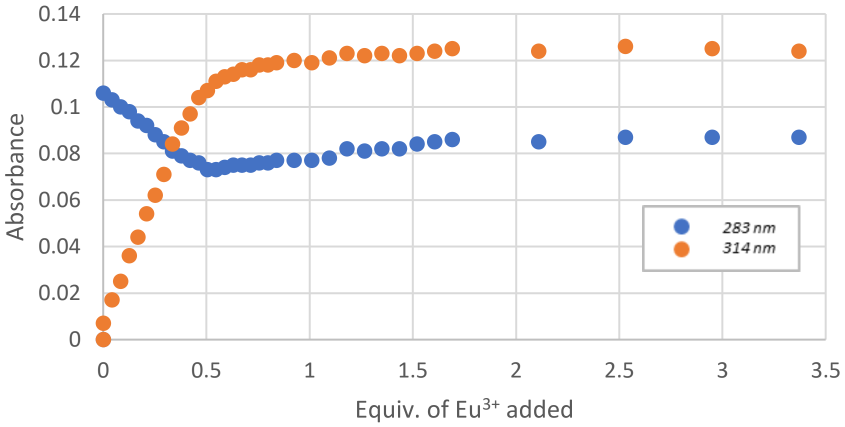

Figure 104. Plot showing the changes in absorbance values of R_3 at 283 nm (blue dots) and 314 nm (orange dots) as a function of equivalents of Eu^{3+} added

In plotting the absorbance at 283 and 314 nm (*i.e.* the peaks showing the key changes in the absorbance spectrum) as a function of the equivalents of Eu^{3+} added, the **R_3**:Eu^{3+} coordination ratio could be investigated (Fig. 104). On the addition of 0 → 0.5 equivalents of $Eu(CF_3SO_3)_3 \cdot 6H_2O$ to **R_3** in acetonitrile, the absorbance of the peak at 314 nm increased rapidly whilst the absorbance of the peak at 283 nm decreased rapidly, consistent with the changes observed in UV/Vis spectrum (Fig. 104). At approximately 0.5 – 0.8 equivalents, the absorbance values at 314 and 283 nm begin to plateau, suggesting that **R_3** was binding to Eu^{3+} in a 2:1 R_3:Eu^{3+} ratio (Fig. 104).[196,209] After approximately 1 equivalent of Eu^{3+} added, the absorbance values remain relatively constant suggesting that the complex forms, and remains stable on the addition of further Eu^{3+} equivalents (Fig. 104).

R_3 fluorescence titrations with $Eu(CF_3SO_3)_3{\cdot}6H_2O$

Next, fluorescence titrations were carried out such that stepwise additions of $Eu(CF_3SO_3)_3{\cdot}6H_2O$ (from 0 → 3.37 equivalents) were made to a solution of $\mathbf{R_3}$ (1 x 10^{-5} M) in acetonitrile and the fluorescence emission spectrum was collected at key excitation wavelengths (Fig. 105). This was carried out to further analyse whether $\mathbf{R_3}$ was able to sensitize Eu^{3+} emission. Since two key changes were observed on the addition of $Eu(CF_3SO_3)_3{\cdot}6H_2O$ to $\mathbf{R_3}$ in the UV/Vis titrations at both 283 and 314 nm, fluorescence titrations were carried out on excitation at both of these wavelengths.[255,281]

On 0 equivalents of $Eu(CF_3SO_3)_3{\cdot}6H_2O$ added, $\mathbf{R_3}$ showed no fluorescence between 500 – 800 nm as expected (Fig. 105). However, on the addition of 0 → 3.37 equivalents of $Eu(CF_3SO_3)_3{\cdot}6H_2O$ to $\mathbf{R_3}$, key sharp peaks characteristic of Eu^{3+} emission were observed on excitation at both 283 and 314 nm (Fig. 105).[28]

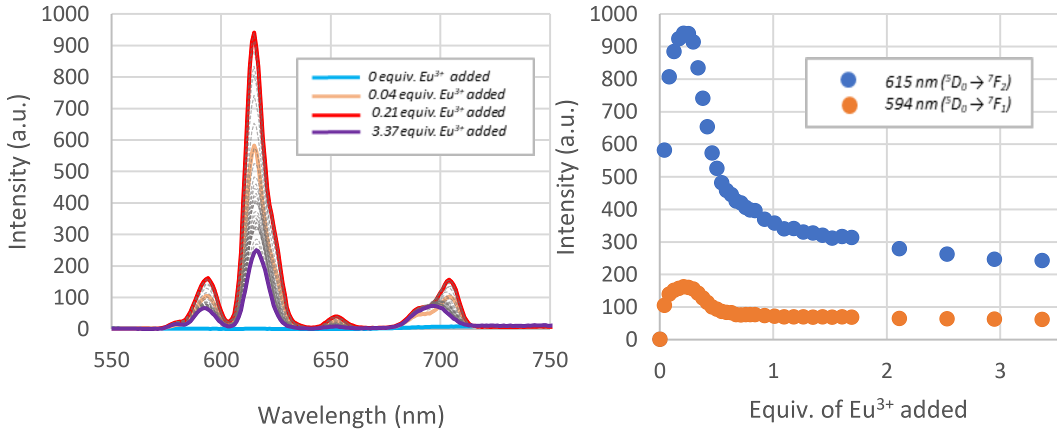

Figure 105. (Left) Fluorescence titration of R_3 (1 x 10^{-5} M) with $Eu(CF_3SO_3)_3{\cdot}6H_2O$ on excitation at 283 nm. (Right) Plot showing the changes in the emission at 615 nm (blue dots) and 594 nm (orange dots) as a function of equivalents of Eu^{3+} added on excitation at 283 nm

On excitation at 283 nm, as 0 → 0.20 equivalents of $Eu(CF_3SO_3)_3{\cdot}6H_2O$ were added, the emission intensity of the bands corresponding to the $^5D_0 \rightarrow {}^7F_2$ (615 nm) and $^5D_0 \rightarrow {}^7F_1$ (594 nm) transitions were observed increase rapidly (Fig. 105).[28] Between approximately 0.20 to 0.30 equivalents, both bands corresponding to the $^5D_0 \rightarrow {}^7F_2$ and $^5D_0 \rightarrow {}^7F_1$ transitions pass through their point of maximum emission intensity. For both transitions, this occurs at 0.20 equivalents of $Eu(CF_3SO_3)_3{\cdot}6H_2O$ added. After 0.30 equivalents, the emission intensity at 615 and 594 nm decreases rapidly until approximately 0.7 – 1.0 equivalents of Eu^{3+} whereby it appears to begin to plateau.

It was assumed that the point of maximum emission would occur when all nine coordination sites of Eu^{3+} are occupied, which would require a 3:1 **R_3**:Eu^{3+} complex.[185,186] Accordingly, a maximum emission was expected at 0.33 equivalents of Eu^{3+} added.[185,186] Although the actual value obtained for the maximum emission of **R_3** at 615 and 594 nm occurred at equivalents before this, there was clear range of values (*i.e.* 0.13 – 0.30 equivalents of Eu^{3+} added) over which a change from increasing emission to decreasing emission was observed, being very close to 0.30 equivalents of Eu^{3+} added. Additionally, large decrease in emission intensity after 0.30 equivalents of Eu^{3+} added was highly indicative of the formation of less emissive 2:1 and 1:1 **R_3**:Eu^{3+} complexes.[185,186]

Another key observation throughout the titration of **R_3** with Eu^{3+} was the change in the form of the band corresponding to the $^5D_0 \rightarrow {}^7F_4$ transition.[28] This peak as a small amount of environment sensitivity, suggesting, a change in symmetry.[26,28]

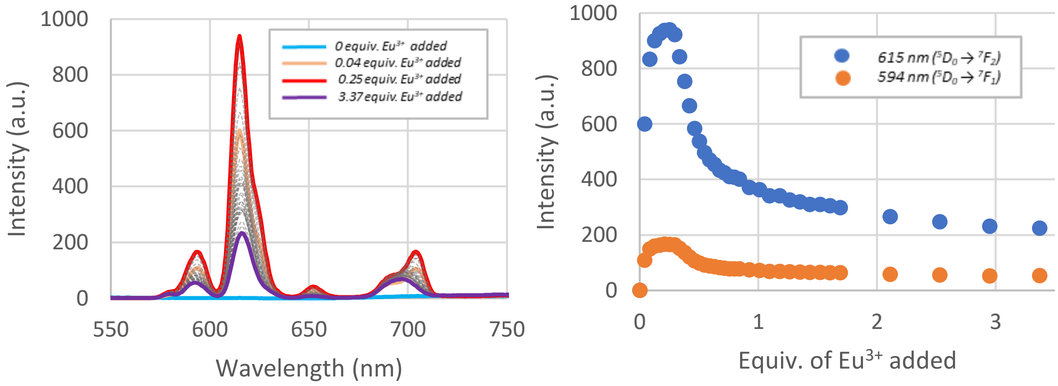

Figure 106. Fluorescence titration of R_3 (1×10^{-5} M) with $Eu(CF_3SO_3)_3{\cdot}6H_2O$ on excitation at 314 nm. (Right) Plot showing the changes in the emission at 615 nm (blue dots) and 594 nm (orange dots) as a function of equivalents of Eu^{3+} added on excitation at 314 nm

On excitation at 314 nm (corresponding to **M_1** bipyridine excitation), the overall results obtained from the titration appeared similar to those obtained on 283 nm excitation, with the emission spectra showing peaks indicative of Eu^{3+} sensitize over the addition of 0.042 – 3.37 equivalents of Eu^{3+} added (Fig. 106).[255,281] On the addition 0 → 0.20 equivalents of $Eu(CF_3SO_3)_3·6H_2O$ to $\mathbf{R_3}$ on excitation at 314 nm, key peaks characteristic of Eu^{3+} emission were observed (Fig. 106).[28] Plotting these changes as a function of Eu^{3+} added, the intensity of emission at the $^5D_0 \rightarrow {}^7F_2$ and $^5D_0 \rightarrow {}^7F_1$ peaks between these 0 → 0.20 equivalent additions increased rapidly (Fig. 106). This was an important finding as it showed that complexation was occurring and that Eu^{3+} sensitization could be achieved through excitation of the $\mathbf{M_1}$ bipyridine motif.[32,41,185,186,192,196,201,207,208] Between approximately 0.20 to 0.30 equivalents of $Eu(CF_3SO_3)_3·6H_2O$ added, the emission intensity passes through its maximum and starts to decline (Fig. 106). For the $^5D_0 \rightarrow {}^7F_2$ transition, this maximum emission occurs at 0.252 equivalents of $Eu(CF_3SO_3)_3·6H_2O$ added whereas for the $^5D_0 \rightarrow {}^7F_1$ transition, it occurs at 0.21 equivalents of $Eu(CF_3SO_3)_3·6H_2O$ added (Fig. 106). The emission intensity decline could be attributed to the formation of 2:1 and 1:1 $\mathbf{R_3}$:Eu^{3+} species.[185,186]

Overall, the UV/Vis and fluorescence titrations showed that $\mathbf{R_3}$ possesses the ability to coordinate with Eu^{3+}, despite the weak binding nature of its methyl-protected DPA chelating motif. Additionally, excitation of both DPA and $\mathbf{M_1}$ components appeared to result in the sensitization of Eu^{3+} emission.[32,34,37,39,40,42-47,50,65,67-69,71,72,74,75,184,196,204] However, conclusions regarding the $\mathbf{R_3}$:Eu^{3+} coordination ratios remained ambiguous. The UV/Vis titration gave results that suggested the formation of a 2:1 $\mathbf{R_3}$:Eu^{3+} species whereas the fluorescence titration results gave results that suggested the formation of 3:1 $\mathbf{R_3}$:Eu^{3+} species. Interestingly, Froidevaux and coworkers (2000), who attached bulky calix[4]arene groups to the 4-pyridyl of DPA and investigated its ability to coordination with Ln^{3+} with different 2- and 6- substituted coordinating groups, found similar results for their system which contained benzimidazol-2-yl groups substituted at the 2- and 6-positions of the DPA motifs.[196] The UV/Vis titration results of this system with Eu^{3+} gave changes that supported the presence of a 2:1 ligand:Ln^{3+} complex.[196] However, this finding did not align with fluorescence titration results, which supported the presence of a 3:1 ligand:Ln^{3+} complex.[196] Thus, further studies are required confirm the $\mathbf{R_3}$:Ln^{3+} binding ratio.

2.6.2.2 Amide-protected rotaxane ligands- simultaneous chelator and stopper

With methyl-protected rotaxanes **R$_2$**, **R$_3$** and **R$_4$** synthesized, we next chose to explore the possibility of synthesizing the secondary or primary amide derivatives through AT-CuAAC chemistry and to investigate the ability of these groups to act as simultaneous stoppers and chelators (Fig. 107). Multiple studies that have reported the formation of 3:1 ligand:Ln^{3+} complexes with the ligand containing the amide chelating motif.[185,186,196,199,201,203,207-209,275,277]

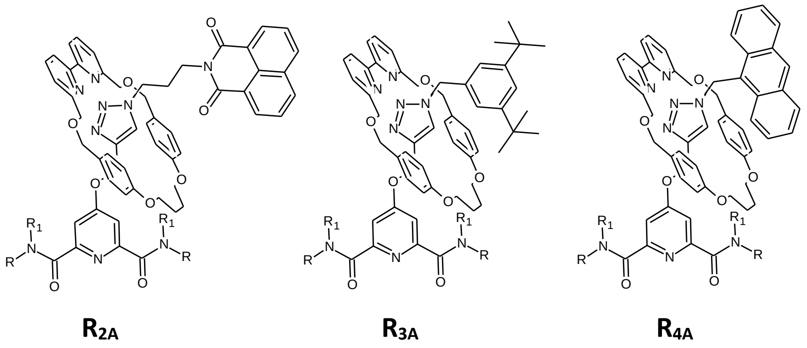

Figure 107. Structures of the target amide-protected rotaxane ligands R$_{2A}$, R$_{3A}$ and R$_{4A}$

The target ligands, shown above, were planned to contain the same stopper groups as their methyl-protected versions (Fig. 107). These were planned to be synthesized through an AT-CuAAC reaction between the required azide *i.e.* **2N$_3$**, **3N$_3$** or **4N$_3$**, **M$_1$** and an amide version of the key intermediate **2** (**2$_A$**) (Fig. 108).

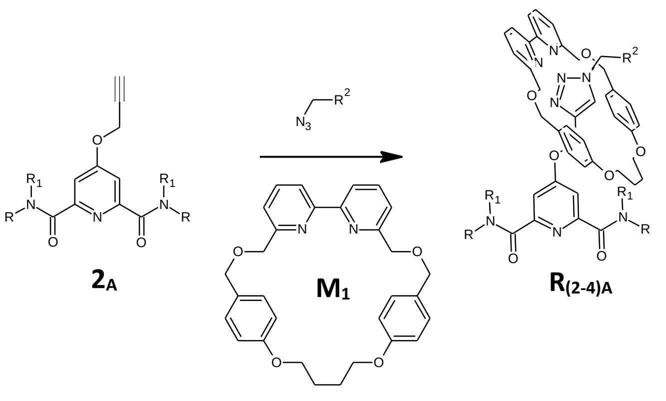

Figure 108. General reaction scheme for the synthesis of R$_{(2-4)A}$ using AT-CuAAC

The first step involved the synthesis of key intermediate **2$_A$**. To do this, two different methods were investigated. The first method began from methyl-protected chelidamic acid (**1**) (A in Fig. 109) whereas the other began from **L$_1$** (B in Fig. B).[185,186,196,199,201-203,207-209,275,277-280]

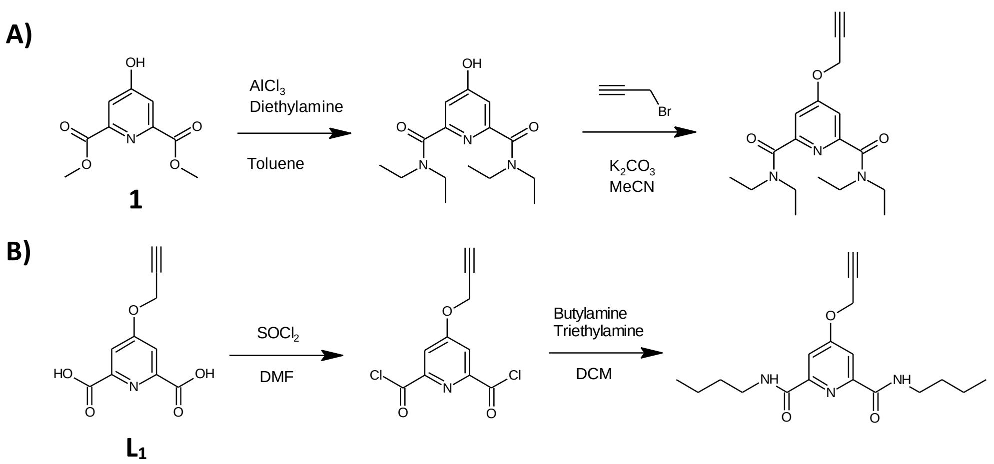

Figure 109. General reaction scheme for the synthesis of alkyne-functionalized amides of the 2$_A$ family showing the AlCl$_3$ method (A) and the SOCl$_2$ (B)

Method A was attempted initially which involved two steps (Fig. 109). The first step was the conversion of the 2,6-ester groups of **1** into 2,6-amide groups using aluminium chloride (AlCl$_3$) in the presence of diethylamine.[196,202,203] To do this, dried toluene was cooled in an ice bath under N$_2$. Next, AlCl$_3$ (6 equivalents) was added to the toluene mixture (in portions) under N$_2$ at 0˚C followed by the addition of diethylamine (15 equivalents) dropwise.[196,202,203] The reaction mixture was left to stir in the ice bath under N$_2$ for an hour. After this, **1** (1 equivalent) was added to the yellow reaction mixture which changed colour to red over approximately 2 hours. The reaction mixture was left to stir at 40˚C under N$_2$ for 12 hours after which it was quenched with deionised H$_2$O and extracted with DCM. After drying of the DCM layer with MgSO$_4$ and solvent removal, an orange/red oil resulted, the ^{1}H NMR of which showed that the product contained a 1:1 mixture of starting material **1** and amide product (Fig. S258). Attempts to purify this contaminated product by column chromatography with a 1:9 hexane:ethyl acetate mobile phase and a silica stationary phase were unsuccessful. The second step (which was not carried out due to time limitations) involved the attachment of the alkyne to the 4-pyridyl position of the 2,6-amide intermediate, making **2$_A$** for use in AT-CuAAC (Fig. 109).[196, 202,203]

Due to difficulties associated with method A, a different method was used beginning from the alkyne-functionalized 2,6-dicarboxylic acid, **L**$_{\mathbf{1}}$, as an attempt to synthesize **2**$_{\textbf{A-bis}}$ (Fig. 109 and Fig. 110). To do this, one equivalent of **L**$_{\mathbf{1}}$ was suspended in an excess of thionyl chloride (10 mL) and the pale beige reaction mixture was left to stir under nitrogen at room temperature for 12 hours (Fig. 109). Next, the thionyl chloride remaining was removed from the pale white reaction mixture under a nitrogen stream leaving a white solid. Following this, the solid was suspended in dried DCM (30 mL) under N_2 forming a pale white suspension (Fig. 109). Next, two equivalents each of butylamine and triethylamine was added to the suspension under nitrogen and the solid appeared to dissolve, forming a yellow reaction mixture that was stirred under nitrogen for 12 hours at room temperature. After this, a pale beige precipitate appeared which was collected by removing the DCM under reduced pressure.

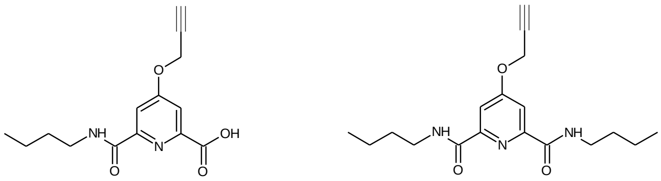

2$_{\textbf{A-mono}}$ **2**$_{\textbf{A-bis}}$

Figure 110. Structures of $2_{\text{A-mono}}$ *and* $2_{\text{A-bis}}$

The resulting ^{1}H NMR spectrum showed evidence of successful amide bond formation, however there appeared to be a mixture of products remaining, including mono- and bis- substituted amides (**2**$_{\textbf{A-mono}}$ and **2**$_{\textbf{A-bis}}$, respectively) (Fig. 111). The ^{1}H NMR showed a range of multiplets between 0 – 2 ppm (indicative of alkyl peak splitting) thus these have been omitted from the image for clarity (Fig. 111). There appeared to be two down-field shifted triplets, one at 9.28 ppm integrating as 2 and another at 9.19 ppm integrating as 1, which could be assigned to the two amide hydrogens in $2_{\text{A-bis}}$ and the one amide hydrogen in $2_{\text{A-mono}}$ (respectively) (Fig. 111 an Fig. S260).[187] These peaks supported the formation of the mono- and bis- substituted amides in the 1:1 ratio as **2**$_{\textbf{A-bis}}$ contains symmetry, thus the amide peaks on each side would be expected to show as a single triplet whereas **2**$_{\textbf{A-mono}}$ is asymmetric and only has one amide proton (Fig. 111).[187] Next, there appeared to be two doublets at 7.79 and 7.75 ppm, each integrating as 1 hydrogen and containing the same

J-coupling constant (2.5 Hz) (Fig. 111).[187] These doublets could be assigned to each of the 3- and 5- substituted pyridyl protons in **2**$_{\textbf{A-mono}}$ (due to asymmetry) (Fig. 111).[187] Additionally, the singlet peak next to these doublets at 7.71 ppm could be assigned to the 3- and 5- substituted pyridyl protons in **2**$_{\textbf{A-bis}}$ (due to symmetry) (Fig. 111).[187]

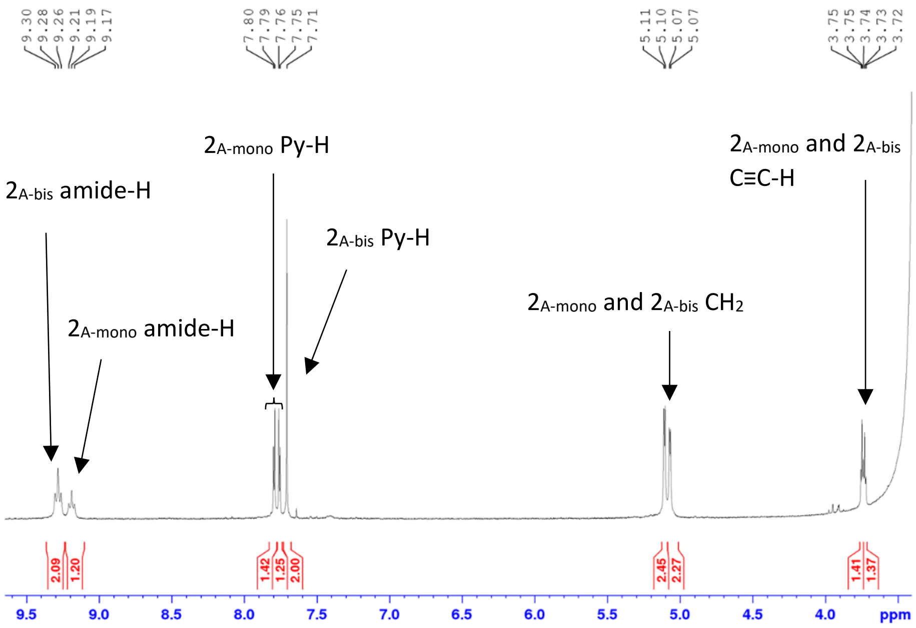

Figure 111. ^{1}*H NMR spectrum of the product obtained using method B, showing a mix of* $2_{\text{A-mono}}$ *and* $2_{\text{A-bis}}$

Two doublets at 5.07 and 5.10 ppm were also observed (each integrating as 2 hydrogens with *J*-coupling constants of 2.3 Hz), one of which could be assigned to the CH_2 protons of **2**$_{\textbf{A-mono}}$ and the other assigned to **2**$_{\textbf{A-bis}}$, appearing as doublets due to allylic coupling from their corresponding alkyne hydrogens, appearing as two triplets at 3.75 and 3.73 ppm (Fig. 111).[187]

In saying this, further studies are required to develop these amide-protected DPA ligands and to carry out AT-CuAAC reactions on their alkyne-substituted derivatives (**2**$_{\textbf{A}}$) for the formation of the target quasi-[4]-rotaxanes.

3. Future work and conclusions

Ligands **L_2** – **L_4** were synthesized using CuAAC ‘click’ chemistry and characterised through spectroscopic techniques. **L_1** – **L_3** were complexed with La^{3+}, Eu^{3+} and Tb^{3+} (*i.e.* made by the preformed ligand route) and their resulting complexes were characterised. Complexes with La^{3+} were used for analysis to support Ln^{3+} binding via NMR spectroscopy. In the case of Eu^{3+} and Tb^{3+}, the resulting complexes were highly luminescent and their photophysical properties were analysed. **L_4** was complexed with La^{3+} and provided NMR data supporting its formation however due to time constraints, complexation with Eu^{3+} and Tb^{3+} was unable to be carried out. The results showed that ligands **L_1** – **L_3**, containing 4-pyridyl substituted groups suitable for rotaxane synthesis were able to sensitize Ln^{3+} emission, providing promising results for the use of these ligands for development into quasi-[4]-rotaxanes.

To synthesize these quasi-[4]-rotaxanes, a proposed method was to perform an AT-CuAAC reaction on an alkyne-appended DPA complexes from the **$[Ln(L_1)_3]^{3-}$** family. Before this method was investigated, a proof-of-concept study was undertaken to ensure that the **$[Ln(L_1)_3]^{3-}$** complexes remain in their stable 3:1 ligand:Ln^{3+} ratio in the presence copper ions (involved in the CuAAC reactions). Under mild conditions, a naphthalimide functionalized azide, **$2N_3$**, appeared to click successfully (based on NMR results) to **$[La(L_1)_3]^{3-}$**, forming **$[La(L_2*)_3]^{3-}$**. Due to this, an AT-CuAAC reaction was attempted on **$[La(L_1)_3]^{3-}$** however difficulties to achieve suitable reaction conditions were faced such that no AT-CuAAC (or normal CuAAC) click reactions appeared to be occurring.

Due to these difficulties, as well as poor stoppering ability of the DPA carboxylate form, we next aimed to synthesize a family of [2]rotaxane DPA-ligands which contained a group suitable for both Ln^{3+} complexation and **M_1** stoppering (*i.e.* methyl-protected DPA and amide-protected DPA groups). This was done so that the AT-CuAAC reaction could be carried out prior to complexation which, on the addition of Ln^{3+}, would self-assemble to form the quasi-[4]-rotaxanes. Methyl-protected rotaxane ligands, **R_2** – **R_4** were synthesized and characterized through NMR and HRMS. Subsequently, the ability of **R_3** to form 3:1 **R_3**:Eu^{3+} complexes was investigated through UV/Vis and fluorescence titrations. UV/Vis titrations supported the formation of a 2:1 species whereas fluorescence titrations supported the formation of a 3:1 species. Thus, $\mathbf{R_3}$ appears to form complexes with Eu^{3+} however further studies are required to determine the binding ratios with Eu^{3+}. Amide-protected rotaxane ligands $\mathbf{R_{2A}}$ – $\mathbf{R_{4A}}$ were unable to be synthesized due to time limitations, however preliminary studies regarding synthesis of a key intermediate $\mathbf{2_A}$ were established.

Future studies may include the introduction water-soluble (*i.e.* charged) groups to the 4-pyridyl DPA position for biological applications. In addition to improved water solubility, the introduction of charged groups into rotaxane axles has been reported to influence macrocycle shuttling which, as proven by the studies, can influence Ln^{3+} emission. Thus, these systems may be promising targets for the development of Ln^{3+} systems with luminescent properties dependant on the macrocycle position.

Additionally, the deposition of these quasi-[4]-rotaxanes onto solid surfaces would also be a key area of future research, particularly for materials development.[9] This could be investigated by attaching long-chains to the 4-DPA position to enable deposition. Additionally, as carried out by Chamas and co-workers, one option may be to click a silyl group to the 4-pyridyl position of DPA as complexes containing these ligands can be deposited onto glass slides using spin-coating.[72]

In summary, the studies throughout this thesis provide foundational research for synthesis of a family of interlocked quasi-[4]-rotaxanes. This research can be used as a springboard for the development of a range of responsive luminescent materials with applications ranging from molecular sensor devices to molecule switches.

4. Experimental

Synthesis of dimethyl 4-hydroxypyridine-2,6-dicarboxylate (1)

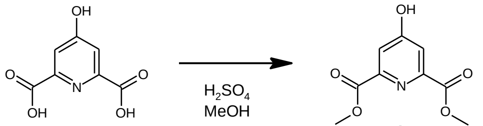

1

Chelidamic acid (1.08 g, 5.90 mmol, 1 equivalent) was suspended in HPLC grade methanol (80 mL) and stirred at approximately 90 ˚C for 5 minutes. Next, concentrated sulfuric acid (0.11 mL, 2.06 mmol, 0.35 equivalents) was added dropwise to the stirring solution of chelidamic acid in methanol. The dark brown reaction mixture was left to reflux at approximately 90 ˚C for 4 hours. The dark brown reaction mixture was cooled, and the methanol was removed by rotary evaporation leaving a dark brown oil. This dark brown oil was suspended in deionised H_2O (100 mL) and extracted four times with ethyl acetate (20 mL aliquots). The organic ethyl acetate layers were combined, dried using magnesium sulfate, filtered and the solvent was removed by rotary evaporation leaving a pale orange solid which was isolated as the product (0.82 g, 3.88 mmol, 66 %), mp 159 ˚C. FTIR (ATR, cm^{-1}): 3222 (O-H), 2966 (C-H), 2708, 2464, 1731 (C=O), 1685 (C=O), 1608 (C=C), 1584, 1477, 1446 (C=C), 1367, 1277, 1259, 1229, 1184, 1147, 1108, 1028, 1003, 991, 978, 940, 919, 893, 804, 786, 737, 701, 610, 585, 545, 436; UV/Vis (λmax, MeOH): 213 nm, ε = 30,120.7 L mol^{-1} cm^{-1}, 243 nm, ε = 5198.2 L mol^{-1} cm^{-1}, 286 nm, 1640.0 L mol^{-1} cm^{-1}; ^{1}H NMR (300.18 MHz, DMSO-*d*$_6$, ppm): δ = 11.65 (br, 1H, *OH*), 7.58 (s, 2H, *Py-H*), 3.88 (s, 6H, CH_3). ^{13}C NMR (75 MHz, DMSO-*d*$_6$, ppm): δ = 166.0, 164.9, 149.3, 115.3, 52.7.

Synthesis of dimethyl 4-[(prop-2-yn-1-yl)oxy]pyridine-2,6-dicarboxylate (2)

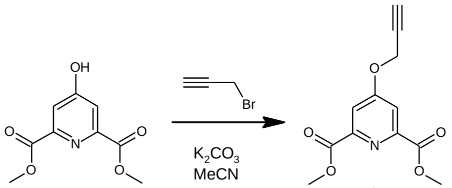

2

Dimethyl 4-hydroxypyridine-2,6-dicarboxylate (**1**) (0.58 g, 2.74 mmol, 1 equivalent) was combined with anhydrous potassium carbonate (3.78 g, 27.4 mmol, 10 equivalents) and HPLC grade acetonitrile (40 mL) and the reaction mixture was stirred under nitrogen for 30 minutes. Next, propargyl bromide solution (80 wt. % in toluene) (0.46 mL, 4.11 mmol, 1.5 equivalents) was added and the reaction mixture was stirred at 90 ˚C for 12 hours. After 12 hours, the cloudy pale orange reaction mixture was filtered through filter paper and the solvent was removed from the filtrate by rotary evaporation. Next, this crude solid was dissolved in chloroform (60 mL) and washed three times with deionised H_2O (50 mL aliquots). After washing, the chloroform layer was dried with $MgSO_4$, filtered, and the solvent was removed by rotary evaporation leaving a pale-yellow solid which was isolated as the product (0.41 g, 1.64 mmol, 60 %), mp 149 ˚C. FTIR (ATR, cm^{-1}): 3243, 3098, 3085, 3003, 2956 (C-H), 2350, 2343, 2330, 2297, 2119 (C≡C-H), 1717 (C=O), 1598 (C=C), 1569, 1439 (C=C), 1385, 1337, 1290, 1268, 1247, 1186, 1155, 1107, 1038, 1022, 989, 975, 937, 912, 879, 785, 733, 700, 670, 647, 588, 557, 537, 452, 409; UV/Vis (λmax, ACN): 212 nm, ε = 34,299.8 L mol^{-1} cm^{-1}, 236 nm, ε = 6161.7 L mol^{-1} cm^{-1}, 268 nm, ε = 263.5 L mol^{-1} cm^{-1}; ^{1}H NMR (300.18 MHz, DMSO-d_6, ppm): δ = 7.81 (s, 2H, *Py-H*), 5.11 (d, *J* = 2.3 Hz, 2H, *CH_2*), 3.91 (s, 6H, *CH_3*), 3.76 (t, *J* = 2.3 Hz, 1H, *Alkyne-H*). ^{13}C NMR (75 MHz, DMSO-d_6, ppm): δ = 165.2, 164.6, 149.4, 114.6, 80.0, 77.7, 56.6, 52.9.

Synthesis of L_1 and $[Ln(L_1)_3]^{3-}$ complexes

Synthesis of 4-[(prop-2-yn-1-yl)oxy]pyridine-2,6-dicarboxylic acid (L_1)

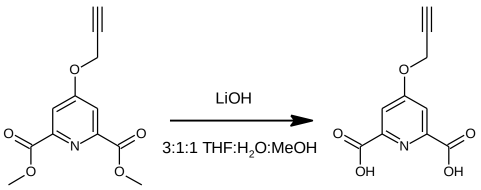

2 **L_1**

Dimethyl 4-[(prop-2-yn-1-yl)oxy]pyridine-2,6-dicarboxylate (**2**) (0.33 g, 1.32 mmol, 1 equivalent) was combined with lithium hydroxide (0.15 g, 6.10 mmol, 4.6 equivalents). These solids were then suspended in a 3:1:1 THF:H_2O:MeOH solvent mixture (20 mL) and stirred under nitrogen at room temperature for 12 hours. After 12 hours, the clear yellow reaction mixture was reduced to a residue using a rotary evaporator and approximately 20 mL of HCl (1 M) was added resulting in the precipitation of a pale-yellow solid. The solid was collected by filtration, followed by a wash through with deionised H_2O (20 mL) leaving the product as a pale yellow/white solid (0.25 g, 1.11 mmol, 84 %), mp 213 – 214 ˚C. FTIR (ATR, cm^{-1}): 3854, 3839, 3736, 3677, 3650, 3629, 3481, 3340, 3295, 3089, 3034 (COOH), 2380, 2343, 2330, 2137 (C≡C-H), 1890, 1735 (C=O), 1654, 1594 (C=C), 1568, 1478, 1463, 1446, 1402 (C=C), 1368, 1331, 1300, 1275, 1188, 1173, 1119, 1032, 998, 944, 902, 872, 835, 801, 787, 750, 703, 677, 641, 605, 579, 507, 409; UV/Vis (λmax, MeOH): 212 nm, $\varepsilon = 29{,}997.9$ L mol^{-1} cm^{-1}, 242 nm, $\varepsilon = 4994.6$ L mol^{-1} cm^{-1}, 273 nm, $\varepsilon = 1377.4$ L mol^{-1} cm^{-1}; ^{1}H NMR (300.18 MHz, DMSO-d_6, ppm): $\delta = 7.78$ (s, 2H, *Py-H*), 5.10 (d, $J = 2.3$ Hz, 2H, *CH_2*), 3.75 (t, $J = 2.2$ Hz, 1H, *Alkyne-H*). ^{13}C NMR (75 MHz, DMSO-d_6, ppm): $\delta = 165.4$, 165.3, 149.9, 114.1, 79.9, 77.8, 56.5.

Synthesis of $[La(L_1)_3]^{3-}$

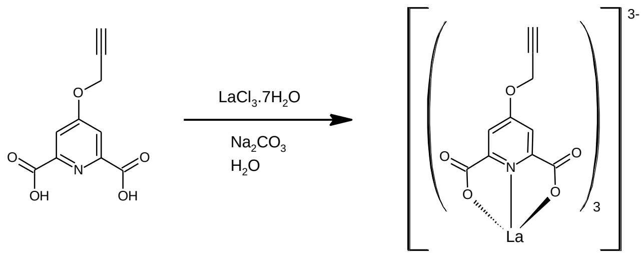

L_1 **$[La(L_1)_3]^{3-}$**

4-[(prop-2-yn-1-yl)oxy]pyridine-2,6-dicarboxylate (**L_1**) (0.0438 g, 0.1982 mmol, 1 equivalent) was combined with anhydrous sodium carbonate (0.0474 g, 0.4472 mmol, 2.3 equivalents), suspended in deionised H_2O (2 mL) and the reaction mixture was stirred at 60 ˚C for 10 minutes. Next, 88.0 µL of a 0.751 M solution of lanthanum(III) chloride heptahydrate in water (0.0245 g, 0.0661 mmol, 0.33 equivalents) was added to the reaction mixture resulting in the precipitation of a white solid. The reaction mixture was left to stir at 60 ˚C for 30 minutes. After stirring, the water was removed by rotary evaporation leaving a white solid which was suspended and stirred in acetone overnight. The white solid was collected by filtration and was isolated as the product (0.0816 g, 0.0943 mmol, quantitative). FTIR (ATR, cm^{-1}): 3610, 3383 (O-H), 3289, 3211, 3068, 2466, 2132, 1920, 1687, 1613 (C=C), 1588 (COO^- asymmetric stretch), 1570, 1441 (C=C), 1414, 1365 (COO^- symmetric stretch), 1301, 1266, 1119, 1036 (C-O), 998, 953, 924, 892, 875, 854, 834, 810, 740, 695, 657, 641, 615, 575, 408; UV/Vis (λmax, H_2O): 208 nm, $\varepsilon = 55{,}347.9$ L mol^{-1} cm^{-1}, 243 nm, $\varepsilon = 8690.0$ L mol^{-1} cm^{-1}, 272 nm, $\varepsilon = 2610.0$ L mol^{-1} cm^{-1}; ^1H NMR (300.18 MHz, DMSO-d_6, ppm): $\delta = 7.44$ (s, 2H, *Py-H*), 5.00 (s, 2H, *CH_2*), 3.66 (s, 1H, *Alkyne-H*). ^{13}C NMR (75 MHz, DMSO-d_6, ppm): $\delta = 169.0$, 165.7, 155.1, 110.3, 79.4, 78.3, 55.9.

Synthesis of [Eu(L_1)$_3$]$^{3-}$

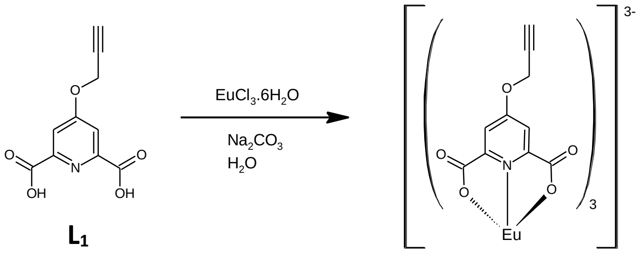

L_1

[Eu(L_1)$_3$]$^{3-}$

4-[(prop-2-yn-1-yl)oxy]pyridine-2,6-dicarboxylate (**L_1**) (0.0620 g, 0.2805 mmol, 1 equivalent) was combined with anhydrous sodium carbonate (0.0601 g, 0.5670 mmol, 2 equivalents), suspended in deionised H_2O (2 mL) and stirred at approximately 60 ˚C for 15 min. Next, 185.8 µL of a 0.504 M solution of europium(III) chloride hexahydrate in water (0.0343 g, 0.0936 mmol, 0.33 equivalents) was added to the reaction mixture resulting in the precipitation of a white solid which redissolved on heating. The reaction mixture was stirred and heated at approximately 60 ˚C for a further 30 min. After stirring, the water was removed by rotary evaporation leaving a white solid. This white solid was stirred in acetone overnight and filtered leaving a white solid which appeared red under short wave UV light and was isolated as the product (0.0754 g, 0.0858 mmol, 92 %). FTIR (ATR, cm^{-1}): 3369 (O-H), 3254, 2122, 1920, 1585 (COO$^-$ asymmetric stretch), 1455, 1405 (COO$^-$ symmetric stretch), 1343, 1305, 1273, 1117, 1042 (C-O), 1012, 939, 902, 884, 833, 810, 742, 686, 635, 566, 504, 422; UV/Vis (λmax, H_2O): 209 nm, ε = 59,155.0 L mol^{-1} cm^{-1}, 243 nm, ε = 9120.0 L mol^{-1} cm^{-1}, 272 nm, ε = 2420.0 L mol^{-1} cm^{-1}; ^{1}H NMR (300.18 MHz, DMSO-d_6, ppm): δ = 4.61 (s, 2H, *Py-H*), 4.21 (s, 2H, *CH$_2$*), 3.26 (s, 1H, *Alkyne-H*). ^{13}C NMR (75 MHz, DMSO-d_6, ppm): δ = 178.4, 165.1, 139.6, 78.9, 77.9, 65.8, 54.9.

Synthesis of $[Tb(L_1)_3]^{3-}$

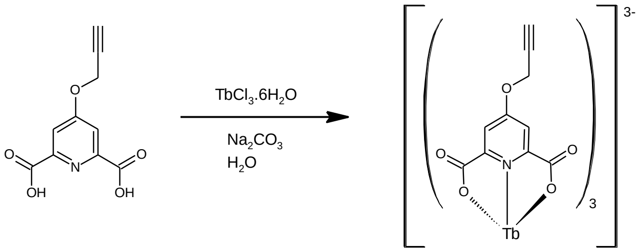

L_1 **$[Tb(L_1)_3]^{3-}$**

L_1 (0.0506 g, 0.2290 mmol, 1 equivalent) was combined with anhydrous sodium carbonate (0.0494 g, 0.4661 mmol, 2 equivalents) and stirred in deionised H_2O (3 mL) at 60 ˚C for 15 minutes. Next, 190.0 µL of a 0.398 M solution of terbium(III) chloride hexahydrate in H_2O was added to the stirring solution of **L_1** and Na_2CO_3 causing a white solid to precipitate out which redissolved on heating. The reaction mixture was further stirred at 60 ˚C for 30 minutes after which the water was removed by rotary evaporation, leaving a white solid. This white solid was suspended and stirred in acetone overnight after which the white solid was collected by filtration. This solid was green under UV light and was isolated as the product (0.050 g, 0.0565 mmol, 75 %). FTIR (ATR, cm^{-1}): 3849, 3741, 3707, 3684, 3654, 3295 (O-H), 2330, 2123, 1947, 1738, 1612, 1587 (COO^- asymmetric stretch), 1503, 1461, 1441, 1410 (COO^- symmetric stretch), 1346, 1307, 1273, 1117, 1044 (C-O), 1013, 941, 902, 884, 837, 807, 745, 700, 685, 624, 561, 506, 424; UV/Vis (λmax, H_2O): 209 nm, ε = 58,930.4 L mol^{-1} cm^{-1}, 243 nm, ε = 9240.0 L mol^{-1} cm^{-1}, 271 nm, ε = 2580.0 L mol^{-1} cm^{-1}; ^1H NMR (300.18 MHz, DMSO-d_6, ppm): δ = 9.07 (br s). ^{13}C NMR (75 MHz, DMSO-d_6, ppm): δ = 87.2.

Synthesis of L_2 and $[Ln(L_2)_3]^{3-}$ complexes

Synthesis of 2-(3-hydroxypropyl)-1H-benzo[de]isoquinoline-1,3(2H)-dione

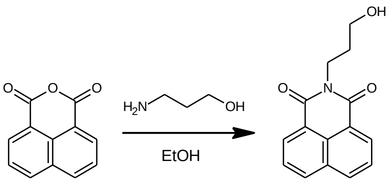

1,8-Naphthalic anhydride (1.39 g, 7.03 mmol, 1 equivalent) was suspended in ethanol (60 mL) and 3-amino-1-propanol (0.54 mL, 0.53 g, 7.03 mmol, 1 equivalent) was pipetted into the reaction mixture. The cloudy yellow reaction mixture slowly turned a transparent yellow colour as it was stirred at 100 ˚C for 2 hours. After cooling to room temperature, the reaction mixture was placed in an ice bath resulting in the precipitation of a pale yellow/white fluffy solid. The solid was collected by filtration, washed with cold ethanol and was isolated as the product (1.10 g, 4.39 mmol, 61 %), mp 123.1 ˚C. FTIR (ATR, cm^{-1}): 3426 (O-H), 3067, 2936, 2875 (C-H), 1692 (C=O), 1640 (C=O), 1617 (C=C), 1586, 1512, 1466, 1438, 1405, 1389, 1366, 1342, 1265, 1244, 1234, 1206, 1172, 1139, 1113, 1081, 1068, 1048, 1028, 1015, 996, 958, 921, 880, 858, 847, 799, 782, 739, 686, 656, 605, 539, 520, 450, 436, 407; UV/Vis (λmax, MeOH): 203 nm, ε = 87,685.6 L mol^{-1} cm^{-1}, 231 nm, ε = 42,586.8 L mol^{-1} cm^{-1}, 331 nm, ε = 11,755.3 L mol^{-1} cm^{-1}, 341 nm, ε = 11,195.0 L mol^{-1} cm^{-1}; ^{1}H NMR (300.18 MHz, $CDCl_3$, ppm): δ = 8.61 (d, *J* = 7.3 Hz, 2H, *Naph-H*), 8.23 (d, *J* = 8.3 Hz, 2H, *Naph-H*), 7.78 (t, *J* = 7.8 Hz, 2H, *Naph-H*), 4.36 (t, *J* = 6.1 Hz, 2H, CH_2), 3.59 (t, *J* = 5.6 Hz, 2H, CH_2), 3.16 (s, 1H, *OH*), 2.00 (quintet, *J* = 5.9 Hz, 2H, CH_2). ^{13}C NMR (75 MHz, $CDCl_3$, ppm): δ = 165.1, 134.5, 131.8, 131.7, 128.3, 127.2, 122.4, 58.9, 36.9, 31.1.

Synthesis of 2-(3-bromopropyl)-1H-benzo[de]isoquinoline-1,3(2H)-dione

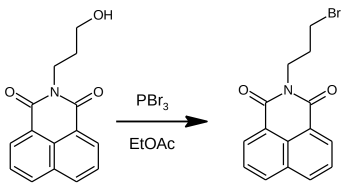

2-(3-hydroxypropyl)-1*H*-benzo[*de*]isoquinoline-1,3(*2H*)-dione (0.94 g, 3.67 mmol, 1 equivalent) was dissolved in dried ethyl acetate (20 mL) and phosphorus tribromide (0.69 mL, 1.97 g, 7.28 mmol, 1.98 equivalents) was added. The cloudy pale-yellow reaction mixture was refluxed at 77 ˚C for 6 hours. After 5 hours, the reaction mixture was cooled to room temperature and ice-cold H_2O (40 mL) was added. Next, the reaction mixture was transferred to a separating funnel and extracted with ethyl acetate. The ethyl acetate layer was then washed two times with deionised H_2O (50 mL aliquots) and dried with $MgSO_4$. The $MgSO_4$ was then filtered off and the solvent was removed by rotary evaporation leaving a solid which was isolated as the product (0.94 g, 2.96 mmol, 81 %), mp 140.3 ˚C. FTIR (ATR, cm^{-1}): 2948 (C-H), 2330, 2301, 1694 (C=O), 1658 (C=O), 1622, 1586, 1510, 1440, 1382, 1359, 1336, 1242, 1210, 1167, 1137, 1084, 1028, 1010, 949, 886, 846, 800, 778, 740, 672, 619, 542, 483 (C-Br), 412; UV/Vis (λmax, MeOH): 203 nm, ε = 76,083.5 L mol^{-1} cm^{-1}, 231 nm, ε = 36,584.9 L mol^{-1} cm^{-1}, 331 nm, ε = 10,610.2 L mol^{-1} cm^{-1}, 341 nm, ε = 10,083.2 L mol^{-1} cm^{-1}; ^{1}H NMR (300.18 MHz, $CDCl_3$, ppm): δ = 8.61 (dd, *J* = 7.3, 1.1 Hz, 2H, *Naph-H*), 8.23 (dd, *J* = 8.3, 1.0 Hz, 2H, *Naph-H*), 7.77 (dd, *J* = 8.2, 7.4 Hz, 2H, *Naph-H*), 4.34 (t, *J* = 7.1 Hz, 2H, CH_2), 3.51 (t, *J* = 6.9 Hz, 2H, CH_2), 2.34 (quintet, *J* = 7.0 Hz, 2H, CH_2). ^{13}C NMR (75 MHz, $CDCl_3$, ppm): δ = 164.4, 134.3, 131.8, 131.5, 128.3, 127.1, 122.6, 39.4, 31.6, 30.7.

Synthesis of 2-(3-azidopropyl)-1H-benzo[de]isoquinoline-1,3(2H)-dione (2N_3)

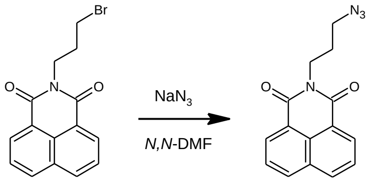

2N_3

2-(3-bromopropyl)-1*H*-benzo[*de*]isoquinoline-1,3(2*H*)-dione (0.55 g, 1.74 mmol, 1 equivalent) was combined with sodium azide (0.23 g, 3.52 mmol, 2.03 equivalents), dissolved in DMF (30 mL) and the transparent yellow/green reaction mixture was stirred at 80 ˚C for 12 hours. After 12 hours, the lime green reaction mixture was quenched with deionised H_2O and extracted with ethyl acetate (40 mL). The ethyl acetate layer was then washed a further six times with deionised H_2O after which it was collected, dried with $MgSO_4$, filtered and the ethyl acetate was removed by rotary evaporation. This left a white solid which was isolated as the product (0.24 g, 0.87 mmol, 50 %). ^{1}H NMR (300.18 MHz, $CDCl_3$, ppm): δ = 8.62 (dd, *J* = 7.3, 1.1 Hz, 2H, *Naph-H*), 8.23 (dd, *J* = 8.4, 1.0 Hz, 2H, *Naph-H*), 7.77 (dd, *J* = 8.2, 7.3 Hz, 2H, *Naph-H*), 4.30 (t, *J* = 7.0 Hz, 2H, CH_2), 3.44 (t, *J* = 6.9 Hz, 2H, CH_2), 2.05 (quintet, *J* = 7.0 Hz, 2H, CH_2). ^{13}C NMR (75 MHz, $CDCl_3$, ppm): δ = 164.4, 134.3, 131.8, 131.5, 128.3, 127.1, 122.6, 49.6, 38.0, 27.8.

Note: 2N_3 was stored in a -18˚C freezer

Synthesis of MeOL$_2$

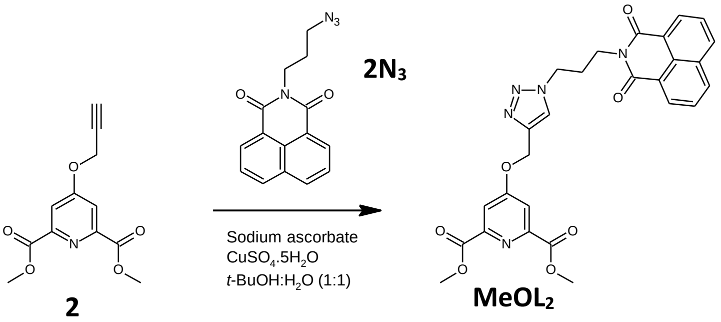

Dimethyl 4-[(prop-2-yn-1-yl)oxy]pyridine-2,6-dicarboxylate (**2**) (0.13 g, 0.54 mmol, 1 equivalent) was combined with sodium ascorbate (0.11 g, 0.54 mmol, 1 equivalent), 2-(3-azidopropyl)-1*H*-benzo[de]isoquinoline-1,3(2*H*)-dione (**2N$_3$**) (0.16 g, 0.56 mmol, 1.05 equivalents) and copper(II) sulfate pentahydrate (0.008 g, 0.03 mmol, 0.06 equivalents). The solids were then suspended in a *tert*-Butanol:H_2O (1:1) mixture (17.5 mL) and the pale-yellow reaction mixture was stirred at 80 ˚C for 4 hours over which the solids appeared to dissolve. The pale orange/yellow reaction mixture was cooled to room temperature and quenched with deionised H_2O causing the precipitation of a fine white solid which was collected by filtration. The solid was then suspended in a 0.5M EDTA/1M NaOH solution (approximately 40 mL) and left to filter by gravity overnight. After drying in a desiccator, the solid which was isolated as the product (0.23 g, 0.43 mmol, 80 %), mp 206.7 ˚C. FTIR (ATR, cm^{-1}): 3499, 3295, 3134, 2953 (C-H), 2337, 2319, 1915, 1750 (C=O), 1696, 1660, 1590 (C=C), 1438, 1422, 1406, 1384, 1343, 1299, 1240, 1192, 1162, 1121, 1104, 1035, 1015, 963, 943, 907, 876, 850, 839, 783, 728, 634, 583, 545, 507, 455, 425. ^{1}H NMR (300.18 MHz, DMSO-*d*$_6$, ppm): $\delta = 8.47$ (t, $J = 7.4$ Hz, 2H, *Naph-H*), 7.85 (m, 4H, *Naph-H* and *Py-H* combined), 5.41 (s, 2H, CH_2), 4.50 (t, $J = 7.1$ Hz, 2H, CH_2), 4.10 (t, $J = 6.9$ Hz, 2H, CH_2), 3.90 (s, 6H, CH_3), 2.23 (q, 3H (overlapping with DMSO-*d*$_6$ peak), CH_2). ^{13}C NMR (75 MHz, DMSO-*d*$_6$, ppm): $\delta = 165.9$, 164.6, 163.6, 149.4, 141.2, 134.3, 131.3, 130.7, 127.5, 127.2, 125.1, 122.2, 114.5, 62.1, 52.7, 47.7, 37.3, 28.4.

^{1}H NMR (300.18 MHz, $CDCl_3$, ppm): 8.60 (d, $J = 7.2$ Hz, 2H, *Naph-H*), 8.23 (d, $J = 8.0$ Hz, 2H, *Naph-H*), 7.96 (s, 1H, *Tz-H*), 7.91 (s, 2H, *Py-H*), 7.78 (t, $J = 7.7$ Hz, 2H, *Naph-H*), 5.34 (s, 2H,

CH_2), 4.52 (t, *J* = 6.7 Hz, 2H, *CH_2*), 4.28 (t, *J* = 6.4 Hz, 2H, *CH_2*), 2.44 (t, *J* = 6.5 Hz, 2H, *CH_2*). ^{13}C NMR (75 MHz, $CDCl_3$, ppm): 166.4, 165.2, 164.5, 150.0, 141.9, 134.5, 131.8, 131.8, 128.3, 127.2, 123.8, 122.4, 114.9, 62.6, 53.4, 48.6, 37.6, 29.0.

Synthesis of L_2

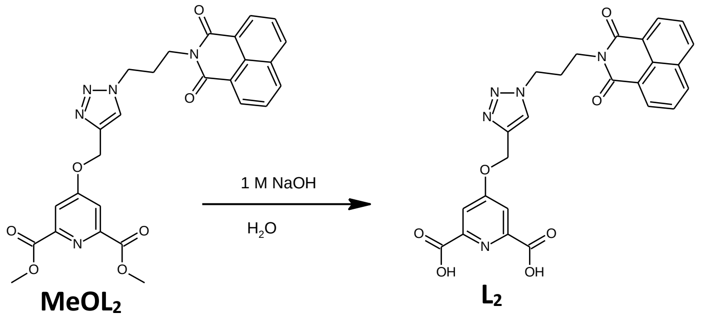

$MeOL_2$ (0.33 g, 0.63 mmol, 1 equivalent) was suspended in 15 mL deionised H_2O. Next, 1 M NaOH (2.52 mL, 2.52 mmol, 4 equivalents) was added and the cloudy white reaction mixture was stirred at 50 ˚C for 4 hours. After 4 hours, 2 M HCl (40 mL) was added to the transparent/slightly pale-yellow reaction mixture causing a white/pale-yellow solid to precipitate out. This solid was collected by filtration and washed with deionised H_2O. The solid was further stirred in acetone after which the acetone-soluble impurities were filtered off leaving a white solid which cause be isolated as the product, **L_2** (0.16 g, 0.33 mmol, 52 %), mp 156.4 – 178.2 ˚C. LRMS (ESI$^+$) (*m/z*): calcd for $(C_{25}H_{19}N_5O_7 + H)^+$ 502.4 found 501.8 and calcd for $(C_{25}H_{19}N_5O_7 + Na)^+$ 524.4 found 523.8 and calcd for $(C_{25}H_{19}N_5O_7 + K)^+$ 540.5 found 540.1. FTIR (ATR, cm^{-1}): 3484 (COOH), 3424, 3160, 3089, 2936, 2551, 1739, 1714 (C=O), 1694, 1646, 1625, 1588 (C=C), 1513, 1482 (C=C), 1444, 1415, 1388, 1348, 1301, 1273, 1238, 1221, 1196, 1169, 1140, 1116, 1069, 1044, 1032, 998, 964, 904, 896, 882, 848, 822, 779, 738, 695, 635, 608, 582, 544, 528, 495, 479, 422; UV/Vis (λmax, MeOH): 203 nm, ε = 89,219.1 L mol^{-1} cm^{-1}, 230 nm, 51,309.5 L mol^{-1} cm^{-1}, 331 nm, 13,112.1 L mol^{-1} cm^{-1}, 340 nm, 12,538.9 L mol^{-1} cm^{-1}; ^{1}H NMR (300.18 MHz, DMSO-*d_6*, ppm): δ = 8.48 (t, *J* = 8.2 Hz, 4H, *Naph-H*), 8.31 (s, 1H, *Tz-H*), 7.87 (t, *J* = 7.8 Hz, 2H, *Naph-H*), 7.82 (s, 2H, *Py-H*), 5.40 (s, 2H, *CH_2*), 4.50 (t, *J* = 6.8 Hz, 2H, *CH_2*), 4.11 (t, *J* = 6.6 Hz, 2H, *CH_2*), 2.24 (quintet, *J* = 7.1 Hz, 2H, *CH₂*). ^{13}C NMR (75 MHz, DMSO-*d₆*, ppm): δ = 166.3, 165.2, 163.6, 149.8, 141.3, 134.3, 131.3, 130.7, 127.5, 127.2, 125.1, 122.2, 113.9, 62.0, 47.7, 37.3, 28.4.

Note: In the ^{1}H NMR spectrum the quintet at 2.24 ppm was only being resolved as a triplet due to effects of underlying solvent peak.

For UV/Vis the 1 x 10^{-5} M solution of L_2 was made from a stock solution of 2:1 $CHCl_3$:MeOH.

Synthesis of $[La(L_2)_3]^{3-}$

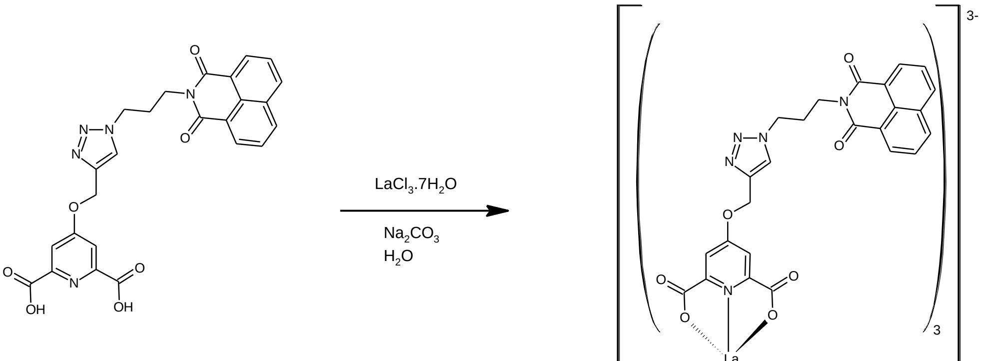

L_2

$[La(L_2)_3]^{3-}$

L_2 (0.0207 g, 0.0413 mmol, 1 equivalent) was combined with anhydrous sodium carbonate (0.0089 g, 0.0840 mmol, 2 equivalents) and dissolved in deionised H_2O (3 mL). Next, 50.6 μL of a 0.272 M solution of lanthanum(III) chloride heptahydrate (0.0051 g, 0.0137 mmol, 0.33 equivalents) in H_2O was added and the reaction mixture was stirred at 90 ˚C for 30 minutes. After this, the H_2O was removed by rotary evaporation leaving a white solid that was isolated as the product (0.0180 g, 0.0105 mmol, 77 %). FTIR (ATR, cm^{-1}): 3858, 3848, 3740, 3706, 3653, 3379 (O-H), 2961, 1696, 1655, 1586 (COO^- asymmetric stretch), 1512, 1502, 1441, 1416, 1384, 1346 (COO^- symmetric stretch), 1303, 1271, 1236, 1173, 1118, 1029 (C-O), 930, 908, 883, 847, 809, 779, 738, 705, 578, 541, 490; ^{1}H NMR (300.18 MHz, DMSO-*d₆*, ppm): δ = 8.48 (dd, *J* = 13.7, 7.8 Hz, 2H, *Naph-H*), 8.26 (s, 1H, *Tz-H*), 7.87 (t, *J* = 7.7 Hz, 2H, *Naph-H*), 7.42 (s, 2H, *Py-H*), 5.27 (s, 2H, *CH₂*), 4.50 (t, *J* = 7.1 Hz, 2H, *CH₂*), 4.14 (t, *J* = 6.8 Hz, 2H, *CH₂*), 2.25 (quintet, *J* =

6.9 Hz, 2H, *CH₂*). ^{13}C NMR (75 MHz, DMSO-d_6, ppm): δ = 168.9, 163.7, 155.3, 141.8, 134.3, 131.3, 130.8, 127.5, 127.2, 122.3, 47.8, 37.3.

Synthesis of [Eu(L₂)₃]$^{3-}$

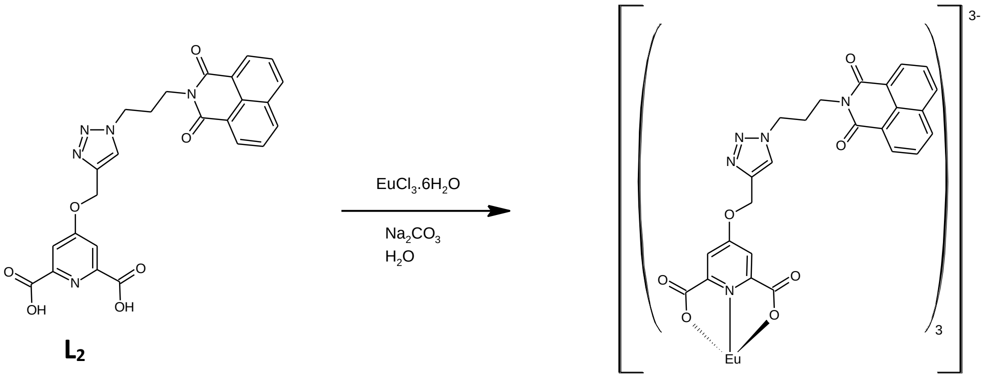

L₂

[Eu(L₂)₃]$^{3-}$

L₂ (0.0200 g, 0.040 mmol, 1 equivalent) was combined with anhydrous sodium carbonate (0.0088 g, 0.083 mmol, 2.1 equivalents) and dissolved in deionised H_2O (3 mL). The reaction mixture was stirred at 50 ˚C for 15 min forming a transparent solution with a yellow tinge. To this reaction mixture, 31.0 µL of a 0.428 M solution of europium(III) chloride hexahydrate (0.0049 g, 0.013 mmol, 0.33 equivalents) dissolved in H_2O was added resulting in the formation of a white precipitate which partially redissolved when heated at 50 ˚C for 5 min. As the reaction mixture cooled to room temperature, the solution turned cloudy and was left to settle for 2 days. After 2 days, a white/pale yellow precipitate appeared on the bottom of the vial which was collected by decanting off the water layer. The resulting white/pale yellow solid was dried and isolated as the product (0.0130 g, 0.0076 mmol, 57 %). HRMS m/z = 550.0883 $[Eu(L_2)_3]^{3-}$ (calc for $[C_{75}H_{51}N_{15}O_{21}Eu]^{3-}$, 550.0867 g mol^{-1}) and m/z = 825.6360 $\{[Eu(L_2)_3]^{3-} + H^+\}^{2-}$ (calc for $\{[C_{75}H_{51}N_{15}O_{21}Eu]^{3-} + H^+\}^{2-}$, 825.6335 g mol^{-1}). FTIR (ATR, cm^{-1}): 3369 (O-H), 1696, 1652, 1619, 1587 (COO^- asymmetric stretch), 1441, 1414, 1384, 1347 (COO^- symmetric stretch), 1273, 1236, 1173, 1116, 1037 (C-O), 930, 907, 839, 811, 780, 739, 700, 618, 582, 541, 409; UV/Vis (λmax, H_2O): 211 nm, ε = 120,853.8 L mol^{-1} cm^{-1}, 232 nm, ε = 79,864.5 L mol^{-1} cm^{-1}, 277 nm, ε = 7480.3 L mol^{-1} cm^{-1}, 342 nm, ε = 23,838.1 L mol^{-1} cm^{-1}; ^{1}H NMR (300.18 MHz, DMSO-d_6, ppm): δ = 8.42 (s, 2H, *Naph-H*), 8.40 (s, 2H, *Naph-H*), 7.81 (t, *J* = 7.5 Hz, 2H, *Naph-H*), 7.74 (s, 1H, *Tz-H*), 4.55 (s, 2H, *CH_2*), 4.41 (m, 2H, *Py-H*), 4.26 (t, *J* = 6.0 Hz, 2H, *CH_2*), 3.97 (t, *J* = 6.0 Hz, 2H, *CH_2*), 2.05 (t, *J* = 7.5 Hz, 2H, *CH_2*). ^{13}C NMR (75 MHz, DMSO-*d_6*, ppm): δ = 163.6, 141.3, 134.3, 131.3, 130.7, 127.4, 127.2, 124.2, 122.2, 60.7, 47.6, 37.2, 28.2.

Synthesis of $[Tb(L_2)_3]^{3-}$

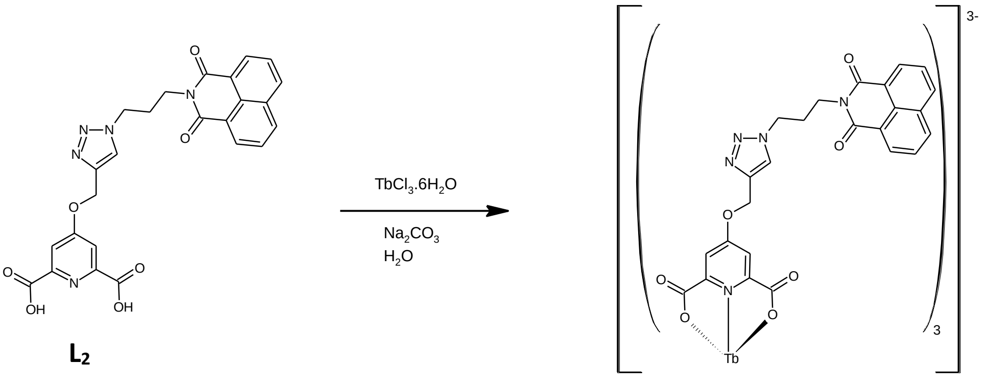

$[Tb(L_2)_3]^{3-}$

L_2 (0.0203 g, 0.040 mmol, 1 equivalent) was combined with anhydrous sodium carbonate (0.0086 g, 0.081 mmol, 2 equivalents) and suspended in deionised H_2O (3 mL). The reaction mixture was stirred at 50 ˚C for 15 min forming a transparent solution with a yellow tinge. To this reaction mixture, terbium(III) chloride hexahydrate (0.0050 g, 0.013 mmol, 0.33 equivalents) was added resulting in the formation of a white precipitate which redissolved partially on heating at 50 ˚C for 2 min. The reaction mixture was left at room temperature forming a cloudy solution which was left to settle. After 2 days, a white/pale yellow precipitate appeared to form on the bottom on the vial which was collected by decanting off the water. This white/pale yellow solid was isolated as the product (0.0152 g). HRMS m/z = 552.0894 $[Tb(L_2)_3]^{3-}$ (calc for $[C_{75}H_{51}N_{15}O_{21}Tb]^{3-}$, 552.0880 g mol^{-1}) and m/z = 828.6374 $\{[Tb(L_2)_3]^{3-} + H^+\}^{2-}$ (calc for $\{[C_{75}H_{51}N_{15}O_{21}Tb]^{3-} + H^+\}^{2-}$, 828.6360 g mol^{-1}). FTIR (ATR, cm^{-1}): 3378 (O-H), 2960, 2347, 2337, 2317, 2202, 2174, 2016, 1977, 1695, 1649, 1587 (COO$^-$ asymmetric stretch), 1513, 1461, 1440, 1412, 1384 (COO$^-$ symmetric stretch), 1342, 1307, 1274, 1236, 1173, 1117, 1037 (C-O), 1003, 932, 882, 848, 811, 779, 740, 710, 693, 649, 580, 540, 468, 448, 427; UV/Vis (λmax, H_2O): 211 nm, ε = 120,446.0 L mol^{-1} cm^{-1}, 228 nm, ε = 85,732.4 L mol^{-1} cm^{-1}, 277 nm, ε = 7711.0 L mol^{-1} cm^{-1}, 343 nm, ε = 23,896.9 L mol^{-1} cm^{-1}; ^{1}H NMR (300.18 MHz, DMSO-*d*$_6$, ppm): δ = 15.95 (br s, 1H), 9.71 (br s, 3H), 9.03 (br s, 3H), 8.54 (br s, 3H), 7.74 (br d, *J* = 56.0 Hz, 2H), 6.49 (br s, 2H), 5.19 (br s, 2H). ^{13}C NMR (75 MHz, DMSO-*d*$_6$, ppm): δ = 135.1, 132.0, 128.2.

Synthesis of $[La(L_2*)_3]^{3-}$

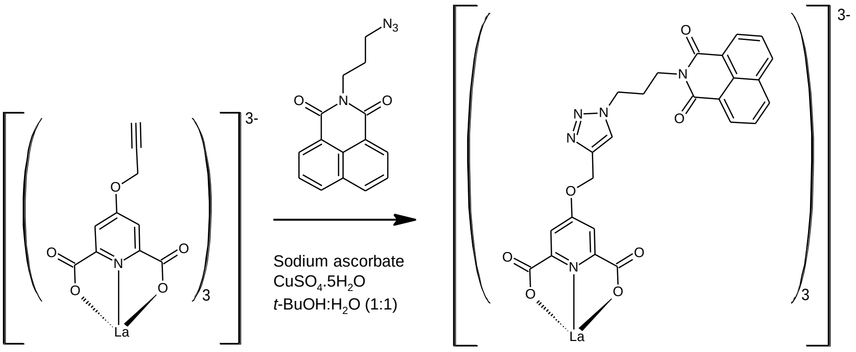

$[La(L_1)_3]^{3-}$ **$[La(L_2*)_3]^{3-}$**

$[La(L_1)_3]^{3-}$ (0.103 g, 0.12 mmol, 1 equivalent) was combined with sodium ascorbate (0.073 g, 0.37 mmol, 3 equivalents), **2N$_3$** (0.108 g, 0.39 mmol, 3.15 equivalents) and copper(II) sulfate pentahydrate (0.007 g, 0.03 mmol, 0.15 equivalents). These solids were subsequently suspended in a *tert*-Butanol:H$_2$O (1:1) (17.5 mL) solvent mixture and the pale-yellow reaction mixture was left to stir at 80 ˚C for 12 hours. After stirring at 80 ˚C for 12 hours, the reaction mixture appeared translucent yellow in colour and went cloudy as it was cooled to room temperature. Next, deionised H$_2$O was added to further encourage precipitation and the reaction mixture was transferred to a separating funnel. This aqueous layer was washed with diethyl ether (40 mL) to remove any unreacted **2N$_3$**. Next, the H$_2$O was removed from the aqueous layer under reduced pressure leaving a crude pale-yellow solid, the NMR of which showed impurities. Thus, the crude solid was resuspended in H$_2$O, heated, filtered whilst warm, and the solid precipitate was collected by filtration. An NMR of this precipitate showed **2N$_3$** remain which, after stirring of this crude product in diethyl ether, gave **$[La(L_2*)_3]^{3-}$** (0.012 g, 0.007 mmol, 5.9 %). FTIR (ATR, cm^{-1}): 3380 (O-H), 2368, 2363, 2358, 2353, 2342, 2332, 2304, 1698, 1656, 1587 (COO$^-$ asymmetric stretch), 1440, 1418, 1384, 1345 (COO$^-$ symmetric stretch), 1271, 1237, 1173, 1118, 1029 (C-O), 930, 894, 847, 809, 780, 738, 706, 634, 588, 541, 469; ^{1}H NMR (300.18 MHz, DMSO-d_6, ppm): δ = 8.49 (dd, *J* = 13.2, 7.7 Hz, 4H, *Naph-H*), 8.28 (s, 1H, *Tz-H*), 7.87 (t, *J* = 7.7 Hz, 2H, *Naph-H*), 7.43 (s, 2H, *Py-H*), 5.30 (s, 2H, CH_2), 4.50 (t, *J* = 7.0 Hz, 2H, CH_2), 4.14 (t, *J* = 6.5 Hz, 2H, CH_2), 2.25 (quintet, *J* = 6.6 Hz, 2H, CH_2). ^{13}C NMR (75 MHz, DMSO-d_6, ppm): δ = 163.7, 141.7, 134.3, 131.3, 130.8, 127.5, 127.2, 122.3.

Synthesis of L_3 and $[Ln(L_3)_3]^{3-}$ complexes

Synthesis of 1-(azidomethyl)-3,5-di-*tert*-butylbenzene ($3N_3$)

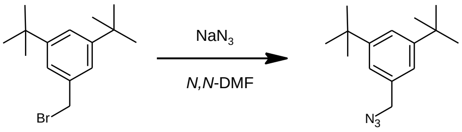

$3N_3$

3,5-di-*tert*-butylbenzyl bromide (0.19 g, 0.68 mmol, 1 equivalent) was combined with sodium azide (0.14 g, 2.08 mmol, 3 equivalents) in a round bottomed flask and the solids were suspended in *N,N*-DMF (5 mL) and stirred at 60 ˚C for 1 hour. After this, the reaction mixture was further stirred for 12 hr at room temperature. The cloudy white reaction mixture was then quenched with deionised H_2O (100 mL) and extracted two times with diethyl ether. These diethyl ether layers were combined and washed two times with deionised H_2O. Next, the diethyl ether was removed by rotary evaporation leaving a colourless oil which was isolated as the product (0.14 g, 0.58 mmol, 85 %). ^{1}H NMR (300.18 MHz, DMSO-d_6, ppm): 7.37 (t, *J* = 1.8 Hz, 1H, *Ar-H*), 7.18 (d, *J* = 1.8 Hz, 2H, *Ar-H*), 4.42 (s, 2H, CH_2), 1.29 (s, 18H, *Tert-butyl H*). ^{13}C NMR (75 MHz, DMSO-d_6, ppm): 150.7, 134.8, 122.6, 121.6, 54.2, 34.5, 31.2.

Synthesis of dimethyl 4-({1-[(3,5-di-tert-butylphenyl)methyl]1H-1,2,3-triazol-4-yl}methoxy)pyridine-2,6-dicarboxylate (MeOL$_3$)

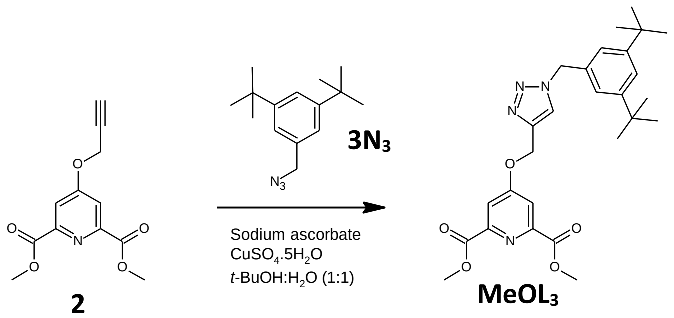

Dimethyl 4-[(prop-2-yn-1-yl)oxy]pyridine-2,6-dicarboxylate (**2**) (0.14 g, 0.57 mmol, 1 equivalent), 1-(azidomethyl)-3,5-di-*tert*-butylbenzene (**3N$_3$**) (0.15 g, 0.60 mmol, 1.05 equivalents), sodium ascorbate (0.12 g, 0.59 mmol, 1 equivalent) and copper(II) sulfate pentahydrate (0.01 g, 0.03 mmol, 0.06 equivalents) were combined in a round bottomed flask. These solids were then suspended in a 1:1 *tert*-Butanol:H_2O solvent mixture (17.5 mL) and the yellow reaction mixture was stirred at 60 ˚C overnight. The next day, the pale orange reaction mixture was quenched with deionised H_2O (50 mL) and filtered. The remaining solid was then suspended in 0.5 M EDTA/1 M NaOH (50 mL) solution and slowly filtered. Following this, the solid was resuspended in deionised H_2O (50 mL) to remove any leftover EDTA/NaOH and filtered leaving a beige solid which was isolated as the product (0.19 g, 0.37 mmol, 65 %). FTIR (ATR, cm^{-1}): 3139, 3089, 2960 (C-H), 2865, 2342, 2330, 2137, 1715 (C=O), 1597 (C=C), 1562, 1455, 1441 (C=C), 1389, 1357, 1330, 1287, 1255, 1228, 1198, 1180, 1156, 1134, 1112, 1056, 1035 (C-O), 1020, 995, 960, 940, 924, 891, 879, 858, 841, 813, 789, 763, 752, 736, 713, 681, 579, 543, 510, 430; UV/Vis (λmax, MeOH): 212 nm, ε = 38,785.8 L mol^{-1} cm^{-1}, 243 nm, ε = 5582.2 L mol^{-1} cm^{-1}, 275 nm, ε = 1362.0 L mol^{-1} cm^{-1}; ^{1}H NMR (300.18 MHz, DMSO-*d$_6$*, ppm): δ = 8.34 (s, 1H, *Tz-H*), 7.86 (s, 2H, *Py-H*), 7.34 (t, *J* = 1.8 Hz, 1H, *Ar-H*), 7.11 (d, *J* = 1.8 Hz, 2H, *Ar-H*), 5.58 (s, 2H, *CH$_2$*), 5.46 (s, 2H, *CH$_2$*), 3.90 (s, 6H, *CH$_3$*), 1.22 (s, 19H, *Tert-butyl H*). ^{13}C NMR (75 MHz, DMSO-*d$_6$*, ppm): δ = 165.9, 164.6, 150.8, 149.4, 141.7, 135.1, 125.2, 122.0, 121.8, 114.5, 62.0, 53.4, 52.8, 34.5, 31.1.

^{1}H NMR (300.18 MHz, $CDCl_3$, ppm): δ = 7.90 (s, 2H, *Py-H*), 7.57 (s, 1H, *Tz-H*), 7.42 (t, *J* = 1.8 Hz, 1H, *Ar-H*), 7.10 (d, *J* = 1.8 Hz, 2H, *Ar-H*), 5.33 (s, 2H, *CH_2*), 5.34 (s, 2H, *CH_2*), 4.00 (s, 6H, *CH_3*), 1.29 (s, 18H, *Tert-butyl H*). ^{13}C NMR (75 MHz, $CDCl_3$, ppm): δ = 166.4, 165.1, 152.1, 150.0, 142.3, 133.4, 123.2, 123.1, 122.6, 114.8, 62.6, 55.1, 53.4, 35.0, 31.5

Synthesis of 4-({1-[(3,5-di-tert-butylphenyl)methyl]1H-1,2,3-triazol-4-yl}methoxy)pyridine-2,6-dicarboxylic acid (L_3)

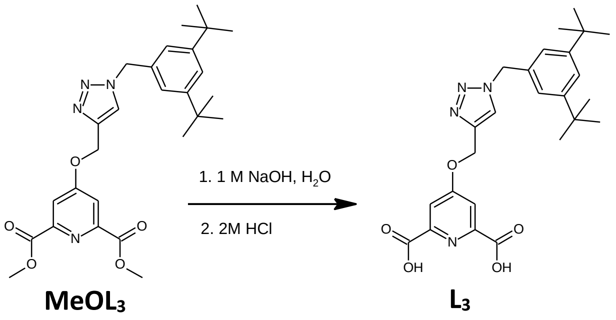

Dimethyl 4-({1-[(3,5-di-*tert*-butylphenyl)methyl]1*H*-1,2,3-triazol-4-yl}methoxy)pyridine-2,6-dicarboxylate (**$MeOL_3$**) (0.11 g, 0.22 mmol, 1 equivalent) was suspended in deionised H_2O (5 mL) and 1 M sodium hydroxide (0.87 mL, 0.87 mmol, 4 equivalents) was added. The pale beige reaction mixture was left to stir at 50 ˚C for approximately 4 hours. The transparent solution with a light-yellow colour was then left to cool to room temperature after which it appeared pale yellow. To this reaction mixture was added 2 M hydrochloric acid (30 mL) resulting in the precipitation of a white solid which was collected by filtration with a glass frit. The solid remaining in the glass frit was further suspended in deionised H_2O (30 mL) and filtered, leaving a pale yellow/white solid which was isolated as the product. (0.07 g, 0.16 mmol, 73 %), mp 205.7 ˚C. FTIR (ATR, cm^{-1}): 3858, 3825, 3740, 3716, 3694, 3681, 3653, 3633, 3461 (O-H), 3306, 3158, 3109 (COOH), 2953 (C-H), 2904 (C-H), 2867 (C-H), 2217, 2067, 1957, 1751 (C=O), 1727 (C=O), 1658, 1650, 1641, 1605 (C=C), 1568, 1536, 1502, 1468 (C=C), 1444, 1431, 1405, 1389, 1363, 1300, 1279, 1246, 1203, 1137, 1124, 1111, 1065, 1041, 1022 (C-O), 981, 944, 902, 884, 851, 811, 780, 710, 687, 672, 576, 514, 487, 469, 439; UV/Vis (λmax, MeOH): 205 nm, ε = 34,597.0 L mol^{-1} cm^{-1}, 212 nm, ε = 37,975.7 L mol^{-1} cm^{-1}, 247 nm, ε = 4100.4 L mol^{-1} cm^{-1}, 1398.3 L mol^{-1} cm^{-1}; ^{1}H NMR (300.18 MHz, DMSO-*d_6*, ppm): δ = 8.34 (s, 1H, *Tz-H*), 7.82 (s, 1H, *Py-*

H), 7.33 (t, *J* = 1.8 Hz, 1H, *Ar-H*), 7.10 (d, *J* = 1.8 Hz, 2H, *Ar-H*), 5.58 (s, 2H, *CH₂*), 5.44 (s, 2H, *CH₂*), 1.22 (s, 19H, *Tert-butyl H*). ^{13}C NMR (75 MHz, DMSO-*d₆*, ppm): δ = 166.2, 165.2, 150.8, 149.8, 141.8, 135.2, 125.2, 122.0, 121.8, 113.9, 61.9, 53.4, 34.5, 31.2.

Synthesis of $[La(L_3)_3]^{3-}$

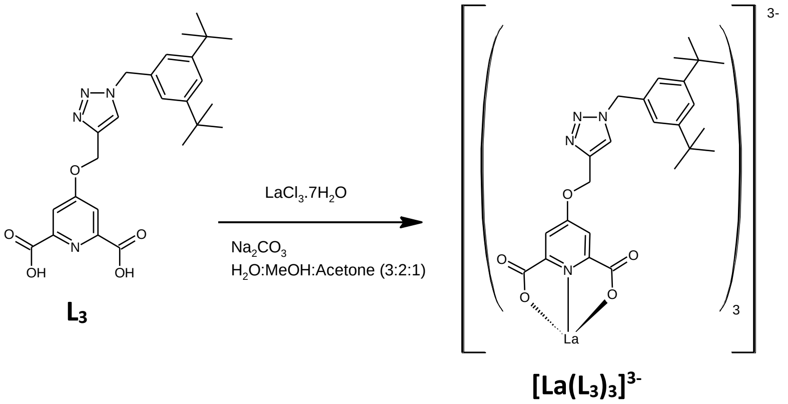

4-({1-[(3,5-di-*tert*-butylphenyl)methyl]1*H*-1,2,3-triazol-4-yl}methoxy)pyridine-2,6-dicarboxylic acid (**L₃**) (0.0189 g, 0.041 mmol, 1 equivalents) was combined with anhydrous sodium carbonate (0.0090 g, 0.085 mmol, 2.1 equivalents) and suspended in an H_2O:MeOH:acetone (3:2:1) (6 mL) solvent mixture. Next, 77.2 μL of a 0.175 M solution of lanthanum(III) chloride heptahydrate (0.0050 g, 0.014 mmol, 0.33 equivalents) in H_2O was added to the reaction mixture resulting in the formation of a white solid precipitate. The reaction mixture was further heated at 50 ˚C for 15 minutes after which it was cooled, and the white solid was collected by filtration. The white solid was subsequently resuspended and stirred in deionised H_2O for a further 2 hours after which it was collected by filtration and isolated as the product. FTIR (ATR, cm^{-1}): 3375 (O-H), 2960 (C-H), 2868 (C-H), 2352, 2342, 2330, 2128, 2019, 1593 (COO$^-$ asymmetric stretch), 1458, 1413 (COO$^-$ symmetric stretch), 1380, 1363, 1345, 1299, 1271, 1248, 1227, 1201, 1118, 1035 (C-O), 936, 882, 811, 790, 738, 711, 669, 638, 584, 560, 526, 472, 414; UV/Vis (λmax, MeOH): 200 nm, ε = 110,230.4 L mol^{-1} cm^{-1}, 203 nm, ε = 109,664.9 L mol^{-1} cm^{-1}, 210 nm, ε = 115,706.9 L mol^{-1} cm^{-1}, 241 nm, ε = 20,990.5 L mol^{-1} cm^{-1}, 273 nm, ε = 4880.0 L mol^{-1} cm^{-1}; ^{1}H NMR (300.18 MHz, DMSO-*d₆*, ppm): δ = 8.32 (s, 1H, *Tz-H*), 7.40 (s, 2H, *Py-H*), 7.35 (t, *J* = 1.7 Hz, 1H, *Ar-H*), 7.20 (d, *J* = 1.7 Hz, 2H, *Ar-H*), 5.57 (s, 2H, *CH₂*), 5.31 (s, 2H,

CH_2), 1.26 (s, 18H, *Tert-butyl H*). ^{13}C NMR (75 MHz, DMSO-*d_6*, ppm): δ = 150.8, 122.4, 34.6, 31.2.

Synthesis of $[Eu(L_3)_3]^{3-}$

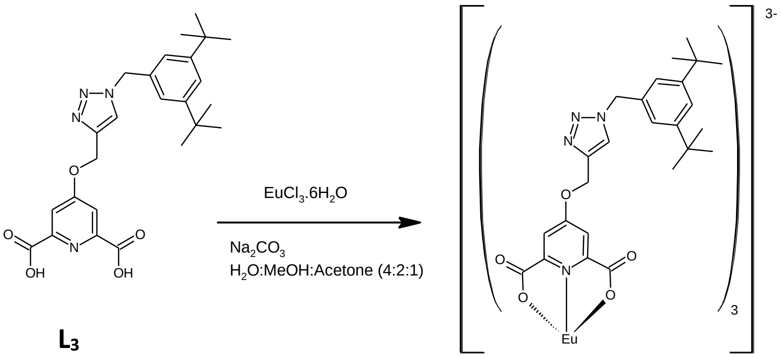

L_3

$[Eu(L_3)_3]^{3-}$

4-({1-[(3,5-di-*tert*-butylphenyl)methyl]1*H*-1,2,3-triazol-4-yl}methoxy)pyridine-2,6-dicarboxylic acid (**L_3**) (0.0212 g, 0.045 mmol, 1 equivalent) was combined with anhydrous sodium carbonate (0.0095 g, 0.090 mmol, 2.0 equivalents) and suspended in an H_2O:MeOH:acetone (4:2:1) (7 mL) solvent mixture. The reaction mixture was stirred at 80 ˚C for 30 minutes after which it appeared clear with a yellow tinge. Next, 28.2 μL of a 0.538 M solution of europium(III) chloride hexahydrate (0.0055 g, 0.015 mmol, 0.33 equivalents) in H_2O was added causing a white solid to precipitate out. The reaction mixture was heated further at 50 ˚C for 15 minutes after which it was left to cool to room temperature. Next, the reaction mixture was diluted with deionised H_2O and the white solid was collected by filtration through a glass frit. To remove any impurities, the solid remaining in the glass frit was resuspended in deionised H_2O (20 mL), collected by filtration and was isolated as the product (0.0147 g, 0.0091 mmol, 61 %). FTIR (ATR, cm^{-1}): 3376 (O-H), 2960 (C-H), 1588 (COO$^-$ asymmetric stretch), 1460, 1412 (COO$^-$ symmetric stretch), 1363, 1345, 1299, 1272, 1248, 1201, 1119, 1037 (C-O), 882, 811, 789, 742, 711, 532, 416; UV/Vis (λmax, MeOH): 201 nm, ε = 123,446.0 L mol^{-1} cm^{-1}, 210 nm, ε = 122,226.9 L mol^{-1} cm^{-1}, 274 nm, ε = 3795.1 L mol^{-1} cm^{-1}; ^{1}H NMR (300.18 MHz, DMSO-*d_6*, ppm): δ = 7.79 (s, 1H, *Tz-H*), 7.25 (s, 1H, *Ar-H*), 7.01 (s, 2H, *Ar-H*), 5.33 (s, 2H, *CH_2*), 4.53 (s, 2H, *CH_2*), 4.44 (m, 2H, *Py-H*), 1.15 (s, 19H, *Tert-butyl H*). ^{13}C NMR (75 MHz, DMSO-*d_6*, ppm): δ = 150.7, 141.8, 134.9, 124.3, 122.2, 121.7, 60.6, 53.2, 34.4, 31.1.

Synthesis of [Tb(L$_3$)$_3$]$^{3-}$

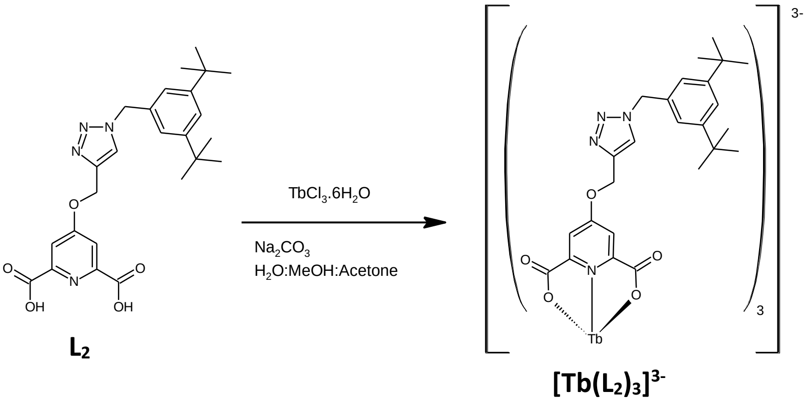

4-({1-[(3,5-di-*tert*-butylphenyl)methyl]1*H*-1,2,3-triazol-4-yl}methoxy)pyridine-2,6-dicarboxylic acid (**L$_3$**) (0.0207 g, 0.044 mmol, 1 equivalent) was combined with anhydrous sodium carbonate (0.0094 g, 0.089 mmol, 2.0 equivalents), suspended in a H_2O:MeOH:acetone (4:2:1) (7 mL) solvent mixture. The reaction mixture was then stirred at 80 ˚C for 30 minutes. Next, 86.4 µL of a 0.171 M solution of terbium(III) chloride hexahydrate (0.0055 g, 0.015 mmol, 0.33 equivalents) in H_2O was added resulting in the precipitation of a white solid. The reaction mixture stirred at 50˚C for 15 minutes after which it was cooled to room temperature and the MeOH and acetone was left to evaporate off. Next, the reaction mixture was diluted with deionised H_2O (10 mL) and the white solid was collected by filtration. The white solid was green under a short wave UV lamp and was isolated as the product (0.0203 g, 0.0125 mmol, 85 %). FTIR (ATR, cm^{-1}): 3382 (O-H), 2958 (C-H), 2867 (C-H), 2204, 2149, 1592 (COO$^-$ asymmetric stretch), 1461, 1415 (COO$^-$ symmetric stretch), 1383, 1362, 1348, 1273, 1249, 1226, 1201, 1120, 1040 (C-O), 1003, 927, 881, 811, 791, 742, 710, 645, 585, 536, 418; UV/Vis (λmax, MeOH): 205 nm, ε = 112,637.0 L mol^{-1} cm^{-1}, 210 nm, ε = 116,253.0 L mol^{-1} cm^{-1}, 275 nm, ε = 3195.5 L mol^{-1} cm^{-1}; ^{1}H NMR (300.18 MHz, DMSO-*d_6*, ppm): δ = 15.95 (br s, 1H), 9.71 (br s, 3H), 9.03 (br s, 3H), 8.54 (br s, 3H), 7.74 (br d, *J* = 56.0 Hz, 2H), 6.49 (br s, 2H), 5.19 (br s, 2H). ^{13}C NMR (75 MHz, DMSO-*d_6*, ppm): δ = 135.1, 132.0, 128.2.

Synthesis of L_4 and $[Ln(L_4)_3]^{3-}$ complexes

Synthesis of 9-(bromomethyl)anthracene

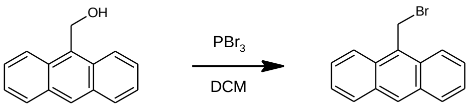

9-Anthracenemethanol (0.44 g, 2.10 mmol, 1 equivalent) was stirred in dried DCM (40 mL) under N_2 for 2 min at 0 ˚C forming a yellow reaction mixture. Next, phosphorus tribromide (0.31 mL, 3.32 mmol, 1.58 equivalents) was added to the reaction mixture under N_2 at 0 ˚C. The lime-green reaction mixture was stirred under N_2 at 0 ˚C for 45 min. Next, the orange reaction mixture was quenched with deionised H_2O (200 mL) and transferred to a separating funnel along with DCM (20 mL) and the organic layer was collected. The aqueous layer was extracted twice more with DCM (50 mL) and the organic layers were combined, dried with $MgSO_4$ and the solvent was removed by rotary evaporation forming a yellow solid which was isolated as the product (0.50 g, 1.72 mmol, 82 %), mp 119.5 – 122.4 ˚C (decomp). FTIR (ATR, cm^{-1}): 3858, 3825, 3739, 3715, 3693, 3679, 3653, 3632, 3369, 3047 (C-H), 2347, 2337, 2319, 2121, 1796, 1776, 1721, 1688, 1657, 1620 (C=C), 1524, 1493, 1461, 1444 (C=C), 1408, 1344, 1257, 1196, 1154, 1112, 1043, 1016, 956, 938, 883, 863, 844, 787, 728, 690, 649, 599, 565, 549, 499, 487 (C-Br), 416; UV/Vis (λmax, MeOH): 201 nm, ε = 25,297.8 L mol^{-1} cm^{-1}, 220 nm, ε = 15,793.6 L mol^{-1} cm^{-1}, 251 nm, ε = 115,903.2 L mol^{-1} cm^{-1}, 314 nm, ε = 1695.1 L mol^{-1} cm^{-1}, 328 nm, ε = 3124.6 L mol^{-1} cm^{-1}, 344 nm, ε = 5506.1 L mol^{-1} cm^{-1}, 362 nm, ε = 8063.8 L mol^{-1} cm^{-1}, 381 nm, ε = 7087.3 L mol^{-1} cm^{-1}; ^{1}H NMR (300.18 MHz, $CDCl_3$, ppm): δ = 8.50 (s, 1H, *Ar-H*), 8.31 (dd, *J* = 8.9, 0.8 Hz, 2H, *Ar-H*), 8.05 (dt, *J* = 8.5, 0.6 Hz, 2H, *Ar-H*), 7.65 (ddd, *J* = 8.9, 6.6, 1.3 Hz, 2H, *Ar-H*), 7.51 (ddd, *J* = 8.4, 6.6, 0.96, 2H, *Ar-H*), 5.55 (s, 2H, CH_2). ^{13}C NMR (75 MHz, $CDCl_3$, ppm): δ = 131.7, 129.8, 129.4, 129.3, 128.0, 126.9, 125.5, 123.6, 27.1.

UV/Vis solutions were made from a stock solution of 1:1 DCM:MeOH

Synthesis of 9-(azidomethyl)anthracene

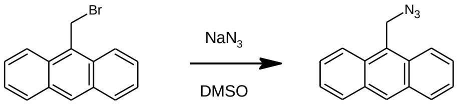

4N$_3$

9-(bromomethyl)anthracene (0.42 g, 1.53 mmol, 1 equivalent) was combined with sodium azide (0.11 g, 1.69 mmol, 1.11 equivalents) and suspended in dimethyl sulfoxide (DMSO) (80 mL) forming a clear yellow reaction mixture. This reaction mixture was stirred at 50 ˚C for 3 hours after which it was quenched with deionised H_2O (300 mL) which formed a pale-yellow precipitate. This reaction mixture was transferred to a separating funnel and extracted with ethyl acetate (100 mL). The aqueous layer was extracted a further two more times with ethyl acetate (50 mL aliquots) and all the ethyl acetate fractions were combined. Next, this ethyl acetate layer was washed a total of six times with saturated brine (NaCl) solution (100 mL aliquots) (*i.e.* four washes were carried out however the product still appeared to have DMSO remaining so it was resuspended in ethyl acetate and washed an additional two times with 20 mL aliquots of saturated brine solution). The ethyl acetate layer was then dried with $MgSO_4$ and the solvent was removed by rotary evaporation leaving the product as a yellow oil which solidified out on cooling (0.24 g, 1.01 mmol, 66 %). ^{1}H NMR (300.18 MHz, $CDCl_3$, ppm): δ = 8.52 (s, 1H, *Ar-H*), 8.30 (dd, *J* = 8.8, 0.8 Hz, 2H, *Ar-H*), 8.06 (dt, *J* = 8.3, 0.6 Hz, 2H, *Ar-H*), 7.60 (ddd, *J* = 8.8, 6.6, 1.4 Hz, 4H, *Ar-H*), 7.52 (ddd, *J* = 8.4, 6.6, 1.1 Hz, 2H, *Ar-H*), 5.34 (s, 2H, *CH_2*). ^{13}C NMR (75 MHz, $CDCl_3$, ppm): δ = 131.5, 130.9, 129.5, 129.2, 127.0, 125.9, 125.4, 123.7, 46.5.

Synthesis of MeOL₄

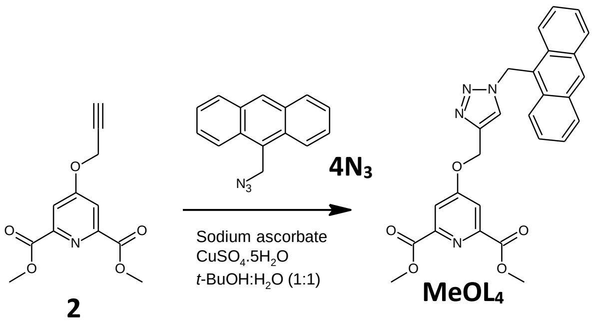

4N₃ (0.07 g, 0.30 mmol, 1.05 equivalents) was combined with **2** (0.07 g, 0.29 mmol, 1.0 equivalent), sodium ascorbate (0.06 g, 0.29 mmol, 1 equivalent), and copper(II) sulfate pentahydrate (0.006 g, 0.02 mmol, 0.1 equivalents) and suspended in a 1:1 *tert*-Butanol:H_2O (17.5 mL) solvent mixture. The yellow reaction mixture (with a beige solid) was stirred at 60 ˚C overnight. After stirring overnight, the reaction mixture appeared pale orange in colour which, after cooling to room temperature, was quenched with deionised H_2O (30 mL) causing an orange solid to precipitate out. This solid was collected by filtering through a glass frit after which it was suspended in 0.5 M EDTA/1 M NaOH (30 mL) and filtered again. The solid was then resuspended in H_2O (20 mL) (to removed remaining base) and collected by filtration. In the case of remaining **4N₃**, the solid was suspended and stirred in diethyl ether (20 mL) after which the purified solid was collected by filtration. In the case of remaining copper, the solid was suspended in chloroform and washed with the 0.5 M EDTA/1 M NaOH solution followed by H_2O after which the chloroform layer was collected, dried with $MgSO_4$ and the solvent was removed by rotary evaporation leaving the product (0.04 g, 0.08 mmol, 27 %), mp 223.5 ˚C. FTIR (ATR, cm^{-1}): 3447, 3107, 3057, 3000, 2951 (C-H), 2350, 2153, 1993, 1742 (C=O), 1623, 1587 (C=C), 1573, 1539, 1496, 1479, 1434 (C=C), 1377, 1356, 1337, 1356, 1337, 1316, 1286, 1235, 1195, 1177, 1161, 1109, 1040, 1016 (C-O), 894, 865, 845, 802, 779, 755, 729, 709, 695, 674, 653, 641, 602, 572, 523, 507, 455, 420; UV/Vis (λmax, MeOH): 203 nm, ε = 93,131.8 L mol^{-1} cm^{-1}, 252 nm, ε = 107,356.7 L mol^{-1} cm^{-1}, 315 nm, ε = 1084.1 L mol^{-1} cm^{-1}, 332 nm, ε = 2645.5 L mol^{-1} cm^{-1}, 347 nm, ε = 4938.2 L mol^{-1} cm^{-1}, 364 nm, ε = 7197.7 L mol^{-1} cm^{-1}, 384 nm, ε = 5751.3 L mol^{-1} cm^{-1}; ^1H NMR (300.18 MHz, DMSO-d_6, ppm): δ = 8.75 (s, 1H, *Tz-H*), 8.58 (d, *J* = 8.9 Hz, 2H, *Ar-H*), 8.15 (d, *J* = 7.7 Hz, 2H, *Ar-H*), 8.12 (s, 1H, *Tz-H*), 7.61 (m, 4H, *Ar-H*), 6.68 (s, 2H, *CH_2*), 5.31 (s, 2H, *CH_2*), 3.87 (s, 6H, *CH_3*). ^{13}C NMR (75 MHz, DMSO-d_6, ppm): δ = 165.9, 164.6, 149.3, 141.3, 131.1, 130.3, 129.2, 129.2, 127.2, 125.7, 125.5, 124.9, 124.0, 114.5, 61.8, 52.8, 45.6.

^{1}H NMR (300.18 MHz, $CDCl_3$, ppm): δ = 8.61 (s, 1H, *Ar-H*), 8.28 (d, *J* = 8.9 Hz, 2H, *Ar-H*), 8.08 (d, *J* = 8.3 Hz, 2H, *Ar-H*), 7.79 (s, 2H, *Py-H*), 7.58 (dt, *J* = 24.2, 7.2 Hz, 4H, *Ar-H*), 7.23 (s, 1H, *Tz-H*), 6.58 (s, 2H, *CH_2*), 5.17 (s, 2H, *CH_2*), 3.97 (s, 6H, *CH_3*). ^{13}C NMR (75 MHz, $CDCl_3$, ppm): δ = 166.3, 165.1, 149.9, 131.6, 130.9, 130.3, 129.7, 128.0, 125.7, 123.4, 123.0, 122.9, 114.7, 62.5, 53.4, 46.8.

UV/Vis solutions were made from a stock 1:1 DCM:MeOH

Synthesis of L_4

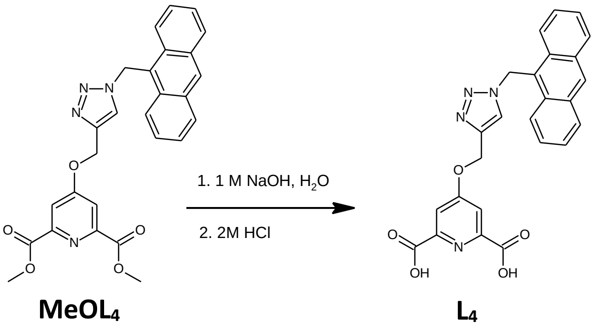

$MeOL_4$ (0.04 g, 0.07 mmol, 1 equivalent) was suspended in deionised H_2O (2.5 mL). Next, 1M sodium hydroxide (0.29 mL, 0.01 g, 0.29 mmol, 4 equivalents) was added to the suspension and the pale orange reaction mixture was stirred at 50 ˚C overnight and a further 80 ˚C for 3 hours after which the reaction mixture appeared slightly more transparent. Next, 2 M HCl (40 mL) was added which resulted in the formation of a yellow/orange precipitate which was collected by filtration (if required for purification, resuspended in deionised H_2O and filter off the impurities) (0.02 g, 0.04 mmol, 58 %), mp 207.5 – 220.4 ˚C. FTIR (ATR, cm^{-1}): 3858, 3848, 3740, 3716, 3695, 3681, 3653, 3252 (COOH), 3087, 2350, 2330, 2303, 2130, 1913, 1729 (C=O), 1679, 1650, 1622, 1597 (C=C), 1565, 1527, 1493, 1462 (C=C), 1441, 1393, 1362, 1325, 1284, 1231, 1193, 1158, 1140, 1110, 1014 (C-O), 951, 886, 866, 844, 797, 779, 724, 694, 664, 628, 601, 575, 511; UV/Vis (λmax, MeOH): 202 nm, ε = 207,960.0 L mol^{-1} cm^{-1}, 206 nm, ε = 181,793.4 L mol^{-1} cm^{-}

^{1}, 214 nm, ε = 176,642.5 L mol^{-1} cm^{-1}, 252 nm, ε = 128,347.3 L mol^{-1} cm^{-1}, 317 nm, ε = 1239.6 L mol^{-1} cm^{-1}, 331 nm, ε = 3084.1 L mol^{-1} cm^{-1}, 347 nm, ε = 5969.3 L mol^{-1} cm^{-1}, 364 nm, ε = 8862.7 L mol^{-1} cm^1, 384 nm, ε = 7042.5 L mol^{-1} cm^{-1}; ^{1}H NMR (300.18 MHz, DMSO-d_6, ppm): 8.75 (s, 1H, *Ar-H*), 8.59 (d, *J* = 8.7 Hz, 2H, *Ar-H*), 8.15 (d, *J* = 8.3 Hz, 2H, *Ar-H*), 8.13 (s, 1H, *Tz-H*), 7.76 (s, 2H, *Py-H*), 7.61 (dt, *J* = 23.8, 7.2 Hz, 4H, *Ar-H*), 6.68 (s, 2H, *CH$_2$*), 5.30 (s, 2H, *CH$_2$*). ^{13}C NMR (75 MHz, DMSO-d_6, ppm): δ = 166.1, 165.3, 149.8, 141.4, 131.1, 130.3, 129.2, 129.2, 127.2, 125.7, 125.5, 124.9, 124.0, 113.9, 61.7, 45.6.

Note UV/Vis solution in MeOH was made from a stock solution of 1:1 DMSO:MeOH

Synthesis of [La(L$_4$)$_3$]$^{3-}$

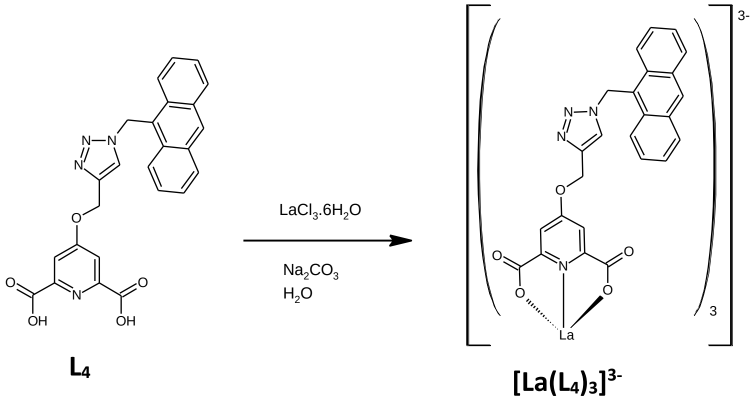

L$_4$ (0.0172 g, 0.038 mmol, 1 equivalent) was combined with anhydrous sodium carbonate (0.0081 g, 0.076 mmol, 2 equivalents) in a vial and suspended in deionised H_2O (2 mL). The yellow suspension was stirred at 80 ˚C for 15 min. Next, 80.8 μL of a 0.156 M lanthanum(III) chloride heptahydrate solution in H_2O (0.0047 g, 0.013 mmol, 0.33 equivalents) was added to the stirring **L$_4$** and Na_2CO_3 reaction mixture resulting in the formation of a yellow precipitate. This reaction mixture was stirred for 1 h at room temperature after which it was diluted with deionised H_2O (10 mL) and filtered to yield a pale yellow/beige solid which was isolated as the product (0.0146 g, 0.009 mmol, 74 %). FTIR (ATR, cm^{-1}): 3858, 3848, 3755, 3740, 3729, 3694, 3653, 3385 (O-H), 2178, 2117, 1996, 1738, 1588 (COO$^-$ asymmetric stretch), 1527, 1493, 1447, 1412 (COO$^-$ symmetric stretch), 1381, 1344, 1305, 1273, 1226, 1159, 1143, 1119, 1032 (C-O), 956, 930, 891, 867, 848, 810, 732, 704, 636, 601, 578, 519, 468. ^{1}H NMR (300.18 MHz, DMSO-d_6, ppm): δ = 8.74 (s, 1H, *Tz-H*), 8.62 (d, *J* = 8.7 Hz, 2H, *Anthracene-H*), 8.18 (s, 1H, *Anthracene-H*), 8.14 (d,

J = 3.6 Hz, 2H, *Anthracene-H*), 7.68 – 7.55 (m, 4H, *Anthracene-H*), 7.36 (d, J = 4.8 Hz, 2H, *Py-H*), 6.68 (s, 2H, *CH_2*), 5.20 (d, J = 4.7 Hz, 2H, *CH_2*). ^{13}C NMR (75 MHz, DMSO-d_6, ppm): δ = 131.1, 130.4, 129.2, 129.1, 127.2, 125.4, 124.2, 124.1, 45.6.

Synthesis of methyl-protected DPA ligands R_2 – R_4

Characterisation of M_1

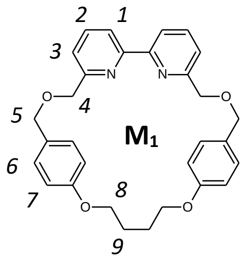

^1H NMR (300.18 MHz, $CDCl_3$, ppm): 7.77 – 7.71 (m, 4H, *H_2 and H_3*), 7.43 (dd, J = 5.7, 3.0 Hz, 2H, *H_1*), 7.23 (d, J = 8.9 Hz, 5H, *H_6*), 6.75 (d, J = 8.7 Hz, 4H, *H_7*), 4.65 (s, 4H, *H_4*), 4.55 (s, 4H, *H_5*), 4.03 (t, J = 5.9 Hz, 4H, *H_8*), 1.96 (quintet, J = 3.0 Hz, 4H, *H_9*). ^{13}C NMR (75 MHz, $CDCl_3$, ppm): δ = 159.2, 158.8, 155.9, 137.3, 130.7, 129.6, 121.5, 120.6, 114.8, 72.8, 71.9, 67.3, 25.4.

Note: **M_1** was supplied by the Goldup research group and characterisation was made based off data from Lahlali et al., 2011

Synthesis of R$_2$

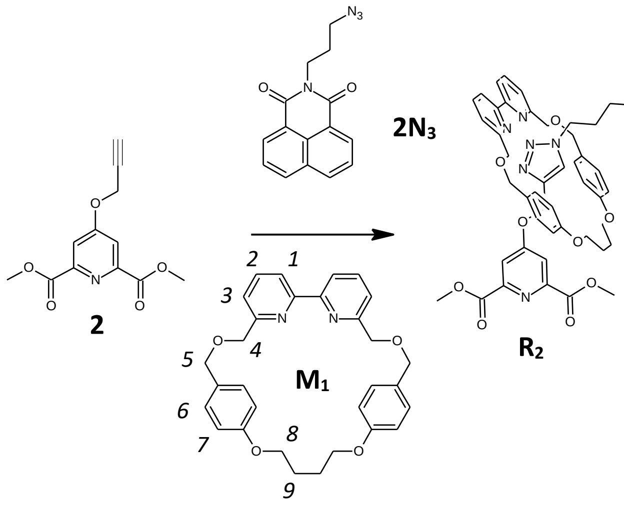

M$_1$ (0.0156 g, 0.032 mmol, 1 equivalent), **2** (0.0100 g, 0.040 mmol, 1.2 equivalents), **2N$_3$** (0.0109 g, 0.039 mmol, 1.2 equivalents) and [(CH$_3$CN)$_4$Cu]PF$_6$ (0.0013 g, 0.0035 mmol, 0.1 equivalents) were combined in a pressure vial and suspended in anhydrous THF (0.647 mL) to make a 0.05 M solution with respect to **M$_1$**. Next, DIPEA (6.19 µL, 0.036 mmol, 1.1 equivalents) was added and the yellow reaction mixture was left to stir under N$_2$ at 30 ˚C for approximately 3 days. After 3 days, the reaction mixture appeared a transparent yellow/orange colour. The reaction mixture was diluted with DCM (50 mL) and washed with a 0.5 M EDTA/NH$_4$OH (50 mL) solution. The aqueous layer was extracted two more times with DCM (50 mL aliquots). All the organic layers were combined, dried with MgSO$_4$, filtered and the solvent was removed by rotary evaporation leaving a white/pale yellow waxy solid (0.0151 g, 0.015 mmol, 46 %), mp 104.6˚C. HRMS m/z = 1012.3859 [R$_2$ + H$^+$]$^+$ (calc. for [C$_{57}$H$_{54}$N$_7$O$_{11}$]$^+$, 1012.3880). ^{1}H NMR (300.18 MHz, CDCl$_3$, ppm): δ = 8.43 (dd, *J* = 7.2, 1.0 Hz, 2H, *Naph-H*), 8.33 (s, 1H, *Tz-H*), 8.18 (dd, *J* = 8.3, 1.0 Hz, 2H, *Naph-H*), 7.73 – 7.67 (m, 2H), 7.57 (s, 2H, *Py-H*), 7.52 (t, *J* = 7.8 Hz, 2H, *H$_2$*), 7.32 (d, *J* = 7.4 Hz, 2H, *H$_1$ or H$_3$*), 7.22 (d, *J* = 8.0 Hz, 2H, *H$_3$ or H$_1$*), 6.93 (d, *J* = 8.6 Hz, 4H, *H$_6$*), 6.65 (d, *J* = 8.6 Hz, 4H, *H$_7$*), 4.67 (s, 2H, *CH$_2$*), 4.57 – 4.45 (m, 4H), 4.32 – 4.24 (m, 2H), 4.22 – 4.17 (m, 2H), 4.07 – 3.98 (m, 8H), 3.94 (s, 6H, *CH$_3$*), 3.84 – 3.78 (m, 2H), 3.77 – 3.71 (m, 5H), 2.04 – 2.02 (m, 4H), 1.85 (quintet, *J* = 3.3 Hz, 4H), 1.76 – 1.70 (m, 2H), 1.25 (t, *J* = 3.5 Hz, 5H), 1.09 (d, *J* = 5.6 Hz, 4H). ^{13}C NMR (75 MHz, CDCl$_3$, ppm): δ = 165.2, 163.9, 159.2, 159.0, 155.6, 149.3, 140.5, 137.0, 133.9, 131.6, 131.2, 130.2, 128.8, 127.0, 125.7, 122.6, 121.1, 120.4, 115.1, 115.1, 73.0, 70.8, 68.1, 66.5, 53.2, 37.3, 31.1, 25.7, 24.7.

Synthesis of R$_3$

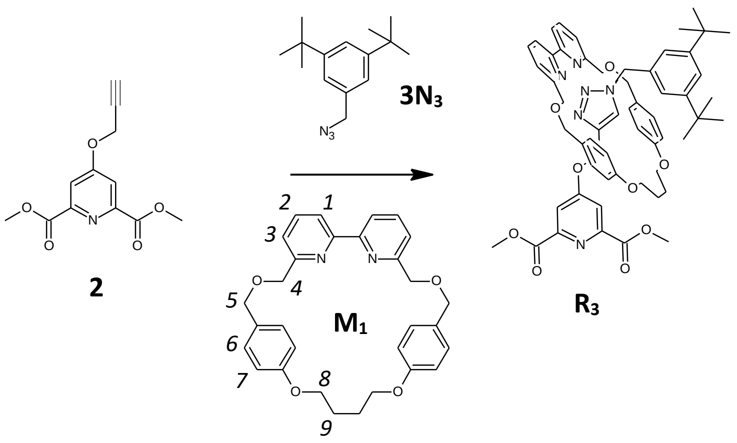

M$_1$ (0.0155 g, 0.032 mmol, 1 equivalent), **2** (0.0098 g, 0.039 mmol, 1.2 equivalents), **3N$_3$** (0.0132 g, 0.054 mmol, 1.7 equivalents) and $[(CH_3CN)_4Cu]PF_6$ (0.0015 g, 0.0040 mmol, 0.13 equivalents) were combined in a vial and suspended in anhydrous THF (0.642 mL) to make a 0.05 M solution with respect to **M$_1$**. The reaction mixture was transferred to a pressure vial under N_2 and DIPEA (6.15 μL, 0.035 mmol, 1.1 equivalents) was added. The bright orange reaction mixture was left to stir under N_2 at 30 ˚C for approximately 2 days. The bright orange reaction mixture was then diluted with DCM (50 mL) and washed with a 0.5 M EDTA/NH_4OH solution (50 mL). The aqueous layer was then extracted a further two times with DCM (50 mL aliquots) and the organic layers were combined. The organic layer was dried with $MgSO_4$, filtered and the solvent was removed under reduced pressure leaving a pale yellow waxy solid that solidified as dried further. This solid was isolated as the product, **R$_3$** (0.0063 g, 0.0064 mmol, 20 %), mp 188.4˚C. HRMS m/z = 977.4793 $[R_3 + H^+]^+$ (calc. for $[C_{57}H_{65}N_6O_9]^+$, 977.4813). ^{1}H NMR (300.18 MHz, $CDCl_3$, ppm): δ = 7.78 (s, 1H, *Tz-H*), 7.58 (t, *J* = 7.8 Hz, 2H, *H_2*), 7.45 (t, *J* = 1.8 Hz, 1H, *Ar-H*), 7.41 (d, *J* = 7.1 Hz, 2H, *H_1 or H_3*), 7.35 (d, *J* = 7.7 Hz, 2H, *H_3 or H_1*), 7.28 (s, 2H, *Py-H*), 6.76 (d, *J* = 8.6 Hz, 4H, *H_6*), 6.52 (d, *J* = 8.6 Hz, 4H, *H_7*), 5.40 (s, 2H, *CH_2*), 4.52 (d, *J* = 12.0 Hz, 2H, *M_1-H*), 4.33 – 3.92 (m, 13H, *CH_2 + M_1-H*), 3.89 (s, 6H, *CH_3*), 2.07 – 1.96 (m, 2H, *H_9*), 1.88 – 1.84 (m, 2H, *H_9*), 1.28 (s, 18H, *Tert-butyl H*).

Note: Assignments were made based off results by Lahlali et al., 2011

Synthesis of R_4

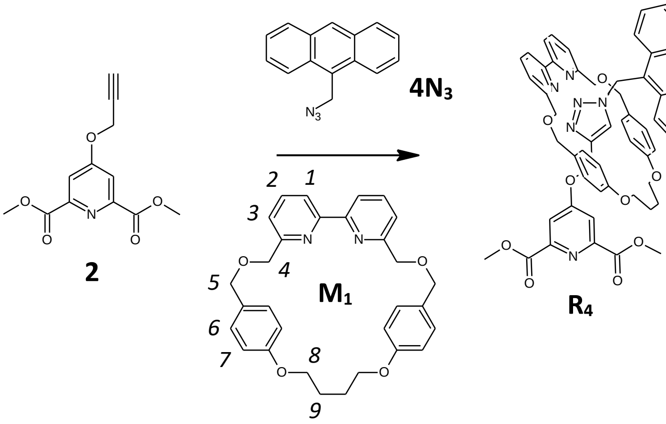

M_1 (0.0184 g, 0.038 mmol, 1 equivalent), **2** (0.0115 g, 0.046 mmol, 1.2 equivalents), **$4N_3$** (0.0109 g, 0.047 mmol, 1.2 equivalents) and $[(CH_3CN)_4Cu]PF_6$ (0.0014 g, 0.0038 mmol, 0.10 equivalents) were combined in a vial and transferred to a pressure vial. The solids were suspended in anhydrous THF (0.765 mL) to make a 0.05 M solution with respect to **M_1**. Next, DIPEA (7.31 µL, 0.042 mmol, 1.1 equivalents) was added and the orange reaction mixture was left to stir under N_2 at 30 ˚C for approximately 3 days. After 3 days, the reaction mixture appeared orange with a slight precipitate. The reaction mixture was diluted with DCM (50 mL) and washed with a 0.5 M EDTA/NH_4OH solution (50 mL). The DCM layer was collected, and the aqueous layer was extracted two more times with DCM (20 mL aliquots). The organic layers were combined, dried with $MgSO_4$, filtered and the solvent was removed by rotary evaporation leaving a yellow oily solid (0.0084 g, 0.009 mmol, 23 %), mp 116.4 ˚C. HRMS m/z 965.3860 $[R_4 + H^+]^+$ (calc. for $[C_{57}H_{53}N_6O_9]^+$, 965.3874). HRMS m/z = 965.3860 $[R_4 + H^+]^+$ (calc. for $[C_{57}H_{53}N_6O_9]^+$, 965.3874). ^1H NMR (300.18 MHz, $CDCl_3$, ppm): δ = 8.56 (s, 1H, *Anthracene-H*), 8.41 (d, *J* = 8.9 Hz, 2H, *Anthracene-H*), 8.05 (m, 2H, *Anthracene-H*), 7.66 (s, 1H, *Tz-H*), 7.57 – 7.46 (m, 6H, *Four from Anthracene-H and* H_2 *from* M_1), 7.26 (d, *J* = 9.3 Hz, 2H, H_1 *or* H_3), 7.18 (m, 4H, *Two from* H_3 *or* H_1 *and 2 from Py-H*), 6.53 (d, *J* = 8.3 Hz, 6H, *Two from axle* CH_2 *and four from* H_6), 6.25 (d, *J* = 8.6 Hz, 4H, H_7), 4.42 (d, *J* = 11.9 Hz, 2H), 4.09 (s, 2H, CH_2), 4.03 – 3.99 (m, 4H), 3.93 – 3.87 (m, 2H), 3.84 (s, 6H, CH_3), 3.80 – 3.70 (m, 12H), 2.04 (s, 1H), 1.96 – 1.89 (m, 2H), 1.85 (quintet,

J = 3.3 Hz, 8H), 1.28 – 1.19 (m, 4H), 1.05 (d, J = 6.4 Hz, 3H), 0.90 – 0.83 (m, 1H). ^{13}C NMR (75 MHz, $CDCl_3$, ppm): δ = 165.8, 165.1, 158.8, 155.8, 148.6, 142.6, 136.8, 131.6, 130.8, 130.1, 129.9, 129.6, 128.9, 127.7, 125.7, 124.7, 124.7, 123.3, 120.7, 120.5, 115.5, 115.0, 114.8, 72.4, 70.2, 68.1, 66.3, 61.6, 53.6, 53.5, 52.9, 46.2, 25.7, 24.5.

5. References

1. Bünzli, J-C. G. (2017). Rising Stars in Science and Technology: Luminescent Lanthanide Materials. *Eur. J. Inorg. Chem.*, *2017*(44), 5058-5063. https://doi.org/10.1002/ejic.201701201
2. Eliseeva, S. V., & Bünzli, J-C. G. (2010). Lanthanide luminescence for functional materials and bio-sciences. *Chem. Soc. Rev.*, *39*(1), 189-227. https://doi.org/10.1039/b905604c
3. Bünzli, J-C. G., & Piguet, C. (2005). Taking advantage of luminescent lanthanide ions. *Chem. Soc. Rev.*, *34*(12), 1048-1077. https://doi.org/10.1039/b406082m
4. Cotton, S. (2006). *Lanthanide and Actinide Chemistry*. John Wiley & Sons. https://doi.org/10.1002/0470010088
5. Werts, M. H. V. (2005). Making sense of lanthanide luminescence. *Science Progress*, *88*(2), 101-131. https://doi.org/10.3184/003685005783238435
6. Hasegawa, Y., Kitagawa, Y., & Nakanishi, T. (2018). Effective photosensitized, electrosensitized, and mechanosensitized luminescence of lanthanide complexes. *NPG Asia Materials*, *10*, 52-70. https://doi.org/10.1038/s41427-018-0012-y
7. Bünzli, J. -C. G. (2005). Rare Earth Luminescent Centers in Organic and Biochemical Compounds. In R. Hull, J. Parisi, R. M. Osgood, H. Warlimont, G. Liu & B. Jacquier (Eds.), *Spectroscopic Properties of Rare Earths in Optical Materials* (pp. 462-499). Springer. https://doi.org/10.1007/3-540-28209-2_9
8. Bünzli, J-C. G. (2010). Lanthanide Luminescence for Biomedical Analyses and Imaging. *Chem. Rev.*, *110*(5), 2729-2755. https://doi.org/10.1021/cr900362e

9. Bünzli, J-C. G. (2016). Lanthanide light for biology and medical diagnosis. *Journal of Luminescence, 170*(3), 866-878. https://doi.org/10.1016/j.jlumin.2015.07.033
10. Bünzli, J-C. G. (2019). Lanthanide Photonics: Shaping the Nanoworld. *Trends in Chemistry, 1*(8), 751-762. https://doi.org/10.1016/j.trechm.2019.05.012
11. Bünzli, J-C. G., & Eliseeva, S. V. (2011). Basics of Lanthanide Photophysics. In P. Hänninen & H. Härma (Eds.), *Lanthanide Luminescence: Photophysical, Analytical and Biological Aspects* (pp. 1-45). Springer. https://doi.org/10.1007/4243_2010_3
12. de Bettencourt-Dias, A. (2014). Introduction to Lanthanide Ion Luminescence. In A. de Bettencourt-Dias (Ed.), *Luminescence of Lanthanide Ions in Coordination Compounds and Nanomaterials* (pp. 1-48). John Wiley & Sons. https://doi.org/10.1002/9781118682760.ch01
13. Barry, D. E., Caffrey, D. F., & Gunnlaugsson, T. (2016). Lanthanide-directed synthesis of luminescent self-assembly supramolecular structures and mechanically bonded systems from acyclic coordinating organic ligands. *Chem. Soc. Rev., 45*(11), 3244-3274. https://doi.org/10.1039/c6cs00116e
14. Heffern, M. C., Matosziuk, L. M., & Meade, T. J. (2014). Lanthanide Probes for Bioresponsive Imaging. *Chem. Rev., 114*(8), 4496-4539. https://doi.org/10.1021/cr400477t
15. Montgomery, C. P., Murray, B. S., New, E. J., Pal, R., & Parker, D. (2009). Cell-Penetrating Metal Complex Optical Probes: Targeted and Responsive Systems Based on Lanthanide Luminescence. *Acc. Chem. Res., 42*(7), 925-937. https://doi.org/10.1021/ar800174z
16. Shuvaev, S., Starck, M., & Parker, D. (2017). Responsive, Water-Soluble Europium(III) Luminescent Probes. *Chem. Eur. J., 23*(42), 9974-9989. https://doi.org/10.1002/chem.201700567
17. Lehr, J., Beer, P. D., Faulkner, S., & Davis, J. J. (2014). Exploiting lanthanide luminescence in supramolecular assemblies. *Chem. Commun., 50*(43), 5678-5687. https://doi.org/10.1039/c4cc01138d

18. Amoroso, A. J., & Pope, S. J. A. (2015). Using lanthanide ions in molecular bioimaging. *Chem. Soc. Rev.*, *44*(14), 4723-4742. https://doi.org/10.1039/c4cs00293h

19. Feng, M., Chen, J., Xun, J., Dai, R., Zhao, W., Lu, H., Xu, J., Chen, L., Sui, G., & Cheng, X. (2020). Development of a Sensitive Immunochromatographic Method Using Lanthanide Fluorescent Microsphere for Raid Serodiagnosis of COVID-19. *ACS Sens.*, *5*(8), 2331-2337. https://doi.org/10.1021/acssensors.0c00927

20. Chen, Z., Zhang, Z., Zhai, X., Li, Y., Lin, L., Zhao, H., Bian, L., Li, P., Yu, L., Wu, Y., & Lin, G. (2020). Rapid and Sensitive Detection of anti-SARS-CoV-2 IgG, Using Lanthanide-Doped Nanoparticles-Based Lateral Flow Immunoassay. *Anal. Chem.*, *92*(10), 7226-7231. https://doi.org/10.1021/acs.analchem.0c00784

21. Moore, E. G., Samuel, A. P. S., & Raymond, K. N. (2009). From Antenna to Assay: Lessons Learned in Lanthanide Luminescence. *Acc. Chem. Res.*, *42*(4), 542-552. https://doi.org/10.1021/ar800211j

22. Muller, G. (2009). Luminescent chiral lanthanide(III) complexes as potential molecular probes. *Dalton Trans.*, (44), 9692-9707. https://doi.org/10.1039/B909430J

23. Mathieu., E., Sipos, A., Demeyere, E., Phipps, D., Sakaveli, D., & Borbas, K. E. (2016). Lanthanide-based tools for the investigation of cellular environments. *Chem. Commun.*, *54*(72), 10021-10035. https://doi.org/10.1039/c8cc05271a

24. Pandya, S., Yu, J., & Parker, D. (2006). Engineering emissive europium and terbium complexes for molecular imaging and sensing. *Dalton Trans.*, (23), 2757-2766. https://doi.org/10.1039/b514637b

25. Monteiro, J. H. S. K., Fetto, N. R., Tucker, M. J., & de Bettencourt-Dias, A. (2020). Luminescent Carbazole-Based Eu^{III} and Yb^{III} Complexes with a High Two-Photon Absorption Cross-Section Enable Viscosity Sensing in the Visible and Near IR and One- and Two-Photon Excitation. *Inorg. Chem.*, *59*(5), 3193-3199. https://doi.org/10.1021/acs.inorgchem.9b03561

26. Binnemans, K. (2015). Interpretation of europium(III) spectra. *Coordination Chemistry Reviews*, *295*, 1-45. https://doi.org/10.1016/j.ccr.2015.02.015

27. Kovacs, D., & Borbas, K. E. (2018). The role of photoinduced electron transfer in the quenching of sensitized Europium emission. *Coordination Chemistry Reviews*, *364*, 1-9. https://doi.org/10.1016/j.ccr.2018.03.004
28. Spangler, C., & Schäferling, M. (2011). Luminescent Chemical and Physical Sensors Based on Lanthanide Complexes. In P. Hänninen & H. Härma (Eds.), *Lanthanide Luminescence: Photophysical, Analytical and Biological Aspects* (pp. 235-262). Springer. https://doi.org/10.1007/4243_2010_1
29. Kitchen, J. A. (2017). Lanthanide-based self-assemblies of 2,6-pyridyldicarboxamide ligands: Recent advances and applications as next-generation luminescent and magnetic materials. *Coordination Chemistry Reviews, 340,* 232-246. https://doi.org/10.1016/j.ccr.2017.01.012
30. Faulkner, S., Pope, S. J. A., & Burton-Pye, B. P. (2007). Lanthanide Complexes for Luminescence Imaging Applications. *Applied Spectroscopy Reviews*, *40*(1), 1-31. https://doi.org/10.1081/ASR-200038308
31. Gassner, A-L., Duhot, C., Bünzli, J-C. G., & Chauvin, A-S. (2008). Remarkable Tuning of the Photophysical Properties of Bifunctional Lanthanide tris(Dipicolinates) and its Consequence on the Design of Bioprobes. *Inorg. Chem.*, *47*(17), 7802-7812. https://doi.org/10.1021/ic800842f
32. Lamture, J. B., Hong Zhou, Z., Suresh Kumar, A., & Wensel, T. G. (1995). Luminescence Properties of Terbium(III) Complexes with 4-Substituted Dipicolinic Acid Analogs. *Inorg. Chem.*, *34*(4), 864-869. https://doi.org/10.1021/ic00108a017
33. George, M. R., Golden, C. A., Grossel, M. C., & Curry, R. J. (2006). Modified Dipicolinic Acid Ligands for Sensitization of Europium(III) Luminescence. *Inorg. Chem.*, *45*(4), 1739-1744. https://doi.org/10.1021/ic051461u
34. Ren, Y-Y., An, B-L., & Xu, Q. (2010). Strong luminescence of novel water-soluble lanthanide complexes sensitized by pyridine-2,4,6-tricarboxylic acid. *Journal of Alloys and Compounds*, *501*(1), 42-46. https://doi.org/10.1016/j.jallcom.2010.04.025

35. Picot, A., D'Aléo, A., Baldeck, P. L., Grichine, A., Duperray, A., Andraud, C., & Maury, O. (2008). Long-Lived Two-Photon Excited Luminescence of Water-Soluble Europium Complex: Applications in Biological Imaging Using Two-Photon Scanning Microscopy. *J. Am. Chem. Soc., 130*(5), 1532-1533. https://doi.org/10.1021/ja076837c
36. Maury, O., D'Aléo, A., Picot, A., Brasselet, S., Baldeck, P. L., Chaput, F., Parola, S., & Andraud, C. (2013). Two-photon excited luminescence of lanthanide complex in monolithic sol-gel hybrid material. *Journal of Luminescence, 133*, 175-179. https://doi.org/10.1016/j.jlumin.2011.09.039
37. D'Aléo, A., Picot, A., Baldeck, P. L., Andraud, C., & Maury, O. (2008). Design of Dipicolinic Acid Ligands for the Two-Photon Sensitized Luminescence of Europium Complexes with Optimized Cross-Sections. *Inorg. Chem., 47*(22), 10269-10279. https://doi.org/10.1021/ic8012975
38. Platas-Iglesias, C., Piguet, C., André, N., & Bünzli, J-C. G. (2001). Lanthanide triple-stranded helical complexes with a substituted 2,6-pyridinedicarboyxlate. *J. Chem. Soc., Dalton Trans.*, (20), 3084-3091. https://doi.org/10.1039/b104448f
39. Nakamura, T., Mizukami, S., Tanaka, M., & Kikuchi, K. (2013). Efficient Formation of Luminescent Lanthanide(III) Complexes by Solid-Phase Synthesis and On-Resin Screening. *Chem. Asian J., 8*(11), 2685-2690. https://doi.org/10.1002/asia.201300759
40. Li, Q-F., Yue, D., Ge, G-W., Du, X., Gong, Y., Wang, Z., & Hao, J. (2015). Water-soluble Tb^{3+} and Eu^{3+} complexes based on task-specific ionic liquid ligands and their application in luminescent poly(vinyl alcohol) films. *Dalton Trans., 44*(38), 16810-16817. https://doi.org/10.1039/C5DT02555A
41. Di Pietro, S., Iacopini, D., Moscardini, A., Bizzarri, R., Pineschi, M., Di Bussolo, V., & Signore, G. (2021). New Coumarin Dipicolinate Europium Complexes with a Rich Chemical Speciation and Tunable Luminescence. *Molecules, 26*(5), 1265. https://doi.org/10.3390/molecules26051265

42. Monteiro, J. H. S. K., Sigoli, F. A., & de Bettencourt-Dias, A. (2017). A water-soluble Tb^{III} complex as a temperature-sensitive luminescent probe. *Can. J. Chem.*, *96*(9), 859-864. https://doi.org/10.1139/cjc-2017-0436

43. Monteiro, J. H. S. K., Machado, D., de Hollanda, L. M., Lancellotti, M., Sigoli, F. A., & de Bettencourt-Dias, A. (2017). Selective cytotoxicity and luminescence imaging of cancer cells with a dipicolinato-based Eu^{III} complex. *Chem. Commun.*, *53*(86), 11818-11821. https://doi.org/10.1039/C7CC06753D

44. Monteiro, J. H. S. K., de Bettencourt-Dias, A., & Sigoli, F. A. (2017). Estimating the Donor-Acceptor Distance To Tune the Emission Efficiency of Luminescent Lanthanide Compounds. *Inorg. Chem.*, *56*(2), 709-712. https://doi.org/10.1021/acs.inorgchem.6b02637

45. Andres, J., & Chauvin, A-S. (2013). Energy transfer in coumarin-sensitised lanthanide luminescence: investigation of the nature of the sensitiser and its distance to the lanthanide ion. *Phys. Chem. Chem. Phys.*, *15*(38), 15981-15994. https://doi.org/10.1039/c3cp52279b

46. Andres, J., & Chauvin, A-S. (2010). Europium Complexes of Tris(dipicolinato) Derivatives Coupled to Methylumbelliferone: A Double Sensitization. *Eur. J. Inorg. Chem.*, *2010*(18), 2700-2713. https://doi.org/10.1002/ejic.201000126

47. An, B-L., Huang, X-D., Zhang, J-M., Zhu, X-Y., & Xu, J-Q. (2017). Synthesis and strong luminescence of water soluble lanthanide complexes sensitized by a new tridentate organic ligand. *Journal of Luminescence*, *187*, 340-346. https://doi.org/10.1016/j.jlumin.2017.03.043

48. Han, M., Zhang, H-Y., Yang, L-X., Jiang, Q., & Liu, Y. (2008). A Reversible Luminescent Lanthanide Switch Based on a Dibenzo[24]-Crown-8-Dipicolinic Acid Conjugate. *Org. Lett.*, *10*(24), 5557-5560. https://doi.org/10.1021/ol802376k

49. Lin, Z-G., Song, F-Q., Wang, H., Song, X-Q., Yu, X-X., & Liu, W-s. (2021). The construction of a novel luminescent lanthanide framework for the selective sensing of

Cu^{2+} and 4-nitrophenol in water. *Dalton Trans.*, *50*(5), 1874-1886. https://doi.org/10.1039/D0DT04089D

50. Tang, R-r., Zheng, Y-h., & Gu, G-l. (2008). Synthesis and fluorescence properties of Tb(III) complexes with pyridine-2,6-dicarboxylic acid derivatives. *Journal of Central South University of Technology*, *15*, 599-605. https://doi.org/10.1007/s11771-008-0112-x
51. Kolb, H. C., Finn, M. G., & Sharpless, K. B. (2001). Click Chemistry: Diverse Chemical Function from a Few Good Reactions. *Angew. Chem. Int. Ed.*, *40*(11), 2004-2021. https://doi.org/10.1002/1521-3773(20010601)40:11<2004::AID-ANIE2004>3.0.CO;2-5
52. Hein, J. E., & Fokin, V. V. (2010). Copper-catalyzed azide-alkyne cycloaddition (CuAAC) and beyond: new reactivity of copper(I) acetylides. *Chem. Soc. Rev.*, *39*(4), 1302-1315. https://doi.org/10.1039/b904091a
53. Liang, L., & Astruc, D. (2011). The copper(I)-catalyzed alkyne-azide cycloaddition (CuAAC) "click" reaction and its applications. An overview. *Coordination Chemistry Reviews*, *255*(23-24), 2933-2945. https://doi.org/10.1016/j.ccr.2011.06.028
54. Rostovtsev, V. V., Green, L. G., Fokin, V. V., & Sharpless, K. B. (2002). A Stepwise Huisgen Cycloaddition Process: Copper(I)-Catalyzed Regioselective "Ligation" of Azides and Terminal Alkynes. *Angew. Chem. Int. Ed.*, *41*(14), 2596-2599. https://doi.org/10.1002/1521-3773(20020715)41:14<2596::AID-ANIE2596>3.0.CO;2-4
55. Tornøe, C. W., Christensen, C., & Meldal, M. (2002). Peptidotriazoles on Solid Phase: [1,2,3]-Triazoles by Regiospecific Copper(I)-Catalyzed 1,3-Dipolar Cycloadditions of Terminal Alkynes to Azides. *J. Org. Chem.*, *67*(9), 3057-3064. https://doi.org/10.1021/jo011148j
56. Odlo, K., Høydahl, E. A., & Hansen, T. V. (2007). One-pot synthesis of 1,4-disubstituted 1,2,3-triazoles from terminal acetylenes and in situ generated azides. *Tetrahedron Lett.*, *48*(12), 2097-2099. https://doi.org/10.1016/j.tetlet.2007.01.130

57. Jin, L., Tolentino, D. R., Melaimi, M., & Bertrand, G. (2015). Isolation of bis(copper) key intermediates in Cu-catalyzed azide-alkyne “click reaction”. *Sci. Adv.*, *1*(5), 1-5. https://doi.org/10.1126/sciadv.1500304
58. Moses, J. E., & Moorhouse, A. D. (2007). The growing applications of click chemistry. *Chem. Soc. Rev.*, *36*(8), 1249-1262. https://doi.org/10.1039/b613014n
59. Hein, C. D., Liu, X-M., & Wang, D. (2008). Click Chemistry, A Powerful Tool for Pharmaceutical Sciences. *Pharmaceutical Research*, *25*(10), 2216-2230. https://doi.org/10.1007/s11095-008-9616-1
60. Worrell, B. T., Malik, J. A., & Fokin, V. V. (2013). Direct Evidence of a Dinuclear Copper Intermediate in Cu(I)-Catalyzed Azide-Alkyne Cycloadditions. *Science*, *340*(6131), 457-460. https://doi.org/10.1126/science.1229506
61. Brinkø, A., Risinger, C., Lambert, A., Blixt, O., Grandjean, C., & Jensen, H. H. (2019). Combining Click Reactions for the One-Pot Synthesis of Modular Biomolecule Mimetics. *Org. Lett.*, *21*(18), 7544-7548. https://doi.org/10.1021/acs.orglett.9b02811
62. Chan, T. R., Hilgraf, R., Sharpless, K. B., & Fokin, V. V. (2004). Polytriazoles as Copper(I)-Stabilizing Ligands in Catalysis. *Org. Lett.*, *6*(17), 2853-2855. https://doi.org/10.1021/ol0493094
63. Berg, R., & Straub, B. F. (2013). Advancements in the mechanistic understanding of the copper-catalyzed azide-alkyne cycloaddition. *Beilstein J. Org. Chem.*, *9*, 2715-2750. https://doi.org/10.3762/bjoc.9.308
64. Finn, M. G., & Fokin, V. V. (2010). Click chemistry: function follows form. *Chem. Soc. Rev.*, *39*(4), 1231-1232. https://doi.org/10.1039/C003740K
65. Mini, P., Springer, M. A., Grace, M. R., Dennison, G. H., & Tuck, K. L. (2020). A highly efficient red-emitting luminescent paper-based chemosensor for hydrogen sulfide. *Chem. Commun.*, *56*(42), 5605-5608. https://doi.org/10.1039/D0CC00745E
66. Wang, N., Wang, J., Zhao, D., Mellerup, S. K., Peng, T., Wang, H., & Wang, S. (2018). Lanthanide Complexes with Photochromic Organoboron Ligand: Synthesis and

Luminescence Study. *Inorg. Chem.*, *57*(16), 10040-10049. https://doi.org/10.1021/acs.inorgchem.8b01209

67. Adumeau, P., Gaillard, C., Boyer, D., Canet, J-L., Gautier, A., & Mahiou, R. (2015). Two-Photon Absorption Properties of Eu^{3+}-DPA-Triazolyl Complexes and the Derived Silica Nanoparticles Embedding These Complexes. *Eur. J. Inorg. Chem.*, *2015*(7), 1233-1242. https://doi.org/10.1002/ejic.201402617
68. Park, H-J., Ko, S-B., Wyman, I. W., & Wang, S. (2014). Selective Sensitization of Eu(III) and Tb(III) Emission with Triarylboron-Functionalized Dipicolinic Acids. *Inorg. Chem.*, *53*(18), 9751-9760. https://doi.org/10.1021/ic501335e
69. Gaillard, C., Adumeau, P., Canet, J-L., Gautier, A., Boyer, D., Beaudoin, C., Hesling, C., Morel, L., & Mahiou, R. (2013). Monodisperse silica nanoparticles doped with dipicolinic acid-based luminescent lanthanide(III) complexes for bio-labelling. *J. Mater. Chem. B.*, *1*(34), 4306-4312. https://doi.org/10.1039/C3TB20515K
70. Talon, R., Nauton, L., Canet, J-L., Kahn, R., Girard, E., & Gautier, A. (2012). Clicked europium dipicolinate complexes for protein X-ray structure determination. *Chem. Commun.*, *48*(97), 11886-11888. https://doi.org/10.1039/C2CC36982F
71. Guo, X., Canet, J-L., Boyer, D., Gautier, A., & Mahiou, R. (2012). Sol-gel emulsion synthesis of biphotonic core-shell nanoparticles based on lanthanide doped organic-inorganic hybrid materials. *J. Mater. Chem.*, *22*(13), 6117-6122. https://doi.org/10.1039/C2JM15470F
72. Chamas, Z. E. A., Guo, X., Canet, J-L., Gautier, A., Boyer, D., & Mahiou, R. (2010). Clicked dipicolinic antennae for lanthanide luminescent probes. *Dalton Trans.*, *39*(30), 7091-7097. https://doi.org/10.1039/C002982C
73. Candelon, N., Hădade, N. D., Matache, M., Canet, J-L., Cisnetti, F., Funeriu, D. P., Nauton, L., & Gautier, A. (2013). Luminogenic “clickable” lanthanide complexes for protein labeling. *Chem. Commun.*, *49*(80), 9206-9208. https://doi.org/10.1039/c3cc44391d

74. Andres, J., & Borbas, K. E. (2015). Expanding the Versatility of Dipicolinate-Based Luminescent Lanthanide Complexes: A Fast Method for Antenna Testing. *Inorg. Chem.*, *54*(17), 8174-8176. https://doi.org/10.1021/acs.inorgchem.5b01579
75. Wang, F., Zhang, J., Ding, X., Dong, S., Liu, M., Zheng, B., Li, S., Wu, L., Yu, Y., Gibson, H. W., & Huang, F. (2010). Metal Coordination Mediated Reversible Conversion between Linear and Cross-Linked Supramolecular Polymers. *Angew. Chem. Int. Ed.*, *49*(6), 1090-1094. https://doi.org/10.1002/anie.200906389
76. Ji, X., Wang, F., Yan, X., Dong, S., & Huang, F. (2020). Construction of Supramolecular Polymers Based on Host-Guest Recognition. *Chinese Journal of Chemistry*, *38*(12), 1473-1479. https://doi.org/10.1002/cjoc.202000314
77. Mastarone, D. J., Harrison, V. S. R., Eckermann, A. L., Parigi, G., Luchinat, C., & Meade, T. J. (2011). A Modular System for the Synthesis of Multiplexed Magnetic Resonance Probes. *J. Am. Chem. Soc.*, *133*(14), 5329-5337. https://doi.org/10.1021/ja1099616
78. Pershagen, E., Nordholm, J., & Borbas, K. E. (2012). Luminescent Lanthanide Complexes with Analyte-Triggered Antenna Formation. *J. Am. Chem. Soc.*, *134*(24), 9832-9835. https://doi.org/10.1021/ja3004045
79. Zhou, Z., Wu, X., Kresak, A., Griswold, M., & Lu, Z-R. (2013). Peptide targeted tripod macrocyclic Gd(III) chelates for cancer molecular MRI. *Biomaterials*, *34*(31), 7683-7693. https://doi.org/10.1016/j.biomaterials.2013.06.057
80. Harrison, V. S. R., Carney, C. E., Macrenaris, K. W., & Meade, T. J. (2014). A multimeric MR-optical contrast agent for multimodal imaging. *Chem. Commun.*, *50*(78), 11469-11471. https://doi.org/10.1039/C4CC05651E
81. Carney, C. E., MacRenaris, K. W., Mastarone, D. J., Kasjanski, D. R., Hung, A. H., & Meade, T. J. (2014). Cell Labelling via Membrane-Anchored Lipophilic MR Contrast Agents. *Bioconjugate Chem.*, *25*(5), 945-954. https://doi.org/10.1021/bc500083t
82. Harrison, V. S. R., Carney, C. E., MacRenaris, K. W., Waters, E. A., & Meade, T. J. (2015). Multimeric Near IR-MR Contrast Agents for Multimodal *In Vivo* Imaging. *J. Am. Chem. Soc.*, *137*(28), 9108-9116. https://doi.org/10.1021/jacs.5b04509

83. Banerjee, S. R., Ngen, E. J., Rotz, M. W., Kakkad, S., Lisok, A., Pracitto, R., Pullambhatla, M., Chen, Z., Shah, T., Artemov, D., Meade, T. J., Bhujwalla, Z. M., & Pomper, M. G. (2015). Synthesis and Evaluation of Gd^{III}-Based Magnetic Resonance Contrast Agents for Molecular Imaging of Prostate-Specific Membrane Antigen. *Angew. Chem. Int. Ed.*, *54*(37), 10778-10782. https://doi.org/10.1002/anie.201503417
84. Pershagen, E., & Borbas, K. E. (2015). Multiplex Detection of Enzymatic Activity with Responsive Lanthanide-Based Luminescent Probes. *Angew. Chem. Int. Ed.*, *54*(6), 1787-1790. https://doi.org/10.1002/anie.201408560
85. Jauregui, M., Perry, W. S., Allain, C., Vidler, L. R., Willis, W. C., Kenwright, A. M., Snaith, J. S., Stasiuk, G. J., Lowe, M. P., & Faulkner, S. (2009). Changing the local coordination environment in mono- and bi- nuclear lanthanide complexes through “click” chemistry. *Dalton Trans.*, (32), 6283-6285. https://doi.org/10.1039/B911588A
86. Stasiuk, G. J., & Lowe, M. P. (2009). Click chemistry with lanthanide complexes: a word of caution. *Dalton Trans.*, (44), 9725-9727. https://doi.org/10.1039/B918891F
87. Stasiuk, G. J. (2010). *Design and Synthesis of Novel Lanthanide Chelates for Use in Magnetic Resonance Imaging* (MRI) [Doctoral dissertation, University of Leicester]. https://leicester.figshare.com/articles/thesis/Design_and_Synthesis_of_Novel_Lanthanide_Chelates_for_Use_in_Magnetic_Resonance_Imaging_MRI_/10105874/1
88. Tropiano, M., Kilah, N. L., Morten, M., Rahman, H., David, J. J., Beer, P. D., & Faulkner, S. (2011). Reversible Luminescence Switching of a Redox-Active Ferrocene-Europium Dyad. *J. Am. Chem. Soc.*, *133*(31), 11847-11849. https://doi.org/10.1021/ja203069s
89. Tropiano, M., Record, C. J., Morris, E., Rai, H. S., Allain, C., & Faulkner, S. (2012). Synthesis and Spectroscopic Study of d-f Hybrid Lanthanide Complexes Derived from triazolylDO3A. *Organometallics*, *31*(16), 5673-5676. https://doi.org/10.1021/om3003569
90. Allain, C., Beer, P. D., Faulkner, S., Jones, M. W., Kenwright, A. M., Kilah, N. L., Knighton, R. C., Sørensen, T. J., & Tropiano, M. (2013). Lanthanide appended rotaxanes

respond to changing chloride concentration. *Chem. Sci.*, *4*(1), 489-493. https://doi.org/10.1039/c2sc21614k

91. Sørensen, T. J., Tropiano, M., Blackburn, O. A., Tilney, J. A., Kenwright, A. M., & Faulkner, S. (2013). Preparation and study of an f,f,f',f'' covalently linked tetranuclear hetero-trimetallic complex – a europium, terbium, dysprosium triad. *Chem. Commun.*, *49*(8), 783-785. https://doi.org/10.1039/C2CC35931F
92. Junker, A. K. R., Tropiano, M., Faulkner, S., & Sørensen, T. J. (2016). Kinetically Inert Lanthanide Complexes as Reporter Groups for Binding of Potassium by 18-crown-6. *Inorg. Chem.*, *55*(23), 12299-12308. https://doi.org/10.1021/acs.inorgchem.6b02063
93. Sørensen, T. J., Tropiano, M., Kenwright, A. M., & Faulkner, S. (2017). Triheterometallic Lanthanide Complexes Prepared from Kinetically Inert Lanthanide Building Blocks. *Eur. J. Inorg. Chem.*, *2017*(15), 2165-2172. https://doi.org/10.1002/ejic.201700027
94. Viguier, R. F. H., & Hulme, A. N. (2006). A Sensitized Europium Complex Generated by Micromolar Concentrations of Copper(I): Toward the Detection of Copper(I) in Biology. *J. Am. Chem. Soc.*, *128*(35), 11370-11371. https://doi.org/10.1021/ja064232v
95. Prasuhn, D. E., Yeh, R. M., Obenaus, A., Manchester, M., & Finn, M. G. (2007). Viral MRI contrast agents: coordination of Gd by native virions and attachment of Gd complexes by azide-alkyne cycloaddition. *Chem. Commun.*, (12), 1269-1271. https://doi.org/10.1039/b615084e
96. Song, Y., Kohlmeir, E. K., & Meade, T. J. (2008). Synthesis of Multimeric MR Contrast Agents for Cellular Imaging. *J. Am. Chem. Soc.*, *130*(21), 6662-6663. https://doi.org/10.1021/ja0777990
97. Song, Y., Xu, X., MacRenaris, K. W., Zhang, X-Q., Mirkin, C. A., & Meade, T. J. (2009). Multimodal Gadolinium-Enriched DNA-Gold Nanoparticle Conjugates for Cellular Imaging. *Angew. Chem. Int. Ed.*, *48*(48), 9143-9147. https://doi.org/10.1002/anie.200904666
98. Sukerkar, P. A., MacRenaris, K. W., Townsend, T. R., Ahmed, R. A., Burdette, J. E., & Meade, T. J. (2011). Synthesis and Biological Evaluation of Water-Soluble Progesterone-

Conjugated Probes for Magnetic Resonance Imaging of Hormone Related Cancers. *Bioconjugate Chem.*, *22*(11), 2304-2316. https://doi.org/10.1021/bc2003555

99. Fernández-Trillo, F., Pacheco-Torres, J., Correa, J., Ballesteros, P., Lopez-Larrubia, P., Cerdán, S., Riguera, R., & Fernandez-Megia, E. (2011). Dendritic MRI Contrast Agents: An Efficient Prelabeling Approach Based on CuAAC. *Biomacromolecules*, *12*(8), 2902-2907. https://doi.org/10.1021/bm2004466

100. Suchý, M., Milne, M., Li, A. X., McVicar, N., Dodd, D. W., Bartha, R., & Hudson, R. H. E. (2011). Mono- and Tetraalkyne Modified Ligands and Their Eu^{3+} Complexes – Utilizing "Click" Chemistry to Expand the Scope of Conjugation Chemistry. *Eur. J. Org. Chem.*, *2011*(32), 6532-6543. https://doi.org/10.1002/ejoc.201100945]

101. Milne, M., Chicas, K., Li, A., Bartha, R., & Hudson, R. H. E. (2012). ParaCEST MRI contrast agents capable of derivatization *via* "click" chemistry. *Org. Biomol. Chem.*, *10*(2), 287-292. https://doi.org/10.1039/C1OB06162C

102. Fredy, J. W., Scelle, J., Guenet, A., Morel, E., de Beaumais, S., Ménand, M., Marvaud, V., Bonnet, C. S., Tóth, E., Sollogoub, M., Vives, G., & Hasenknopf, B. (2014). Cyclodextrin Polyrotaxanes as a Highly Modular Platform for the Development of Imaging Agents. *Chem. Eur. J.*, *20*(35), 10915-10920. https://doi.org/10.1002/chem.201403635

103. O'Malley, W. I., Rubbiani, R., Aulsebrook, M. L., Grace, M. R., Spiccia, L., Tuck, K. L., Gasser, G., & Graham, B. (2016). Cellular Uptake and Photo-Cytotoxicity of a Gadolinium(III)-DOTA-Naphthalimide Complex "Clicked" to a Lipidated Tat Peptide. *Molecules*, *21*(2), 194. https://doi.org/10.3390/molecules21020194

104. O'Malley, W. I., Abdelkader, E. H., Aulsebrook, M. L., Rubbiani, R., Loh, C-T., Grace, M. R., Spiccia, L., Gasser, G., Otting, G., Tuck, K. L., & Graham, B. (2016). Luminescent Alkyne-Bearing Terbium(III) Complexes and Their Application to Bioorthogonal Protein Labeling. *Inorg. Chem.*, *55*(4), 1674-1682. https://doi.org/10.1021/acs.inorgchem.5b02605

105. Fredy, J. W., Schelle, J., Ramniceanu, G., Doan, B-T., Bonnet, C. S., Tóth, É., Ménand, M., Sollogoub, M., Vives, G., & Hasenknopf, B. (2017). Mechanostereoselective One-Pot Synthesis of Functionalized Head-to-Head Cyclodextrin [3]Rotaxanes and Their Application as Magnetic Resonance Imaging Contrast Agents. *Org. Lett.*, *19*(5), 1136-1139. https://doi.org/10.1021/acs.orglett.7b00153

106. Song, Y., Zong, H., Trivedi, E. R., Vesper, B. J., Waters, E. A., Barrett, A. G. M., Radosevich, J. A., Hoffman, B. M., & Meade, T. J. (2010). Synthesis and Characterization of New Porphyrazine-Gd(III) Conjugates as Multimodal MR Contrast Agents. *Bioconjugate Chem.*, *21*(12), 2267-2275. https://doi.org/10.1021/bc1002828

107. Szíjjártó, C., Pershagen, E., & Borbas, K. E. (2012). Functionalisation of lanthanide complexes *via* microwave-enhanced Cu(I)-catalysed azide-alkyne cycloaddition. *Dalton Trans.*, *41*(25), 7660-7669. https://doi.org/10.1039/C2DT30569K

108. Molloy, J. K., Kotova, O., Peacock, R. D., & Gunnlaugsson, T. (2012). Synthesis of luminescent homo-dinuclear cationic lanthanide cyclen complexes bearing amide pendant arms through the use of copper catalysed (1,3-Huisgen, CuAAC) click chemistry. *Org. Biomol. Chem.*, *10*(2), 314-322. https://doi.org/10.1039/C1OB06203D

109. Smolensky, E. D., Zhou, Y., & Pierre, V. C. (2012). Magnetoluminescent Agents for Dual MRI and Time-Gated Fluorescence Imaging. *Eur. J. Inorg. Chem.*, *2012*(12), 2141-2147. https://doi.org/10.1002/ejic.201200045

110. Tropiano, M., Kenwright, A. M., & Faulkner, S. (2015). Lanthanide Complexes of Azidophenacyl-DO3A as New Synthons for Click Chemistry and the Synthesis of Heterometallic Lanthanide Arrays. *Chem. Eur. J.*, *21*(15), 5697-5699. https://doi.org/10.1002/chem.201500188

111. Tropiano, M., Blackburn, O. A., Tilney, J. A., Hill, L. R., Sørensen, T. J., & Faulkner, S. (2015). Exploring the effect of remote substituents and solution structure on the luminescence of three lanthanide complexes. *Journal of Luminescence*, *167*, 296-304. https://doi.org/10.1016/j.jlumin.2015.06.035

112. Sørensen, T. J., & Faulkner, S. (2018). Multimetallic Lanthanide Complexes: Using Kinetic Control To Define Complex Multimetallic Arrays. *Acc. Chem. Res.*, *51*(10), 2493-2501. https://doi.org/10.1021/acs.accounts.8b00205

113. Faulkner, S., & Tropiano, M. (2014). Heterometallic Complexes Containing Lanthanides. In A. de Bettencourt-Dias (Ed.), *Luminescence of Lanthanide Ions in Coordination Compounds and Nanomaterials* (pp. 331-358). John Wiley & Sons. https://doi.org/10.1002/9781118682760.ch09

114. Leigh, D. A., Pirvu, L., Schaufelberger, F., Tetlow, D. J., & Zhang, L. (2018). Securing a Supramolecular Architecture by Tying a Stopper Knot. *Angew. Chem. Int. Ed.*, *57*(33), 10484-10488. https://doi.org/10.1002/anie.201803871

115. Leigh, D. A., Pirvu, L., & Schaufelberger, F. (2019). Stereoselective Synthesis of Molecular Square and Granny Knots. *J. Am. Chem. Soc.*, *141*(14), 6054-6059. https://doi.org/10.1021/jacs.9b01819

116. Butler, S. J., Delbianco, M., Evans, N. H., Frawley, A. T., Pal, R., Parker, D., Puckrin, R. S., & Yufit, D. S. (2014). Utility of tris(4-bromopyridyl) europium complexes as versatile intermediates in the divergent synthesis of emissive chiral probes. *Dalton Trans.*, *43*(15), 5721-5730. https://doi.org/10.1039/C4DT00253A

117. Gil-Ramírez, G., Hoekman, S., Kitching, M. O., Leigh, D. A., Vitorica-Yrezabal, I. J., & Zhang, G. (2016). Tying a Molecular Overhand Knot of Single Handedness and Asymmetric Catalysis with the Corresponding Pseudo-D_3-Symmetric Trefoil Knot. *J. Am. Chem. Soc.*, *138*(40), 13159-13162. https://doi.org/10.1021/jacs.6b08421

118. Carina, R. F., Dietrich-Buchecker, C., & Sauvage, J-P. (1996). Molecular Composite Knots. *J. Am. Chem. Soc.*, *118*(38), 9110-9116. https://doi.org/10.1021/ja961459p

119. Adams, H., Ashworth, E., Breault, G. A., Guo, J., Hunter, C. A., & Mayers, P. C. (2001). Knot tied around an octahedral metal centre. *Nature*, *411*, 763. https://doi.org/10.1038/35081143

120. Zhang, G., Gil-Ramírez, G., Markevicius, A., Browne, C., Vitorica-Yrezabal, I. J., & Leigh, D. A. (2015). Lanthanide Template Synthesis of Trefoil Knots of Single Handedness. *J. Am. Chem. Soc.*, *137*(32), 10437-10442. https://doi.org/10.1021/jacs.5b07069

121. Kim, E., & Koo, H. (2019). Biomedical applications of copper-free click chemistry: *in vitro, in vivo,* and *ex vivo*. *Chem. Sci.*, *10*(34), 7825-8048. https://doi.org/10.1039/c9sc03368h

122. Debets, M. F., van Berkel, S. S., Dommerholt, J., Dirks, A. J., Rutjes, F. P. J. T., & van Delft, F. (2011). Bioconjugation with Strained Alkenes and Alkynes. *Acc. Chem. Res.*, *44*(9), 805-815. https://doi.org/10.1021/ar200059z

123. Jewett, J. C., & Bertozzi, C. R. (2010). Cu-free click cycloaddition reactions in chemical biology. *Chem. Soc. Rev.*, *39*(4), 1272-1279. https://doi.org/10.1039/B901970G

124. Chen, B., Wen, G., Wu, J., & Feng, J. (2015). Preparation of Lanthanide-Polymer Composite Material via Click Chemistry. *Macromol. Rapid Commun.*, *36*(20), 1836-1840. https://doi.org/10.1002/marc.201500341

125. Bishop, S. C., Winefield, R., Anbanandam, A., & Lampe, J. N. (2019). Aqueous synthesis of a small-molecule lanthanide chelator amenable to copper-free click chemistry. *PloS ONE, 14*(3), 1-16. https://doi.org/10.1371/journal.pone.0209726

126. Stoddart, J. F. (2017). Mechanically Interlocked Molecules (MIMs)-Molecular Shuttles, Switches, and Machines (Nobel Lecture). *Angew. Chem. Int. Ed.*, *56*(37), 11094-11125. https://doi.org/10.1002/anie.201703216

127. Bruns, C. J., & Stoddart, J. F. (2016). *The Nature of the Mechanical Bond: From Molecules to Machines*. John Wiley & Sons. https://doi.org/10.1002/9781119044123

128. Shahraki, B. T., Maghsoudi, S., Fatahi, Y., Rabiee, N., Bahadorikhalili, S., Dinarvand, R., Bagherzadeh, M., & Verpoort, F. (2020). The flowering of Mechanically Interlocked Molecules: Novel approaches to the synthesis of rotaxanes and catenanes.

Coordination Chemistry Reviews, *423*(213484), 1-50. https://doi.org/10.1016/j.ccr.2020.213484

129. Crowley, J. D., Goldup, S. M., Lee, A-L., Leigh, D. A., & McBurney, R. T. (2009). Active metal template synthesis of rotaxanes, catenanes and molecular shuttles. *Chem. Soc. Rev.*, *38*(6), 1530-1541. https://doi.org/10.1039/B804243H

130. Mena-Hernando, S., & Pérez, E. M. (2019). Mechanically interlocked materials. Rotaxanes and catenanes beyond the small molecule. *Chem. Soc. Rev.*, *48*(19), 5016-5032. https://doi.org/10.1039/C8CS00888D

131. Denis, M., & Goldup, S. M. (2017). The active template approach to interlocked molecules. *Nat. Rev. Chem.*, *1*(0061), 1-17. https://doi.org/10.1038/s41570-017-0061

132. Xue, M., Yang, Y., Chi, X., Yan, X., & Huang, F. (2015). Development of Pseudorotaxanes and Rotaxanes: From Synthesis to Stimuli-Responsive Motions to Applications. *Chem. Rev.*, *115*(15), 7398-7501. https://doi.org/10.1021/cr5005869

133. Chambron, J-C., & Sauvage, J-P. (2011). Transition metal-templated synthesis of catenanes and rotaxanes. *Sci China Chem*, *54*(12), 2028-2031. https://doi.org/10.1007/s11426-011-4420-x

134. Lewis, J. E. M., Galli, M., & Goldup, S. M. (2017). Properties and emerging applications of mechanically interlocked ligands. *Chem. Commun.*, *53*(2), 298-312. https://doi.org/10.1039/c6cc07377h

135. Lewis, J. E. M., Beer, P. D., Loeb, S. J., & Goldup, S. M. (2017). Metal ions in the synthesis of interlocked molecules and materials, *46*(9), 2577-2591. https://doi.org/10.1039/c7cs00199a

136. Evans, N. H. (2020). Lanthanide-Containing Rotaxanes, Catenanes, and Knots. *ChemPlusChem*, *85*(4), 783-792. https://doi.org/10.1002/cplu.202000135

137. Lewis, J. E. M., Winn, J., & Goldup, S. M. (2017). Stepwise, Protecting Group Free Synthesis of [4]Rotaxanes. *Molecules*, *22*(1), 89. https://doi.org/10.3390/molecules22010089

138. Affeld, A., Hübner, G. M., Seel, C., & Schalley, C. A. (2001). Rotaxane or Pseudorotaxane? Effects of Small Structural Variations on the Deslipping Kinetics of Rotaxanes with Stopper Groups of Intermediate Size. *Eur. J. Org. Chem.*, *2001*(15), 2877-2890. https://doi.org/10.1002/1099-0690(200108)2001:15<2877::AID-EJOC2877>3.0.CO;2-R

139. Schalley, C. A., Beizai, K., & Vögtle, F. (2001). On the Way to Rotaxane-Based Molecular Motors: Studies in Molecular Mobility and Topological Chirality. *Acc. Chem. Res.*, *34*(6), 465-476. https://doi.org/10.1021/ar000179i

140. Ashton, P. R., Fyfe, M. C. T., Schiavo, C., Stoddart, J. F., White, A. J. P., & Williams, D. J. (1998). A new slippage synthesis. *Tetrahedron Lett.*, *39*(31), 5455-5458. https://doi.org/10.1016/S0040-4039(98)01071-5

141. Zhou, W., Chen, Y., Dai, X., Zhang, H-y., & Liu, Y. (2019). Cucurbit[8]uril-Mediated Polypseudorotaxane for Enhanced Lanthanide Luminescence Behavior in Water. *Org. Lett.*, *21*(23), 9363-9367. https://doi.org/10.1021/acs.orglett.9b03597

142. Aucagne, V., Hänni, K. D., Leigh, D. A., Lusby, P. J., & Walker, D. B. (2006). Catalytic “Click” Rotaxanes: A Substoichiometric Metal-Template Pathway to Mechnically Interlocked Architectures. *J. Am. Chem. Soc.*, *128*(7), 2186-2187. https://doi.org/10.1021/ja056903f

143. Aucagne, V., Berná, J., Crowley, J. D., Goldup, S. M., Hänni, K. D., Leigh, D. A., Lusby, P. J., Ronaldson, V. E., Slawin, A. M. Z., Viterisi, A., & Walker, D. B. (2007). Catalytic “Active-Metal” Template Synthesis of [2]Rotaxanes, [3]Rotaxanes, and Molecular Shuttles, and Some Observations on the Mechanism of the Cu(I)-Catalyzed Azide-Alkyne 1,3-Cycloaddition. *J. Am. Chem. Soc.*, *129*(39), 11950-11963. https://doi.org/10.1021/ja073513f

144. Dietrich-Buchecker, C. O., & Sauvage, J. P. (1983). Une nouvelle famille de molecules : les metallo-catenanes. *Tetrahedron Lett.*, *24*(46), 5095-5098. https://doi.org/10.1016/S0040-4039(00)94050-4

145. Wasserman, E. (1960). The Preparation of Interlocking Rings: A Catenane. *J. Am. Chem. Soc.*, *82*(16), 4433-4434. https://doi.org/10.1021/ja01501a082

146. Schill, G., & Lüttringhaus, A. (1964). The Preparation of Catena Compounds by Directed Synthesis. *Angew. Chem. Int. Ed. Engl.*, *3*(8), 546-547. https://doi.org/10.1002/anie.196405461

147. Wu, C., Lecavalier, P. R., Shen, Y. X., & Gibson, H. W. (1991). Synthesis of a rotaxane via the template method. *Chem. Mater.*, *3*(4), 569-572. https://doi.org/10.1021/cm00016a002

148. Aricó, F., Badjic, J. D., Cantrill, S. J., Flood, A. H., Leung, K. C. -F., Liu, Y., & Stoddart, J. F. (2005). Templated Synthesis of Interlocked Molecules. In C. A. Schalley, F. Vögtle, K. H. Dötz (Eds), *Templates in Chemistry II* (pp. 203-259). Springer. https://doi.org/10.1007/b104330

149. Hänni, K. D., & Leigh, D. A. (2010). The application of CuAAC ‘click’ chemistry to catenane and rotaxane synthesis. *Chem. Soc. Rev.*, *39*(4), 1240-1251. https://doi.org/10.1039/b901974j

150. Crowley, J. D., Hänni, K. D., Lee, A-L., & Leigh, D. A. (2007). [2]Rotaxanes through Palladium Active-Template Oxidative Heck Cross-Couplings. *J. Am. Chem. Soc.*, *129*(40), 12092-12093. https://doi.org/10.1021/ja075219t

151. Goldup, S. M., Leigh, D. A., Long, T., McGonigal, P. R., Symes, M. D., & Wu, J. (2009). Active Metal Template Synthesis of [2]Catenanes. *J. Am. Chem. Soc.*, *131*(43), 15924-15929. https://doi.org/10.1021/ja9070317

152. Lahlali, H., Jobe, K., Watkinson, M., & Goldup, S. M. (2011). Macrocycle Size Matters: “Small” Functionalized Rotaxanes in Excellent Yield Using the CuAAC Active Template Approach. *Angew. Chem. Int. Ed.*, *50*(18), 4151-4155. https://doi.org/10.1002/anie.201100415

153. Meldal, M., & Tornøe, C. W. (2008). Cu-Catalyzed Azide-Alkyne Cycloaddition. *Chem. Rev.*, *108*(8), 2952-3015. https://doi.org/10.1021/cr0783479

154. Heard, A. W., & Goldup, S. M. (2020). Simplicity in the Design, Operation, and Applications of Mechanically Interlocked Molecular Machines. *ACS Cent. Sci.*, *6*(2), 117-128. https://doi.org/10.1021/acscentsci.9b01185

155. Acevedo-Jake, A., Ball, A. T., Galli, M., Kukwikila, M., Denis, M., Singleton, D. G., Tavassoli, A., & Goldup, S. M. (2020). AT-CuAAC Synthesis of Mechanically Interlocked Oligonucleotides. *J. Am. Chem. Soc.*, *142*(13), 5985-5990. https://doi.org/10.1021/jacs.0c01670

156. Neal, E. A., & Goldup, S. M. (2015). Competitive formation of homocircuit [3]rotaxanes in synthetically useful yields in the bipyridine-mediated active template CuAAC reaction. *Chem. Sci.*, *6*(4), 2398-2404. https://doi.org/10.1039/C4SC03999H

157. Winn, J., Pinczewska, A., & Goldup, S. M. (2013). Synthesis of a Rotaxane Cu^{I} Triazolide under Aqueous Conditions. *J. Am. Chem. Soc.*, *135*(36), 13318-13321. https://doi.org/10.1021/ja407446c

158. Modicom, F., Jamieson, E. M. G., Rochette, E., & Goldup, S. M. (2019). Chemical Consequences of the Mechanical Bond: A Tandem Active Template Rearrangement Reaction. *Angew. Chem. Int. Ed.*, *58*(12), 3875-3879. https://doi.org/10.1002/anie.201813950

159. Lewis, J. E. M., Winn, J., Cera, L., & Goldup, S. M. (2016). Iterative Synthesis of Oligo[*n*]rotaxanes in Excellent Yield. *J. Am. Chem. Soc.*, *138*(50), 16329-16336. https://doi.org/10.1021/jacs.6b08958

160. Lewis, J. E. M., Bordoli, R. J., Denis, M., Fletcher, C. J., Galli, M., Neal, E. A., Rochette, E. M., & Goldup, S. M. (2016). High yielding synthesis of 2,2'-bipyridine macrocycles, versatile intermediates in the synthesis of rotaxanes. *Chem. Sci.*, *7*(5), 3154-3161. https://doi.org/10.1039/C6SC00011H

161. Raymo, F. M., Houk, K. N., & Stoddart, J. F. (1998). The Mechanism of the Slippage Approach to Rotaxanes. Origin of the "All-or-Nothing" Substituent Effect. *J. Am. Chem. Soc.*, *120*(36), 9318-9322. https://doi.org/10.1021/ja9806229

162. Yeung, C-T., Chan, W. T. K., Yan, S-C., Yu, K-L., Yim, K-H., Wong, W-T., & Law, G-L. (2015). Lanthanide supramolecular helical diastereoselective breaking induced by point chirality: mixture or *P*-helix, *M*-helix. *Chem. Commun.*, *51*(3), 592-595. https://doi.org/10.1039/C4CC08362H

163. Hoffart, D. J., & Loeb, S. J. (2005). Metal-Organic Rotaxane Frameworks: Three-Dimensional Polyrotaxanes from Lanthanide-Ion Nodes, Pyridinium *N*-Oxide Axles, and Crown-Ether Wheels. *Angew. Chem. Int. Ed.*, *44*(6), 901-904. https://doi.org/10.1002/anie.200461707

164. Cheng, H-B., Zhang, H-Y., & Liu, Y. (2013). Dual-Stimulus Luminescent Lanthanide Molecular Switch Based on an Unsymmetrical Diarylperfluorocyclopentene. *J. Am. Chem. Soc.*, *135*(28), 10190-10193. https://doi.org/10.1021/ja4018804

165. Sambrook, M. R., Curiel, D., Hayes, E. J., Beer, P. D., Pope, S. J. A., & Faulkner, S. (2006). Sensitised near infrared emission from lanthanides via anion-templated assembly of d-f heteronuclear [2]pseudorotaxanes. *New J. Chem.*, *30*(8), 1133-1136. https://doi.org/10.1039/B601017B

166. Zapata, F., Blackburn, O. A., Langton, M. J., Faulkner, S., & Beer, P. D. (2013). Lanthanide cation-templated synthesis of rotaxanes. *Chem. Commun.*, *49*(74), 8157-8159. https://doi.org/10.1039/c3cc45404e

167. Langton, M. J., Blackburn, O. A., Lang, T., Faulkner, S., & Beer, P. D. (2014). Nitrite-Templated Synthesis of Lanthanide-Containing [2]Rotaxanes for Anion Sensing. *Angew. Chem.*, *126*(43), 11647-11650. https://doi.org/10.1002/ange.201405131

168. Ding, Z-J., Zhang, Y-M., Teng, X., & Liu, Y. (2011). Controlled Photophysical Behaviors between Dibenzo-24-crown-8 Bearing Terpyridine Moiety and Fullerene-Containing Ammonium Salt. *J. Org. Chem.*, *76*(6), 1910-1913. https://doi.org/10.1021/jo102311m

169. Yao, J., Fu, X., Zheng, X-L., Cao, Z-Q., & Qu, D-H. (2015). Two functional [2]rotaxanes featuring efficient intercomponent interactions between chromophores. *Dyes and Pigments*, *121*, 13-20. https://doi.org/10.1016/j.dyepig.2015.05.005

170. Jiao, D., Biedermann, F., Tian, F., & Scherman, O. A. (2010). A Systems Approach to Controlling Supramolecular Architecture and Emergent Solution Properties via Host-Guest Complexation in Water. *J. Am. Chem. Soc.*, *132*(44), 15734-15743. https://doi.org/10.1021/ja106716j

171. Lee, E., Heo, J., & Kim, K. (2000). A Three-Dimensional Polyrotaxane Network. *Angew. Chem. Int. Ed.*, *39*(15), 2699-2701. https://doi.org/10.1002/1521-3773(20000804)39:15<2699::AID-ANIE2699>3.0.CO;2-Z

172. Kovacs, D., Kocsi, D., Wells, J. A. L., Kiraev, S. R., & Borbas, K. E. (2021). Electron transfer pathways in photoexcited lanthanide(III) complexes of picolinate ligands. *Dalton Trans.*, *50*(12), 4244-4254. https://doi.org/10.1039/D1DT00616A

173. Horie, M., Suzaki, Y., & Osakada, K. (2004). Formation of Pseudorotaxane Induced by Electrochemical Oxidation of Ferrocene-Containing Axis Molecules in the Presence of Crown Ether. *J. Am. Chem. Soc.*, *126*(12), 3684-3685. https://doi.org/10.1021/ja039899l

174. Horie, M., Suzaki, Y., & Osakada, K. (2005). Chemical and Electrochemical Formation of Pseudorotaxanes Composed of Alkyl(ferrocenylmethyl)ammonium and Dibenzo[24]crown-8. *Inorg. Chem.*, *44*(16), 5844-5853. https://doi.org/10.1021/ic050215f

175. Kihara, N., Hashimoto, M., & Takata, T. (2004). Redox Behavior of Ferrocene-Containing Rotaxane: Transposition of the Rotaxane Wheel by Redox Reaction of a Ferrocene Moiety Tethered at the End of the Axle. *Org. Lett.*, *6*(11), 1693-1696. https://doi.org/10.1021/ol049817d

176. Sambrook, M. R., Beer, P. D., Wisner, J. A., Paul, R. L., & Cowley, A. R. (2004). Anion-Templated Assembly of a [2]Catenane. *J. Am. Chem. Soc.*, *126*(47), 15364-15365. https://doi.org/10.1021/ja045080b

177. Cockerill, A. F., Davies, G. L. O., Harden, R. C., & Rackham, D. M. (1973). Lanthanide Shift Reagents for Nuclear Magnetic Resonance Spectroscopy. *Chem. Rev.*, *73*(6), 553-588. https://doi.org/10.1021/cr60286a001

178. Hemmilä, I., & Laitala, V. (2011). Sensitized Bioassays. In P. Hänninen & H. Härmä (Eds), *Lanthanide Luminescence: Photophysical, Analytical and Biological Aspects* (pp. 361-380). Springer. https://doi.org/10.1007/4243_2010_10

179. Ahamed, B. N., Duchêne, R., Robeyns, K., & Fustin, C-A. (2016). Catenane-based mechanically-linked block copolymers. *Chem. Commun.*, *52*(10), 2149-2152. https://doi.org/10.1039/C5CC09775D

180. Ahamed, B. N., Velthem, P. V., Robeyns, K., & Fustin, C-A. (2017). Influence of a Single Catenane on the Solid-State Properties of Mechanically Linked Polymers. *ACS Macro Lett.*, *6*(4), 468-472. https://doi.org/10.1021/acsmacrolett.7b00204

181. Tarasenko, E. A., & Beletskaya, I. P. (2016). Poly(ethylene glycol)-supported chiral pyridine-2,6-bis(oxazoline): synthesis and application as a recyclable ligand in Cu^{I}–catalyzed enantioselective direct addition of terminal alkynes to imines. *Mendeleev Commun.*, *26*(6), 477-479. https://doi.org/10.1016/j.mencom.2016.11.005

182. Wu, C., Li, D., Yang, L., Lin, B., Zhang, H., Xu, Y., Cheng, Z., Xia, C., Gong, Q., Song, B., & Ai, H. (2015). Multivalent manganese complex decorated amphiphilic dextran micelles as sensitive MRI probes. *J. Mater. Chem. B*, *3*(8), 1470-1473. https://doi.org/10.1039/C4TB02036G

183. Jeong, K-S., & Park, E-J. (2004). Self-Assembly of Interlocked Supramolecular Dendrimers. *J. Org. Chem.*, *69*(7), 2618-2621. https://doi.org/10.1021/jo035798u

184. D'Aléo, A., Toupet, L., Rigaut, S., Andraud, C., & Maury, O. (2008). Guanidinium as powerful cation for the design of lanthanate tris-dipicolinate crystalline materials: Synthesis, structure and photophysical properties. *Optical Materials*, *30*(11), 1682-1688. https://doi.org/10.1016/j.optmat.2007.07.007

185. O'Neil, A. T., Zhang, N., Harrison, J. A., Goldup, S. M., & Kitchen, J. A. (2021). Synthesis, photophysical and assembly studies of novel luminescent lanthanide(III) complexes of 1,2,3-triazolyl-pyridine-2,6-dicarboxamide-based ligands. *Supramolecular Chemistry*, *33*(5), 160-173. https://doi.org/10.1080/10610278.2021.1955120

186. O'Neil, A. T., Harrison, J. A., & Kitchen, J. A. (2021). Ultra-thin films of amphiphilic lanthanide complexes: multi-colour emission from molecular monolayers. *Chem. Commun.*, *57*(65), 8067-8070. https://doi.org/10.1039/D1CC02628C

187. Pavia, D. L., Lampman, G. M., Kriz, G. S., & Vyvyan, J. R. (2009). *Introduction to Spectroscopy* (4th ed.). Brooks/Cole, Cengage Learning.

188. Ouali, N., Bocquet, B., Rigault, S., Morgantini, P-Y., Weber, J., & Piguet, C. (2002). Analysis of Paramagnetic NMR Spectra of Triple-Helical Lanthanide Complexes with 2,6-Dipicolinic Acid Revisited: A New Assignment of Structural Changes and Crystal-Field Effects 25 Years Later. *Inorg. Chem.*, *41*(6), 1436-1445. https://doi.org/10.1021/ic010801i

189. Donato, H. J., & Martin, R. B. (1972). Dipolar shifts and structure in aqueous solutions of 3:1 lanthanide complexes of 2,6-dipicolinate. *J. Am. Chem. Soc.*, *94*(12), 4129-4131. https://doi.org/10.1021/ja00767a011

190. Chu, K. C., Xu, Y., Balschi, J. A., & Springer, C. S. (1990). Bulk Magnetic Susceptibility Shifts in NMR Studies of Compartmentalized Samples: Use of Paramagnetic Reagents. *Magnetic Resonance in Medicine*, *13*(2), 239-262. https://doi.org/10.1002/mrm.1910130207

191. Lessmann, J. J., & Horrocks, W. DeW. (2000). Supramolecular Coordination Chemistry in Aqueous Solution: Lanthanide Ion-Induced Triple Helix Formation. *Inorg. Chem.*, *39*(15), 3114-3124. https://doi.org/10.1021/ic990698l

192. Binnemans, K., Van Herck, K., & Görller-Walrand, C. (1997). Influence of dipicolinate ligands on the spectroscopic properties of europium(III) in solution. *Chemical Physical Letters*, *266*(3-4), 297-302. https://doi.org/10.1016/S0009-2614(97)00012-2

193. Kotova, O., Blasco, S., Twamley, B., O'Brien, J., Peacock, R. D., Kitchen, J. A., Martínez-Calvo, M., & Gunnlaugsson, T. (2015). The application of chiroptical spectroscopy (circular dichroism) in quantifying binding events in lanthanide directed

synthesis of chiral luminescent self-assembly structures. *Chem. Sci.*, *6*(1), 457-471. https://doi.org/10.1039/c4sc02474e

194. Barry, D. E., Kitchen, J. A., Albrecht, M., Faulkner, S., & Gunnlaugsson, T. (2013). Near Infrared (NIR) Lanthanide Emissive Langmuir-Blodgett Monolayers Formed Using Nd(III) Directed Self-Assembly Synthesis of Chiral Amphiphilic Ligands. *Langmuir, 29*(36), 11506-11515. https://doi.org/10.1021/la402274s

195. Barry, D. E., Kitchen, J. A., Mercs, L., Peacock, R. D., Albrecht, M., & Gunnlaugsson, T. (2019). Chiral luminescent lanthanide complexes possessing strong (samarium, Sm^{III}) circularly polarised luminescence (CPL), and their self-assembly into Langmuir-Blodgett films. *Dalton Trans.*, *48*(30), 11317-11325. https://doi.org/10.1039/c9dt02003a

196. Froidevaux, P., Harrowfield, J. M., & Sobolev, A. N. (2000). Calixarenes as Scaffolds: Introduction of Tridentate Rare Earth Metal Binding Units into Calix[4]arene. *Inorg. Chem.*, *39*(21), 4678-4687. https://doi.org/10.1021/ic000353z

197. Jagannathan, R., & Soundararajan, S. (1979). Complexes of Lanthanide Perchlorates with N,N,N’,N’-Tetramethyl Pyridine Dicarboxamide. *J. Coord. Chem.*, *9*(1), 31-35. https://doi.org/10.1080/00958977908073098

198. Sokolnicki, J., Legendziewicz, J., Muller, G., & Riehl, J. P. (2005). The luminescence, molecular and electronic structure, and excited state energetics of tris complexes of 4-phenylethylnyl-2,6-pyridinedicarboxylic acid with Eu(III) and Tb(III) prepared in sol-gel. *Optical Materials*, *27*(9), 1529-1536. https://doi.org/10.1016/j.optmat.2005.01.010

199. Picot, A., Malvolti, F., Le Guennic, B., Baldeck, P. L., Williams, J. A. G., Andraud, C., & Maury, O. (2007). Two-Photon Antenna Effect Induced in Octupolar Europium Complexes. *Inorg. Chem.*, *46*(7), 2659-2665. https://doi.org/10.1021/ic062181x

200. Albin, M., & Horrocks, W. D. (1985). Europium(III) Luminescence Excitation Spectroscopy. Quantitative Correlation between the Total Charge on the Ligands and the

$^7F_0 \rightarrow {}^5D_0$ Transition Frequency in Europium(III) Complexes. *Inorg. Chem.*, *24*(6), 895-900. https://doi.org/10.1021/ic00200a020

201. Muller, G., Schmidt, B., Jiricek, J., Hopfgartner, G., Riehl, J. P., Bünzli, J-C. G., & Piguet, C. (2001). Lanthanide triple helical complexes with a chiral ligand derived from 2,6-pyridinedicarboxylic acid. *J. Chem. Soc., Dalton Trans.*, (18), 2655-2662. https://doi.org/10.1039/B102728J

202. Tigaa, R. A., Aerken, X., Fuchs, A., & de Bettencourt-Dias, A. (2017). Sensitization of Ln^{III} (Ln = Eu, Tb, Tm) Ion Luminescence by Functionalized Polycarbonate-Based Materials and White Light Generation. *Eur. J. Inorg. Chem.*, *2017*(44), 5310-5317. https://doi.org/10.1002/ejic.201700655

203. Tigaa, R. A., Lucas, G. J., & de Bettencourt-Dias, A. (2017). ZnS Nanoparticles Sensitize Luminescence of Capping-Ligand-Bound Lanthanide Ions. *Inorg. Chem.*, *56*(6), 3260-3268. https://doi.org/10.1021/acs.inorgchem.6b02638

204. Li, B., Ding, Z-J., Li, Z., & Li, H. (2018). Simultaneous enhancement of mechanical strength and luminescence performance in double-network supramolecular hydrogels. *J. Mater. Chem. C.*, *6*(25), 6869-6874. https://doi.org/10.1039/C8TC02154F

205. Xu, Q., Li, Z., & Li, H. (2016). Water-Soluble Luminescent Hybrid Composites Consisting of Oligosilsesquioxanes and Lanthanide Complexes and their Sensing Ability for Cu^{2+}. *Chem. Eur. J.*, *22*(9), 3037-3043. https://doi.org/10.1002/chem.201504300

206. Wen, T., Li, H., Wang, Y., Wang L., Zhang, W., & Zhang, L. (2013). Ln^{3+}-mediated formation of luminescent ionogels. *J. Mater. Chem. C*, *1*(8), 1607-1612. https://doi.org/10.1039/C2TC00625A

207. Renaud, F., Piguet, C., Bernardinelli, G., Bünzli, J-C. G., & Hopfgartner, G. (1997). In Search for Mononuclear Helical Lanthanide Building Blocks with Predetermined Properties: Lanthanide Complexes with Diethyl Pyridine-2,6-Dicarboxylate. *Chem. Eur. J.*, *3*(10), 1660-1667. https://doi.org/10.1002/chem.19970031015

208. Renaud, F., Piguet, C., Bernardinelli, G., Bünzli, J-C. G., & Hopfgartner, G. (1997). In Search for Mononuclear Helical Lanthanide Building Blocks with Predetermined Properties: Triple-Stranded Helical Complexes with *N,N,N',N'*-Tetraethylpyridine-2,6-dicarboxamide. *Chem. Eur. J.*, *3*(10), 1646-1659. https://doi.org/10.1002/chem.19970031014

209. Johnson, K. R., & de Bettencourt-Dias, A. (2019). $^1O_2$ Generating Luminescent Lanthanide Complexes with 1,8-Naphthalimide-Based Sensitizers. *Inorg. Chem.*, *58*(19), 13471-13480. https://doi.org/10.1021/acs.inorgchem.9b02431

210. Piguet, C., Bünzli, J-C. G., Bernardinelli, G., Bochet, C. G., & Froidevaux, P. (1995). Design of Luminescent Building Blocks for Supramolecular Triple-helical Lanthanide Complexes. *J. Chem. Soc., Dalton Trans.*, (1), 83-97. https://doi.org/10.1039/DT9950000083

211. Lincheneau, C., Destribats, C., Barry, D. E., Kitchen, J. A., Peacock, R. D., & Gunnlaugsson, T. (2011). Lanthanide directed self-assembly synthesis and photophysical evaluation of chiral Eu(III) luminescent "half-helicates". *Dalton Trans.*, *40*(45), 12056-12059. https://doi.org/10.1039/C1DT11225B

212. Sauer, M., Hofkens, J., & Enderlein, J. (2011). *Handbook of Fluorescence Spectroscopy and Imaging: From Ensemble to Single Molecules.* Wiley-VCH Verlag GmbH & Co. KGaA. https://doi.org/10.1002/9783527633500

213. Brayshaw, P. A., Bünzli, J-C. G., Froidevaux, P., Harrowfield, J. M., Kim, Y., & Sobolev, A. N. (1995). Synthetic, Structural, and Spectroscopic Studies on Solids Containing Tris(dipicolinato) Rare Earth Anions and Transition or Main Group Metal Cations. *Inorg. Chem.*, *34*(8), 2068-2076. https://doi.org/10.1021/ic00112a019

214. Li, Q-F., Ge, G-W., Sun-Y., Yu, M., Wang, Z. (2019). Influence of counter ions on structure, morphology, thermal stability of lanthanide complexes containing dipicolinic acid. *Spectrochimica Acta Part A: Molecular and Biomolecular Spectroscopy, 214*, 333-338. https://doi.org/10.1016/j.saa.2019.02.056

215. Niu, Z., Fang, S., Ma, J-G., Zhang, X-P., & Cheng, P. (2014). Enhancement of adsorption selectivity for MOFs under mild activation and regeneration conditions. *Chem. Commun.*, *50*(58), 7797-7799. https://doi.org/10.1039/C4CC00426D

216. Mirzaei, M., Eshtiagh-Hosseini, H., Lotfian, N., Salimi, A., Bauzá, A., Van Deun, R., Decadt, R., Barceló-Oliver, M., & Frontera, A. (2014). Syntheses, structures, properties and DFT study of hybrid inorganic-organic architectures constructed from trinuclear lanthanide frameworks and Keggin-type polyoxometalates. *Dalton Trans.*, *43*(4), 1906-1916. https://doi.org/10.1039/C3DT51971F

217. Blackman, A., Bottle, S. E., Schmid, S., Mocerino, M., & Wille, U. (2016). *Chemistry* (3rd ed.). John Wiley & Sons Australia.

218. Cai, M., Gao, X., & Chen, J. (2015). Structural refinement and luminescent property of a novel europium(III) complex with a proton transfer compound containing 2,6-pyridinedicarboxylate and 2,6-pyridinediammonium ligands synthesized by ultrasonic method. *Journal of Molecular Structure*, *1086*, 93-98. https://doi.org/10.1016/j.molstruc.2014.12.039

219. Harrowfield, J. M., Koutsantonis, G. A., Skelton, B. W., Strong, A. J., & White, A. H. (2010). Structural Systematics for Lanthanide(III) Systems: Lattice Interactions in Salts $[CoL_3][Ln(dipic)_3]\cdot \mathit{N}h_2O$ (L = *N,N'*-Aromatic Bidentate Ligand; dipic = Dipicolinate = pyridine-2,6-dicarboxylate) Containing Complex Ions of D_3 Symmetry. *Z. Anorg. Allg. Chem.*, *636*(5), 808-817. https://doi.org/10.1002/zaac.200900409

220. Tei, L., Blake, A. J., Wilson, C., & Schröder, M. (2004). Lanthanide complexes of new nonadentate imino-phosphonate ligands derived from 1,4,7-triazacyclononane: synthesis, structural characterisation and NMR studies. *Dalton Trans.*, (13), 1945-1952. https://doi.org/10.1039/B404425H

221. SeethaLekshmi, S., Ramya, A. R., Reddy, M. L. P., & Varughese, S. (2017). Lanthanide complex-derived white-light emitting solids: A survey on design strategies. *Journal of Photochemistry and Photobiology C: Photochemistry Reviews*, *33*, 109-131. https://doi.org/10.1016/j.jphotochemrev.2017.11.001

222. Goprikrishna, P., Meher, N., & Iyer, P. K. (2018). Functional 1,8-Naphthalimide AIE/AIEEgens: Recent Advances and Prospects. *ACS Appl. Mater. Interfaces*, *10*(15), 12081-12111. https://doi.org/10.1021/acsami.7b14473

223. Xiaolian, L., Tingting, Y., Yingli, Z., Liming, M., Yang, M., & Siyu, C. (2014). *Synthesis and Application of a Class of Naphthalimide Derivatives Containing 1,2,3-Triazole in Amide Side Chain.* (China CN104059053B). https://patents.google.com/patent/CN104059053B/de

224. Hossain, U., Sengupta, S., & Bhattacharya, S. (2005). Synthesis and evaluation of antioxidative properties of a series of organoselenium compound. *Bioorg. Med. Chem.*, *13*(20), 5750-5758. https://doi.org/10.1016/j.bmc.2005.06.011

225. Hossain, U., & Bhattacharya, S. (2006). Prevention of cadmium induced lipid peroxidation, depletion of some antioxidative enzymes and glutathione by a series of novel organoselenocyanates. *Environmental Toxicology and Pharmacology*, *22*(3), 298-308. https://doi.org/10.1016/j.etap.2006.04.004

226. Ramchander, J., Rameshwar, N., Reddy, T. S., Raju, G., & Reddy, A. (2014). Synthesis and photophysical properties of 1, 4-disubstituted naphthyloxymethyl-*N*-alkyl naphthimido-1,2,3-triazole. *J. Chem. Sci.*, *126*(4), 1063-1074. https://doi.org/10.1007/s12039-014-0677-x

227. Carter, A. B., Zhang, N., Kühne, I. A., Keene, T. D., Powell, A. K., & Kitchen, J. A. (2019). Layered Ln(III) Complexes from a Sulfonate-Based 1,8-Naphthalimide: Structures, Magnetism and Photophysics. *ChemistrySelect*, *4*(6), 1850-1856. https://doi.org/10.1002/slct.201900152

228. Zhang, J., Li, H., Chen, P., Sun, W., Gao, T., & Yan, P. (2015). A new strategy for achieving white-light emission of lanthanide complexes: effective control of energy transfer from blue-emissive fluorophore to Eu(III) centres. *J. Mater. Chem. C.*, *3*(8), 1799-1806. https://doi.org/10.1039/c4tc02512a

229. Bonnet, C. S., Devocelle, M., & Gunnlaugsson, T. (2012). Luminescent lanthanide-binding peptides: sensitising the excited states of Eu(III) and Tb(III) with a 1,8-naphthalimide-based antenna. *Org. Biomol. Chem.*, *10*(1), 126-133. https://doi.org/10.1039/c1ob06567j

230. Shelton, A. H., Sazanovich, I. V., Weinstein, J. A., & Ward, M. D. (2012). Controllable three-component luminescence from a 1,8-naphthalimide/Eu(III) complex: white light emission from a single molecule. *Chem. Commun.*, *48*(22), 2749-2751. https://doi.org/10.1039/C2CC17182A

231. Plyusnin, V. F., Kupryakov, A. S., Grivin, V. P., Shelton, A. H., Sazanovich, I. V., Meijer, A. J. H. M., Weinstein, J. A., & Ward, W. D. (2013). Photophysics of 1,8-naphthalimide/Ln(III) dyads (Ln = Eu, Gd): naphthalimide → Eu(III) energy-transfer from both singlet and triplet states. *Photochem. Photobiol. Sci.*, *12*(9), 1666-1679. https://doi.org/10.1039/c3pp50109d

232. Alcala, M. A., Shade, C. M., Uh, H., Kwan, S. Y., Bischof, M., Thompson, Z. P., Gogick, K. A., Meier, A. R., Strein, T. G., Bartlett, D. L., Modzelewski, R. A., Lee, Y. J., Petoud, S., & Brown, C. K. (2011). Preferential accumulation within tumors and *in vivo* imaging by functionalized luminescent dendrimer lanthanide complexes. *Biomaterials*, *32*(35), 9343-9352. https://doi.org/10.1016/j.biomaterials.2011.07.076

233. Reger, D. L., Leitner, A., & Smith, M. D. (2015). Homochiral, Helical Coordination Complexes of Lanthanides(III) and Mixed-Metal Lanthanides(III): Impact of the 1,8-Naphthalimide Supramolecular Tecton on Structure, Magnetic Properties, and Luminescence. *Cryst. Growth Des.*, *15*(11), 5637-5644. https://doi.org/10.1021/acs.cgd.5b01387

234. Reger, D. L., Leitner, A. P., & Smith, M. D. (2016). Supramolecular Metal-Organic Frameworks of s- and f-Block Metals: Impact of 1,8-Naphthalimide Functional Group. *Cryst. Growth Des.*, *16*(1), 527-536. https://doi.org/10.1021/acs.cgd.5b01575

235. Wang, Z., Liu, N., Li, H., Chen, P., & Yan, P. (2017). The Role of Blue-Emissive 1,8-Naphthalimidopyridine *N*-Oxide in Sensitizing Eu^{III} Photoluminescence in Dimeric

Hexafluoroacetylacetonate Complexes. *Eur. J. Inorg. Chem.*, *2017*(15), 2211-2219. https://doi.org/10.1002/ejic.201700019

236. Liu, W., Chen, C., Huang, X., Xie, E., & Liu, W. (2019). Functional Construction of Dual-Emitting 4-Aminonaphthalimide Encapsulated Lanthanide MOFs Composite for Ratiometric Temperature Sensing. *Chem. Eur. J.*, *25*(43), 10054-10058. https://doi.org/10.1002/chem.201901924

237. Ozdemir, S., Varlikli, C., Oner, I., Ocakoglu, K., & Icli, S. (2010). The synthesis of 1,8-naphthalimide groups containing imidazolium salts/ionic liquids using I^-, PF_6^-, $TFSI^-$ anions and their photophysical, electrochemical and thermal properties. *Dyes and Pigments*, *86*(3), 206-216. https://doi.org/10.1016/j.dyepig.2010.01.005

238. Izawa, H., Nishino, S., Sumita, M., Akamatsu, M., Morihashi, K., Ifuku, S., Morimoto, M., & Saimoto, H. (2015). A novel 1,8-naphthalimide derivative with an open space for an anion: unique fluorescence behaviour depending on the binding anion's electrophilic properties. *Chem. Commun.*, *51*(41), 8596-8599. https://doi.org/10.1039/C5CC01709B

239. Han, X., Zhang, B., Chen, J., Liu, S. H., Tan, C., Liu, H., Lang, M. J., Tan, Y., Liu, X., & Yin, J. (2017). Modulating aggregation-induced emission *via* a non-conjugated linkage of fluorophores to tetraphenylethenes. *J. Mater. Chem. B*, *5*(26), 5096-5100. https://doi.org/10.1039/C7TB00623C

240. Felip-León, C., Galindo, F., & Miravet, J. F. (2018). Insights into the aggregation-induced emission of 1,8-naphthalimide-based supramolecular hydrogels. *Nanoscale*, *10*(36), 17060-17069. https://doi.org/10.1039/C8NR03755H

241. Zhang, Y., Jiao, P-C., Xu, H-B., Tang, M-J., Yang, X-P., Huang, S., & Deng, J-G. (2015). Switchable sensitizers stepwise lighting up lanthanide emission. *Scientific Reports*, *5*(9335), 1-5. https://doi.org/10.1038/srep09335

242. Huang, K., Wu, H., Shi, M., Li, F., Yi, T., & Huang, C. (2009). Reply to comment on 'aggregation-induced phosphorescent emission (AIPE) of iridium(III) complexes':

origin of the enhanced phosphorescence. *Chem. Commun.*, (10), 1243-1245. https://doi.org/10.1039/B816056B

243. Hong, Y., Lam, J. W. Y., & Tang, B. Z. (2009). Aggregation-induced emission: phenomenon, mechanism and applications. *Chem. Commun.*, (29), 4332-4353. https://doi.org/10.1039/B904665H

244. Cho, D. W., & Cho, D. W. (2014). Excimer and exciplex emissions of 1,8-naphthalimides caused by aggregation in extremely polar or nonpolar solvents. *New J. Chem.*, *38*(6), 2233-2236. https://doi.org/10.1039/C3NJ01473H

245. *Aggregation-Induced Emission.* (2022). AIE Research. https://tangbz.ust.hk/res1.html

246. de Sousa, M., Kluciar, M., Abad, S., Miranda, M. A., de Castro, B., & Pischel, U. (2004). An inhibit (INH) molecular logic gate based on 1,8-naphthalimide-sensitised europium luminescence. *Photochem. Photobiol. Sci.*, *3*(7), 639-642. https://doi.org/10.1039/B406415A

247. Samanta, A., Ramachandram, B., & Saroja, G. (1996). An investigation of the triplet state properties of 1,8-naphthalimide: a laser flash photolysis study. *Journal of Photochemistry and Photobiology A: Chemistry, 101*(1), 29-32. https://doi.org/10.1016/S1010-6030(96)04392-4

248. Jones, G., & Kumar, S. (2003). Participation of chromophore pairs in photoinduced intramolecular electron transfer for a naphthalimide spermine conjugate. *Journal of Photochemistry and Photobiology A: Chemistry, 160*(3), 139-149. https://doi.org/10.1016/S1010-6030(03)00207-7

249. Supkowski, R. M., & Horrocks, W. DeW. (2002). On the determination of the number of water molecules, *q*, coordinated to europium(III) ions in solution from luminescence decay lifetimes. *Inorganica Chimica Acta, 340*, 44-48. https://doi.org/10.1016/S0020-1693(02)01022-8

250. Beeby, A., Clarkson, I. M., Dickins, R. S., Faulkner, S., Parker, D., Royle, L., de Sousa, A. S., Williams, J. A. G., & Woods, M. (1999). Non-radiative deactivation of the

excited states of europium, terbium and ytterbium complexes by proximate energy-matched OH, NH and CH oscillators: an improved luminescence method for establishing solution hydration states. *J. Chem. Soc., Perkin Trans. 2,* (3), 493-504. https://doi.org/10.1039/A808692C

251. Horrocks, W. D., & Sudnick, D. R. (1981). Lanthanide ion luminescence probes of the structure of biological macromolecules. *Acc. Chem. Res., 14*(12), 384-392. https://doi.org/10.1021/ar00072a004

252. Horrocks, W. D., & Sudnick, D. R. (1979). Lanthanide Ion Probes of Structure in Biology. Laser-Induced Luminescence Decay Constants Provide a Direct Measure of the Number of Metal-Coordinated Water Molecules. *J. Am. Chem. Soc., 101*(2), 334-340. https://doi.org/10.1021/ja00496a010

253. Horrocks, W. D., & Sudnick, D. R. (1979). Time-Resolved Europium(III) Excitation Spectroscopy: A Luminescence Probe of Metal Ion Binding Sites. *Science, 206*(4423), 1194-1196. https://doi.org/10.1126/science.505007

254. Harrowfield, J. M., Kim, Y., Skelton, B. W., & White, A. H. (1995). Mixed Transition Metal/Lanthanide Complexes: Structural Characterization of Solids Containing Cage Amine Chromium(III) Cations and Tris(dipicolinato)lanthanide Anions. *Aust. J. Chem., 48*(4), 807-823. https://doi.org/10.1071/CH9950807

255. Solea, A. B., Yang, L., Crochet, A., Fromm, K. M., Allemann, C., & Mamula, O. (2022). Complexation Behavior of Pinene-Bipyridine Ligands towards Lanthanides: The Influence of the Carboxylic Arm. *Chemistry, 4*(1), 18-30. https://doi.org/10.3390/chemistry4010002

256. An, B-L., Liu, P-Y., Shi, J-X., Gong, M-L., Yang, Y-S., & Xu, N-S. (2003). Preparation, photoluminescence and thermal stability of sodium tris(pyridine dicarboxylato) europate(III) complex incorporated into silica matrix. *Journal of Materials Science: Materials in Electronics, 14*, 125-128. https://doi.org/10.1023/A:1022363305343

257. Müller, S., Sanders, D. A., Di Antonio, M., Matsis, S., Riou, J-F., Rodriquez, R., & Balasubramanian, S. (2012). Pyridostatin analogues promote telomere dysfunction and long-term growth inhibition in human cancer cells. *Org. Biomol. Chem.*, *10*(32), 6537-6546. https://doi.org/10.1039/C2OB25830G

258. Triboni, E. R., Filho, P. B., de Souza Berlinck, R. G., & Politi, M. J. (2004). Efficient Sonochemical Synthesis of 3- and 4-Electron Withdrawing Ring Substituted *N*-Alkyl-1,8-naphthalimides from the Related Anhydrides. *Synthetic Communications, 34*(11), 1989-1999. https://doi.org/10.1081/SCC-120037911

259. Ragazzon, G., Credi, A., & Colasson, B. (2017). Thermodynamic Insights on a Bistable Acid-Base Switchable Molecular Shuttle with Strongly Shifted Co-conformational Equilibria. *Chem. Eur. J.*, *23*(9), 2149-2156. https://doi.org/10.1002/chem.201604783

260. Song, B., Wang, G., Tan, M., & Yuan, J. (2006). A Europium(III) Complex as an Efficient Singlet Oxygen Luminescence Probe. *J. Am. Chem. Soc.*, *128*(41), 13442-13450. https://doi.org/10.1021/ja062990f

261. Tron, A., de Rouville, H-P. J., Ducrot, A., Tucker, J. H. R., Baroncini, M., Credi, A., & McClenaghan, N. D. (2015). Photodriven [2]rotaxane-[2]catenane interconversion. *Chem. Commun.*, *51*(14), 2810-2813. https://doi.org/10.1039/c4cc09472g

262. Yang, W., Li, Y., Zhang, J., Yu, Y., Liu, T., Liu, H., & Li, Y. (2011). Synthesis of a [2]rotaxane operated in basic environment. *Org. Biomol. Chem.*, *9*(17), 6022-6026. https://doi.org/10.1039/C1OB05726J

263. Bondi, R., Via, L. D., Hyeraci, M., Pagot, G., Labella, L., Marchetti, F., & Samaritani, S. (2021). Cytotoxicity and DNA interaction in a series of aryl terminated iminopyridine Pt(II) complexes. *Journal of Inorganic Biochemistry*, *216*, 111335. https://doi.org/10.1016/j.jinorgbio.2020.111335

264. Lan, P., Berta, D., Porco, J. A., South, M. S., & Parlow, J. J. (2003). Polymer-Assisted Solution-Phase (PASP) Suzuki Couplings Employing an Anthracene-Tagged

Palladium Catalyst. *J. Org. Chem.*, *68*(25), 9678-9686. https://doi.org/10.1021/jo035129g

265. Xie, F., Sivakumar, K., Zeng, Q., Bruckman, M. A., Hodges, B., & Wang, Q. (2008). A fluorogenic 'click' reaction of azidoanthracene derivatives. *Tetrahedron*, *64*(13), 2906-2914. https://doi.org/10.1016/j.tet.2008.01.080

266. Wang, Y-H., & Wan, P. (2011). Excited state intramolecular proton transfer (ESIPT) in dihydroxyphenyl anthracenes. *Photochem. Photobiol. Sci.*, *10*(12), 1934-1944. https://doi.org/10.1039/c1pp05187c

267. Suh, H. R., Suh, H. S., Yun, S. S., Lee, E. K., & Kang, S. K. (2002). Triaquatris(2,6-dinitrophenolato)neodymium(III). *Acta Cryst.*, (E58), m284-m286. https://doi.org/10.1107/S1600536802008267

268. Sørensen, T. J., Kenwright, A. M., & Faulkner, S. (2015). Bimetallic lanthanide complexes that display a ratiometric response to oxygen concentrations. *Chem. Sci.*, *6*(3), 2054-2059. https://doi.org/10.1039/C4SC03827D

269. Tropiano, M., Blackburn, O. A., Tilney, J. A., Hill, L. R., Placidi, M. P., Aarons, R. J., Sykes, D., Jones, M. W., Kenwright, A. M., Snaith, J. S., Sørensen, T. J., & Faulkner, S. (2013). Using Remote Substituents to Control Solution Structure and Anion Binding in Lanthanide Complexes. *Chem. Eur. J.*, *19*(49), 16566-16571. https://doi.org/10.1002/chem.201303183

270. Placidi, M. P., Villaraza, A. J. L., Natrajan, L. S., Sykes, D., Kenwright, A. M., & Faulkner, S. (2009). Synthesis and Spectroscopic Studies on Azo-Dye Derivatives of Polymetallic Lanthanide Complexes: Using Diazotization to Link Metal Complexes Together. *J. Am. Chem. Soc.*, *131*(29), 9916-9917. https://doi.org/10.1021/ja904362f

271. Averill, D. J., Garcia, J., Siriwardena-Mahanama, B. N., Vithanarachchi, S. M., & Allen, M. J. (2011). Preparation, Purification, and Characterization of Lanthanide Complexes for Use as Contrast Agents for Magnetic Resonance Imaging. *J. Vis. Exp.*, (53), 1-6. https://doi.org/10.3791/2844

272. Dichtel, W. R., Miljanić, O. Š., Spruell, J. M., Heath, J. R., & Stoddart, J. F. (2006). Efficient Templated Synthesis of Donor-Acceptor Rotaxanes Using Click Chemistry. *J. Am. Chem. Soc.*, *128*(32), 10388-10390. https://doi.org/10.1021/ja063127i

273. Mónico, A., Martínez-Senra, E., Cañada, F. J., Zorrilla, S., & Pérez-Sala, D. (2017). Drawbacks of Dialysis Procedures for Removal of EDTA. *PLoS ONE*, *12*(1), 1-9. https://doi.org/10.1371/journal.pone.0169843

274. Jamieson, E. M. G., Modicom, F., & Goldup, S. M. (2018) Chirality in rotaxanes and catenanes. *Chem. Soc. Rev.*, *47*(14), 5266-5311. https://doi.org/10.1039/c8cs00097b

275. Johnson, K. R., & de Bettencourt-Dias, A. (2021). Azido- and amino-substituted dipicolinates for the sensitization of the luminescent lanthanides Eu^{III} and Tb^{III}. *Inorganica Chimica Acta*, *514*, 120003. https://doi.org/10.1016/j.ica.2020.120003

276. Pointillart, F., Bourdolle, A., Cauchy, T., Maury, O., Gal, Y.L., Golhen, S., Cador, O., & Ouahab, L. (2012). In Solution Sensitization of Er(III) Luminescence by the 4-Tetrathiafulvalene-2,6-pyridinedicarboxylic Acid Dimethyl Antenna Ligand. *Inorg. Chem.*, *51*(2), 978-984. https://doi.org/10.1021/ic202045a

277. Johnson, K. R., Vittardi, S. B., Gracia-Nava, M. A., Rack, J. J., & de Bettencourt-Dias, A. (2020). Wavelength-Dependent Singlet Oxygen Generation in Luminescent Lanthanide Complexes with a Pyridine-Bis(Carboxamide)-Terthiophene Sensitizer. *Chem. Eur. J.*, *26*(32), 7274-7280. https://doi.org/10.1002/chem.202000587

278. Johnson, K. R., Vittardi, S. B., Gracia-Nava, M. A., Rack, J. J., & de Bettencourt-Dias, A. (2020). Luminescent lanthanide complexes with a pyridine-bis(carboxamide)-bithiophene sensitizer showing wavelength-dependent singlet oxygen generation. *Dalton Trans.*, *49*(20), 6661-6667. https://doi.org/10.1039/D0DT01034K

279. Yim, S-L., Chow, H-F., & Chan, M-C. (2014). Transition from low molecular weight non-gelating oligo(amide-triazole)s to a restorable, halide-responsive poly(amide-triazole) supramolecular gel. *Chem. Commun.*, *50*(23), 3064-3066. https://doi.org/10.1039/C3CC49323G

280. Yim, S-L., Chow, H-F., Chan, M-C., Che, C-M., & Low, K-H. (2013). Synthesis and Thermoreversible Gelation Properties of Main-Chain Poly(pyridine-2,6-dicarboxamide-triazole)s. *Chem. Eur. J.*, *19*(7), 2478-2486. https://doi.org/10.1002/chem.201203684

281. Charbonnière, L. J., Ziessel, R., Montalti, M., Prodi, L., Zaccheroni, N., Boehme, C., & Wipff, G. (2002). Luminescent Lanthanide Complexes of a Bis-bipyridine-phosphine-oxide Ligand as Tools for Anion Detection. *J. Am. Chem. Soc.*, *124*(26), 7779-7788. https://doi.org/10.1021/ja0200847

282. Harrison, I. T., & Harrison, S. (1967). Synthesis of a Stable Complex of a Macrocycle and a Threaded Chain. *J. Am. Chem. Soc.*, *89*(22), 5723-5724. https://doi.org/10.1021/ja00998a052

283. Dolomanov, O. V., Bourhis, L. J., Gildea, R. J., Howard, J. A. K., & Puschmann, H. (2009). OLEX2: A complete structure solution, refinement and analysis programe. *J. Appl. Crys.*, *42*, 339-341.